

The Development and Processing of Nickel Titanium Shape Memory Alloys Containing Palladium using Selective Laser Melting

By

Hollie L. Baker

A thesis submitted to
The University of Birmingham
for the degree of
DOCTOR OF PHILOSOPHY

Metallurgy and Materials
School of Engineering
University of Birmingham
September 2018

UNIVERSITY OF
BIRMINGHAM

University of Birmingham Research Archive

e-theses repository

This unpublished thesis/dissertation is copyright of the author and/or third parties. The intellectual property rights of the author or third parties in respect of this work are as defined by The Copyright Designs and Patents Act 1988 or as modified by any successor legislation.

Any use made of information contained in this thesis/dissertation must be in accordance with that legislation and must be properly acknowledged. Further distribution or reproduction in any format is prohibited without the permission of the copyright holder.

Abstract

Nitinol (NiTi) is a commonly used biomaterial, due to its unique superelasticity and shape memory effect. However, NiTi has a low radiopacity, so it is difficult to observe using electromagnetic radiation once inside the body. The radiopacity of NiTi can be improved by alloying with a denser, ternary element. Platinum (Pt) is a popular choice as a result of its biocompatibility and corrosion resistance. However, alloying with palladium (Pd) is fast becoming a viable alternative due to its similar properties and much lower cost. The overall purpose of this thesis is to investigate the suitability of selective laser melting (SLM) for manufacturing palladium (Pd) modified nickel-titanium (NiTi) shape memory alloys (SMAs), that can be used in biomedical devices within the human body.

This study presents a methodology for in-situ alloying Pd into NiTi using selective laser melting (SLM) to manufacture dense, defect free components. The influence of melt pool dimensions on chemical homogeneity was investigated. The laser power, laser scanning velocity and laser scan spacing were independently varied to alter the energy density of the laser and in turn, modify the dimensions of the melt pool. It has been found that the SLM process parameters can be manipulated to fully diffuse Pd into the NiTi matrix, providing a homogenous microstructure. Out of the three process parameters investigated, the scan velocity had the greatest influence on the melt pool. Thus, increasing the dissolution of Pd as a result of the Marangoni effect and increased melt pool liquid life span.

The suitability of the dense and chemically homogeneous SLM fabricated TiNiPd alloys were investigated for their use in biomedical applications. Furthermore, the effects of Pd on the properties of the binary NiTi alloy were also studied. This was performed by testing the alloy's phase transformation behaviour, cell biocompatibility, corrosion resistance, superelastic response and X-ray visibility. Overall, it can be concluded that the addition of Pd had advantageous benefits towards improving the properties of binary NiTi for use in biomedical applications. Alloying with 7 at % Pd in substitution for Ni, was found to improve the alloy's corrosion resistance, X-ray visibility and biocompatibility, thus making the ternary TiNiPd alloy a promising biomaterial.

Acknowledgements

Firstly, I would like to express my sincere gratitude to Prof. Moataz Attallah and Dr. Nick Adkins. I have been very fortunate to have them as my supervisors and I cannot express how appreciative I am for their continued advice, support and valuable feedback during my Ph.D. write up. I would also like to express my deepest thanks to my industrial Johnson Matthey supervisors Dr. Hugh Hamilton and Dr. Andrew Fones, for all the assistance and time they have provided me during the three year duration of my Ph.D. Furthermore, I am grateful to Johnson Matthey for the supply of nitinol and precious metal powders used through-out my Ph.D.

I would like to thank Dr. Parastoo Jamshidi and Dr. Sophie Constance Cox for their guidance and time on the testing performed in the Chemical Engineering department at the University of Birmingham. In addition, I would like to express my gratitude towards Dr. Erik Hughes for his support and time when working in the Biochemical Engineering department.

I'd like to thank the EPSRC and Johnson Matthey, for the provision of funding for this project through the Strategic Partnership.

Finally, I would like to express my sincere gratitude to my family and Radhika Raja for all of their encouragement, patience and endless support that they have provided me through my Ph.D.

Table of Contents

Chapter 1: Introduction, Aims and Objectives.....	1
1.1. Introduction.....	1
1.2. References.....	5
Chapter 2: Literature Review	6
2.1. The Physical Metallurgy of NiTi SMA	6
2.1.1. The NiTi Phase Diagram	6
2.1.2. The Crystal Structure of the Austenite and Martensite Phase	7
2.1.3. The Crystallographic Description of the Martensitic Transformation.....	9
2.1.4. The Temperatures Defining the Phase Transformation	14
2.1.5. The Shape Memory Effect	14
2.1.6. The Superelastic Response	16
2.2. Influencing Factors on the Phase Transformation Temperature.....	17
2.2.1. The Influence of Heat Treatment on the Phase Transformation Temperature	17
2.2.2. The Influence of Impurities on the Phase Transformation Temperature	20
2.2.3. The Influence of Palladium and Platinum on the Phase Transformation Temperature	22
2.3. The use of NiTi SMA in Biomedical Applications	25
2.3.1. Metallic Implant Material Requirements:.....	28
2.3.2 Limitations of NiTi for use in Biomedical Applications	30
2.4. The Additive Manufacturing of NiTi SMA	33
2.4.1. The Influence of Processing Parameters on NiTi Build Density: Porosity & Cracking.....	33
2.4.2 The Influence of Processing Parameters on the Microstructure of Additively Manufactured NiTi: Room Temperature Phases	38
2.4.3. The Influence of Processing Parameters on Contamination during Additive Manufacturing:.....	39

2.4.4. The Influence of Processing Parameters on the DSC Curve and Phase Transformation Temperature of Additively Manufactured NiTi:.....	40
2.4.5. The Influence of Heat Treatment on the Phase Transformation Temperature of Additively Manufactured Ni-rich NiTi:.....	44
2.4.6. The Tensile Behaviour of Additively Manufactured NiTi:	47
2.4.7 Improving the superelastic response through the use of Ni-rich NiTi SMAs.....	51
2.4.8 The Compressive Behaviour of Additively Manufactured Ni-rich NiTi.....	52
2.4.9. The Superelastic Response of Additively Manufactured Ni-rich NiTi	57
2.4.10. Micro-hardness Testing of Additively Manufactured NiTi	64
2.4.11. Selective Laser Melting ‘In-Situ’ Alloying	66
2.4.12. The Corrosion Resistance of Additively Manufactured NiTi.....	69
2.4.13. The Biocompatibility of Additively Manufactured NiTi.....	74
2.5. Current State of Knowledge on Additively Manufactured NiTi SMA.....	78
2.5.1. Conclusions.....	78
2.6. Project Aims and Objectives.....	80
2.7. Novel areas of Thesis Research	81
2.8. References.....	83
Chapter 3: Materials and Experimental Methods.....	92
3.1. Selective Laser Melting	92
3.1. Materials	94
3.1.1. Powder Blending.....	95
3.2. Powder Particle Size Distribution.....	96
3.3. Hall Flowmeter	96
3.4. Chemical Compositional Analysis.....	97
3.5. Heat Treatment.....	98
3.6. Metallurgical Sample Preparation.....	98
3.7. Chemical Homogeneity Methodology	99
3.8. Optical Microscopy.....	100
3.9. Scanning Electron Microscopy (SEM)	101

3.10. X-ray Diffraction (XRD)	102
3.11. Differential Scanning Calorimetry (DSC)	102
3.12. Mechanical Testing	102
3.12.1. Elevated Temperature Compression Testing	102
3.12.2. Hardness Testing.....	103
3.13. Micro Computed Tomography (Micro-CT).....	104
3.14. Electrochemical Testing.....	104
3.15. Cell Viability Testing.....	106
3.16. References.....	107
Chapter 4: The Influence of the SLM Processing Parameters on the Microstructure and Structural Integrity	108
4.1. Introduction.....	108
4.2: Pre-alloyed NiTi Powder Characterisation	109
4.2.1. Pd Powder Blended Mixture Characterisation.....	119
4.3. The influence of SLM Processing Parameters on the Microstructure and Structural Integrity of Binary NiTi	121
4.3.1. The Influence of SLM Processing Parameters on the Microstructure and Structural Integrity of Ternary TiNiPd	134
4.3.1 a. The In-Situ Alloying Methodology.....	142
4.1.3 b. The In- Situ Alloying Optimised Processing Parameters	149
4.4. Conclusion	150
4.5. References.....	153
Chapter 5: The Thermal Behaviour of NiTi SMA	156
5.1. Introduction.....	156
5.2. Evaporation of Elements in SLM	156
5.2.1. The Vapour Pressure of Ni and Ti	156
5.2.2. The Influence of SLM Processing Parameters on Ni Evaporation	159
5.2.3. Overcoming Ni Evaporation During SLM	165

5.3. The Influence of Post Processing Heat Treatment.....	166
5.3.1. The Effects of Homogenising Solution Heat Treatment.....	166
5.3.2. Compositional and Microstructural Analysis of Ti-rich Secondary Phases present in SLM Binary NiTi and Ternary TiNiPd.....	169
5.3.3. The Influence of Post Processing Heat Treatment on the Transformation Temperature of Ternary TiNiPd (at %):	175
5.4.1. The Influence of Pd on the Transformation Temperature of Binary SLM NiTi .	182
5.5. Conclusion	186
5.6. References.....	188
Chapter 6: An Investigation into the Suitability of SLM Pd Modified NiTi for use in Biomedical Applications.....	191
6.1. Introduction.....	191
6.2. The Superelastic Response of SLM Fabricated NiTi and TiNiPd.....	192
6.3. The Radiopacity of SLM Pd modified NiTi SMAs	201
6.4. The Biocompatibility of SLM binary NiTi and ternary TiNiPd	204
6.5. The Corrosion Resistance of SLM binary NiTi and Ternary TiNiPd.....	208
6.6. Conclusion	217
6.7. References.....	219
Chapter 7: Conclusion, Evaluation and Future Work.....	222
7.1. Overall Conclusions.....	222
7.2. An Evaluation of the SLM Process for Manufacturing Ternary TiNiPd Alloys for Biomedical Applications.....	224
7.3 Future Work.....	224
7.4. References.....	226

Table of Figures

Figure 1.1: SMA phases and crystal structure	2
Figure 1.2: A schematic diagram of a SLM machine system	4
Figure 2.1: The binary NiTi phase diagram	7
Figure 2.2: The lattice parameters of the austenite and martensite (B19') phase in a NiTi SMA	8
Figure 2.3: A schematic diagram of the habit plane at the austenite-martensite interface	9
Figure 2.4: A schematic diagram of martensitic atomic twinning	10
Figure 2.5: A schematic diagram of a twinning boundary	11
Figure 2.6: A schematic diagram of the five elements which define the twin mode	11
Figure 2.7: A schematic diagram representing the transformation from twinned to de-twinned martensite	13
Figure 2.8: The relationship between martensite and temperature	14
Figure 2.9: A schematic diagram of the shape memory effect	15
Figure 2.10: An example of a stress-strain curve for a superelastic material	17
Figure 2.11: A graph showing the relationship between M_s temperature and Ni content	18
Figure 2.12: The relationship between aging time, temperature and precipitation	19
Figure 2.13: The influence of oxygen and carbon on the M_s temperature	21
Figure 2.14: The influence of ternary elements on the M_s temperature	23
Figure 2.15: The relationship between VED and A_s and M_s temperatures	24
Figure 2.16: The crystal structure for the B2, B19 and B19' phase	25
Figure 2.17: The Stress – strain behaviour of NiTi and stainless steel compared to human body tissues	27

Figure 2.18: Common difficulties associated with machining NiTi: (a) high tool wear (b) adverse chip form (c) formation of burrs (d) grinding	31
Figure 2.19: The x-ray visibility of binary NiTi compared to $\text{Ti}_{50}\text{Ni}_{42.5}\text{Pt}_{7.5}$ (at %)	32
Figure 2.20: A stress-strain graph showing full recovery for NiTi, NiTiPd & NiTiPt	33
Figure 2.21: Micrographs showing the cross sections with different formations of porosity defined by a). scanning speed b). laser power c). scan spacing	34
Figure 2.22: Density and cross-section micrographs of the NiTi samples produced by low and high powers adjusted to a small range of energy densities	35
Figure 2.23: The relative density of SLM NiTi parts as a function of scan speed for different laser powers with optical micrographs of selected cross-sections	36
Figure 2.24: The correlation of energy density with a). Porosity fraction and b). Cracking density	38
Figure 2.25: The concentration of B2 austenite and B19' martensite phases in relation to processing parameters	39
Figure 2.26: The influence of energy input on the phase transformation behaviour for a). Ti-rich b). near equiatomic c). Ni-rich NiTi alloys.....	43
Figure 2.27: The influence of subsequent solution annealing treatments on the transformation temperature of a). Ti-rich b). Ni-rich NiTi alloy	44
Figure 2.28: The DSC response of solutionised SLM $\text{Ni}_{50.8}\text{Ti}_{49.2}$ alloys aged at a). 350° C b). 450 ° C	46
Figure 2.29: Transformation temperatures plotted as a function of aging hold time for a). 450 ° C b). 550 ° C	47
Figure 2.30: Stress- strain curves of a). vertically generated specimens b). horizontally generated specimens. Reference = conventionally manufactured NiTi	49

Figure 2.31: SEM micrograph of the fracture surface after tensile testing. The white arrows highlight unsuccessful layer fusion	49
Figure 2.32: A comparison of the tensile behaviour for wrought and additively manufactured NiTi	50
Figure 2.33: A STEM-HAADF image from a Ni- alloy to give perspective of Ni_4Ti_3 spacing and narrow B2 NiTi channels between the precipitates	52
Figure 2.34: The influence of build orientation on the compressive behaviour of additively manufactured NiTi	53
Figure 2.35: The critical stress for stress-induced martensitic transformation (solid line) and plastic transformation (dashed line) with aging time	55
Figure 2.36: The compressive stress strain behaviour for conventionally produced and SLM fabricated NiTi	56
Figure 2.37: The superelastic response of SLM $\text{Ni}_{50.8}\text{Ti}$ aged for a). The initial ingot b). SLM as-fabricated c). 30 mins 350 °C d). 1 hour 350°C e). 30 mins 600°C f). 1.5 hours 600°C, at room temperature (24°C) and body temperature (37°C)	59
Figure 2.38: The superelastic response of SLM $\text{Ni}_{50.7}\text{Ti}$ for a). HT1 aged 1 hour 550°C b). HT2 solution heat treated 3 minutes 550°C and aged 3 hours 550°C	61
Figure 2.39: The superelasticity of as-fabricated, solution annealed and 350°C, 450°C aged samples.....	62
Figure 2.40: The stress-strain response obtained at 50°C for a). sample aged at 400°C b). sample aged at 500°C	63
Figure 2.40: Vickers hardness of additively manufactured NiTi as a function of aging conditions	66
Figure 2.41: XRD results for all laser parameters: scan speed 0.05 m/s – 0.4 m/s; power = 100 W	67

Figure 2.42: Density and porosity of Ti6Al4V-xCu alloys	68
Figure 2.43: Backscattered SEM images showing the Ti64 powder particles and the Pd distribution after mixing	69
Figure 2.44: Concentration of B2 (austenite) and B19' martensite phases in additively manufactured NiTi	70
Figure 2.46: The potential dynamic polarization curves of Ti4Al4V alloys with different Cu contents	71
Figure 2.47 a). Electrochemical polarisation curve for forged + annealed Ti64	73
Figure 2.47 b). Electrochemical polarisation curves for SLM Ti64	74
Figure 2.47 c). Electrochemical polarisation curves for SLM Ti64-0.2Pd	74
Figure 2.48: Illustrations of the SLM NiTi samples used in cell testing	75
Figure 2.49: Fluorescence micrographs of NiTi specimens a). Sample I b). sample II c). sample III d). sample IV e). high mag sample I f). high mag sample II g). high mag sample III h). high mag sample IV (scale bar= 1mm)	76
Figure 2.50: The morphology of BMSCs on Ti6Al4V-xCu samples after 1, 3, 7 days incubation. (a),(e),(i): Ti6Al4V. (b),(f),(j): 2C. (c),(g),(k): 4C. (d),(h),(l): 6C	78
Figure 3.1: The Concept Laser M2 Cusing SLM System.....	92
Figure 3.2: Schematic diagram of the island scanning strategy.....	93
Figure 3.1: A schematic diagram of the plasma atomisation process	95
Figure 3.2: A schematic diagram of the roller ball mill set up	96
Figure 3.3: A diagram of the grid used to take 20 BSE SEM images across the XY plane	99
Figure 3.4: The melt pool depth measurement	100
Figure 3.5: The GILL12 potentiostat	105
Figure 3.6: Experimental set up of electrochemical tests	106

Figure 4.1: SEM micrographs a). the overall NiTi powder morphology b). the powder morphology at a higher magnification c). an irregular shaped particle d). small satellites e). a coated particle f). a dented particle g). visible dendrites on the surface of a powder particle h). connected powder particles	110
Figure 4.2: A histogram displaying the particle circularity of the 2000 powder particles tested	111
Figure 4.3: A pie chart displaying the particle circularity of the 2000 powder particles tested	111
Figure 4.4 (a): The PSD curve for the NiTi pre-alloyed powder	112
Figure 4.4 (b): The relationship between the powder particle size and oxygen content	114
Figure 4.5: a). The internal cross section of a NiTi pre-alloyed powder particle revealing internal porosity b). porosity due to molten collision c). porosity due to gas entrapment.....	115
Figure 4.6: a). A BSE image of the internal cross section of a NiTi pre-alloyed powder particle b). a SEM image of Ti ₂ Ni phase on the powder surface.....	116
Figure 4.7: EDX mapping on the surface of a pre-alloyed NiTi powder particle	117
Figure 4.8: EDX mapping of the NiTi pre-alloyed powder	118
Figure 4.8: A SEM image showing the Pd powder morphology	119
Figure 4.9: An elemental EDX map of the Ti ₅₀ Ni ₄₃ Pd ₇ (at %) powder mixture	121
Figure 4.10 (a): Porosity plotted against the laser VED	124
Figure 4.10 (b): Porosity plotted against scan spacing	126
Figure 4.11: The oxygen content of the as-fabricated SLM parts manufactured using differing VEDs.....	127
Figure 4.12: A micrograph display the porosity in SLM parts for samples manufactured using a). 100 W and 250 mm/s b). 200 W and 500 mm/s	128
Figure 4.13: The influence of scan speed on the porosity of SLM manufactured NiTi	129

Figure 4.14: The influence of high scan speeds on the porosity of SLM NiTi manufactured using a laser power of 100 W	130
Figure 4.15: A micrograph of the irregular porosity formed when processing at high scan speeds.....	130
Figure 4.16: Inter-layer cracking produced when manufacturing at scan speeds above 1000 mm/s.....	131
Figure 4.17: A surface contour plot for samples manufactured using a layer thickness of 20 μm and laser power of 100 W.....	133
Figure 4.18: Surface contour plot for samples manufactured using a layer thickness of 40 μm and laser power of 100 W.	134
Figure 4.19: The influence of scan speed on the porosity of ternary $\text{Ti}_{50}\text{Ni}_{48}\text{Pd}_2$ (at %)	136
Figure 4.20: A BSE image of the $\text{Ti}_{50}\text{Ni}_{48}\text{Pd}_2$ (at %) sample processed using the optimised processing parameters for high density and no cracking	136
Figure 4.21: a). BSE image of a Pd particle within the NiTi matrix b). EDX analysis of the Pd particle.....	137
Figure 4.22: A BSE image of a Ti powder particle within the NiTi matrix	138
Figure 4.23: The EDX line scan over the Ti powder particle within the NiTi matrix	139
Figure 4.24: EPMA mapping of Pd within the NiTi matrix	140
Figure 4.25: EPMA mapping of Pd within the NiTi matrix	141
Figure 4.26: The relationship between scan speed, melt pool depth and undissolved Pd powder particles	143
Figure 4.27: The relationship between $\frac{1}{2}$ melt pool cross sectional area and the laser VED	144
Figure 4.28: The relationship between the melt pool area, laser VED and undissolved Pd powder particles for samples processed at 80 W	145

Figure 4.29: Optical images of the melt pools processed at (a). 80 W, 500 mm/s, 56 μm (b). 80 W, 120 mm/s, 56 μm	146
Figure 4.30: EDX quantification of the white swirling phase visible under backscatter imaging	147
Figure 4.31: The relationship between scan spacing, melt pool depth and undissolved Pd powder particles	148
Figure 4.32: Optical images of the melt pools processed at (a). 80 W, 500 mm/s, 90 μm (b). 80 W, 500 mm/s, 45 μm	149
Figure 4.33: The microstructure of the $\text{Ti}_{50}\text{Ni}_{48}\text{Pd}_2$ alloy, SLM fabricated using the optimised processing parameters	150
Figure 5.1: Vaporisation curves for Ni and Ti	159
Figure 5.2: The Ni loss after SLM processing as a function of laser power and scan speed. Ni loss was measured using EDX	161
.....	162
Figure 5.3 (a): The influence of laser VED on Ni evaporation	162
Figure 5.3 (b): The influence of VED on the A_F transformation temperature	163
Figure 5.4: A NiTi alloy displaying keyhole porosity (processed at 1066.6 J/mm^3)	164
Figure 5.5: The XRD pattern for the as-fabricated NiTi manufactured using the optimised processing parameters	165
Figure 5.6: Bse image of the $\text{Ti}_{50}\text{Ni}_{48}\text{Pd}_2$ (at %) SLM alloy containing extra Ni to account for the Ni evaporation and achieve the target composition	166
Figure 5.6 (a): The DSC curves for SLM as-fabricated and solution heat treated NiTi	168
Figure 5.6 (b): The DSC curves for SLM as-fabricated and solution heat treated $\text{Ti}_{50}\text{Ni}_{48}\text{Pd}_2$	168

Figure 5.6 (c): The DSC curves for SLM as-fabricated and solution heat treated $\text{Ti}_{50}\text{Ni}_{43}\text{Pd}_7$	169
Figure 5.7 (a): The microstructure of an as-fabricated NiTi build processed at 1067 J/mm^3	
(b): The microstructure of an as-fabricated NiTi build processed at 100 J/mm^3	171
Figure 5.8: A phase contour plot showing the area fraction percentage of Ti_2Ni precipitation along the XZ plane of an as-fabricated NiTi cubic SLM part	172
Figure 5.10: EDX mapping of the $\text{Ti}_2\text{Ni(Pd)}$ precipitation within a TiNiPd matrix taken along the XY plane	172
Figure 5.11: EPMA elemental distribution maps for the $\text{Ti}_2\text{Ni(Pd)}$ intermetallic taken along the XY plane	174
Figure 5.12: A phase distribution map for solution heat treated $\text{Ti}_{50}\text{Ni}_{43}\text{Pd}_7$ (at %)	175
Figure 5.13: The DSC responses of the heat treated $\text{Ti}_{50}\text{Ni}_{43}\text{Pd}_7$ (at %)	178
Figure 5.16: $\text{Ti}_2\text{Ni(Pd)}$ precipitation in an alloy aged at (a) 350°C for 1.5 hours (b) 350°C for 3 hours (c) 350°C for 18 hours	180
Figure 5.15: The DSC curves for samples aged at 350°C and 450°C	181
Figure 5.16: The microstructure and corresponding hardness for samples (a) aged at 350°C for 1.5 hours (b) aged at 450°C for 1.5 hours	182
Figure 5.17: The A_F temperatures for binary and Pd modified NiTi	183
Figure 5.18: Literature data published on the M_S temperatures of TiNiPd alloys (16)	184
Figure 5.18 (a): The A_F temperatures of the solution heat treated binary, ternary and quaternary alloy compositions (b): The microstructure of solution heat treated $\text{Ti}_{50}\text{Ni}_{42}\text{Pd}_7\text{Cr}_1$ at % alloy (c): The DSC austenitic transformation curve for the treated $\text{Ti}_{50}\text{Ni}_{42}\text{Pd}_7\text{Cr}_1$ at % alloy	186
Figure 6.1: A stress-strain curve for the $\text{Ti}_{50}\text{Ni}_{43}\text{Pd}_7$ (at %) alloy under compression	193
Figure 6.2: A stress-strain curve for the binary NiTi under compression	194

Figure 6.3 (a): The superelastic response for the binary NiTi and ternary TiNiPd alloys when loaded to 1100 MPa and unloaded.....	195
Figure 6.3 (b): The superelastic response of the ternary TiNiPd alloy when loaded to 900 MPa and unloaded.....	196
Figure 6.4: The superelastic response for samples solution heat treated and aged for 350°C for 1.5hrs, 3hrs and 5 hrs	196
Figure 6.5: The superelastic response for samples solution heat treated and aged for 450°C for 1.5 hrs, 3hrs and 5 hrs	199
Figure 6.6: A micrograph showing the Ti ₂ Ni(Pd) precipitation in a sample solution heat treated and aged at 350°C for 1.5 hrs.....	199
Figure 6.7: A micrograph showing the Ti ₂ Ni(Pd) precipitation in a sample solution heat treated and aged at 450°C for 1.5 hrs.....	200
Figure 6.8: A micrograph showing the Ti ₂ Ni(Pd) precipitation in a sample solution heat treated and aged at 350°C for 5 hrs.....	200
Figure 6.9: SEM image of the SLM fabricated stent	201
Figure 6.10: SEM image of the SLM fabricated stent's struts	202
Figure 6.11: X-ray images comparing the x-ray absorptivity between (a) ternary TiNiPd (b) binary NiTi.....	203
Figure 6.12: The greyscale of the X-ray image across the width of the binary and ternary stents	204
Figure 6.13: A histogram showing quantitative values of the contrast of samples against the X-ray background	204
Figure 6.14: Live/dead imaging for cells seeded onto the polished surface of Ti, NiTi and TiNiPd after 1, 3 and 7 days	206
Figure 6.15: A live/dead cell.....	207

Figure 6.16: The open circuit potential of NiTi, TiNiPd (SLM fabricated) and conventionally produced NiTi ingot in PBS solution.....	209
Figure 6.17: The potentiodynamic polarisation curve for SLM binary NiTi in PBS solution	212
Figure 6.18: The potentiodynamic polarisation curve for SLM ternary $\text{Ti}_{50}\text{Ni}_{43}\text{Pd}_7$ (at%)...	212
Figure 6.19: The potentiodynamic polarisation curve for conventionally produced NiTi ingot	213
Figure 6.20: A comparison of the potentiodynamic polarisation curves for all three samples	213
Figure 6.21: An optical image showing the occurrence of pitting on the surface of the SLM fabricated NiTi alloy	214
Figure 6.22: An optical image showing a non-corroded region on the surface of the SLM fabricated NiTi alloy	214
Figure 6.23: A SEM image of the pitting corrosion on the surface of the SLM fabricated NiTi alloy (x150 magnification).....	215
Figure 6.24: A SEM image of the pitting corrosion and resultant corrosion products on the surface of the SLM fabricated NiTi alloy (x400 magnification)	215
Figure 2.25: A SEM image of the pitting corrosion on the surface of the SLM fabricated NiTi alloy (x 1500 magnification).....	216
Figure 6.26: A SEM image of the surface of the SLM fabricated ternary $\text{Ti}_{50}\text{Ni}_{48}\text{Pd}_7$ (at %) alloy (x 800 magnification).....	216
Figure 6.27: A SEM image of the surface of the conventionally produced NiTi alloy (x 800 magnification)	217

List of Tables

Table 2.1: Twinning modes of B19' martensite	12
Table 2.2: The effect of Pd and Pt on transformation temperature	22
Table 2.3: A table showing the Young's modulus of metallic implant materials	28
Table 2.4: The tensile properties for wrought and additively manufactured NiTi	51
Table 2.5: Mechanical data of compression testing to failure for a SLM fabricate Ni _{50.2} (at %)Ti alloy	54
Table 2.6: The present heat treatments used to investigate the superelastic response of SLM Ni-rich alloys	57
Table 2.7: Mechanical properties of additively manufactured NiTi	64
Table 2.8: Electrochemical data of Ti ₄ Al ₄ V alloys with different Cu contents from OCP curves and potential-dynamic polarization curves	72
Table 3.1: The technical specifications of the Concept Laser M2 machine	92
Table 4.1: The PSD data for the NiTi pre-alloyed powder.....	112
Table 4.2: A table showing the densities and flow-ability of the pre-alloyed NiTi powder..	113
Table 4.3: A table showing the internal porosity within a sample of the NiTi pre-alloyed powder.....	115
Table 4.4: The chemical composition and A _F temperature of the NiTi pre-alloyed powder.	118
Table 4.5: A table showing the quantities within 100g of the Ti ₅₀ Ni ₄₃ Pd ₇ (at %) powder mixture	120
Table 4.6: The list of parameters used during the parametric study	122
Table 4.7: The oxygen content of the pre-alloyed powder and SLM fabricated part.....	127
Table 4.8: The optimised SLM processing parameters for NiTi	132

Table 4.9: The EDX compositional analysis results for the three phases shown in figure 4.22	138
Table 4.10: The optimised SLM processing parameters to in-situ alloy elemental Pd powder into pre-alloyed NiTi powder	150
Table 5.1: ICP results of Ni loss with VED	162
Table 5.2: A comparison of the Ni content and A_F temperature for the pre-alloyed powder and SLM part fabricated using the optimised processing parameters	164
Table 5.3: A table comparing the composition before and after adding extra Ni into the powder mixture used during SLM. $Ti_{50}Ni_{48}Pd_2$ (at %) being the target composition	166
Table 5.4: The chemical composition of the secondary phase Ti_2Ni	170
Table 5.5: The chemical composition of the secondary phase $Ti_2Ni(Pd)$	173
Table 5.6: A table showing the effects of aging time on the A_F temperature and the average precipitate size	180
Table 5.8: The M_s temperature of solution heat treated binary NiTi and ternary TiNiPd alloys	183
Table 5.9: The SLM processing parameters for manufacturing TiNiPdCr	185
Table 6.1: A table showing the recoverable and irrecoverable strains of the heat treated samples	200
Table 6.2: The general properties for elements Pd, Ni and Ti	202

Chapter 1

Introduction, Aims and Objectives

1.1. Introduction

NiTi SMAs belong to a class of smart materials which exhibit two properties, superelasticity and the shape memory effect. These materials are able to memorise their shape or previous form when subjected to a thermo-mechanical treatment. Due to their unique characteristics, they have found use in a broad range of industries, including: automotive, aerospace, robotics and biomedical industry.

Arnie Ölander first discovered SMAs in 1932 but the potential of these alloys was not established until 1962, when William Buehler and Frederick Wang discovered the shape memory effect in the NiTi system (1). The basic concept behind this phenomenon can be seen in figure 1.1. The material is deformed by applying an external force but its original shape can be recovered when heated beyond a certain temperature. A few years after this discovery in 1962, the NiTi alloy became a popular material of choice in dentistry and the first NiTi superelastic brace was introduced by Andreasen in 1971 (2). Despite the expense of the NiTi SMAs its break through into the biomedical sector has meant that it has found use in many medical equipment and devices including: endodontics, implants, stents, glass frames and guide wires.

Due to their corrosion resistance and biocompatibility, NiTi SMAs were first suggested as implantable materials in the late 1960s. The first NiTi stent was produced in 1983 by Dotter's group (3). In comparison to the conventional stainless steel used, it was found that the alloy

was more compliant to bends in the vessels, hence reducing the tendency of the stent to force the vessel straight.

In 1986, NiTi was first used in orthopaedic implants, where the insertion of NiTi rods were used to correct scoliosis (4). As the alloy showed up to 8 % recoverable strain, it had similarities to the stress-strain behaviour of human bone and tissues. Due to this, it is believed the alloy improves the osseointegration of the implant.

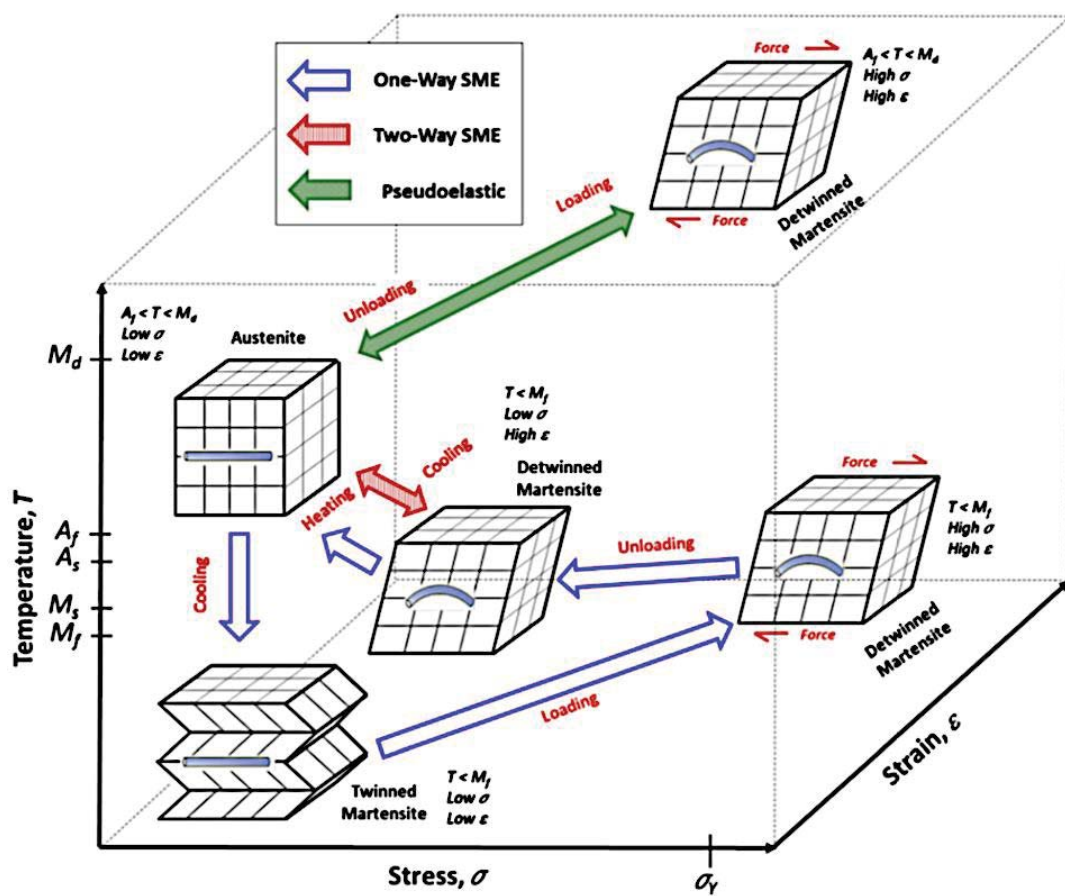


Figure 1.1: SMA phases and crystal structure (5)

The most common processing route for manufacturing NiTi is casting. The casting technique involves high temperature melting and post processing machining to form the final shape of the alloy. The two main melting methods are Vacuum Induction Melting (VIM) and Vacuum Arc Re-melting (VAR). VIM involves melting the raw materials inside a graphite crucible

under vacuum in an inert gas atmosphere. Electrical eddy currents sourced from an induction coil are induced in the graphite crucible and the electrodynamic forces results in stirring and mixing of the melt. During VAR, the furnace uses consumable electrodes that consists of the raw materials required. The electrode is heated by the argon arc and the molten alloy droplets are collected into a mould to form a cylindrical ingot (6).

These conventional casting techniques bring processing challenges such as melt segregation and contamination (7). The carbon from the crucible used in VIM, combines with the titanium to form TiC precipitates. Furthermore, due to the rapid work hardening of the alloy, machining the alloy into its final shape can cause severe tool wear.

Additive manufacturing techniques such as SLM, have emerged as a promising method for fabricating NiTi parts. The processing route enables the possibility of manufacturing complex, net shape components directly from a CAD file using metallic powders. SLM utilises a layer based technique to precisely produce a complex geometry that is expressed as a CAD file. A laser is used as a thermal heat source to selectively scan the surface of a powder bed. The heat energy input melts and consolidates powder particles. After each scan, the powder bed is lowered by a pre-defined layer thickness. New powder is spread over the previously melted layer and the process is repeated until a final 3D shaped component is produced. Figure 1.2. displays a schematic diagram of a typical SLM machine system.

As SLM can fabricate a net shaped component directly from metallic powder, it reduces the need to machine NiTi. Thus, it eliminates the tool wear which can result in additional manufacturing expenses. Furthermore, due to the direct fabrication without the need for machining, the lead time from concept to prototype is significantly reduced.

SLM can manufacture NiTi parts with precise geometries, and complex features as small as 200 microns. This would not be possible using conventional machining techniques due to the high hardness of the alloy. The reduced impurity pick up related with this manufacturing technique results in fewer brittle intermetallic phases forming. These phases have a detrimental effect on the NiTi alloy properties and will be discussed in greater detail in the following chapters.

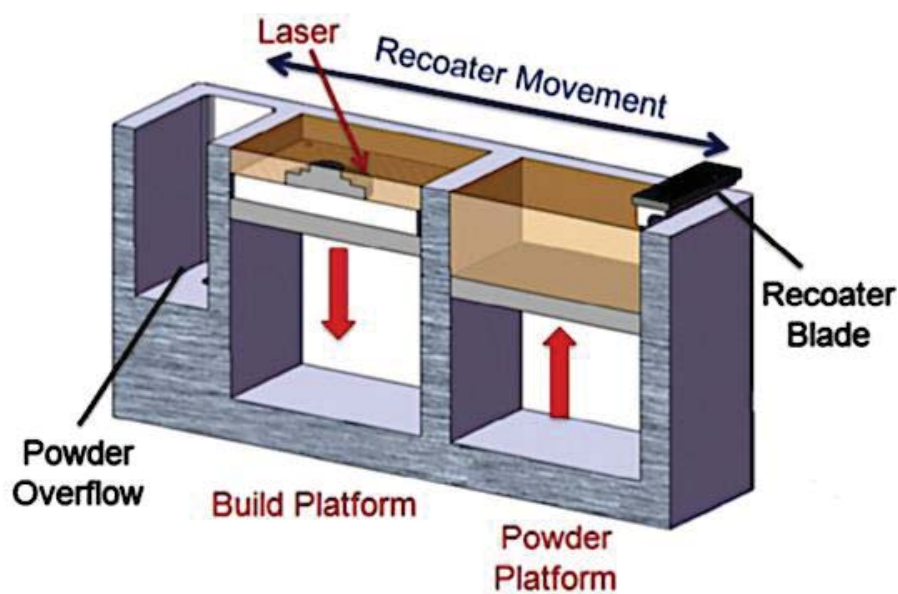


Figure 1.2: A schematic diagram of a SLM machine system (8)

1.2. References

1. Kumar PK, Lagoudas DC. Shape Memory Alloys. 2008;1.
2. De Santis R, Dolci F, Laino A, Martina R, Ambrosio L, Nicolais L. The Eulerian buckling test for orthodontic wires. *Eur J Orthod*. 2008;30(2):190–8.
3. Balcon R, Beyar R, Chierchia S, De Scheerder I, Hugenholtz PG, Kiemeneij F, et al. Recommendations on stent manufacture, implantation and utilization. *Eur Heart J*. 1997;18(10):1536–47.
4. Ryhänen J. Biocompatibility Evaluation of Nickel- Titanium Shape Memory Metal Alloy of Nickel-Titanium Shape [Internet]. Vol. 41, *Surger*. 1999. 481-8 p.
5. Mohd Jani J, Leary M, Subic A, Gibson MA. A review of shape memory alloy research, applications and opportunities. *Mater Des* [Internet]. 2014;56:1078–113.
6. Mitchell A. Melting Processes and Solidification in Alloys 718-625. *Superalloys 718, 625 Var Deriv* [Internet]. 1991;15–27.
7. Schetky LM, Wu MH. Issues in the Further Development of Nitinol Properties And Processing for Medical Device Applications.
8. Carter LN, Martin C, Withers PJ, Attallah MM. The influence of the laser scan strategy on grain structure and cracking behaviour in SLM powder-bed fabricated nickel superalloy. *J Alloys Compd* [Internet]. 2014;615:338–47.

Chapter 2

Literature Review

2.1. The Physical Metallurgy of NiTi SMA

2.1.1. The NiTi Phase Diagram

Binary NiTi is an intermetallic phase within the NiTi alloy system. As shown in figure 2.1, it has a very narrow processing window and is present at near equiatomic compositions. On the Ti-rich side of the phase diagram, the NiTi region is practically vertical at about 50 at % and bordered by a Ti_2Ni phase. This shows that the NiTi phase has no solubility for Ti and the intermetallic phase Ti_2Ni will precipitate if excess Ti is present (1).

However, on the Ni-rich side of the phase diagram, the NiTi region is sloped and neighboured by a TiNi_3 phase. Illustrating that up to 6 at % excess Ni can be dissolved into the NiTi solution at 1115 °C, as the solubility of Ni increases with temperature (2). Although TiNi_3 is the stable phase on the Ni-rich side, if a Ni-rich alloy is subjected to heat treatment, two more intermediate, meta-stable phases can form: Ti_2Ni_3 and Ti_3Ni_4 (3). The effect of these phases will be discussed in subsequent paragraphs.

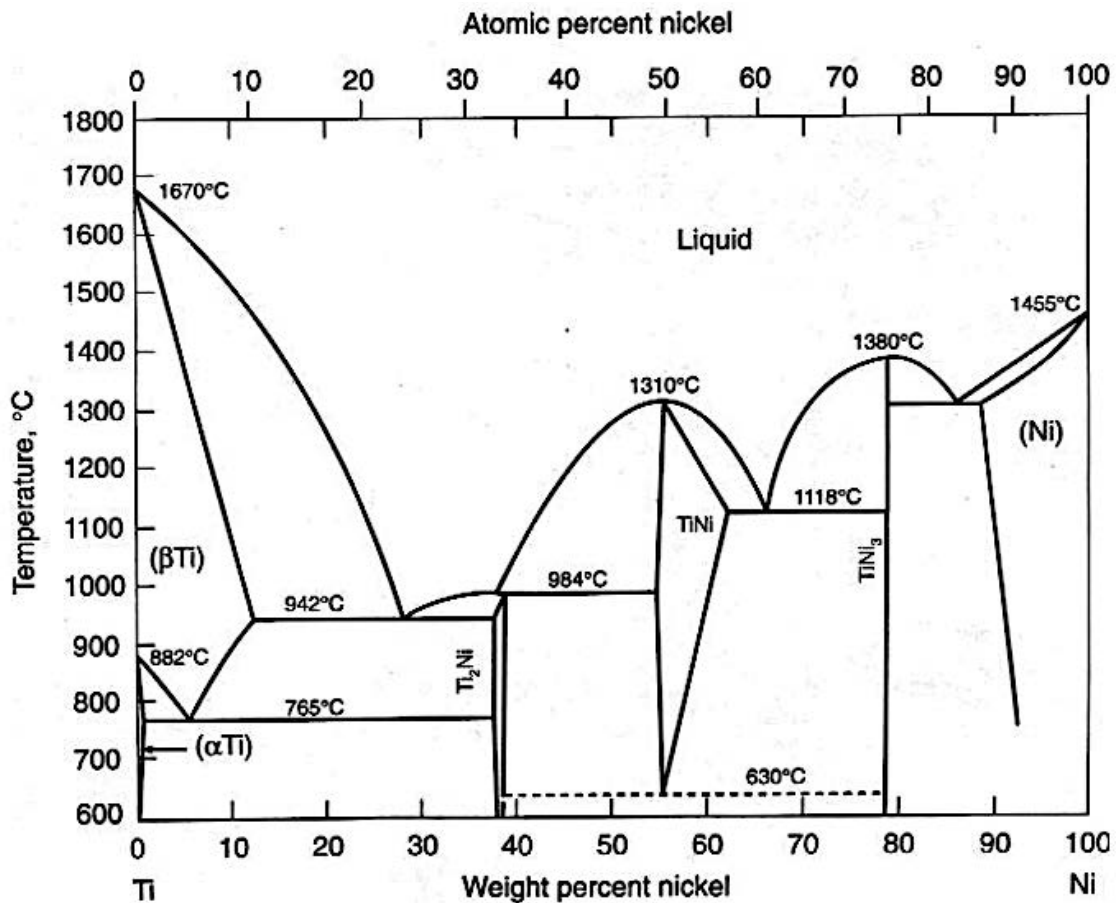


Figure 2.1: The binary NiTi phase diagram (4)

2.1.2. The Crystal Structure of the Austenite and Martensite Phase

The martensitic phase transformation is responsible for SMA's two unique characteristics: the shape memory effect and the superelastic response. The martensitic transformation is a diffusion-less, solid-solid first-order transformation (5). Due to the alloy's reversible thermo-elastic behaviour, changes in crystalline symmetry can be thermally activated. Resulting in a structural change from the austenite to martensite phase (6). Austenite is stable at high temperatures and low stress. Whereas martensite is stable at lower temperatures and higher stress (7).

The latent heat of NiTi defines the amount of heat energy required to initiate the phase transformation (8). At higher temperatures, the alloy is austenitic and has a lattice parameter

of: $a = 0.3015$ (9). It has a B2 cubic, ordered type structure and belongs to Pm-3m space group. At 1090°C, the alloy undergoes an order-disorder transformation from B2 to BCC (7).

At lower temperatures, the alloy can transform to either of the following phases: R phase or the orthorhombic B19 phase. However, at some critical temperature, the alloy will ultimately transform into a martensitic, B19' monoclinic structure with space group $P2_1/m$ (10). This phase has lattice parameters of: $a = 0.2889$ nm, $b = 0.4120$ nm, $c = 0.4622$ and $\beta = 96.8^\circ$ (11). It forms when the B2 austenite phase shears on (110) $[1\bar{1}0]$ and (001) $[1\bar{1}0]$ (12). Figure 2.2 displays the lattice parameters of the austenite and martensite phase.

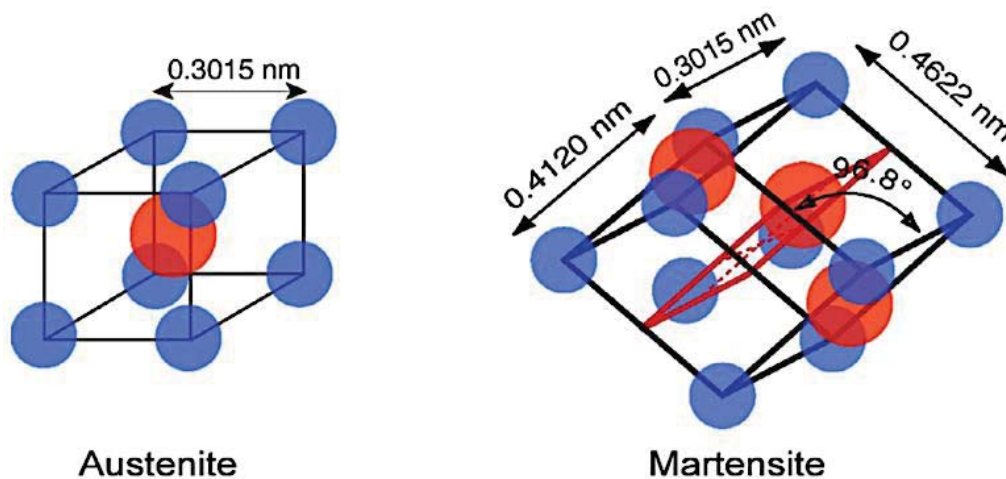


Figure 2.2: The lattice parameters of the austenite and martensite (B19') phase in a NiTi SMA (13)

The R-phase is a rhombohedral distortion of the B2 austenitic phase in the $[111]$ direction and it belongs to the $P\bar{3}1m$ space group (14). The occurrence of the R phase is dependent on alloy composition or thermomechanical treatments. It is known as an intermediate phase, with a trigonal structure and results in a two-stage phase transformation: $B2 \rightarrow R \rightarrow B19'$ (15). The orthorhombic B19 phase is known as a pre-martensitic phase which can occur before the B19' martensite. It forms by a (110) $[1\bar{1}0]$ shear on the B2 austenite structure (12).

2.1.3. The Crystallographic Description of the Martensitic Transformation

The martensitic transformation in crystallographic terms can be considered to occur in two parts: the Bain strain and the lattice invariant shear. The Bain strain refers to the lattice deformation that occurs when the alloy transforms from an austenite to a martensite lattice structure. Thus, the strain accounts for the atomic movement required (16).

During the phase transformation, as the martensite phase grows within the austenitic matrix, the interface between the two phases is called the habit plane (17). As the atoms progressively move very small amounts, the habit plane moves through each atomic layer, as shown by the schematic diagram in figure 2.3 (18). Once all the atoms have co-ordinately moved the required distance, the resulting structure is said to be fully martensitic. Thus, the Bain strain can be described as the atomic movements which are required to produce a fully martensitic structure.

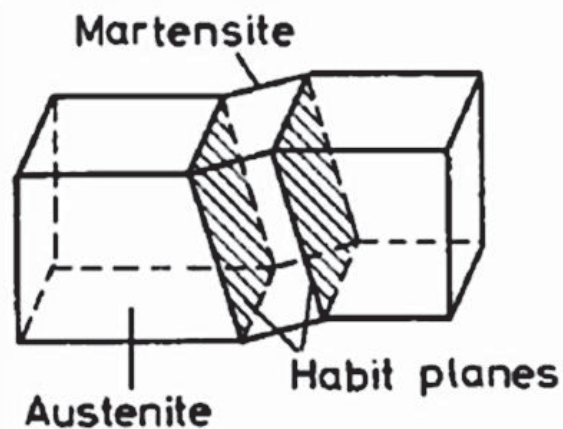


Figure 2.3: A schematic diagram of the habit plane at the austenite-martensite interface (19)

As the martensitic transformation is thermally induced, the driving force for the phase change is the difference in the total energy as a function of temperature. Meaning, the process is governed by energy minimisation and the atoms will move to produce a microstructure with

the lowest overall total energy (20). In order to reduce the microstructure's overall energy, atoms within the microstructure will twin (21), as shown in figure 2.4.

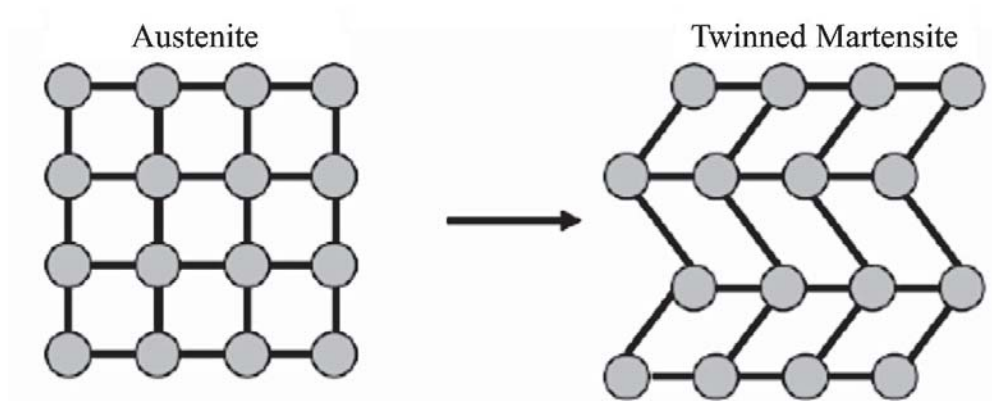


Figure 2.4: A schematic diagram of martensitic atomic twinning

Twinning relates to the co-existence of two martensitic variants. During twinning, variants of martensite, in adjacent regions of the crystal structure, undergo a simple shear. This results in atoms being displaced a fraction of an inter-atomic spacing relative to their neighbouring atoms (22). Therefore, it can be said that twins within the NiTi crystal structure are martensitic variants related by symmetry at a twinning boundary (23). As shown in figure 2.5, twinning boundaries are mirror image planes, where the atoms have the same number and types of bonds in both directions.

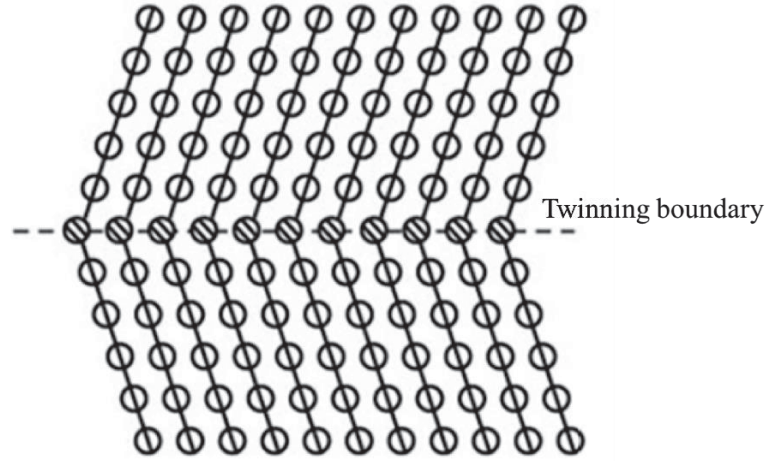


Figure 2.5: A schematic diagram of a twinning boundary (24)

Martensitic twins can be characterised by five elements which are systematically shown in figure 2.6. The elements: K_1 – represents the twinning plane, η_1 – represents the twinning shear direction, K_2 – represents another undistorted plane, η_2 – represents the intersection of K_2 and the plane of shear, s - represents the magnitude of twinning shear. Lattice points before shear are represented by the white circles and the black show the lattice points after shear. The dashed line shows two units of the original lattice before shear and the solid lines represent a unit cell for each of the lattices after shear (25).

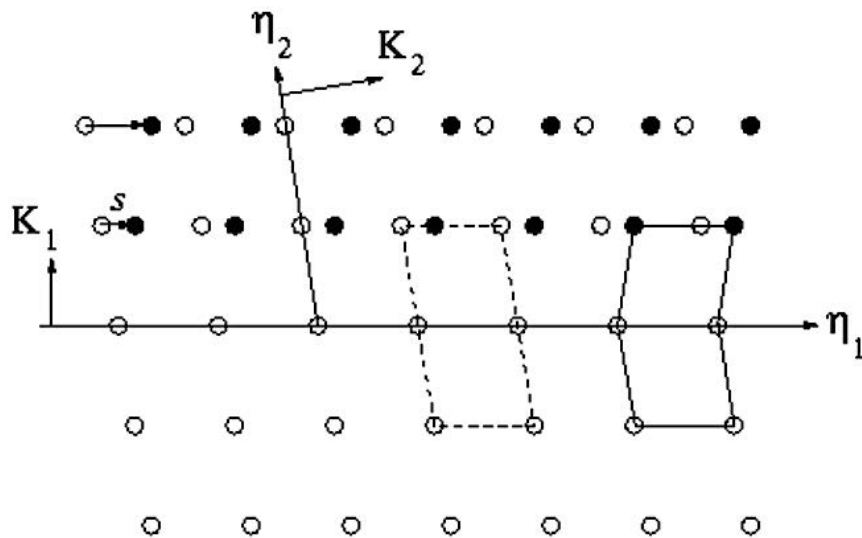


Figure 2.6: A schematic diagram of the five elements which define the twin mode

To create a twin by the shearing process during the martensitic transformation, the original lattice, represented by the dashed lines, must be able to be recovered. To enable this reversible, structural change, different types of twinning occur:

1). Type I twinning: Two lattice vectors lie on the K_1 plane, and the third lattice vector is parallel to the η_2 direction. K_1 and η_2 have rational indices and K_2 and η_1 are irrational. Thus, the crystals between each are symmetrical to the K_1 plane.

2). Type II twinning: Two lattice vectors lie on the K_2 plane, and the third lattice vector is parallel to the η_1 direction. K_2 and η_1 have rational indices and K_1 and η_2 are irrational. Thus, a crystal is related to its neighbouring crystal by rotating 180° around the η_1 .

3). Compound twinning: As type I and type II are connected, K_1 , K_2 , η_1 , η_2 all have rational indices, meaning the twinned structure has symmetrical properties of both type I and type II twinning.

The possible twinning types in B19' martensite are shown in table 2.1.

Table 2.1: Twinning modes of B19' martensite (26)

Twinning modes of B19' martensite						
Twinning mode	K_1	η_1	K_2	η_2	s	
{ $\bar{1}\bar{1}1$ }	$(\bar{1}\bar{1}1)$	$(\bar{1}\bar{1}0)_p$	$[0.540430.459571]$	$(0.246950.506111)$	$[\bar{2}\bar{1}1]$	0.30961
	$(\bar{1}11)$	$(\bar{1}01)_p$	$[0.540430.459571]$	$(0.246950.506111)$	$[\bar{2}11]$	0.30961
{ 111 }	(111)	$(101)_p$	$[\bar{1}.511720.511721]$	$(\bar{0}.668750.337501)$	$[211]$	0.14222
	$(1\bar{1}1)$	$(1\bar{1}0)_p$	$[\bar{1}.511720.511721]$	$(\bar{0}.668750.337501)$	$[2\bar{1}1]$	0.14222
{ 011 }	(011)	$(001)_p$	$[1.572711\bar{1}]$	$(0.720531\bar{1})$	$[011]$	0.28040
	$(01\bar{1})$	$(010)_p$	$[1.5727111]$	$(\bar{0}.7205311)$	$[01\bar{1}]$	0.28040
{ 011 }	$(0.720531\bar{1})$		$[011]_p$	(011)	$[1.572711\bar{1}]$	0.28040
	$(\bar{0}.7205311)$		$[010]_p$	$(01\bar{1})$	$[\bar{1}.5727111]$	0.28040
Compound	(001)	$(0\bar{1}1)_p$	$[100]$	$[100]_p$	$[001]$	0.23848
	(100)	$(100)_p$	$[001]$	$[0\bar{1}1]_p$	$[100]$	0.23848
{ $20\bar{1}$ }	$(20\bar{1})$	$(41\bar{1})_p$	$[\bar{1}0\bar{2}]$	$[\bar{1}22]_p$	$[100]$	0.4250

The remaining part of the martensitic transformation is referred to as the lattice invariant shear. As the martensitic phase has a different shape to that of the original austenite, the shape must be altered to accommodate for the alloy's new structure. Thus, the lattice invariant shear can be described as an accommodation step. This accommodation can take place in two ways: slip or twinning. As NiTi SMA exhibit reversible deformation with no volume change, the twinning mechanism is required. For shape changes to occur in a reversible manner, twinning must be the dominant accommodation method as slip involves the breaking of atomic bonds.

When martensitic NiTi is deformed, the applied stress will cause the martensite to initially deform elastically. Continued stress will cause the twin boundaries to move through the structure. These moving boundaries will re-orientate the martensitic twins into a preferred variant that has the most energetically favourable orientation for the applied stress. The resultant structure is called de-twinned martensite, as shown in figure 2.7.

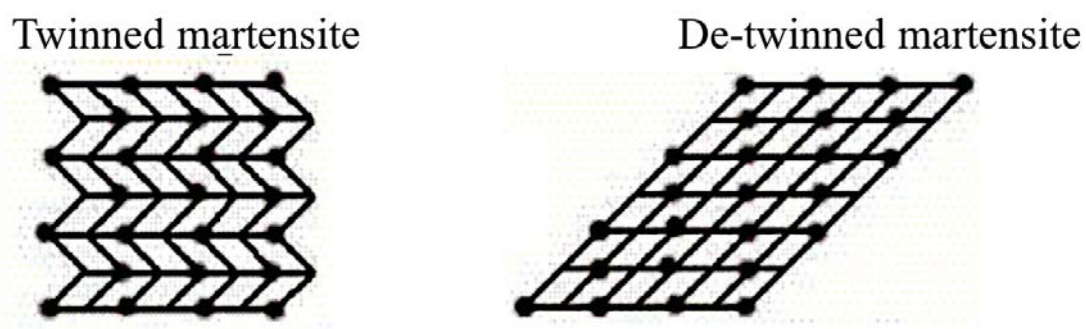


Figure 2.7: A schematic diagram representing the transformation from twinned to de-twinned martensite

2.1.4. The Temperatures Defining the Phase Transformation

Four temperatures define the martensitic phase transformation for SMA. If the alloy is fully austenitic and cooled, at a specific temperature called the M_s , martensite will start to form. The transformation will proceed until the M_f temperature. At this point the alloy is fully martensitic. On heating, a reverse transformation will occur. A_s is the temperature at which austenite starts to form, and A_f is the temperature at which alloy is fully austenitic. The relationship between the martensite content and phase transformation temperature can be seen in figure 2.8.

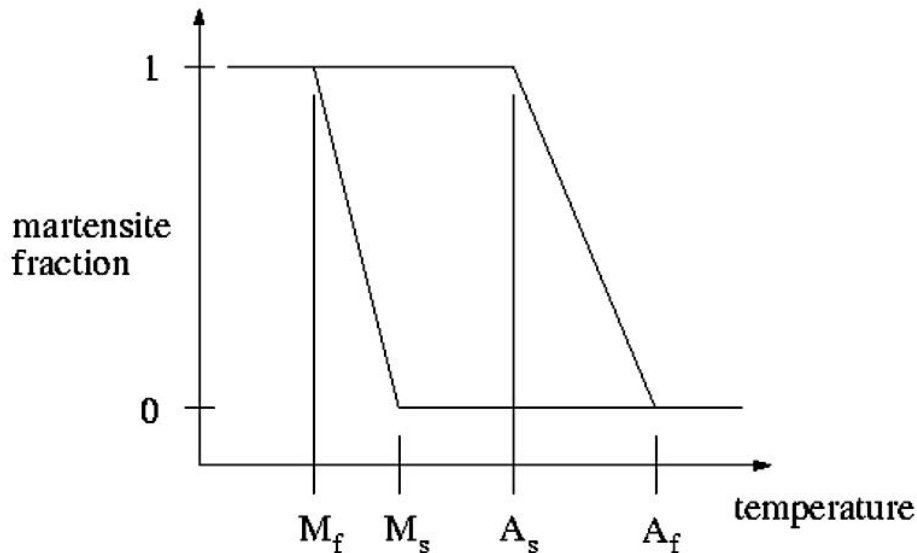


Figure 2.8: The relationship between martensite and temperature (27)

2.1.5. The Shape Memory Effect

As mentioned previously, the martensitic transformation and its thermo-elastic behaviour is responsible for NiTi's two unique characteristics: shape memory effect and the superelastic response. The shape memory effect involves a temperature-induced transformation and it refers to the alloy's ability to memorise a pre-determined structure (28). When in the martensitic

phase, the material is soft, malleable and easily deformed. However, the austenitic phase is hard and rigid.

The austenite is the parent phase and stable at high temperatures. As shown in the schematic diagram in figure 2.9, in a stress-free environment, austenite will transform to martensite when cooled. There are no macroscopic changes due to the twinned martensitic structure. Twinned martensite will stay stable at any temperature below the A_s . When applying stress, the self-accommodating twinned variants will re-orientate to a preferred orientation, to produce de-twinned martensite. This means reversible deformation can take place in the martensitic phase because the strain is accommodated by twinning, as opposed to slipping. Thus, by deforming the material at temperatures below the A_s , the original shape of the parent, austenite phase can be recovered once heating above the A_f , as this structure is the most stable and energetically preferred at higher temperatures.

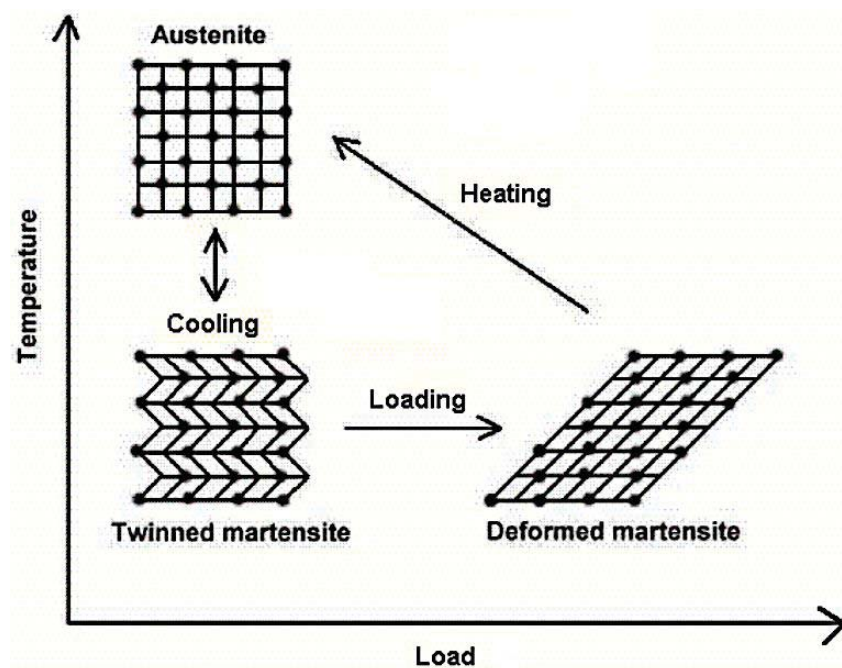


Figure 2.9: A schematic diagram of the shape memory effect

Recovering an original shape by heating above the A_f is called the one-way shape memory effect. However, the ability of a SMA to recover a shape upon heating and return to an alternate shape upon cooling below the M_f is called the two-way shape memory effect (29).

2.1.6. The Superelastic Response

The superelastic response is due to a stress-induced martensitic transformation. Unlike the shape memory effect, it occurs without any changes in temperature.

As shown in figure 2.10, when stress is applied at temperatures above the A_f , the alloy will elastically deform until a critical stress is reached. At this critical stress, a stress-induced martensitic transformation occurs. During loading, deformation is accommodated by de-twinned martensite. As the stress-induced phase transformation progresses, the alloy undergoes a significant increase in strain with little corresponding increase in stress, creating a stress plateau. As martensite is the stable phase under high stress, the material will stay in the deformed state during loading. However, once this load is removed, the martensitic phase is less energetically favourable and unstable at temperatures above the A_s . As the load is removed, the reduction in stress decreases the strain. The stress will continue to decrease and the strain will be recovered as the stress-induced martensite reverts to the austenitic phase.

Recoverable strains of up to 8% in superelastic NiTi alloys have been reported. However, it is vital to know the yield stress of the material, as loading past this point will cause plastic deformation as the alloy will deform by slip.

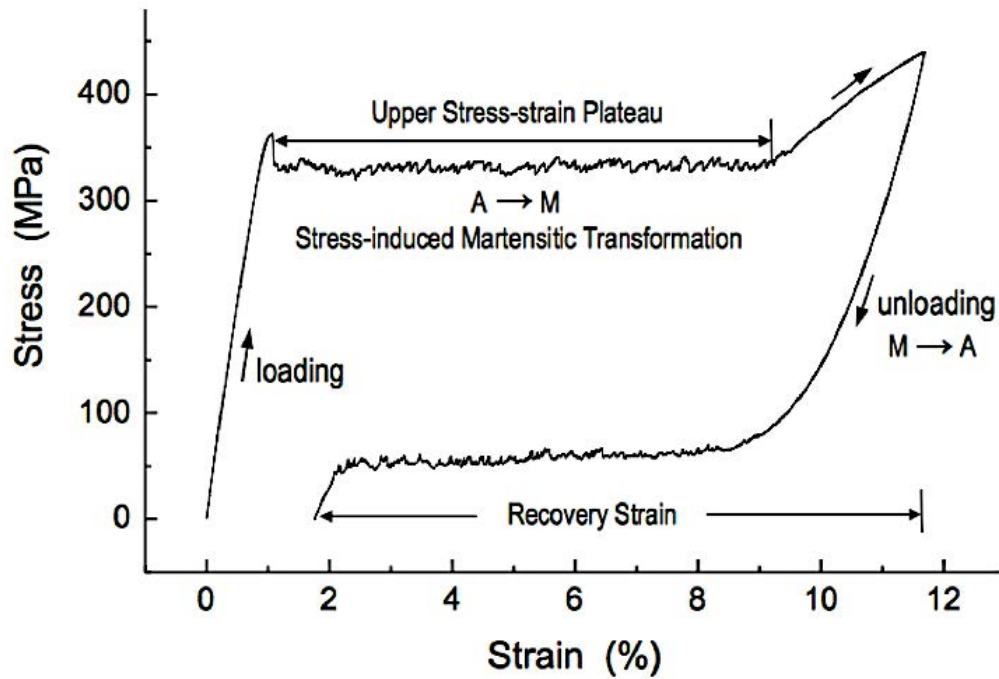


Figure 2.10: An example of a stress-strain curve for a superelastic material (30)

2.2. Influencing Factors on the Phase Transformation Temperature

2.2.1. The Influence of Heat Treatment on the Phase Transformation Temperature

Due to the solubility differences of Ni and Ti in solution, the alloy's transformation temperature is extremely sensitive to alloy composition. A 0.1 at % change in Ni can alter the M_s temperature by as much as 10 °C (31). Figure 2.11 shows that the M_s transformation temperature will stay constant at approximately 340 K, regardless of increases in Ti content. However, as the alloy composition increases in Ni, the M_s transformation temperature drastically decreases.

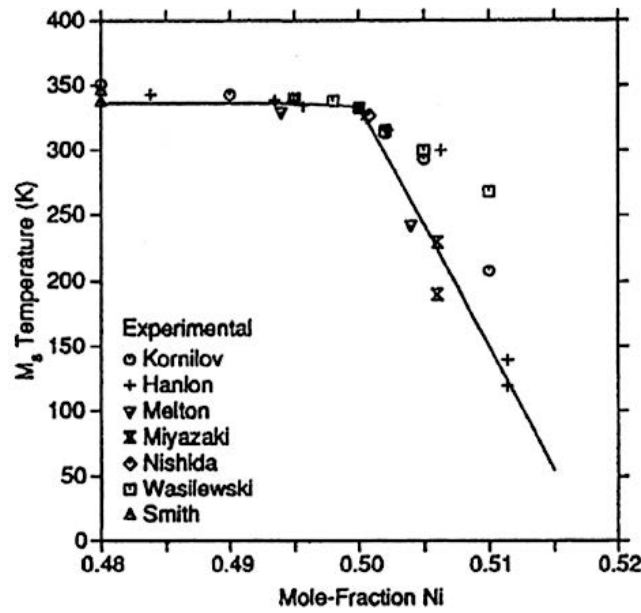


Figure 2.11: A graph showing the relationship between M_s temperature and Ni content (32)

As the phase transformation can be modified by tailoring the composition, it means NiTi alloys can be modified for certain applications. For example, applications requiring a low transformation temperature will use Ni-rich compositions. Whereas, high temperature applications will seek Ti-rich alloys.

In addition to controlling the composition, thermomechanical heat treatments can also tailor the transformation temperature through the formation of precipitates. When a Ni-rich NiTi alloy is rapidly quenched from high temperatures, the over-stoichiometric phase can reach a metastable state without the precipitation of secondary, intermetallic phases. However, once this metastable alloy is heat treated, it will reach a thermodynamic stable state by the diffusion and precipitation process (33). The occurrence of secondary phases or precipitates deplete Ni or Ti from the matrix, and this change in composition leads to an increase or decrease in the phase transformation temperature.

As mentioned previously, Ni_3Ti_2 , Ni_4Ti_3 and TiNi_3 are phases which can occur in Ni-rich alloys. As Ni_3Ti_2 is stable up to 680°C , and Ni_4Ti_3 is meta-stable within that range, ageing treatments can be performed to influence the formation of these phases. When aging a Ni-rich alloy at low temperatures for short periods of time, the meta-stable Ni_4Ti_3 will precipitate in the NiTi matrix. When increasing the aging time and temperature, the Ni_4Ti_3 will absorb into the matrix and meta-stable Ni_3Ti_2 will form. Only at very high temperatures and aging times will the stable TiNi_3 phase precipitate and the meta-stable Ni_3Ti_2 dissolve into the matrix (12). The relationships between aging treatment and Ni-rich precipitation can be shown in figure 2.12.

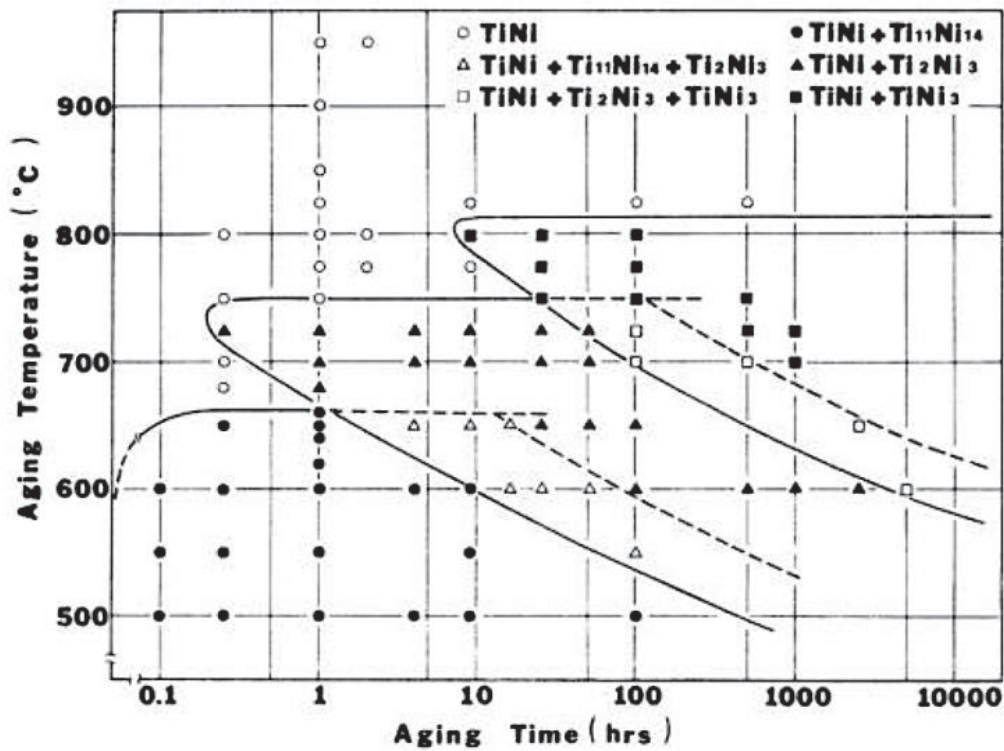


Figure 2.12: The relationship between aging time, temperature and precipitation (34)

In addition to altering the phase transformation temperature, the formation of these precipitates also affect the martensitic transformation by creating stress fields within the B2 matrix (35). This can lead to the formation of an R-phase, turning the phase transformation into a two-step process: $\text{B2} \rightarrow \text{R} \rightarrow \text{B19}'$. The transition from B2 austensite to the R-phase exhibits a

transformation strain of around 1% (36). The transformation from the R-phase to B19' martensite has a 10% transformation strain. Creating a two-step transformation is more energetically favourable when overcoming the overall resistance for the B19' transformation (37). This is because the transformation is split into two transformations both with lower partial energy barriers.

It has also been reported that Ni_4Ti_3 acts as nucleation sites for martensite. Thus, reducing the critical stress needed to start the transformation. Furthermore, the precipitation hardening effect of the Ni_4Ti_3 particles lead to an increase in the yield strength. In turn, this can have a positive effect on the superelastic response of the alloy.

2.2.2. The Influence of Impurities on the Phase Transformation Temperature

Due to the high reactivity of Ti, NiTi is extremely sensitive to oxygen and carbon contamination. The solubility of oxygen in the NiTi matrix is very low at around 0.045 at %. Thus, oxygen can either dissolve into the matrix as an interstitial impurity or form an oxide phase: Ti_2NiO_x (38). The precipitation of Ti_2Ni in Ti-rich alloys can also encourage the development of this brittle, Ti_2NiO_x phase, as Ti_2Ni picks up oxygen to form the thermodynamically stable Ti_2NiO_x (39).

The presence of Ti_2NiO_x depletes Ti from the matrix. This produces a composition that is richer in Ni and a decrease in the transformation temperature. The influence of the oxygen content on the M_s temperature can be predicted using the following equation:

$$M_s (\text{°C}) = 78 - 92.63 \times X_{\text{O}} (\text{wt. \%})$$

Where M_s represents the start temperature of the martensitic transformation and X_O is the oxygen content (40).

Unlike oxygen, carbon has no solubility in the NiTi matrix and forms a carbide called TiC (38). The presence of this carbide reduces the transformation temperature of the alloy by depleting Ti from the matrix. Figure 2.13 shows the influence of oxygen and carbon on the M_s temperature.

According to the standard for wrought NiTi SMA for medical devices and surgical implants (ASTM F2063), the maximum allowable content of carbon is 0.02 wt % (and of oxygen is 0.05wt%). Vacuum induction melting (VIM) and vacuum arc re-melting (VAR) are the two most common methods for fabricating NiTi alloys. However, VIM uses graphite crucibles, meaning there is a high probability of carbon pick up as the melt contacts the crucible. During VAR, the crucible is surrounded by an induction coil which eliminates the risk of crucible-melt interaction. Thus, carbon contamination is reduced and VAR is viewed as a much cleaner method (41).

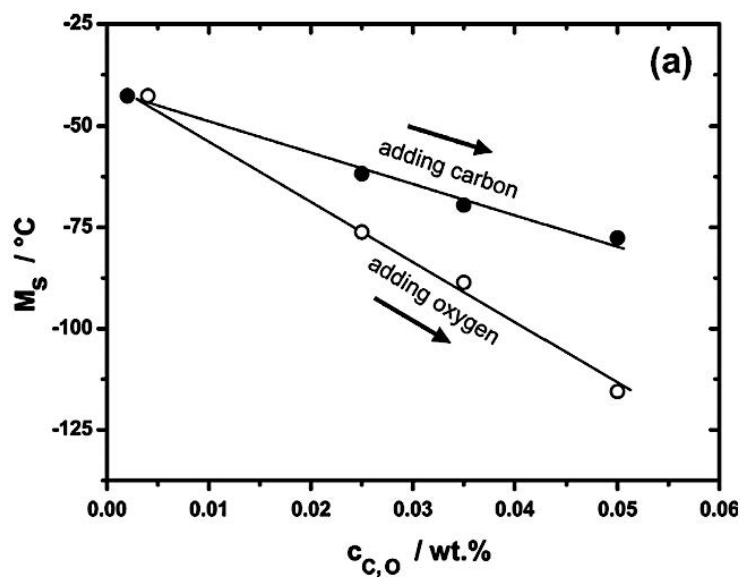


Figure 2.13: The influence of oxygen and carbon on the M_s temperature (42)

2.2.3. The Influence of Palladium and Platinum on the Phase Transformation Temperature

Many ternary elements can be added to binary NiTi SMA to modify and tailor their transformation temperatures. Platinum and palladium can be alloyed into NiTi as a ternary element for both low and high temperature applications. Replacing Ni in an equi-atomic NiTi alloy with up to 10 at % of either element can initially depress the transformation temperature. However, past this concentration, the transformation temperature increases linearly with Pt or Pd content, as shown in table 2.2 and figure 2.14.

Table 2.2: The effect of Pd and Pt on transformation temperature (43)

Elemental Composition (at%)	M_s Temperature (°C)
Ti ₅₀ Ni ₄₀ Pd ₁₀	-26
Ti ₅₀ Ni ₄₀ Pt ₁₀	-10
Ti ₅₀ Pd ₅₀	563
Ti ₅₀ Pt ₅₀	1040

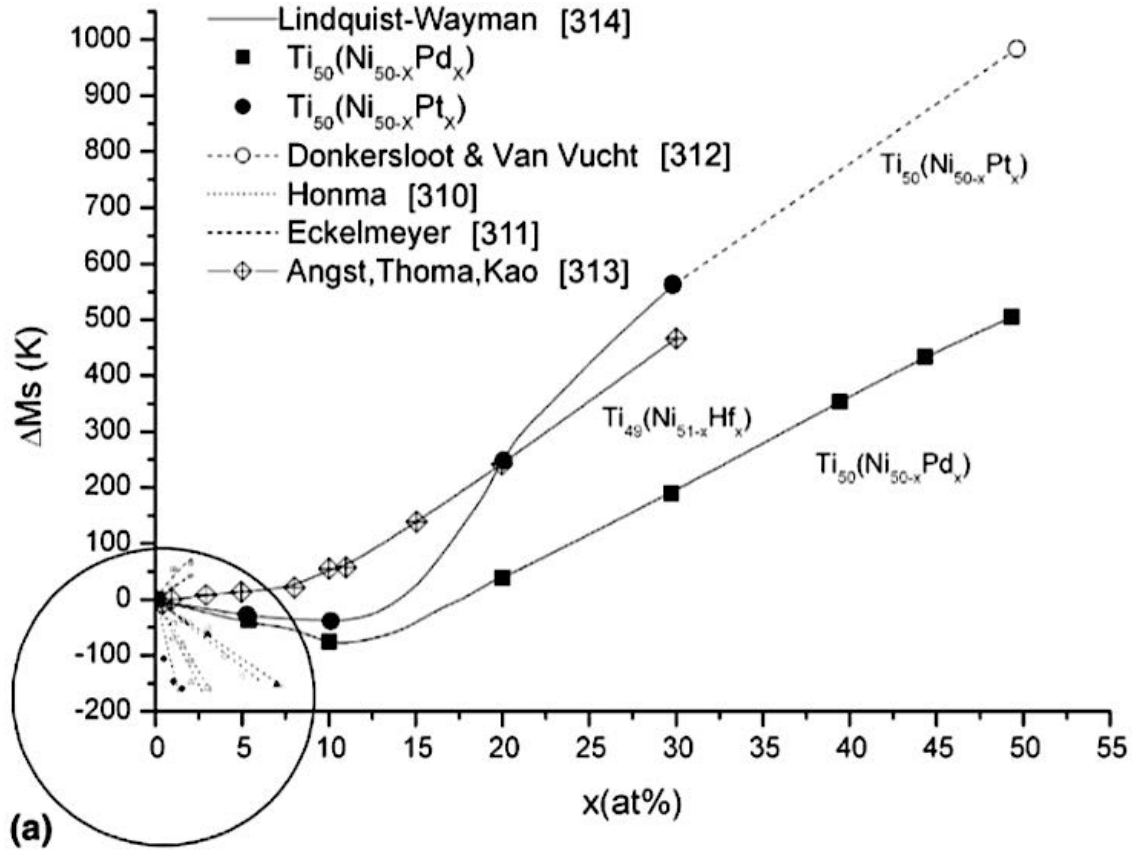


Figure 2.14: The influence of ternary elements on the M_s temperature (12)

To explain this, *Zarinejad et al.* found correlations between the electronic band structure of ternary NiTi SMA and their transformation temperatures. The alloy's average valence electron concentration (c_v) helps to fundamentally explain the relationship between alloying element and transformation temperature (43).

Valence electrons are considered the outer-shell electrons which participate in chemical bonding. They also act to bond non-valence electrons and the nuclei together. Non-valence electrons contribute towards the total atomic volume of the alloy.

NiTi alloys with a higher concentration of c_v , also have larger valence electron densities (VED). VED refers to the number of valence electrons in the unit volume of the crystal. A trend can be seen between the VED and the A_s and M_s temperatures in figure 2.15.

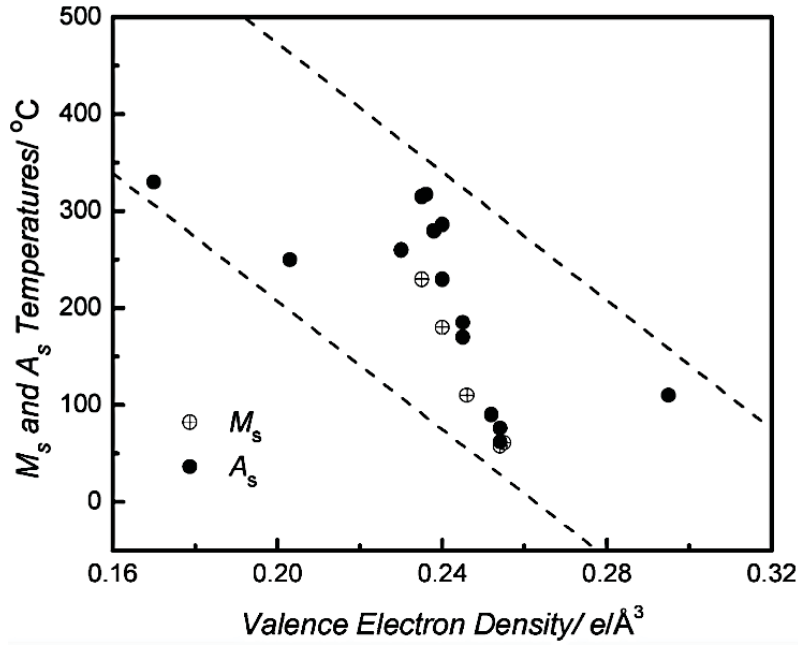


Figure 2.15: The relationship between VED and A_s and M_s temperatures (43)

Alloying a ternary element into NiTi, effects its elastic constants due to changes in the electronic structure and interatomic bonding. When alloying with up to 10 at % Pd or Pt, the alloy's electronic band structure alters as the concentration of valence electrons increases. This increase in VED translates to a strengthening of bonds and an increase in the elastic constants of the B2 phase. There is an increase in the shear modulus of the basal plane (c') and the shear modulus of the monoclinic plane (c_{44}). c' represents the resistance for $\{110\} \langle 1\bar{1}0 \rangle$ shear, and c_{44} represents the resistance for $\{001\} \langle 100 \rangle$ shear (12).

When cooling the Pd or Pt modified NiTi in its B2 austenitic parent phase towards the critical value required for the monoclinic martensitic transformation, a pre-martensitic softening occurs forming a B19 orthorhombic structure. This produces a hardening of the elastic constants and results in an increase in the energy barrier for the B19' martensitic transformation. Consequently, more cooling is required before the B19 pre-martensitic orthorhombic structure reaches the critical value for the B19' monoclinic martensitic

transformation (12). Thus, a decrease in the overall phase transformation temperature occurs.

The B2, B19 and B19' crystal structures can be seen in figure 2.16.

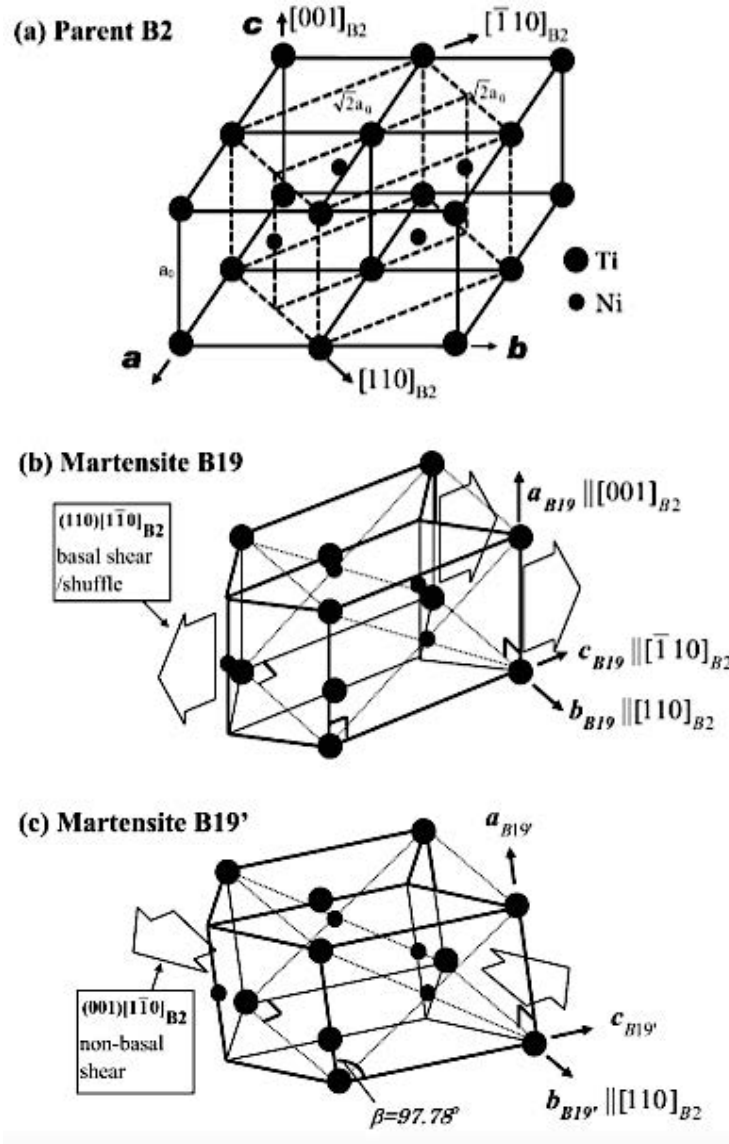


Figure 2.16: The crystal structure for the B2, B19 and B19' phase (12)

2.3. The use of NiTi SMA in Biomedical Applications

NiTi is an exceptionally successful material used in the biomedical industry. Metallic orthopaedic and cardiovascular implants can especially take advantage of NiTi's unique characteristics:

1). Cardiovascular applications – Angioplasty is a method used to treat blocked arteries or blood vessels. Small devices called stents are used to open the narrowed artery or blood vessel to aid the flow of blood. There are two types of stent: Balloon expandable stents and self-expanding stents.

Balloon stents are conventionally made using stainless steel and are very stiff. This lack in flexibility can often cause problems for the patient. Stents are commonly implanted in vessels that are close to the surface of the body, making them particularly vulnerable to impact forces. Due to stainless steel's lack of elasticity, these forces can cause the stent to plastically deform and collapse within the vessel (44).

Self-expanding stents are the most favourable type of stent to use. Their ability to reversibly deform helps to aid minimally invasive surgeries (41). In order to utilise NiTi's superelastic behaviour, the stent requires a fully austenitic structure at body temperature. When a load is applied to a stent, a stress-induced martensitic transformation occurs and the stent elastically deforms and collapses. The collapsed stent is then placed inside a small delivery portal which facilitates the insertion of the stent into the body. Additionally, the delivery portal continues to exert a stress so that the stent remains in the deformed martensitic state. Once placed inside the body, the delivery portal is removed and the stress being applied on the stent is removed. As the A_f temperature is below that of the human body, the reduction in load results in the deformed, stress-induced martensitic stent transforming back to the austenitic phase. Thus, returning to its original austenitic shape (45).

Vascular implants, such as stents, take advantage of NiTi's low stiffness and stress-strain behaviour as vessels are very tortuous. From figure 2.17, similarly to bone and tendon, over a

constant stress, NiTi shows high elasticity and can reversibly deform up to 8% strains. Stiffer stent materials such as stainless steel, are deployed in a straight configuration once inside the body. This forces the vessels to become straight which can ultimately lead to high bending stresses. However, stents made from NiTi are much more accommodating and can contour to the vessel wall, reducing bending stresses (45).

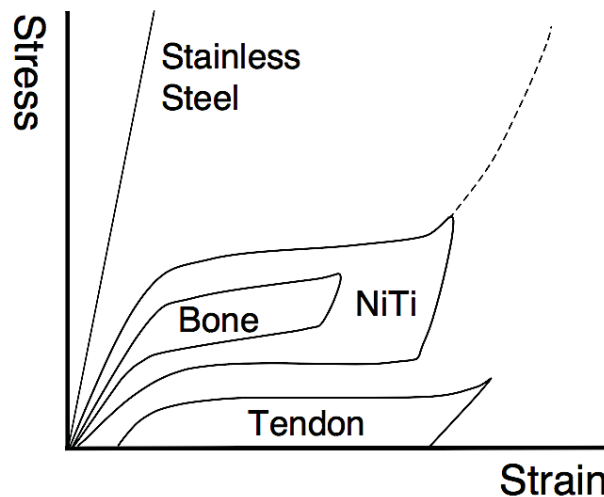


Figure 2.17: The Stress – strain behaviour of NiTi and stainless steel compared to human body tissues (46)

2). Orthopaedic applications – Due to NiTi’s similarity in Young’s modulus to that of human bone, it is a desirable material to be used in metallic implants for hip or knee replacements. Conventional implant materials such as stainless steel or Ti are much stiffer than bone. Table 2.3 shows the Young’s modulus of metallic implant materials in comparison to the Young’s modulus of bone. Large differences between the elastic modulus of the implant and bone can lead to stress shielding. This effect will weaken the bone and deteriorate the implant-bone interface. The presence of a much stiffer implant results in a redistribution of loads from the surrounding tissue to the implant itself. Consequently, the surrounding bone issue degrades, potentially leading to aseptic loosening. Implant loosening is one of the most common reasons for implant failure and if revision surgery is not implemented, it can reduce the implant life span and lead to catastrophic failure (47). Thus, NiTi is the most mechanically similar metal in

comparison to biological materials. Orthopaedic implants such as hip implants utilise this to promote bone growth and healing as the alloy can share adequate loads with the surrounding tissue.

Table 2.3: A table showing the Young's modulus of metallic implant materials (48)

Material	Density (g/cm³)	Young's Modulus (GPa)
Nitinol	6.45	Austenite: 53.5 Martensite: 29.2
Stainless Steel (316L)	7.95	193
Titanium (Ti-6Al-4V)	4.43	113.8
Bone	1.7 -2	0.2 – 19.4

Since NiTi cardiovascular and orthopaedic implants are long term implantable devices, biocompatibility is important. Although NiTi is considered biocompatible, appropriate surface treatments must be carried out to passivate the surface layer and reduce the risk of Ni release into the human body (47).

2.3.2. Metallic Implant Material Requirements:

Metallic implant materials improve the quality of human life by substituting for damaged structural components and restoring lost functions within the human body. Despite exploiting NiTi's shape memory and superelastic properties, the alloy still possesses many of the required properties for long-term metallic implants.

High strength is required to avoid fracture. Furthermore, ductility is needed to avoid brittle fracture under mechanical loading. A high yield strength needs to be coupled with a similar Young's modulus to that of human bone.

High wear and corrosion resistance are required to reduce the release of non-biocompatible metal ions from the implant into the body. The accumulation of toxic dissolved metal ions can accumulate in bodily tissues that are near the implant. They can also be transported to other parts of the body, possibly decreasing human life. Furthermore, as wear debris is biologically active, it can damage the bone in contact with the implant by inducing severe inflammatory responses (49).

Osseointegration is required for successful bone healing. When an implant material is unable to bond with the surrounding bone tissue, it leads to the formation of fibrous tissue around the implant and can promote implant loosening (50).

Biocompatibility refers to the ability of a material to exist in contact with tissues without producing an unacceptable amount of damage to the human body. As all implant materials will cause a foreign body reaction, the degree of biocompatibility is related to the extent of this reaction. Despite atomic bonding forces, making it difficult for atoms to easily leave the bulk material, the biocompatibility of NiTi is often questioned. This is because of Ni being in the presence of corrosive bodily fluids. The dissolution of this ion into the body is a cause for concern due to its toxic, allergic and carcinogenic effects (51).

It can be said that the biocompatibility of NiTi reflects its corrosion resistance. The material's corrosion resistance arises from the formation of a passive, protective Ti_2O_3 layer. This layer acts as a chemical and physical barrier to inhibit the release of harmful metal ions. *Wever et al.* stated that NiTi has good short-term biocompatibility and a Ni ion release similar to stainless steel (52). *Es-Souni et al.* concluded that the corrosion resistance, hence the biocompatibility, depended on the surface topography and finish (52). Rough and inhomogeneous surfaces can

promote corrosion (53). The corrosion resistance of the alloy can be improved by chemical treatments and passivation which lead to the build-up of smooth and dense protective Ti_2O layers. Besides Ti, both in vitro and in vivo studies showed that NiTi were more biocompatible than conventional implant metals (stainless steel, Co-Cr-Mo) (47).

2.3.2 Limitations of NiTi for use in Biomedical Applications

One of the main limitations for using NiTi alloys in biomedical devices is the challenges it presents when trying to fabricate the alloy into a required shape. Medical devices require highly accurate and precise geometries to the micron size. However, machining the alloy is extremely difficult due to its rapid work hardening (54). Furthermore, as NiTi has poor thermal conductivity, great heat is generated during machining and consequently due to the alloy's thermo-elastic behaviour, a phase transformation initiates. Machining in the austenitic phase is challenging due to its high strength and toughness. These properties generate considerable tool wear which degrade the machinability of the alloy. Loading during machining can initiate a stress induced martensitic transformation. Due to the elasticity and ductility of the martensite phase, burr formation can arise. The martensite phase generates a thicker burr than the austenite phase. Reducing the cutting speed can thin the burr (55). However, this is time consuming and not economically viable in certain situations. Common machining limitations can be seen in figure 2.18.

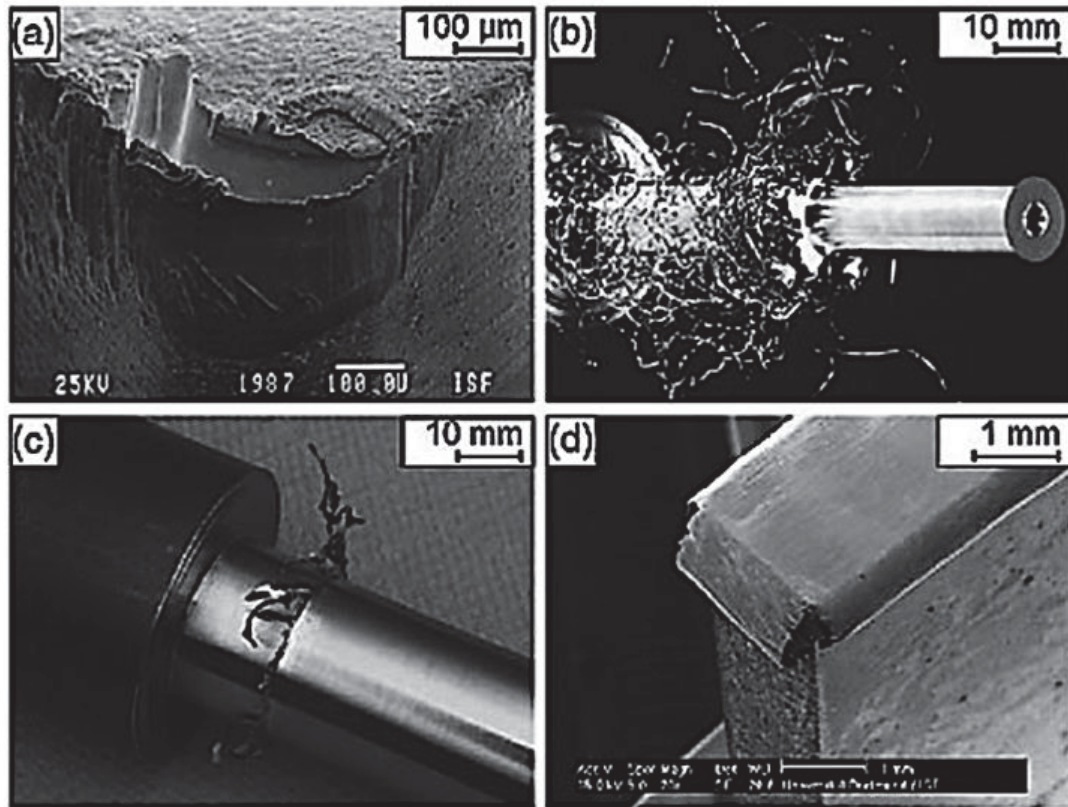


Figure 2.18: Common difficulties associated with machining NiTi: (a) high tool wear (b) adverse chip form (c) formation of burrs (d) grinding (55)

For self-expanding stents, binary NiTi is one of the most important biomaterials used in these minimally invasive surgical devices. However, the poor X-ray visibility of the alloy is a major disadvantage as its lack of radiopacity means it is hard for the surgeon to visualise and locate the device once inside the body (56). Radiopacity refers to the material's ability to absorb X-rays.

Increasing the strut size of the stent can improve radiopacity, hence the visibility of the stent. However, this can hinder the superelastic response of the alloy which is essential for its application. Likewise, the visibility can be improved by placing markers or coatings made from heavier elements onto the stent. This approach brings the complications of galvanic corrosion, increased manufacturing costs, coating adhesion or degradation of the coating integrity once the stent has been crushed into the delivery portal (57).

It is well known that radiopacity will improve when alloying with a third, much denser element. Commonly, platinum is used. *Boyan et al.* (57) found to improve the radiopacity whilst maintaining the superelastic properties of binary NiTi alloy, an equi-atomic composition should be used where Ni is substituted by Pt. The preferred embodiment was found to be $\text{Ti}_{50}\text{Ni}_{42.5}\text{Pt}_{7.5}$ (at %) (shown in figure 2.19), however the addition of Pt can be equal to or above 2.5 (at %) or less than or equal to 15 (at %). Additionally, *Boyan et al.* stated that palladium could be alloyed as a ternary element in quantities equal or above 2.5 (at %) to less than or equal to 20 (at %).

To examine the superelastic response of these ternary compositions, their loading-unloading behaviour was tested on wires. Wires were placed under increasing tension. As evident in figure 2.20, full recovery was observed for all alloys, showing that high radiopacity can be achieved in NiTi, whilst maintaining its superelastic response. 1 ksi is equal to 6.89 MPa in the stress-strain graph shown in figure 2.20.

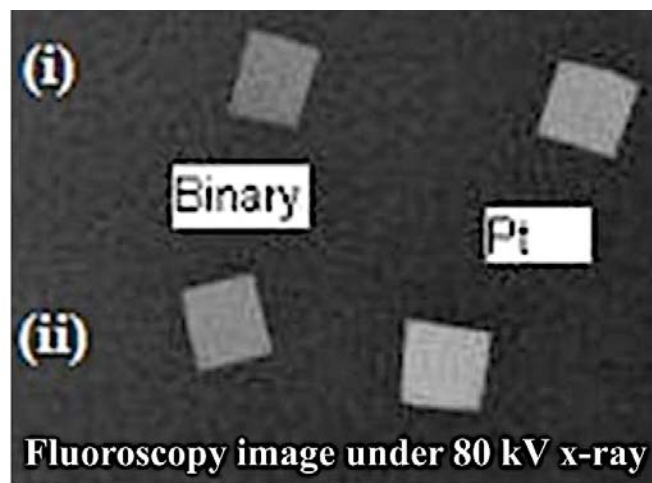


Figure 2.19: The x-ray visibility of binary NiTi compared to $\text{Ti}_{50}\text{Ni}_{42.5}\text{Pt}_{7.5}$ (at %) (58)

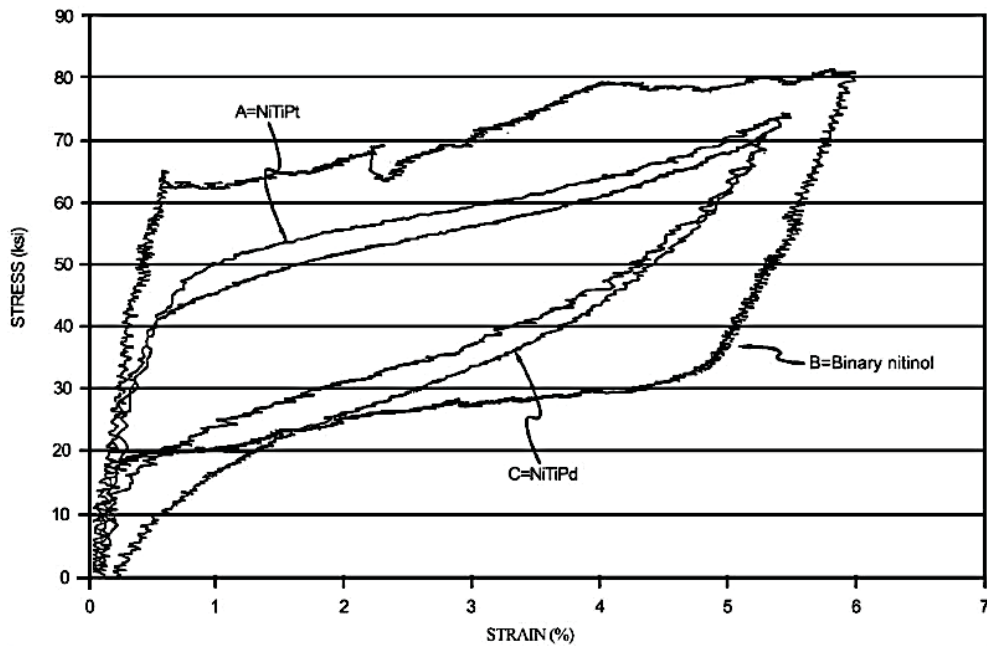


Figure 2.20: A stress-strain graph showing full recovery for NiTi, NiTiPd & NiTiPt (57)

2.4. The Additive Manufacturing of NiTi SMA

2.4.1. The Influence of Processing Parameters on NiTi Build Density: Porosity & Cracking

During SLM, solidification is driven by changes in temperature and no external pressure is involved. Due to this porosity is one of the main defects associated with this manufacturing route. As stated by *Saedi et al.* irregular shaped pores can form when there is not enough energy input from the laser to achieve complete fusion. Whilst spherical shaped pores can form due to gas entrapment as the melt pool overheats and/or Ni evaporates (59).

The micrographs in figure 2.21, highlight how processing parameters can affect the morphology of porosity within the manufactured builds. *Meier et al.* reported that when the scan spacing is too large, the pores will appear lattice-like. On the other hand, when the pores are irregular, it means the scanning speed is too fast or the laser power is too low (60).

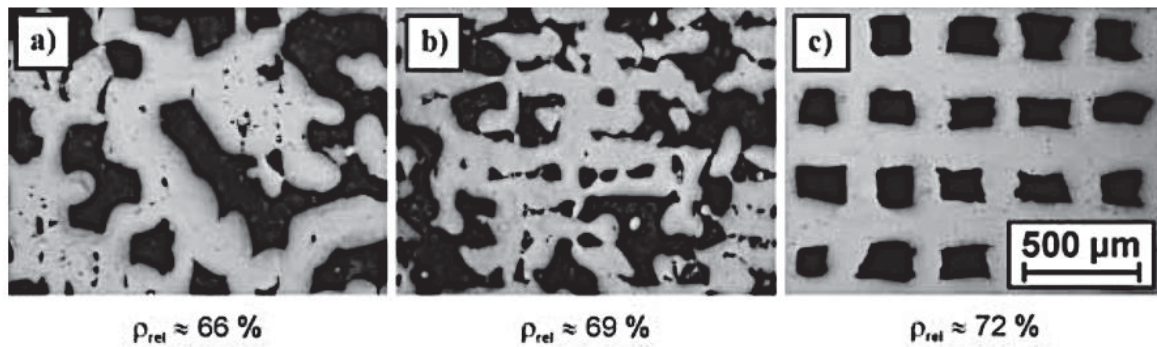


Figure 2.21: Micrographs showing the cross sections with different formations of porosity defined by a). scanning speed b). laser power c). scan spacing (60)

Krishna et al. reported similar behaviour when additively manufacturing NiTi. The bulk density of NiTi decreased when either the laser power was too low or the scan speed too fast. At higher scan speeds, the interaction time between the powder particles and laser beam is very short, resulting in higher porosity. Likewise, when the laser power is too low, the metallic powder particles only partially melt. These partially melted powders then only join at their liquid metal state interfaces (61).

Dadbakhsh et al. demonstrated that regardless of the heating and cooling rates during SLM manufacturing, as long as processing parameters combined to produce a similar energy density, high density builds can be fabricated. Sample 3 (power (P) = 40 W, scan speed (v) = 160 mm s⁻¹, scan spacing (h) = 75 μm, energy density = 111 J/mm³), shown in figure 2.22. experienced slower heating and cooling rates during production. This is due to the low power and scanning speed used. However, sample 4 was manufactured using processing parameters (P = 250 W, v = 1100 mm s⁻¹, h = 60 μm, energy density = 126 J/mm³) that involved faster heating and cooling rates. From figure 2.22, it is evident that both fast and slow heating/ cooling conditions can produce high density builds if they have comparable laser energy densities (62).

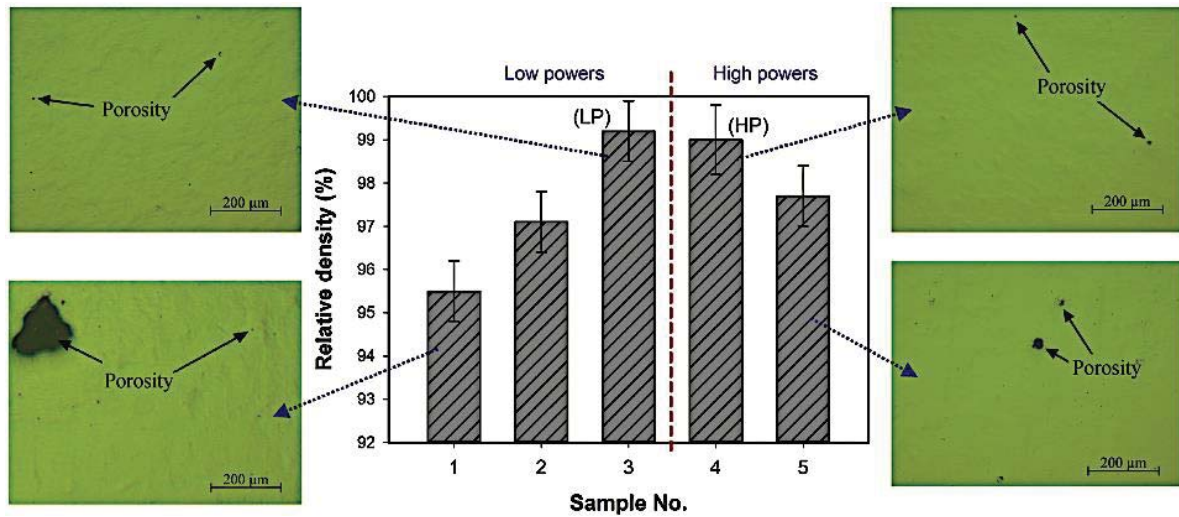


Figure 2.22: Density and cross-section micrographs of the NiTi samples produced by low and high powers adjusted to a small range of energy densities (62)

Walker *et al.* stated that increases in scan speed for a constant laser power reduced the overall energy density from the laser. As shown in figure 2.23, this resulted in a noticeable decrease in build density. The drop in density was especially evident in samples processed with a laser power between 50 W and 100 W. This was due to the energy density from the laser being too high and causing an unstable melt pool, affecting the powder deposition of subsequent layers. On the other hand, a decrease in density was also observed when the scan speed decreased for each laser power. Overall, Walker *et al.* found that 55 J/mm^3 was the optimum laser energy density for manufacturing high density parts. Below this value, the density immediately decreased. Above the 55 J/mm^3 optimum energy density, the part density gradually decreased (63).

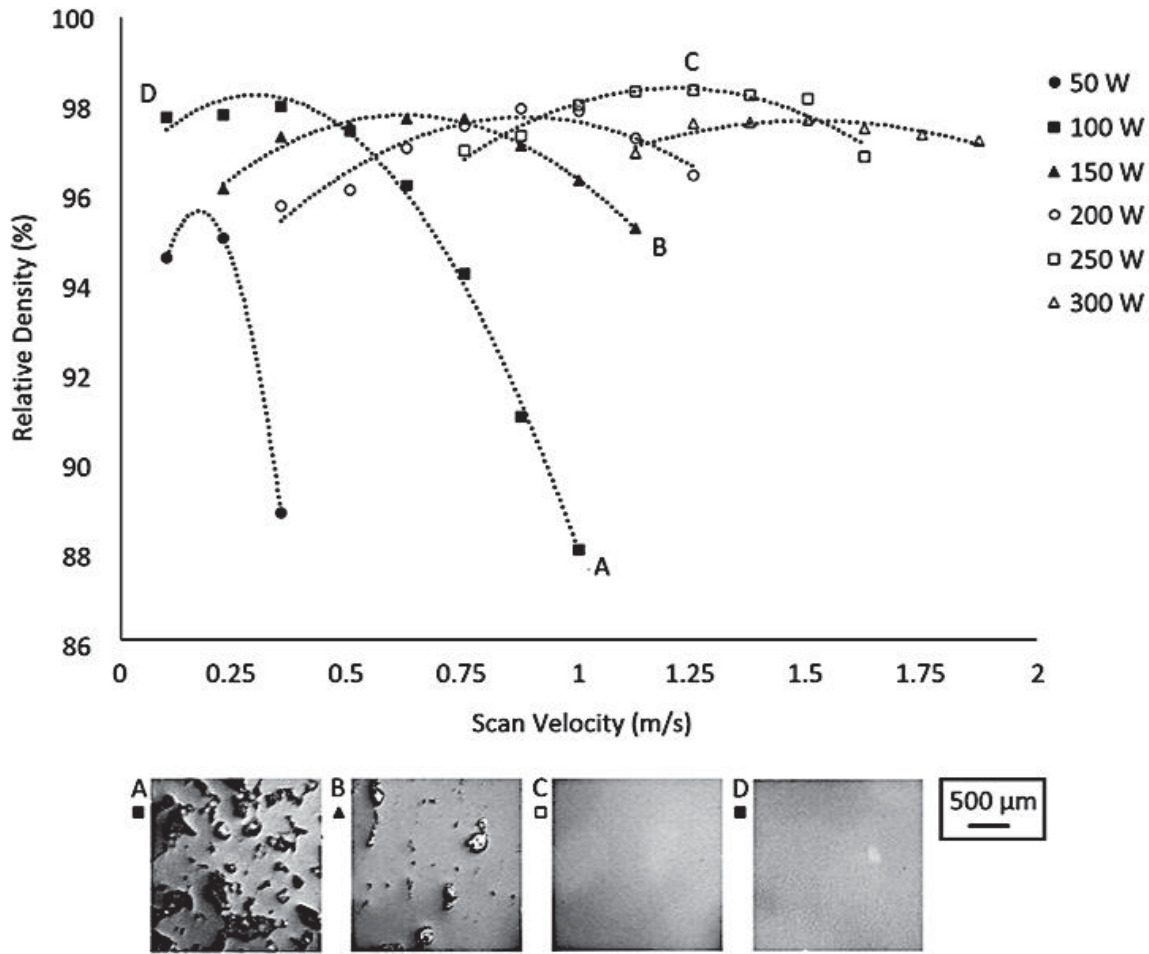


Figure 2.23: The relative density of SLM NiTi parts as a function of scan speed for different laser powers with optical micrographs of selected cross-sections (63)

Likewise, *Meier et al.* found that for manufacturing high density parts there was a narrow laser energy density processing window from 40 J/mm^3 to 90 J/mm^3 . Processing within this range could fabricate builds with nearly 100 percent full density. When manufacturing below 40 J/mm^3 , full density was impossible due to lack of full consolidation. Manufacturing above 90 J/mm^3 , a decrease in density was also observed due to melt pool turbulences and overheating (60).

Haberland et al. reported contrasting findings. A laser energy density of 200 J/mm^3 was required to achieve full build density. Manufacturing at energies above this value did not significantly alter the density. However, at energies below 200 J/mm^3 , non-molten or

insufficiently molten powder was visible within the pores. Indicating, the energy input was too low for complete consolidation (64).

In addition, *Walker et al.* also studied the influence of scan spacing on part density. A scan spacing of 120 μm created a 36 % overlap between adjacent tracks, and the relative density increased above 98 %. Increasing the scan spacing to 360 μm , produced no overlap between adjacent tracks and open pores were visible. Likewise, further increasing the scan spacing to 700 μm provided no overlap and the part density decreased to below 50 %. It can be concluded that increasing the scan spacing reduces the overlap between tracks. Consequently, this has negative impact towards porosity and the build density decreases (63).

Microstructural defects such as cracking are rarely reported during the additive manufacturing of NiTi. This is due to the majority of studies concentrating on Ni-rich compositions. *Li et al.* studied SLM of Ti-rich NiTi compositions and found that cracking was a major issue. The reason for this is believed to be due to the formation of the Ti_2Ni intermetallic. This intermetallic precipitates along interdendritic regions in the microstructure. As the phase is very brittle, it acts as a crack initiation site with cracks appearing to propagate from the intermetallic phase. At high laser energy densities, the crack density appeared to decrease. However, the increased energy input causes turbulences in the melt pool, thus increases in build porosity. As visible in figure 2.24. builds with a high porosity coincide with a low cracking density. Furthermore, this suggests that as pores allow for more deformation, they reduce the residual stresses within the build. In turn, relaxing the residual stresses within the build, decreases the cracking density (65).

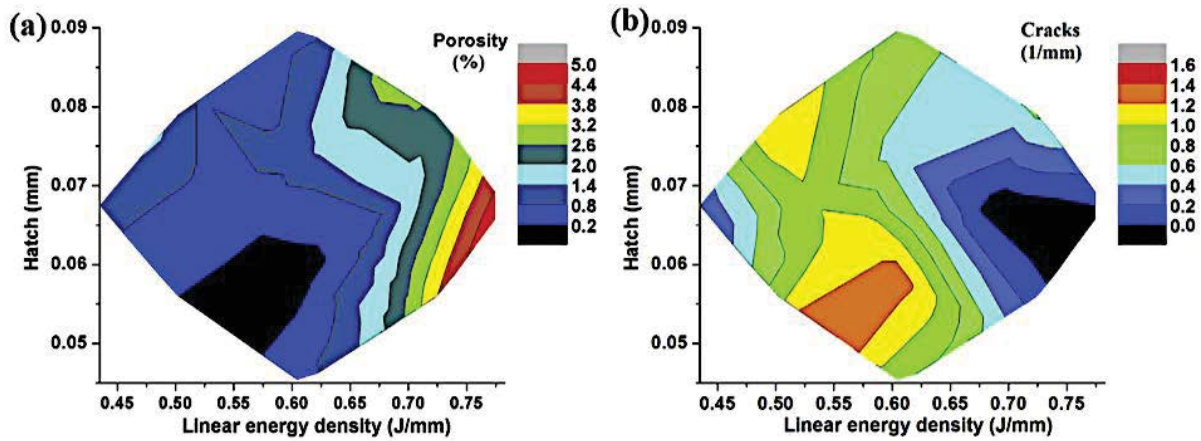


Figure 2.24: The correlation of energy density with a). Porosity fraction and b). Cracking density (65)

2.4.2 The Influence of Processing Parameters on the Microstructure of Additively Manufactured NiTi: Room Temperature Phases

As austenite is the stable phase at high temperatures and B19' is stable at lower temperatures, processing parameters can influence the concentrations of each phase in the final SLM build. *Marattukalam et al.* observed a relationship between the alloy phase and the heating/cooling rate. The results are shown in figure 2.25. The amount of each phase was calculated using PANalytical –X'Pert software. It was found that increasing the laser power or decreasing the scan speed, increased the laser energy density and decreased the cooling rate. Reductions in the cooling rate increases grain size, the formation of precipitation and does not act to stabilise the austenite sub-grains. Thus, when the laser energy input increases, the concentration of austenite decreases whilst the martensite increases (51). *Krishna et al.* confirmed this relationship by comparing the X-ray diffraction of the as-received NiTi pre-alloyed powder and the as-fabricated build. The build had a higher concentration of B2 austenite as the rapid cooling rate during processing resulted in the retention of the high temperature B2 austenite phase (61).

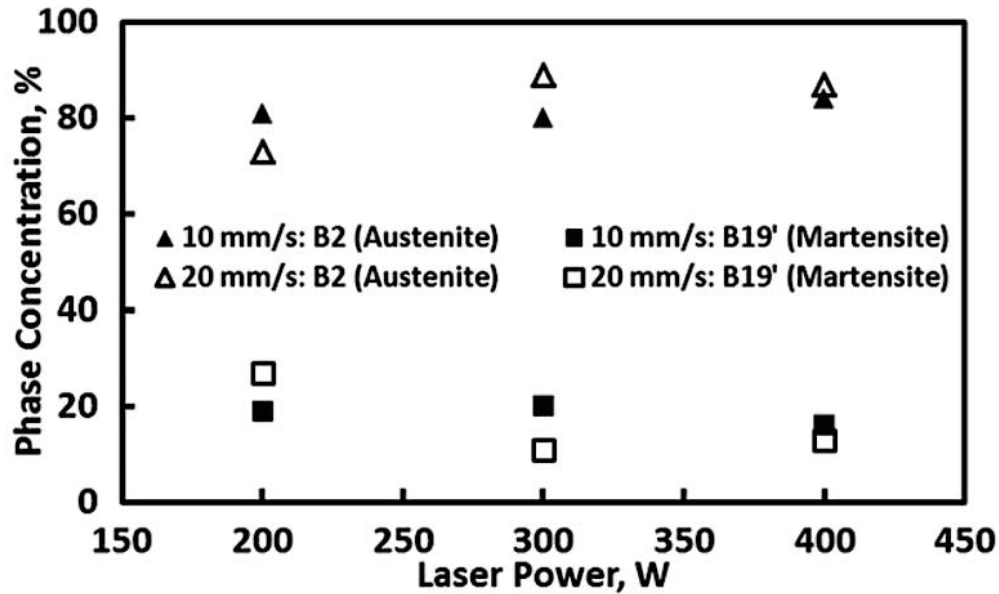


Figure 2.25: The concentration of B2 austenite and B19' martensite phases in relation to processing parameters (51)

2.4.3. The Influence of Processing Parameters on Contamination during Additive Manufacturing:

Maintaining a low impurity content in NiTi during additive manufacturing is of great importance for biomedical applications. This is due to the very strict standards regulating the maximum allowable contents of nitrogen, oxygen and carbon allowed in implantable medical devices.

To reduce the pick-up of impurities from the surrounding atmosphere during SLM, the process is performed in an inert argon atmosphere. Furthermore, emphasis is placed on the quality of the raw material used to make the powder. If the powder starts with a relatively high impurity content due to the atomisation process the further high temperature processing will inevitably result in more contamination and ultimately the impurity limits for medical applications will be exceeded.

Haberland et al. stated that nitrogen and oxygen pick up increased with energy input from the laser. Interestingly, the laser energy input had no influence on the carbon pick up. At the laser energy density (200 J/mm^3) required for high density parts, SLM processing resulted in an approximately 0.04 wt % oxygen and 0.02 wt % nitrogen increase (64). *Walker et al.* found conflicting results, where the carbon and oxygen increased with energy input and the nitrogen level remained consistent before and after SLM manufacturing. However, both authors concluded that a low laser energy density is required to help minimise impurity pick up during processing (63).

Heat treatment after SLM fabrication is a necessary process to complete the homogenisation process of the microstructure. *Bormann et al.* noted that the oxygen content increased by 0.02 wt % after solution heat treating, forming the undesirable $\text{Ti}_4\text{Ni}_2\text{O}_x$ impurity phase (66).

2.4.4. The Influence of Processing Parameters on the DSC Curve and Phase Transformation Temperature of Additively Manufactured NiTi:

Krishna et al. reported a difference in the DSC transformation curves for the as-fabricated SLM part and the as-received equi-atomic NiTi powder. The transformation sequence for the laser processed samples were one stage with one peak visible for the $\text{B19}' \rightarrow \text{B2}$ transformation on heating and another $\text{B2} \rightarrow \text{B19}'$ transformation peak upon cooling. However, the DSC curve for the NiTi powder showed a secondary peak on heating and cooling. This peak was attributed to the presence of Ti_3Ni_4 precipitates. After SLM processing, the transformation temperature increased by 10°C for the austenitic transformation and 7.1°C for the martensitic transformation (61). *Krishna et al.* did not know the reason for this increase in phase transformation temperature but attributed it to the resetting of microstructure and phases during laser processing. It was suggested that due to an incomplete $\text{B19}' \rightarrow \text{B2}$ transformation, after

heating the remaining B19' phase acted as preferential nucleation sites for the B19' transformation leading to higher M_s temperatures.

Haberland et al. studied the phenomenon of the increase in transformation temperature for SLM manufactured parts. It was concluded that laser processing can be associated with the evaporation of Ni. Depending on processing parameters, Ti has a higher evaporation temperature, thus a lower tendency to evaporate in comparison to Ni (64). *Walker et al.* supported the theory that the increase in transformation temperature should be attributed to Ni evaporation (63). As previously mentioned, NiTi alloys are extremely sensitive to composition and their transformation temperature is dependent on the Ni-Ti ratio. Processing with higher energy inputs results in a melt pool with larger dimensions and the material experiences elevated temperatures for a longer period. Consequently, whilst being kept in its molten state for longer, there is more time for Ni to evaporate. Furthermore, processing at very high energy inputs results in a decrease in density due to the keyholing effect. The formation of this spherical porosity can be attributed to elemental evaporation causing the material to collapse in on itself and form voids.

Saedi et al. confirmed the relationship between laser energy density and transformation temperature for Ni_{50.8} (at %) rich NiTi alloys. For samples processed using a 100 W laser power with a laser energy density above 120 J/mm³, the transformation temperature drastically increased. When processing at a 250 W laser power with a laser energy density between 45 – 80 J/mm³, the transformation temperature only slightly increased (59). Thus, it can be said that regardless of the laser power used, the transformation temperature will increase according to the laser energy density.

As mentioned previously, impurity pick up is unavoidable during SLM processing. Despite impurity pick up causing a decrease in the transformation temperature by the depletion of Ti to form $\text{Ti}_4\text{Ni}_2\text{O}_x$, the effects of Ni evaporation override the decrease in transformation temperature caused by Ti depletion in the matrix.

Not only does processing at high laser energy densities increase the transformation temperature due to Ni evaporation. It also affects the transformation temperature due to the formation of precipitates. The intermetallic NiTi phase in Ni-rich alloys has limited solubility for Ni as temperatures decrease. Once the solubility limit has been exceeded, Ni-rich phases form (Ni_4Ti_3 , Ni_3Ti_2 and Ni_3Ti). Although these phases do not participate in the martensitic transformation, they still effect the transformation temperature as Ni is depleted from the matrix. When processing at high energy inputs, a higher volume fraction of Ni-rich precipitates is formed. This shifts the matrix composition to higher Ti contents, thus increases the transformation temperature.

As shown by *Haberland et al.* in figure 2.26, regardless of the laser energy density used to manufacture the samples, during DSC testing the sharpness of the transformation peak remained constant for Ti-rich and equiatomic NiTi alloys. However, processing at low energy inputs for Ni-rich alloys led to significant changes in the transformation peak characteristics. Broad and very flat transformation peaks were observed for Ni-rich alloys processed at low energy inputs (around 45 J/mm^3). At these energy inputs, there was not enough energy to allow for full melting and as a consequence the microstructure was less homogeneous. The concentration differences within the SLM build result in inhomogeneous phase transformations. This leads to the formation of flatter peaks, which in turn make it difficult to detect the transformation temperatures. On the other hand, processing Ni-rich alloys at high energy inputs (545 J/mm^3), results in a multi-step phase transformation. As previously

mentioned, Ni-rich precipitates form when processing at high energy densities. These phases cause local deviations in chemical composition, meaning that the alloy will transform over a temperature range, resulting in multi-step transformations (67).

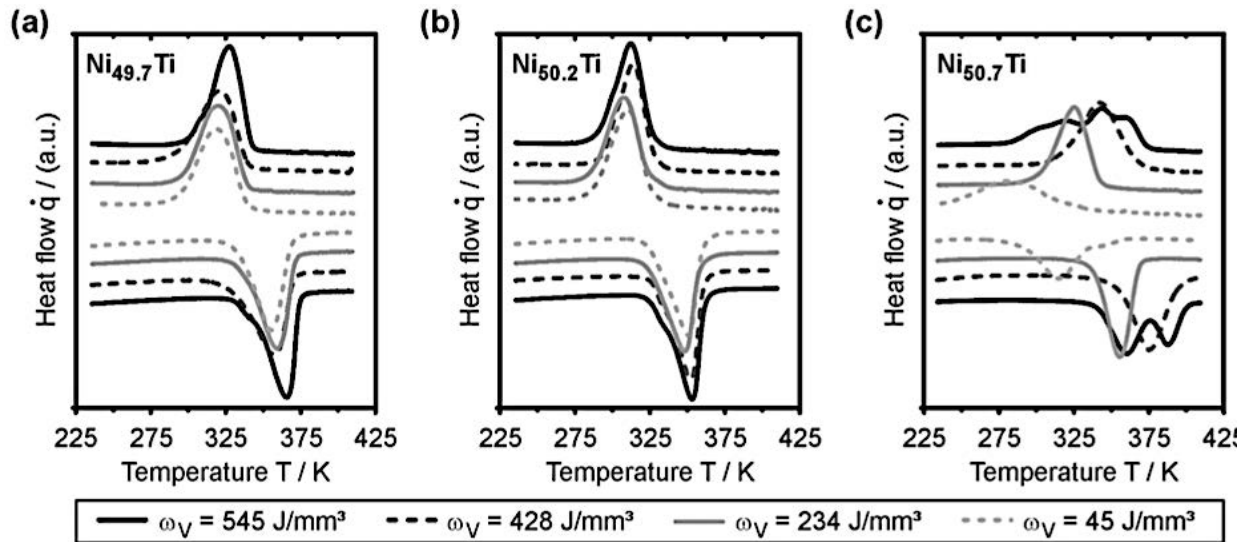


Figure 2.26: The influence of energy input on the phase transformation behaviour for a). Ti-rich b). near equiatomic c). Ni-rich NiTi alloys(67)

It is accepted that the precipitation of Ni-rich precipitates during SLM processing will alter the transformation temperature. However, these effects are not permanent and can be reversed by an effective solution heat treatment. *Haberland et al.* carried out a solution heat treatment at 950°C for 5.5 hours on Ni-rich NiTi alloys in order to disperse precipitation. Water quenching was performed immediately afterwards to suppress re-precipitation and this resulted in a homogeneous, single phase NiTi alloy with a matrix supersaturated in Ni. Consequently, as shown in figure 2.27. after the solution heat treatment, the transformation temperature of the alloy will decrease below the transformation temperature of the as-fabricated alloy.

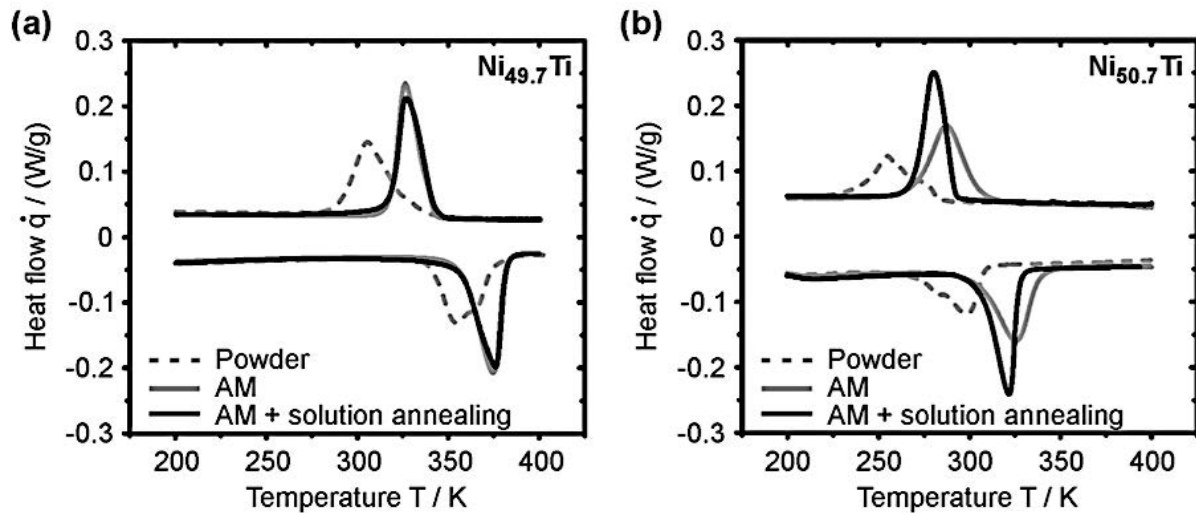


Figure 2.27: The influence of subsequent solution annealing treatments on the transformation temperature of a). Ti-rich b). Ni-rich NiTi alloy (67)

Bormann *et al.* concluded that manufacturing with a laser energy density between 60 and 100 J/mm³ led to an increase in transformation temperature up to 75 K. However, after solution heat treating at 800 °C for 30 minutes followed by water quenching, the transformation temperature reduced by approximately 12-18 K (68).

Hamilton *et al.* confirmed the need for heating treatment after SLM processing Ni-rich NiTi alloys to homogenise the microstructure. This was because the phase transformation could not be observed during DSC testing whilst the alloy was in the as-fabricated state (69).

2.4.5. The Influence of Heat Treatment on the Phase Transformation Temperature of Additively Manufactured Ni-rich NiTi:

Saedi *et al.* studied the effects of aging on the superelastic response of Ni-rich SLM Ni_{50.8}Ti_{49.2} alloys. During the study it was found that heat treatments will not only affect the alloy's mechanical behaviour, but also the transformation temperature due the formation of precipitates. A solution heat treatment (950°C for 5.5 hours) was performed. This was followed by water quenching to suppress the re-precipitation. Due to the dissolution of the secondary

phases creating a Ni-rich matrix. It was found that the transformation temperature of the as-fabricated alloy decreased by 20 °C, as shown in figure 2.28 (70).

After the solution heat treatment, the effects of aging at two different temperatures (350 °C and 450 °C) for varying time periods (5 minutes to 18 hours) were studied. It was found that the transformation temperature gradually increased with aging time for both aging temperatures. As mentioned earlier, Ni has a limited solubility in the intermetallic NiTi matrix. Consequently, Ni-rich secondary phases form to accommodate the excess Ni. The size of the secondary phases increases with aging time. This causes more Ni to be depleted from the matrix and results in a higher transformation temperature.

Additionally, samples aged at 450 °C consistently had a slightly higher transformation temperature in comparison to the samples aged at 350 °C. Aging at higher temperatures increases the size of secondary phases. As expected, this depletes Ni from the matrix and increases the transformation temperature.

Furthermore, it was found that the characteristics of the transformation curve changes with aging time for both the 350 °C and 450 °C temperatures. When heating at 350°C and 450°C for longer than 30 minutes, a multi-step transformation takes place. *Saedi et al.* suggested multiple reasons as to why this occurs. The secondary phase precipitates cause an inhomogeneous Ni concentration throughout the sample. Alternatively, because the alloy is Ni-rich, the R-phase could form due to changes in the energy required for the B19' martensite transformation.

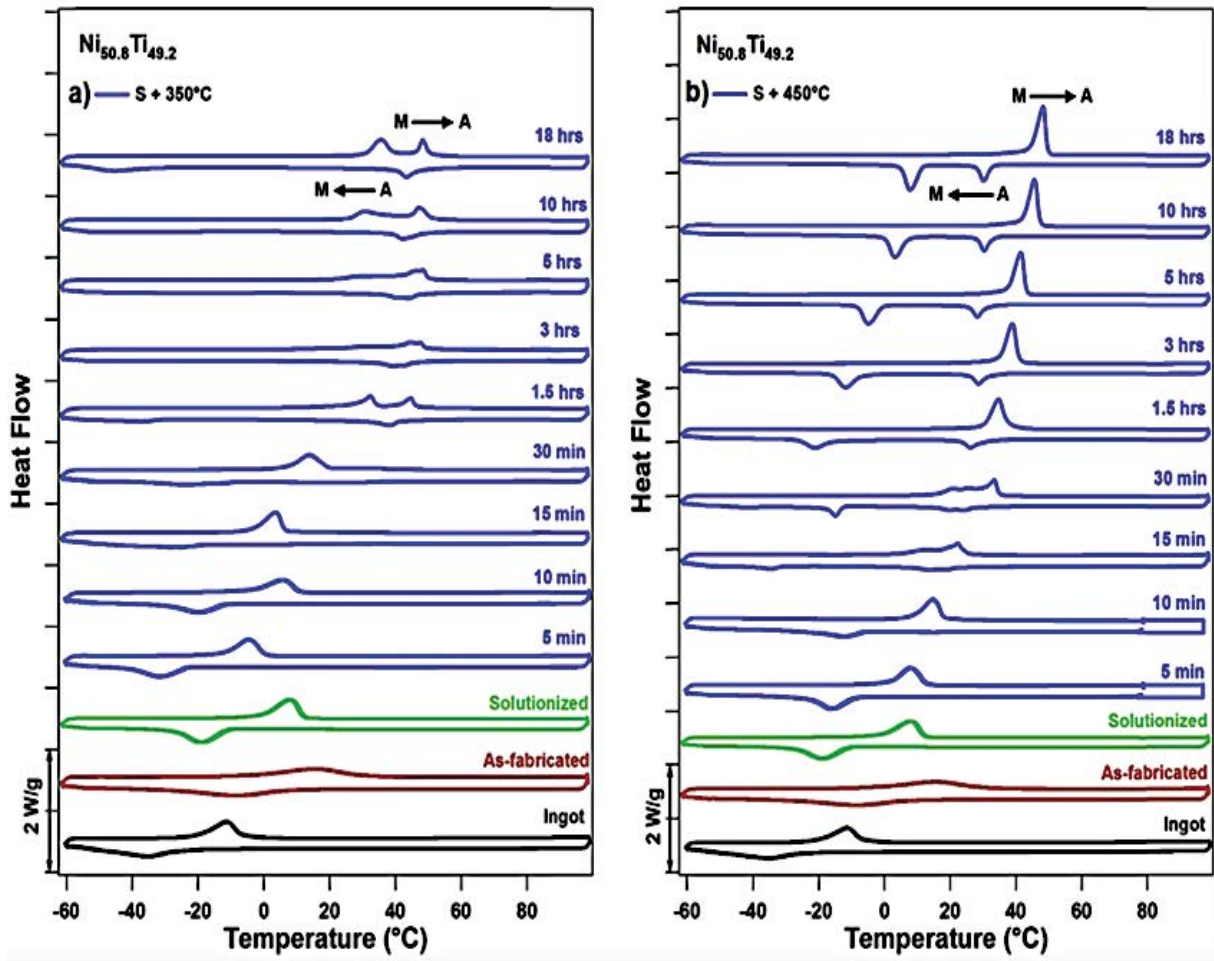


Figure 2.28: The DSC response of solutionised SLM $\text{Ni}_{50.8}\text{Ti}_{49.2}$ alloys aged at a). 350°C b). 450°C (70)

Hamilton *et al.* studied the effects of aging (450°C , 500°C and 550°C) for differing durations (1.5 to 10 hours) on a Ni-rich $\text{Ni}_{53}\text{Ti}_{47}$ at % alloy (69). Trends similar to Saedi *et al.* were observed. As shown in figure 2.29, increasing the aging time from 1.5 to 10 hours increased the transformation temperature for all samples. However, in contrast to results reported by Saedi *et al.*, when comparing the transformation temperature for samples aged at different temperatures for equal periods of time, the transformation temperature decreased with increasing aging temperature.

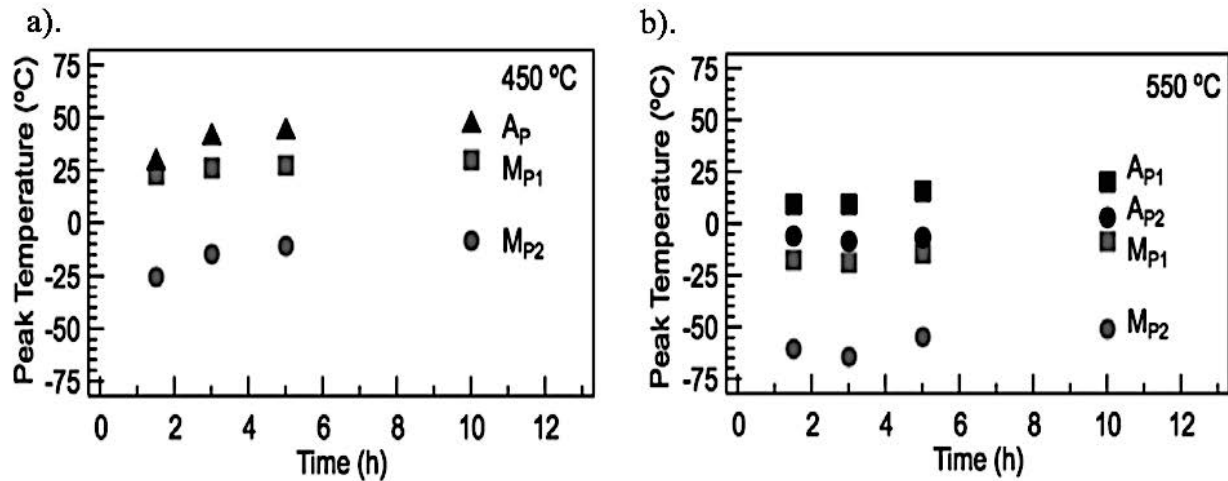


Figure 2.29: Transformation temperatures plotted as a function of aging hold time for a). 450 °C b). 550 °C (69)

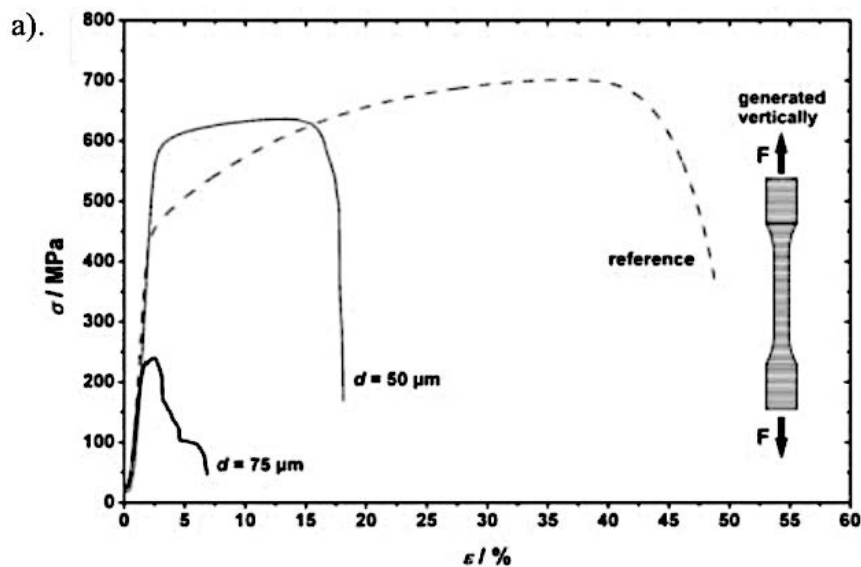
2.4.6. The Tensile Behaviour of Additively Manufactured NiTi:

Very little literature is published regarding the tensile behaviour of SLM NiTi alloys. Internal defects such as pores, cracks or residual stresses commonly associated with the layer based manufacturing technique, lead to premature failure of the part. Furthermore, most biomedical applications deal with compressive loading. Thus, information on the tensile behaviour is less necessary.

Meier et al. studied the effects of build orientation on the tensile behaviour of as-fabricated SLM NiTi alloys (60). Specimens were fabricated in the horizontal and vertical direction, using the same processing parameters but with different layer thicknesses (75 μm and 50 μm). The tensile behaviour of the SLM fabricated samples were compared to the tensile behaviour of conventionally manufactured NiTi. As shown in figure 2.30, SLM fabricated NiTi is less ductile with a lower elongation before failure.

As expected the stress-strain curves highlight the anisotropic behaviour of SLM fabricated NiTi. The vertically manufactured samples have a lower tensile strength. Additionally, they exhibit a more brittle behaviour with less elongation in comparison to the horizontally

manufactured specimens. Although loading normal to the layer formation creates significantly poorer mechanical properties, it was found that decreasing the layer thickness for the specimens manufactured in this orientation can improve the mechanical behaviour. The larger layer thickness (75 μm) experienced dramatic failure at approximately 250 MPa. This premature failure is the result of inadequate bonding between the layers, which can be observed in the SEM micrograph of the fracture surface in figure 2.31. When the layer thickness is reduced to 50 μm , the specimen fails at approximately 650 MPa. The fusion between the molten powder layer and the solidified layer beneath is dominated by heat transfer. It can be said that when reducing the layer thickness, the absorption of the laser energy in the previously solidified layer will increase. Thus, creating a broader melt pool and leading to stable and successful fusion of subsequent layers.



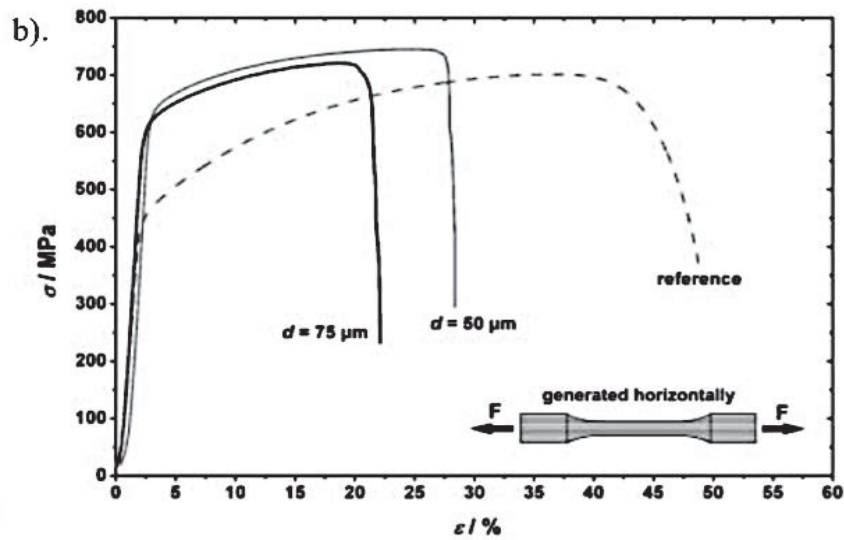


Figure 2.30: Stress- strain curves of a). vertically generated specimens b). horizontally generated specimens. Reference = conventionally manufactured NiTi (60)

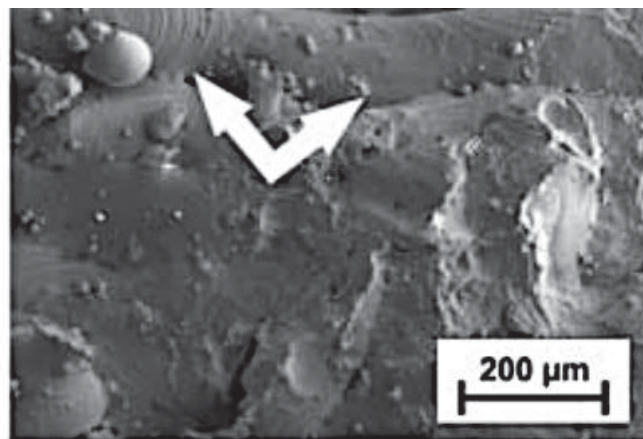


Figure 2.31: SEM micrograph of the fracture surface after tensile testing. The white arrows highlight unsuccessful layer fusion (60)

Bagheri *et al.* compared the tensile behaviour between conventionally manufactured and additively manufactured NiTi which had been heat treated (71). The results are shown in figure 2.32. Heat treatment 1 (HT1) involved aging the specimen at 550 °C for 1 hour followed by air cooling. Heat treatment 2 (HT2) involved solution heat treating at 550 °C for 3 minutes with subsequent water quenching, following aging for 3 hours at 550°C. These heat treatments were selected to provide a fully austenitic phase structure during testing.

Both heat treated specimens showed plateau stresses comparable to the wrought NiTi. As previously shown by *Meier et al.* additively manufactured NiTi was less ductile and experienced a shorter elongation to failure. HT1 and HT2 samples elongated at approximately a 4 % and 5 % strain, respectively. Whereas, the wrought material elongated to nearly 12 % strain. The smaller elongation of additively manufactured NiTi could be due to microstructural defects, such as porosity. The presence of these pores could have resulted from entrapped gas or unmelted regions due to lack of fusion. Additionally, from a low laser penetration depth which would have a detrimental effect on layer bonding.

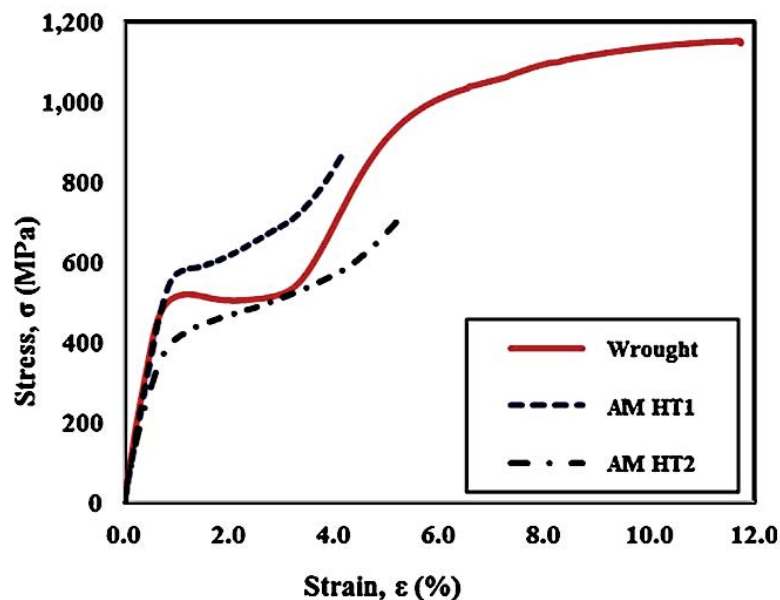


Figure 2.32: A comparison of the tensile behaviour for wrought and additively manufactured NiTi (71)

Table 2.4 shows the tensile properties of the wrought and additively manufactured NiTi alloys. The austenitic modulus of the wrought and HT1 additively manufactured tensile sample was 73 GPa. However, the austenite modulus decreased to 58 GPa for the HT2 additively manufactured specimen. This behaviour is of interest for biomedical applications, as the elastic modulus of additively manufactured NiTi could potentially be adjusted to patient specific values e.g. the elastic modulus of NiTi in orthopaedic hip implants could be adjusted closer to that of human bone, to create a more compatible and durable implant. It is important to point

out that the stress-induced martensitic modulus for the additively manufactured specimens could be not obtained because the materials fractured before reaching the fully martensitic region of the stress-strain curve.

Table 2.4: The tensile properties for wrought and additively manufactured NiTi (71)

Property	Wrought	AM HT1	AM HT2
Austenite modulus E_A	~ 73 GPa	~ 73 GPa	~ 58 GPa
A \rightarrow M start stress, σ_s^{AM}	~ 515 MPa	~ 580 MPa	~ 430 MPa
A \rightarrow M start strain, ϵ_s^{AM}	1.0%	1.0%	1.0%

2.4.7 Improving the superelastic response through the use of Ni-rich NiTi SMAs

Superelasticity is a characteristic which was be exploited in Ni-rich SMA. As a single phase NiTi alloy is heated above $\sim 625^\circ\text{C}$, the structure can accommodate an increasingly Ni rich occupancy. Thus, upon cooling from high temperatures, precipitation of Ni-rich secondary phases is expected. These include the thermodynamic Ni_3Ti phase and meta-stable Ni_4Ti_3 , Ni_3Ti_2 phases. Using heat treatments, these phases can increase the intrinsic strength of the alloy due to their precipitation hardening effect.

Hornbuckle et al. investigated the effects of the precipitation hardening effect on Ni-rich NiTi arc-melted buttons (71). Following solutionising and subsequent heat treating, it was found that the rhombohedral Ni_4Ti_3 precipitate phase had the most significant effect on improving the superelasticity of Ni-rich NiTi alloys. Furthermore, for this phase to be precipitated, the alloy must undergo a solution heat treatment followed by water quenching. Solution heat treating a Ni_{55}Ti at % alloy at 1050°C for 10 hours followed by immediate water quenching, produces a large volume of nanoscale Ni_4Ti_3 platelets. B2 matrix channels form between Ni_4Ti_3

platelets (shown in figure 2.33) and this morphology increases the shear stress required for dislocations to propagate within the structure. Water quenching is essential in producing a high density and fine platelet morphology of the Ni_4Ti_3 phase. Air cooling forms coarser precipitation which lowers the hardening effect.

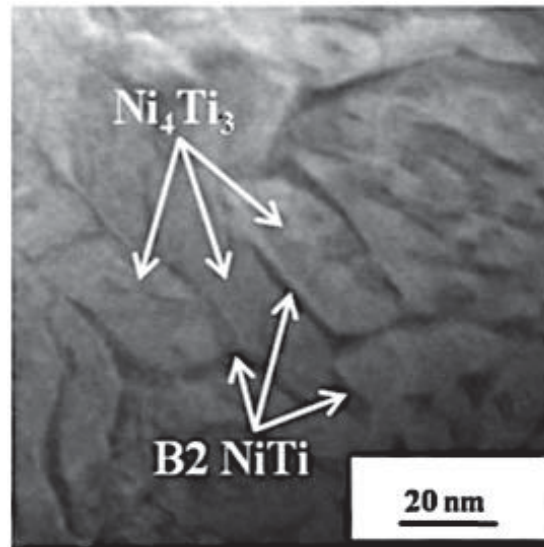


Figure 2.33: A STEM-HAADF image from a Ni alloy to give perspective of Ni_4Ti_3 spacing and narrow B2 NiTi channels between the precipitates (71)

2.4.8 The Compressive Behaviour of Additively Manufactured Ni-rich NiTi

Meier et al. investigated the compressive strength of as-fabricated SLM $\text{Ni}_{50.2}\text{Ti}$ (at%) alloys (72). A Zwick/Roell Z100 tensile-compression test instrument, with a displacement rate of 0.5 mm/min and a temperature of 20°C (30°C below the A_F temperature) was used to perform the tests. To ensure a fully martensitic structure, samples were chilled in ice prior to testing. As previously mentioned, it is important to look at the effects of build orientation due to epitaxial solidification. *Meier et al.* selected five orientations so that the specimen rotation axes form angles of 0°, 45° or 90° to the coordinate axes. It was found that unlike the tensile behaviour of the alloy, build orientation during SLM does not have a significant effect on the compressive mechanical behaviour. As shown in figure 2.34, the fracture stress deviated approximately 8

% for all orientations. This is believed to be because the small pores or localised layer based defects collapse during compression testing, thus they play a less significant role in part failure.

At strains up to 10 %, the SLM fabricated alloy displays a similar stress-strain behaviour to the conventionally produced (hot worked and annealed) reference alloy. Above 10 % strain, all SLM alloys fail at a stress approximately 750 MPa lower than the stress required for the first crack initiation in the reference alloy (table 2.5). Despite this, *Meier et al.* claimed that for biomedical applications it can be said that SLM and conventionally produced NiTi alloys display a similar stress strain behaviour during compression. This is because biomedical applications will not require deformation above a 10 % strain.

A distinct stress plateau can be observed on the stress-strain curves for all the samples. *Liu et al.* explained that the curve under compression can be divided into three regions. As initial loading increases from 0 MPa, twinned martensite is elastically deformed. Upon further loading, de-twinning occurs and a stress-induced martensitic transformation occurs. This transformation is represented by a plateau on the curve. If the loading increases further, dislocation plasticity and crack initiation will occur (26).

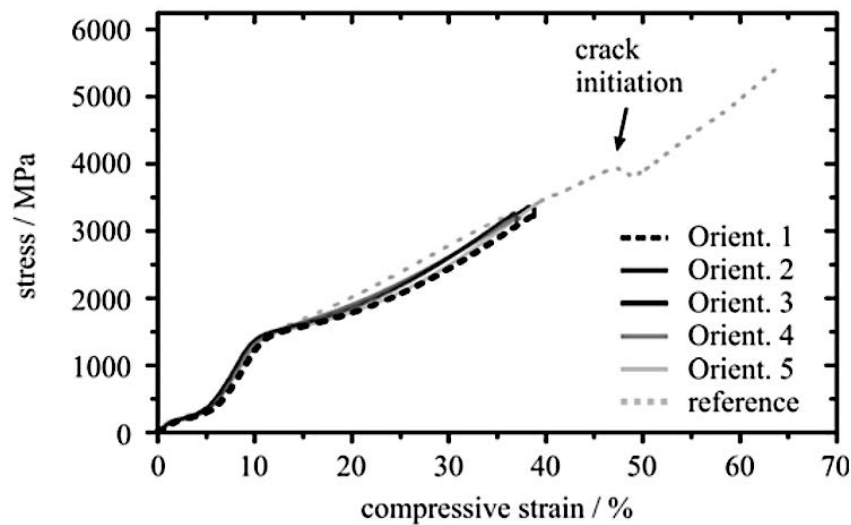


Figure 2.34: The influence of build orientation on the compressive behaviour of additively manufactured NiTi (72)

Table 2.5: Mechanical data of compression testing to failure for a SLM fabricate Ni_{50.2} (at %)Ti alloy (72)

Sample	Detwinning stress (MPa)	Fracture stress (MPa)	Fracture strain (%)
Orient. 1	155-168	3245-3343	39-40
Orient. 2	165-166	3256-3349	37-39
Orient. 3	157-160	3231-3403	39-40
Orient. 4	148-160	3209-3366	37-39
Orient. 5	159-167	3458-3469	40-42
Reference	191-210	3942-3975*	47*
*first crack initiation			

Saedi *et al* furthered this work by looking at the influence of heat treatment on the compressive behaviour of a Ni_{50.8}Ti (at %) additively manufactured alloy (70). A solution heat treatment at 950°C for 5.5 hours followed by water quenching was carried out all of the samples. Aging at 350°C and 450°C was employed for various time periods. Mechanical behaviour was analysed using a 100kN MTS Landmark servo-hydraulic test platform, loading up to 2000 MPa with a strain rate of 10^{-4} s^{-1} . All tests were performed 15 °C above their A_F, so that the samples were fully austenitic.

It was found that subsequent aging of solution heat treated samples can increase the yield strength by approximately 700 MPa. However, continued aging for longer periods of time does not significantly increase the yield stress. Aging the SLM alloy at 350 °C for 5 hours, increased the yield stress to 1650°C. Continued aging for 10 hours increased the yield stress to 1820 MPa. Aging for up to 18 hours has no significant impact on the yield stress. A similar behaviour

was found for samples aged at 450 °C. The yield strength of the alloy stabilised after 10 hours of aging.

Furthermore, the stress required for the stress-induced martensitic transformation is approximately 100 MPa higher for samples aged at 350 °C, in comparison to the samples aged at 450 °C (shown in figure 2.35). Ni_4Ti_3 particles during the aging treatment. When these particles are fine and coherent, they will increase the strength of the material as they hinder dislocation movement. However, increasing the aging temperature results in larger sized Ni_4Ti_3 particles, with a greater distance between them. These characteristics reduce the precipitation hardening effect.

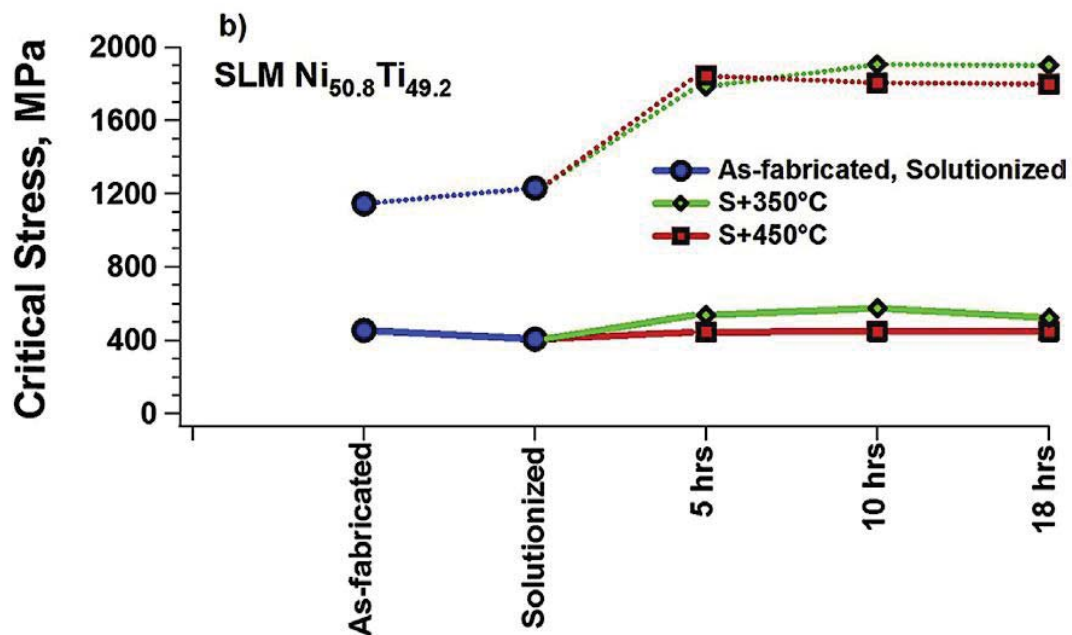


Figure 2.35: The critical stress for stress-induced martensitic transformation (solid line) and plastic transformation (dashed line) with aging time (70)

In a different study, *Saedi et al.* studied the impact of SLM fabrication on the microstructure and texture of Ni-rich NiTi alloys (73). It was found that SLM as-fabricated NiTi alloys have a higher yield stress for plastic deformation in comparison to conventionally produced alloys.

The yield stress to initiate plastic deformation for the ingot was 1175 MPa, however for SLM NiTi it was 1335 MPa. As expected this increase in strength is due to the formation of Ni_4Ti_3 particles during the high temperature SLM processing

Walker et al. studied the compressive behaviour of SLM and conventionally produced NiTi alloys (63). Testing was conducted at 21°C (44°C below the A_s temperature) to ensure a fully martensitic microstructure. As shown in figure 2.36, at approximately 150 MPa the material experiences the onset of martensitic de-twinning. SLM produced NiTi appears to complete de-twinning before the conventionally produced alloy. Furthermore, the SLM fabricated NiTi plastically deforms at a lower stress. This could be caused by the higher residual stresses affecting the ductility of the SLM part. The plateau for the stress-induced martensitic transformation is inclined, this is due to a large accumulation of dislocations forming during compression testing which lead to rapid work hardening.

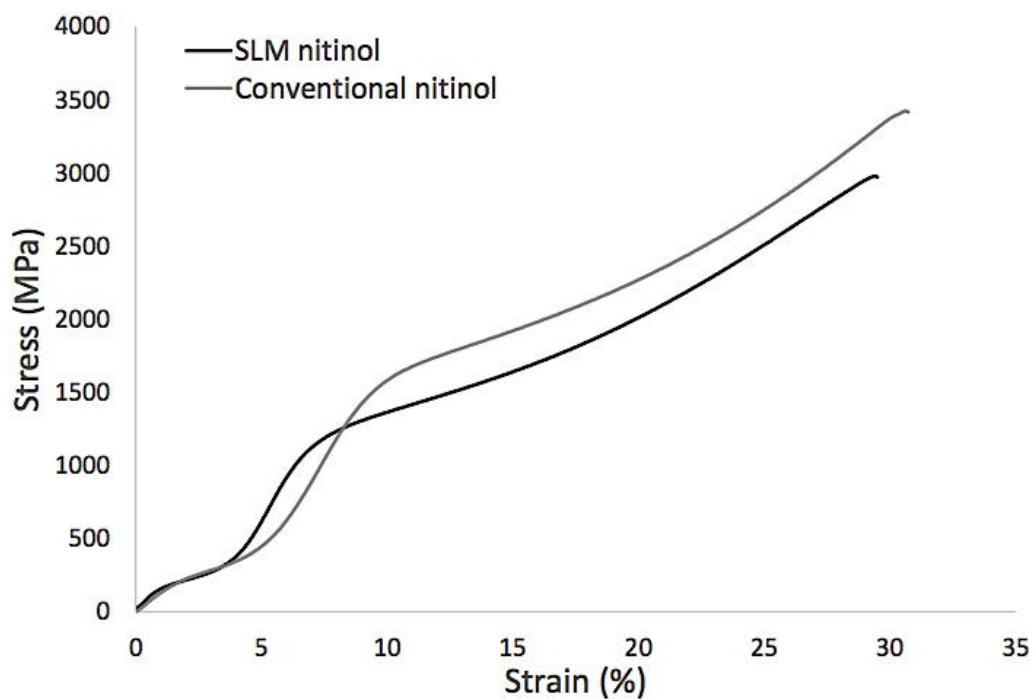


Figure 2.36: The compressive stress strain behaviour for conventionally produced and SLM fabricated NiTi (63)

2.4.9. The Superelastic Response of Additively Manufactured Ni-rich NiTi

Biomedical applications that require superelastic behaviour favour Ni-rich NiTi compositions. This is due to their higher strength and lower transformation temperature. Heat treatment is one of the most effective ways to modify the strength and transformation temperature of Ni-rich NiTi alloys. Table 2.6 identifies the heat treatments that have currently been used to investigate the superelastic response of SLM fabricated Ni-rich NiTi alloys.

Table 2.6: The present heat treatments used to investigate the superelastic response of SLM Ni-rich alloys

Ni Composition (at %)	Solution Annealing Temperature (°C)	Solution Annealing Duration (h)	Quenching	Aging Temperature (h)	Aging Duration (h)	Author
50.7	950	5.5	H ₂ O	350	24	<i>Haberland et al. (67)</i>
50.8	-	-	-	350, 600	30 min, 1, 1.5	<i>Saedi et al. (73)</i>
50.8	950	5.5	H ₂ O	350, 450	5, 10, 18	<i>Saedi et al. (70)</i>
57	1050	10	Oil	400, 500 followed by water quenching	1	<i>Halani et al. (74)</i>
50.7	-	-	-	550	1	<i>Bagheri et al. (71)</i>
	550	3 min	H ₂ O	550	3	

Saedi et al. conducted compression tests using the 100kN MTS Landmark servo-hydraulic test platform, with a strain rate of 10^{-4} s^{-1} during loading and a force control rate of 100N/s during unloading. The strain rate was measured using an MTS high temperature extensometer. To control the temperature during testing, samples were heated using mica band heaters attached to the extensometer grips. Furthermore, cooling of the sample was achieved through the

internal flow of liquid nitrogen in the grips. To assess the practicality of the SLM Ni-rich alloy for biomedical applications, compression tests were carried out at 24 °C or 37 °C (body temperature) regardless of their A_F . Additionally, to avoid the risk of oxidation or melting, no prior solution heat treatment was carried out before aging.

The loading-unloading curves in figure 2.37 show that at 24 °C the conventionally produced NiTi showed perfect recovery at a 2 % strain. However, when loaded to 4 % strain, a 0.6 % irrecoverable deformation occurred. As predicted by *Haberland et al.* the as-fabricated SLM alloy did not show full recovery at any strain. This is due to the thermally induced residual stresses that arise during laser processing. The fast heating rates and comparatively low heat conduction produces a large temperature gradient, which cause residual stresses that can lead to plastic deformation.

To investigate the effects of aging on the superelastic response, the alloy was heated at 350 °C for 30 minutes. Following this heat treatment, full recovery was not observed at any strain. *Saedi et al.* explained this was due to an increase in the A_F temperature. When aged at 350°C for 30 minutes, the A_F temperature increased to 42 °C and full recovery was not observed. However, when the alloy was aged at 600 °C for 30 minutes, the A_F was 29°C and full recovery was observed at a 2% strain, as the alloy's crystal structure was mostly austenitic at the 24 °C testing temperature. Following this, the testing temperature was increased to 37 °C and perfect recovery up to 4% strain was observed for a sample aged at 350°C for 1 hour.

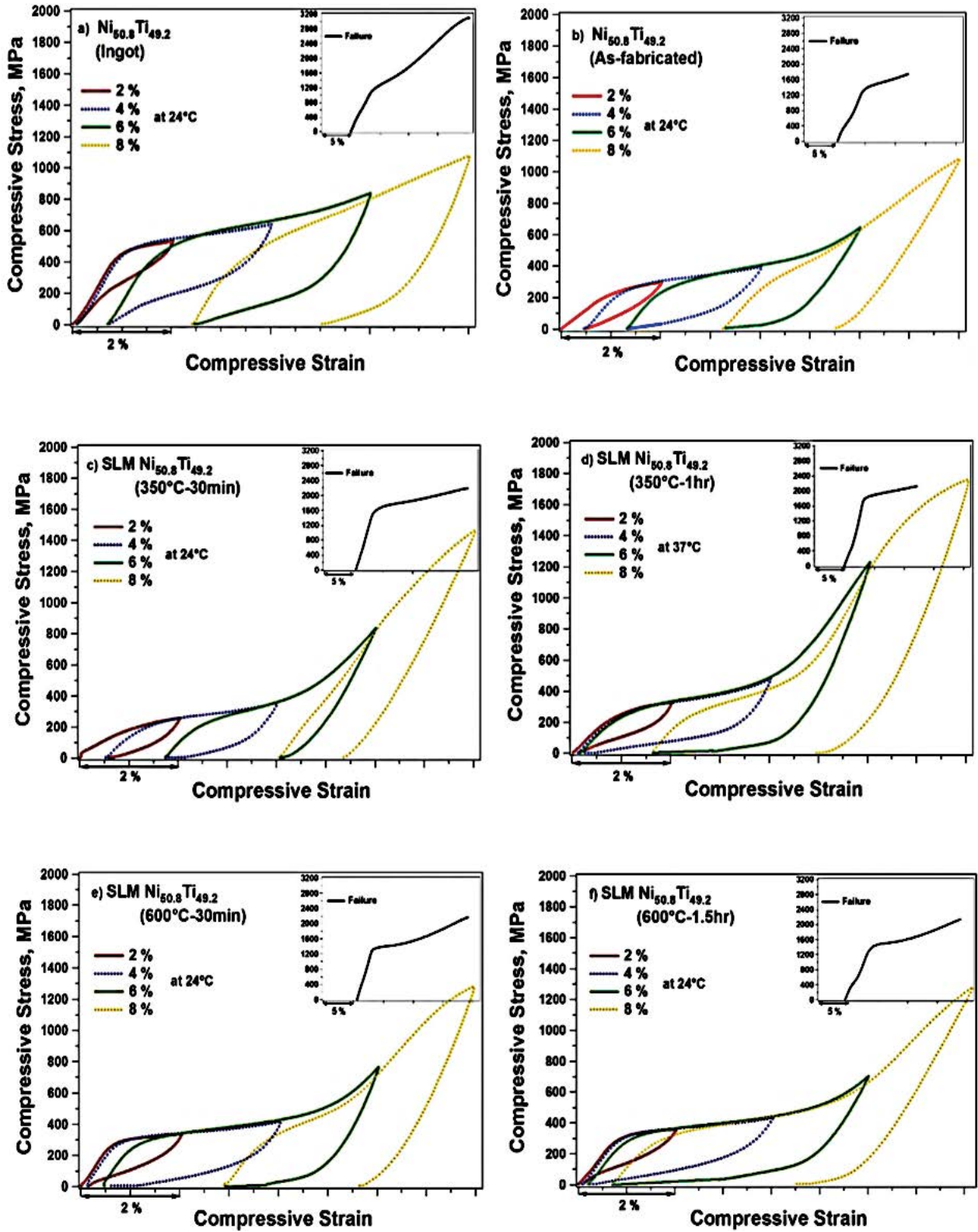
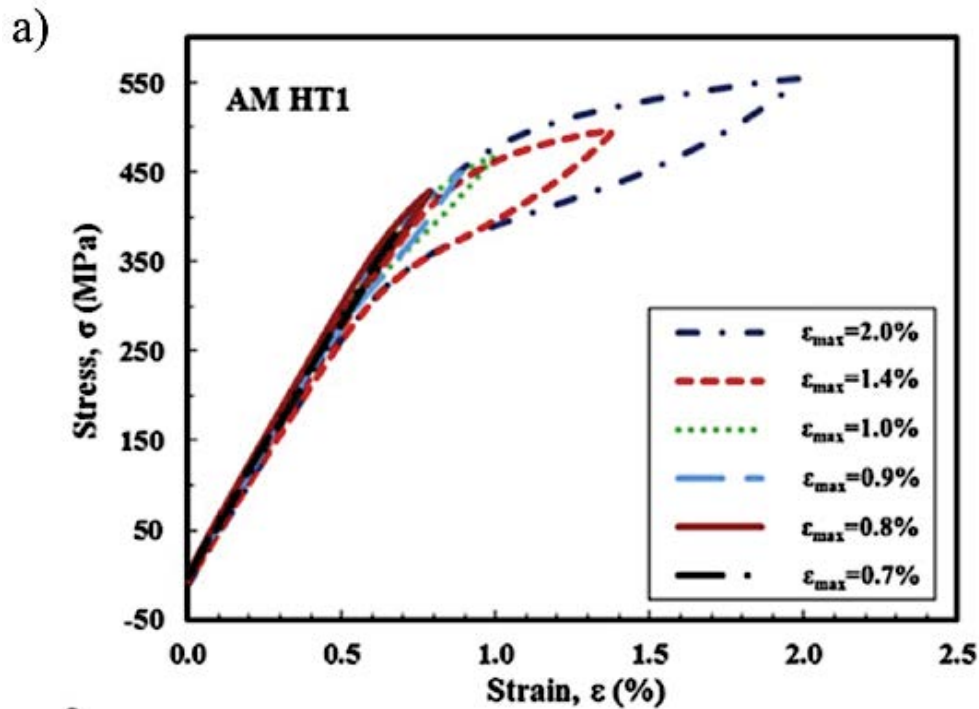


Figure 2.37: The superelastic response of SLM $\text{Ni}_{50.8}\text{Ti}$ aged for a). The initial ingot b). SLM as-fabricated c). 30 mins 350 °C d). 1 hour 350 °C e). 30 mins 600 °C f). 1.5 hours 600 °C, at room temperature (24 °C) and body temperature (37 °C) (73)

Bagheri et al. found similar results when investigating the superelastic response of additively manufactured Ni-rich alloys aged with no prior solution heat treatment. Heat treatments were chosen to ensure the alloy was fully austenitic at room temperature. The as-fabricated alloy aged at 550 °C for 1 hour, experienced perfect recovery when loaded to a 2 % strain at 550 MPa. A second heat treatment was tested which involved a solution heat treatment at 550°C for 3 minutes followed by water quenching and subsequent aging at 550°C for 3 hours. Likewise, this alloy also exhibited full recovery at 2% strain.



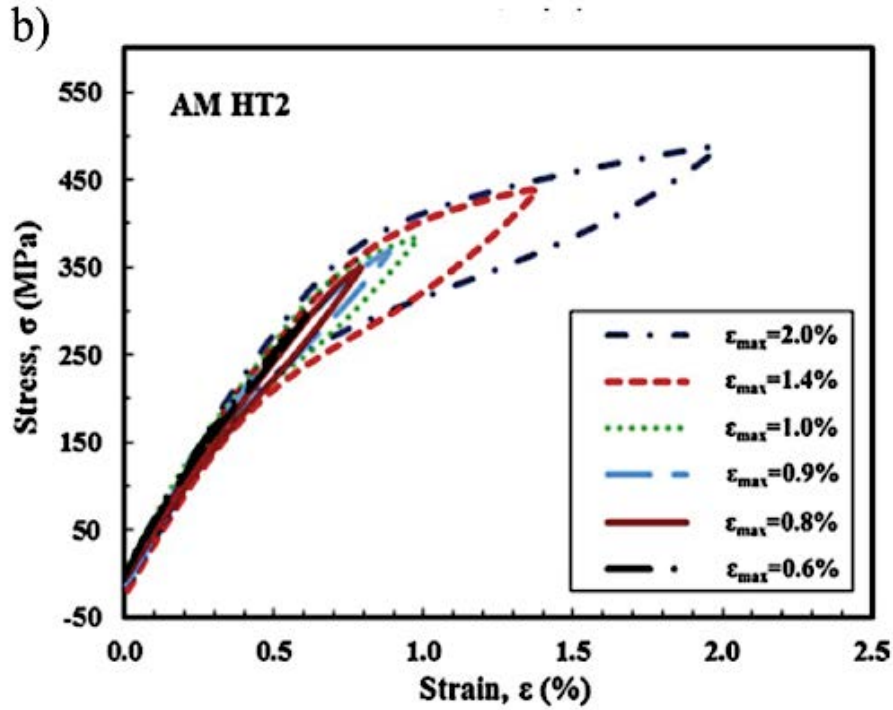


Figure 2.38: The superelastic response of SLM $\text{Ni}_{50.7}\text{Ti}$ for a). HT1 aged 1 hour 550°C b). HT2 solution heat treated 3 minutes 550°C and aged 3 hours 550°C (71)

As previously mentioned, solution heat treatment followed by water quenching can lead to the formation of Ni_4Ti_3 platelets. These platelets increase the strength of the alloy, thus improve the superelastic response. *Saedi et al.* additionally studied the effects of solution and aging heat treatment on the superelastic response. Using the same $\text{Ni}_{50.8}$ (at%) rich composition, the samples were loaded up to 1000 MPa (just before the critical stress for plastic deformation), at a temperature 15°C above their A_F .

In agreement with literature, the as-fabricated alloy showed no superelasticity (shown in figure 2.39). Solution heat treating for 5.5 hours at 950°C improved the superelastic response, due to the precipitation of Ni_4Ti_3 . The sample aged at 350°C for 18 hours demonstrated near perfect superelasticity, with the highest recoverable strain (5.5 %) and lowest irrecoverable strain (0.3 %). For all samples aged at 450°C , the irrecoverable strain is high in comparison to the samples aged at 350°C . This difference was ascribed to the morphology of the Ni_4Ti_3 precipitates.

Aging at higher temperatures lowers the hardening effect because of increases in precipitate size and reductions in the interparticle distance.

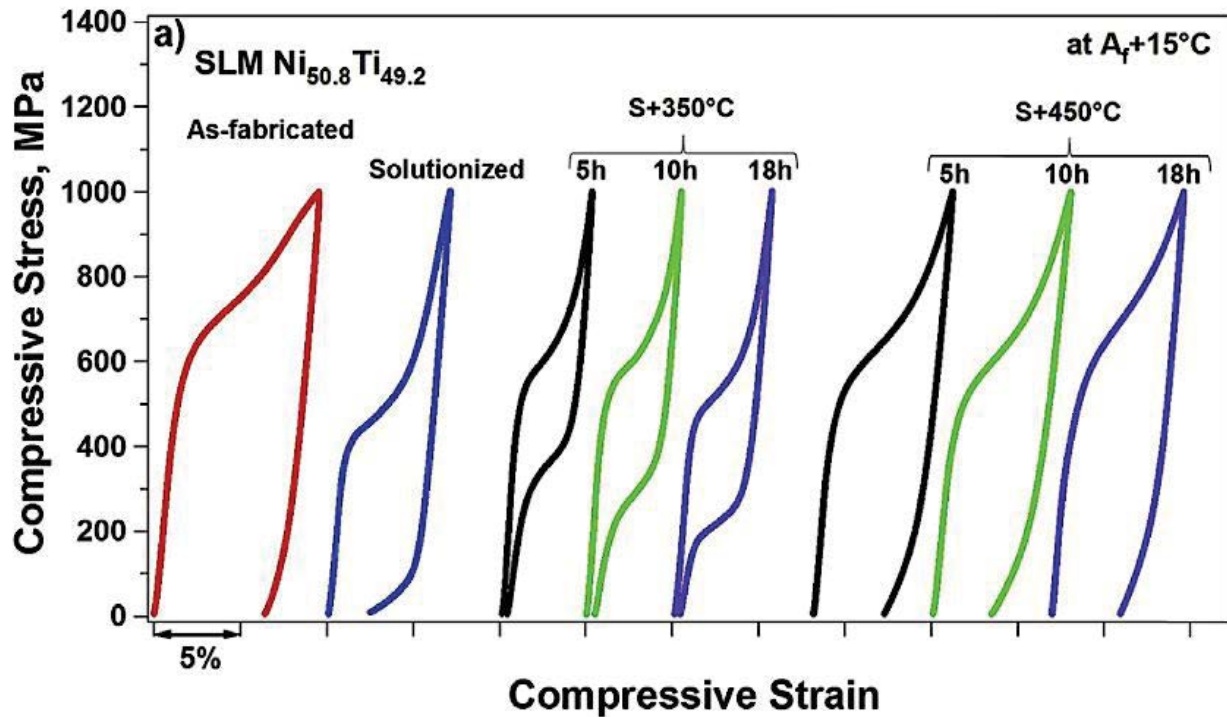


Figure 2.39: The superelasticity of as-fabricated, solution annealed and 350 °C, 450 °C aged samples(70)

Halani *et al.* carried out a solution heat treatment at 1050°C for 10 hours followed by oil quenching. It was found that after performing this solution heat treatment, the superelastic response of the alloys increased with aging temperature. As shown in figure 2.40. compression tests were performed at 50°C to ensure a fully austenitic microstructure. When aging at 500 °C, the alloy showed perfect recovery up to 3 % strain. However, when aged at 400 °C, perfect recovery could only be achieved up to 2 % strain. For both aging temperatures, the pronounced stress-induced martensitic transformation cannot be seen on the stress-strain curves. This is due to the alloy's inhomogeneous microstructure where martensitic variants interact with each other, precipitates and secondary phases.

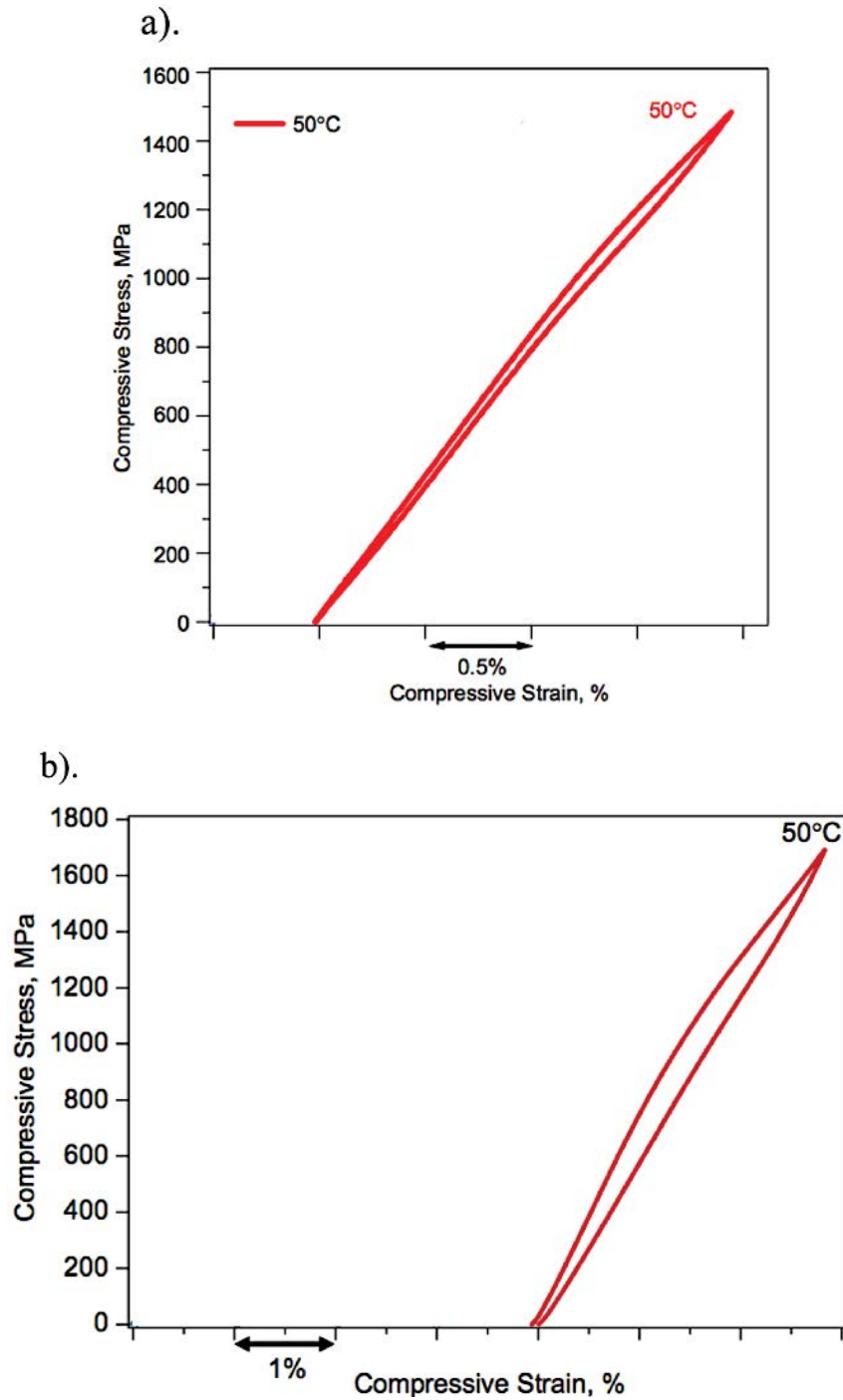


Figure 2.40: The stress-strain response obtained at 50 °C for a). sample aged at 400 °C b). sample aged at 500 °C (74)

Haberland et al. compared the superelastic response between conventionally produced and additively manufactured Ni-rich Ni_{50.7}Ti (at %). It was concluded that heat treatment is necessary for additively manufactured NiTi alloys to show similar recoverable deformation to conventionally produced alloys.

2.4.10. Micro-hardness Testing of Additively Manufactured NiTi

Shishkovsky et al. compared the micro-hardness between SLM as-fabricated Ni₅₅Ti₄₅ (wt %) to conventionally produced cast ingot NiTi (75). The values for SLM NiTi ranged between 540 to 735 HV. These values are around 1.5 - 2 times higher than the conventionally produced NiTi (~ 350-440 HV for the martensitic phase). This increase in hardness can be explained by the rapid cooling associated with SLM which hardens the NiTi matrix.

Shiva et al. studied the influence of composition in the development of additively manufacturing NiTi (76). Three compositions were investigated: Ni₅₅Ti₄₅, Ni₅₀Ti₅₀ & Ni₄₅Ti₅₅ (wt %). It was found that as the alloy's Ti content increased, so did the average micro-hardness. Furthermore, the higher hardness was accompanied with a reduction in ductility and ultimate strength (MPa), as shown in table 2.7. This behaviour can be explained by the hard, brittle Ti₂Ni intermetallic which forms in Ti-rich NiTi alloys.

Mokgalaka et al. studied the in-situ laser deposition of NiTi intermetallic coatings (77). Using the same compositions as *Shiva et al.* had previously used, the microhardness of each coating was tested. Similarly, *Mokgalaka et al.* found that the hardness value of each coating increased with Ti content.

Table 2.7: Mechanical properties of additively manufactured NiTi (76)

Sample (wt%)	Ultimate Strength (MPa)	Elastic Modulus (GPa)
NiTi ₅₅	296	20
NiTi ₅₀	315	21
NiTi ₄₅	320	21

Saedi et al. examined the effects of heat treatment on the micro-hardness of Ni-rich SLM $\text{Ni}_{50.8}\text{Ti}_{49.2}$ (at %) (70). As the testing was performed at room temperature, the samples could potentially be in different phases. This could affect the hardness results, as a stress-induced martensitic transformation could occur during testing and martensite is known to be a much softer phase in comparison to austenite. It was found that after SLM fabrication, the micro-hardness drops (278 HV \rightarrow 224 HV). However, when solutionising the alloy for 5.5 hours at 950 °C followed by water quenching, the hardness will increase. Additionally, the solution heat treated alloy has a higher micro-hardness in comparison to the micro-hardness of the NiTi ingot (288 HV). When the samples were aged at 350 °C and 450 °C, it was found that hardness increased with aging time. Additionally, samples aged at 350 °C were harder in comparison to samples aged at 450 °C.

Marattukalam et al. found that increases in the laser power increased the hardness of additively manufactured NiTi (51). Furthermore, as scan speed increased from 10 mm/s to 20 mm/s, the hardness decreased. However, this effect was only marginal. This behaviour is expected as large amounts of austenite are associated with increases in laser power. Thus, as the austenite phase is harder than the martensitic phase, the micro-hardness increases with laser power.

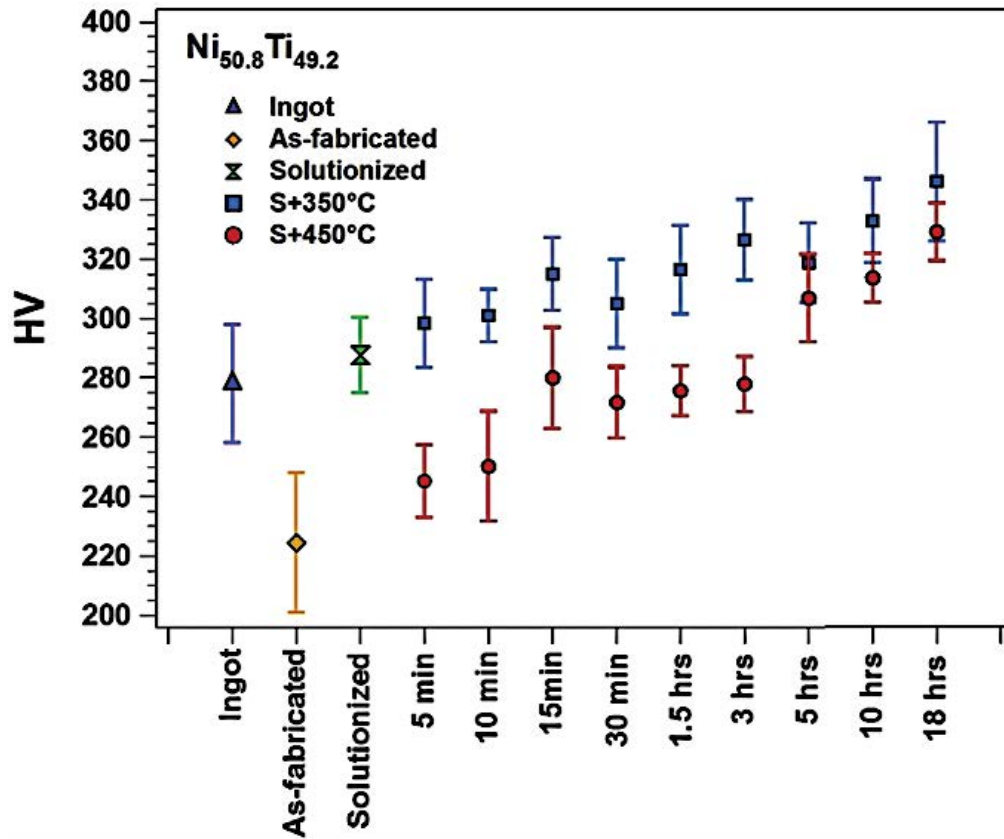


Figure 2.40: Vickers hardness of additively manufactured NiTi as a function of aging conditions (70)

2.4.11. Selective Laser Melting ‘In-Situ’ Alloying

Zhang *et al.* used SLM to fabricate NiTi alloys directly from elemental Ni and Ti powder (78). The Ni and Ti powder particles had D_{50} values of 30 μm and 35 μm , respectively. The powders were mixed using a tumbling mixer for 45 minutes. The overall powder blend composition was Ni₅₅Ti₄₅ wt %. An alternate laser scanning pattern with equal line spacing in the X and Y directions was used, with processing parameters: laser power = 100 W, scan speed = 0.05 – 0.4 m/s, layer thickness = 0.05 mm.

Visible from the XRD, shown in figure 2.41, after SLM fabrication no diffraction peaks can be observed for elemental Ti and Ni, indicating successful SLM in-situ alloying. Zhang *et al.* concluded that the temperature of the melt pool is dependent on the scanning speed. A slower

scanning speed will increase the duration of the laser-powder interaction. The melt pool will continually absorb laser energy and there will be an increase in the melt pool temperature. Strong diffraction peaks for the Ti_2Ni phase were observed in samples processed at the fastest scanning speed of 0.4 m/s. When processing at higher scanning speeds, the temperature of the melt pool decreases. As a result, elemental Ni and Ti cannot blend successfully in the melt pool.

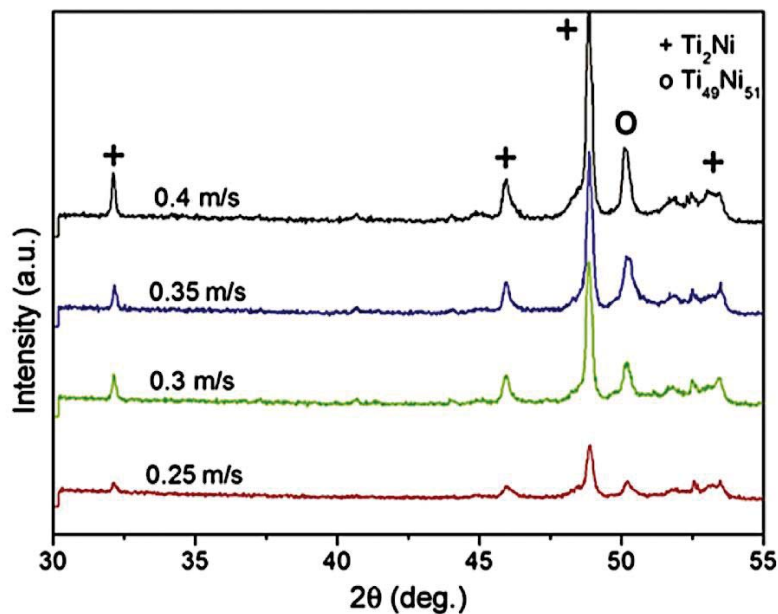


Figure 2.41: XRD results for all laser parameters: scan speed 0.05 m/s – 0.4 m/s; power = 100 W (78)

Guo *et al.* used SLM to alloy elemental Cu into Ti6Al4V (79). The corrosion resistance and antibacterial activity of the Ti6Al4V-Cu alloy was then assessed. Builds were processed from a blend of both powders using the cross-hatching technique on the Mlab-R, Concept Laser SLM machine. XRD reveals no diffraction peaks for elemental Cu, showing that Cu had been successfully fused into the Ti6Al4V matrix. When examining the influence of increasing Cu concentration on the density of the Ti6Al4V- x Cu alloys, it was clear that increasing Cu content from 2 – 6 wt %, had a negative effect on build density. Figure 2.42 shows that porosity increased to 3.78 % in alloys containing 6 wt % Cu. Furthermore, optical images showed an

increasingly visible number of micro-pores in the Ti6Al4V-xCu alloys, especially noticeable in the 6 wt % alloys.

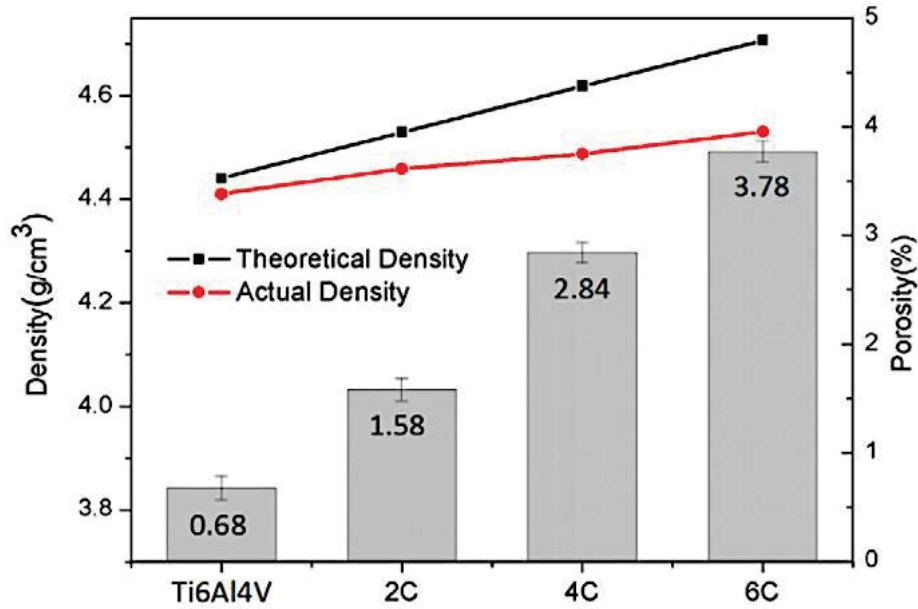


Figure 2.42: Density and porosity of Ti6Al4V-xCu alloys (79)

Qiu et al. took an alternative approach to SLM in-situ alloying and doped 0.2 wt % Pd onto Ti6Al4V powder, using a proprietary powder mixing machine (80). The machine involves the use of dual centrifugal forces and consists of a bottom plate with a basket attached in a slanted angle. During mixing, the bottom plate rotates clockwise around its central axis at speeds up to 3500 r/min. Whilst the basket rotates anticlockwise at a quarter of the rotation speed of the plate. This creates two dual asymmetrical forces which push the powder mixing. Following this, the doped powder was used during SLM processing.

After mixing, the distribution of Pd (bright particles) can be seen on the surface of the Ti6Al4V powder particles (figure 2.43). As the powder particles remained spherical, it can be said that high speed mixing occurred without any observable damage. The Pd was homogeneously distributed and had good bonding with the Ti6Al4V powder particles.

During SLM processing, samples were manufactured using a 400 W laser power. It was found that the porosity significantly increased at scan speeds greater than 3000 mm/s. EMPA analysis was performed on the sample processed at 400 W laser power and 2300 mm/s scan speed. It showed a homogeneous distribution of Pd through-out the Ti64 matrix. Indicating, the Pd had successfully melted and dissolved.

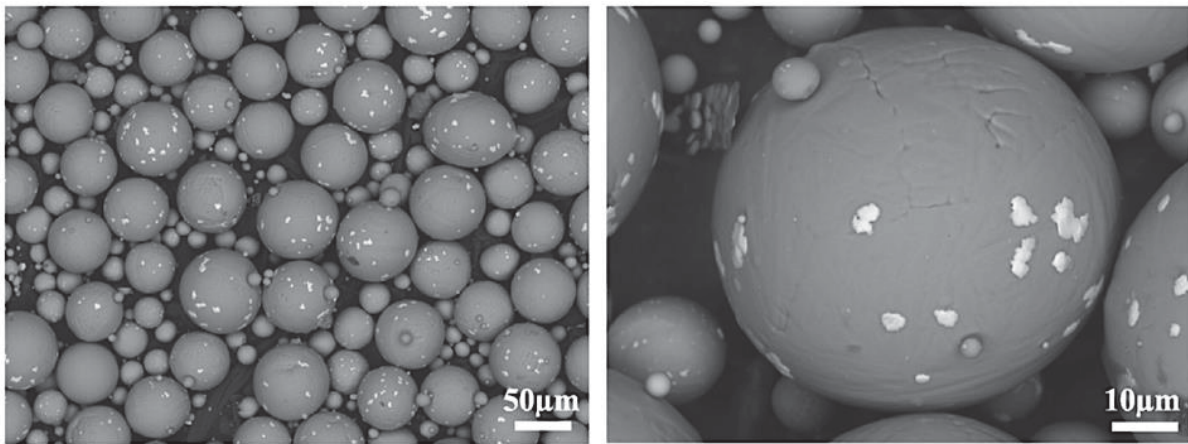


Figure 2.43: Backscattered SEM images showing the Ti64 powder particles and the Pd distribution after mixing (80)

2.4.12. The Corrosion Resistance of Additively Manufactured NiTi

To date, very little research has considered the corrosive properties of additively manufactured NiTi. *Marattukalam et al.* studied how the grain size of laser processed NiTi changed with laser power and scan speed (51). Moreover, the effects this had on the corrosion resistance of the alloy. High energy inputs form larger grains due to slower cooling rates. Thus, when the laser power increased from 200 W to 400 W, at a constant speed of 20 mm/s, the grains became larger. Tafel plots were used to obtain the corrosion current (I_{corr}) and corrosion potential (E_{corr}) of the additively manufactured NiTi when in Ringer's solution. I_{corr} represents the metal corrosion kinetics and E_{corr} indicates the thermodynamic characteristics of the system. The overall corrosion resistance of the alloy is the combined effect of I_{corr} and E_{corr} . As shown in figure 2.44, samples processed at higher laser powers had a more noble E_{corr} , as less electrons

were released from the surface and a decreased I_{corr} , signifying an increase in corrosion resistance.

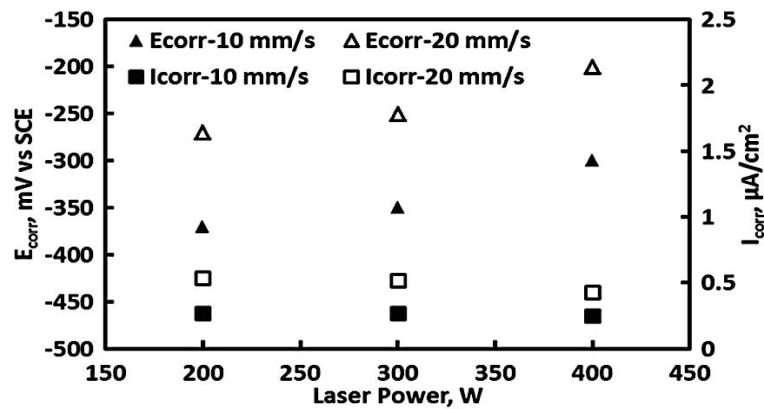


Figure 2.44: Concentration of B2 (austenite) and B19' martensite phases in additively manufactured NiTi (51)

Both *Guo et al.* and *Qiu et al.* investigated the effects of alloying elements on the corrosion resistance of SLM Ti-based alloys. *Guo et al.* conducted electrochemical tests to evaluate the corrosion resistance of Ti6Al4V alloyed with Cu (79). A standard three-electrode configuration was used and the results are shown in figure 2.46. A saturated calomel electrode (SCE) was used as the reference electrode, the counter electrode was a platinum electrode. The testing solution used was 0.9 % NaCl and the pH was adjusted to be at 7.2-7.4 in the quartz corrosion cell. Furthermore, an electric-heated thermostatic water bath was used to keep the temperature constant at $37 \pm 1^\circ\text{C}$.

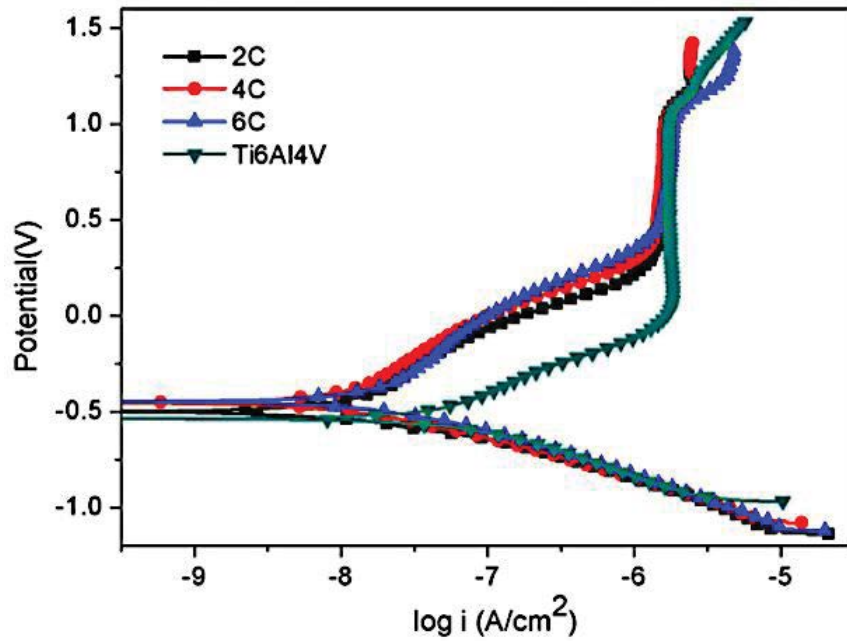


Figure 2.46: The potential dynamic polarization curves of Ti6Al4V alloys with different Cu contents (79)

The alloys Ti6Al4V- x Cu ($x = 0, 2, 4, 6$ wt %) were tested and the results are displayed in table 2.8. It was found that increasing the Cu content up to 4 wt % improved the resistance of the passive layer. However, alloying above 4 wt % had an adverse impact on the corrosion resistance. The polarisation curves show that as Ti6Al4V is alloyed with up to 4 wt % Cu, the curve shifts upwards causing an increase of E_{corr} and a decrease of I_{corr} , hence an increase in the corrosion resistance. However, it is evident that as Cu content increases up to 6 wt %, there is an increase in the I_{corr} from 10.0 nA to 18.2 nA, indicating a reduction in the corrosion resistance. Nevertheless, the Cu 6 wt % alloyed sample still had a lower I_{corr} value in comparison to the original Ti6Al4V alloy. Thus, indicating a more noble alloy.

Table 2.8: Electrochemical data of Ti4Al4V alloys with different Cu contents from OCP curves and potential-dynamic polarization curves (79)

Samples	I _{corr} (nA)	E _{corr} (mV)	E _b (mV)	Corrosion rate (mg.cm ⁻² .yr ⁻¹)
2 wt % Cu	12.9	-500	1017	0.154
4 wt % Cu	10.0	-453	1014	0.119
6 wt % Cu	18.2	-447	1016	0.217
Ti6Al4V	58.6	-536	1018	0.669

Theoretically, increasing the Cu content to 6 wt % should further improve the corrosion resistance, as Cu is a nobler element. The Cu helps to form a passive film with higher thermodynamical stability. However, the sample's porosity and Ti₂Cu intermetallic phases can be used to explain this unexpected behaviour. Intermetallic phases are generally more noble compared to the metallic matrix. However, Ti₂Cu exists in two different states for Ti6Al4V- *x* Cu wt % alloys. Firstly, in an interstitial solid solution in the α and β phases and secondly, the precipitation of the intermetallic Ti₂Cu phase. The Ti₂Cu intermetallic is a stable phase. However, in the presence of Ti₂Cu in an interstitial solid solution, the Cu ions are released easier due to their spontaneous diffusion under the driving force provided by concentration gradient.

Qiu et al. studied the influence of Pd on the corrosion resistance of Ti6Al4V. Similar, to *Guo et al.* a saturated calomel reference electrode and platinum counter electrode was used. However, tests were conducted in 2M HCL solution at room temperature, deaerated by argon bubbling for 1 hour prior to testing.

Firstly, *Qiu et al.* compared the corrosion resistance of wrought Ti6Al4V (figure 2.47(a)) to the SLM processed alloy (figure 2.47(b)) (80). It was found that the latter had a higher

corrosion resistance as no active anodic region is visible on the polarisation curves. This can be explained by the differences microstructure and the coarser grain structure associated with SLM processing. Following this, the influences of Pd on the SLM Ti6Al4V were studied (figure 2.47(c)). It was found that the addition of 0.2 wt % Pd shifted the corrosion potential into a passive region for Ti6Al4V. Furthermore, as the polarisation curves for the Pd modified samples showed more consistent behaviour, it can be concluded that a more stable passive film may have been developed.

To study the effects of porosity on the corrosion resistance of the SLM Ti6Al4V-0.2 wt % Pd alloy, samples were processed at higher laser scan speeds to contain more porosity. The higher porosity sample had a comparable passive current to those with lower porosity. Suggesting that for the current tests, porosity had little effect on the corrosion resistance behaviour. Secondary electron and optical microscopy was employed to study the changes in the microstructure after electrochemically testing the samples. The pores showed no obvious change in size or morphology, indicating pores are not preferential corrosion attack sites. Additionally, alloying with 0.2 wt % Pd appeared to prevent the dissolution of grains during the corrosive attack.

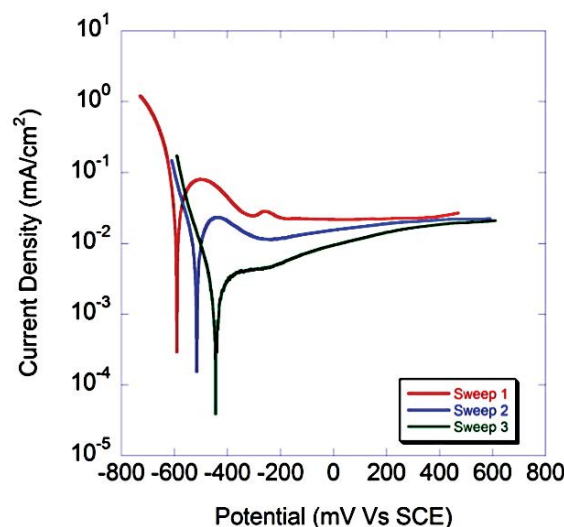


Figure 2.47 a). Electrochemical polarisation curve for forged + annealed Ti64 (80)

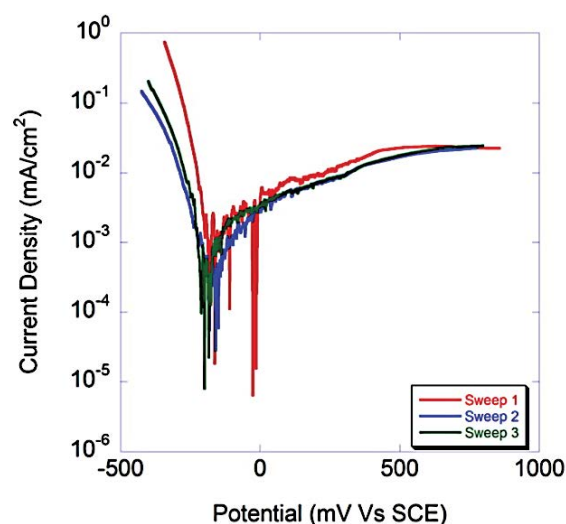


Figure 2.47 b). Electrochemical polarisation curves for SLM Ti64(80)

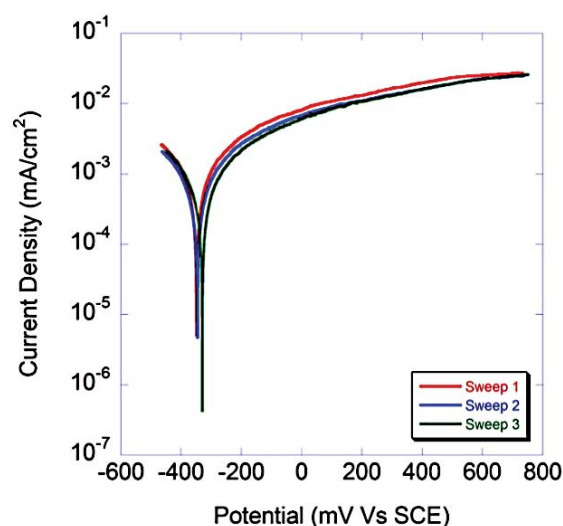


Figure 2.47 c). Electrochemical polarisation curves for SLM Ti64-0.2Pd (80)

2.4.13. The Biocompatibility of Additively Manufactured NiTi

Habijan et al. studied the biocompatibility of dense and porous NiTi produced by SLM (81). During the study, hMSC cells were incubated on four NiTi samples for eight days. Following this, samples were stained using Calcein AM (live cells) and propidium iodide (dead cells) and fluorescence micrographs were taken to observe the cell-material interaction and cell morphology. Sample I was dense and the cells were grown on the top face of the as-fabricated cylinder. Sample II was dense and the cells were grown on the side walls of the as-fabricated

cylinder. Sample III was porous due to processing at a 400 μm scan spacing (dense samples were processed at small scan spaces of 120 μm). Cells were grown on the top face of the as-fabricated cylinder. Sample IV was designed using a CAD file to manufacture porous cylinders with 500 μm quadratic pores. Illustrations of the samples can be seen in figure 2.48.


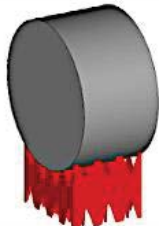

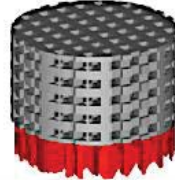



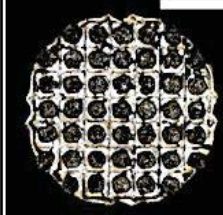
	sample type I	sample type II	sample type III	sample type IV
CAD models illustrating building orientations (red elements are support structures)				
porosity produced by	no designated porosity	no designated porosity	large hatch distance	CAD model
relative density	99.1 %	99.1 %	88.5 %	65.4 %
surfaces to be cultured with hMSC				

Figure 2.48: Illustrations of the SLM NiTi samples used in cell testing (81)

Figure 2.49 displays fluorescence micrographs of the NiTi samples stained with Calcein AM and propidium iodide: green represents living cells and red represents dead cells. Viable cells adhered on the surfaces of all the samples, with higher concentrations being located inside porous structures. The viability of cells were improved on the testing face of sample II compared to sample I, indicating that cell morphology is influenced by surface roughness. The testing face of sample II was rougher, as this face was formed by the sidewalls of the scanning tracks of the stacked layers. However, the surface of sample I was formed by the upsides of the hatches. The low hatch distances produced a slight overlap of adjacent hatches and thus closed surface structure.

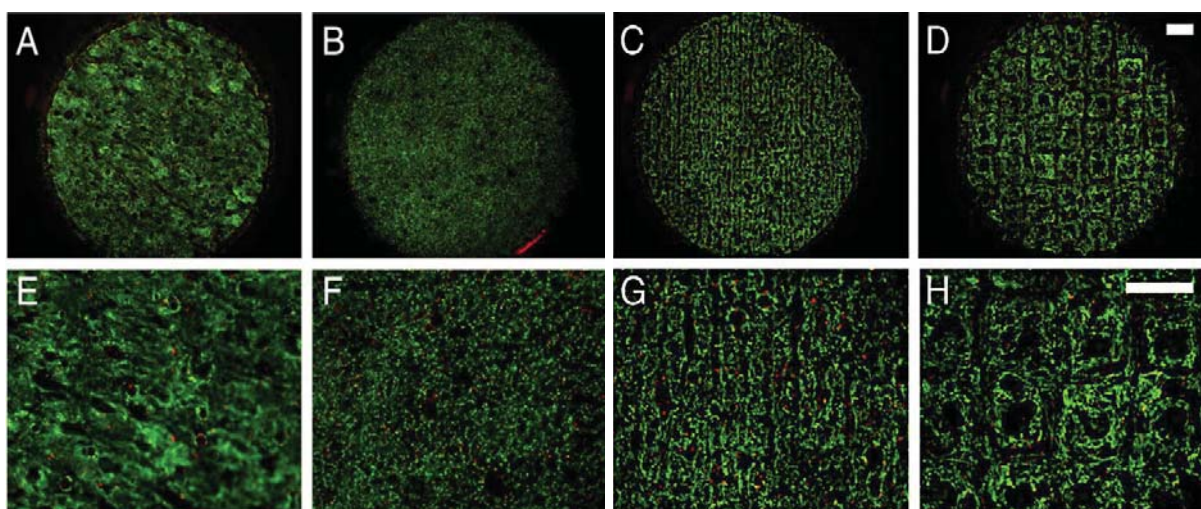


Figure 2.49: Fluorescence micrographs of NiTi specimens a). Sample I b). sample II c). sample III d). sample IV e). high mag sample I f). high mag sample II g). high mag sample III h). high mag sample IV (scale bar= 1mm) (81)

As SLM is a powder based process, the release of loosely adhered powder particles can have a negative impact on the biocompatibility of the alloy. It was found that prevention of particle release is impossible. However, long term ultrasonic cleaning after SLM processing can be used to reduce loose powder particle release. Furthermore, sample orientation and laser focus adjustment can be used to improve surface quality, creating a smoother surface with less loose powder particles. The testing face of sample I improved when the laser beam diameter was less focused at 128 μm . In contrast, the testing face of sample II was enhanced when processed with a focused laser beam diameter at 61 μm .

Cox et al. showed that surface tomography played a critical impact on cell attachment and viability (82). MC3T3 cells were seeded onto Ti6Al4V SLM samples and incubated for 1, 3 and 7 days. It was found that on day 1 and 3, MC3T3 cells clustered in localised areas with higher roughness. Thus, it can be said that rough areas support initial attachment more in comparison to polished surfaces. After 7 days, cells had migrated and proliferated across the surfaces of the samples, except for regions where partially melted particles were present. The

large angle between the partially melted spherical particles and the bulk surface may explain why cells were unable to spread across these regions.

Guo et al. studied the effect of Cu on the biocompatibility of SLM Ti6Al4V alloys (79). BMSCs cells were seeded onto the top surface of as-fabricated SLM Ti6Al4V- Cu (2, 4, 6 wt %) alloys and incubated for 1, 3 and 7 days at 37°C. To observe cell attachment and morphology, a Phenom G2 SEM was used.

As shown in figure 2.50, a confluent layer of cells attached to the surface of all the Ti6Al4VCu alloys after day 1. Additionally, it is evident that the addition of Cu does not negatively impact the biocompatibility of the alloy as there is no significant difference between the cell morphology after 1 day cultivation for all samples. For all samples, the cells became denser and better spread after being incubated for 3 and 7 days. Thus, it can be concluded that Cu addition had no negative effect on cell activity.

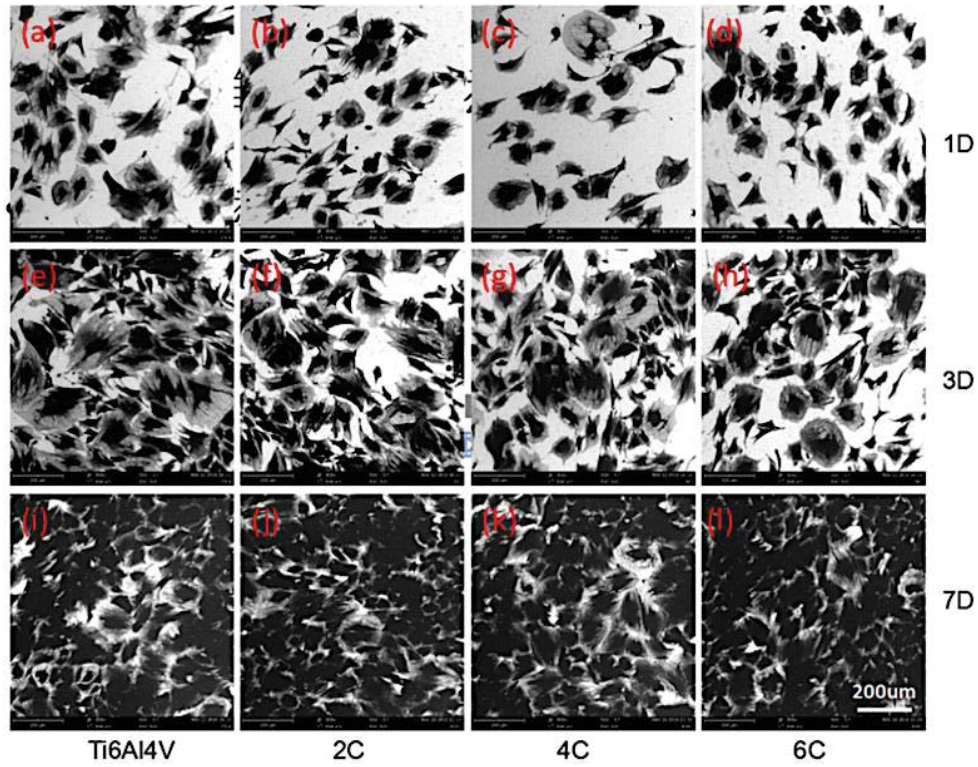


Figure 2.50: The morphology of BMSCs on Ti6Al4V-xCu samples after 1, 3, 7 days incubation. (a),(e),(i): Ti6Al4V. (b),(f),(j): 2C. (c),(g),(k): 4C. (d),(h),(l): 6C (79)

2.5. Current State of Knowledge on Additively Manufactured NiTi SMA

2.5.1. Conclusions

Within this chapter, the physical metallurgy and the experimental studies related to the SLM of NiTi SMA have been discussed. The current state of knowledge within of the SLM of NiTi is summarised in the following points:

1). As solidification is a temperature driven process and no external pressure is involved, porosity is the main defect associated with the SLM of NiTi. Overall, high density NiTi has a narrow processing window with a peak laser energy density between $40 - 90 \text{ J/mm}^3$, proving this is an alloy which requires lower energy input processing. However, laser power and scan speed seem to have an insignificant effect if they combine to produce the same laser energy density.

- 2). Differences in the cooling rate of the melt will influence the concentration of phases and the microstructure of the SLM NiTi build. Faster cooling rates stabilise the austenite phase, whereas reductions in cooling rate will encourage increased concentrations of martensite, the precipitation of intermetallic phases, such as Ti_2Ni and the coarsening of grain size.
- 3). Although the SLM process is performed under argon atmosphere, impurity pick up during fabrication is unavoidable. However, processing at lower laser energy densities will minimise contamination.
- 4). There is an increase in transformation temperature after SLM processing. This difference is due to the Ni evaporation associated with laser processing. Higher energy inputs increase Ni evaporation as the melt pool is kept at elevated temperatures for longer periods of time.
- 5). The strength and superelastic response of Ni-rich SLM NiTi alloys can be improved through heating treating to induce precipitation. SLM defects such as porosity were found to have little effect on the compressive strength of the alloy. However, porosity was found to have a detrimental effect on the alloy's tensile strength.
- 6). The Ni:Ti ratio influences the micro-hardness of the alloy. The Vickers hardness number increases with Ti content. Furthermore, rapid cooling rates during SLM processing results in a harder NiTi matrix due to the presence of the austenite phase.
- 7). Processing at higher energy inputs improves the corrosion resistance of NiTi. This is due to an increase in grain size and reduction of grain boundaries.

8). Studies suggest SLM processing can produce biocompatible NiTi. Cells can adhere to and cultivate on the surface of SLM parts. Rougher surfaces indicate higher cell attachment. Loose powder particles remaining on SLM parts after processing have a negative impact on cell growth. Although loose powder after processing is unavoidable, it can be improved by ultrasonic cleaning.

2.6. Project Aims and Objectives

The work presented in this thesis focuses on the development and processing of NiTi SMAs containing Pd using SLM. The research investigates the use of laser-based additive manufacturing to produce dense and homogeneous NiTi and TiNiPd SMAs, which can be used in biomedical applications. The aim of alloying Pd into NiTi is to fabricate a material with enhanced corrosion resistance, biocompatibility and X-ray visibility and therefore improve the alloy for its intended biomedical application. Additionally, manufacturing using SLM offers a better processing route as it circumvents the current issues with manufacturing NiTi SMAs. Offering increased freedom of design and reduced tool wear.

Thesis objectives:

- 1). Assess the impact of powder quality on the manufactured builds, through characterisation of the powder used in SLM trials. Investigate how the type of atomisation affects the morphology, oxygen content, particle size distribution and flowability of powder. Furthermore, how changes in impurity content and thermal behaviour can be related to powder particle size.
- 2). Optimise the process parameters of SLM as a function of cracking and porosity. Determine the effects of laser power (W), speed (mm/s) and hatch spacing, to achieve an optimum parameter set up for SLM.

- 3). Examine the melt pool formation during SLM and chemical homogeneity of the builds to identify possible trends.
- 4). Study the phase transformations and microstructural evolution of builds with differing process parameters (thus, laser energy densities).
- 5). Determine the transformation temperature of additive manufactured NiTiPd, in order to establish the effects of Pd, precipitation and energy density on the martensitic transformation.
- 6). The significance of additive manufacturing and processing parameters on impurity pick up (oxygen, carbon and nitrogen) will be assessed.
- 7). Explore the superelastic response of the SLM fabricated Pd modified TiNiPd.
- 8). Examine the biological response and corrosion behaviour of TiNiPd in physiological solutions at body temperature (37°C) for samples manufactured using the optimised parameter set up for SLM.
- 9). Post heat-treatments will be used to tailor the microstructure, strength, superelasticity and transformation temperature of the SLM. A comparison between as fabricated, solution annealed and post heat-treated samples will be drawn.
- 10). The difference in radiopacity between the binary and ternary alloy will be determined. Thus, the improvement in X-ray visibility against the X-ray background will be quantified.

2.7. Novel areas of Thesis Research

- 1). Much research has considered the SLM of austenitic NiTi SMA at body temperature for biomedical applications. However, very little research has investigated the SLM of martensitic

Ti-rich binary and ternary NiTi SMA for biomedical applications.

2). Proven by *Qiu et al.* it is possible to coat up to 0.2 at % Pd onto powder particles, which can then be used in SLM. There is currently no in-situ alloying methodology for alloying larger amounts of Pd (> 0.2 at %) into binary NiTi.

3). Although the influence of Pd on the transformation temperature of binary NiTi has been investigated, this has only been for conventionally produced alloys. Currently no research has considered the transformation temperatures of ternary TiNiPd alloys manufactured using SLM.

4). Novel areas of research also lie in modifying the characteristics of TiNiPd secondary phases by the use of heat treatments. This work was done in an attempt to tailor alloy properties such as the superelastic response and phase transformation temperatures.

2.8. References

1. Bertheville B, Bidaux JE. Alternative powder metallurgical processing of Ti-rich NiTi shape-memory alloys. *Scr Mater*. 2005;52(6):507–12.
2. Frenzel J, Zhang Z, Neuking K, Eggeler G. High quality vacuum induction melting of small quantities of NiTi shape memory alloys in graphite crucibles. *J Alloys Compd*. 2004;385(1–2):214–23.
3. Pelton AR, Russell SM, DiCello J. The physical metallurgy of nitinol for medical applications. *J Mater*. 2003;55(5):33–7.
4. Chen KC. NiTi – Magic or Phase Transformations? *Am Soc Eng Educ Annu Conf Expo*. 2003;1–7.
5. Roytburd A L. Principal concepts of martensitic theory. *J Phys Iv*. 1995;5(C8, Part 1):21–30.
6. Bhattacharya K, Conti S, Zanzotto G, Zimmer J. Crystal symmetry and the reversibility of martensitic transformations. *Nature*. 2004;428(6978):55–9.
7. Kök M, Dağdelen F, Aydoğdu A, Aydoğdu Y. The change of transformation temperature on NiTi shape memory alloy by pressure and thermal ageing. *J Phys Conf Ser*. 2016;667(1).
8. Amini A, Cheng C, Kan Q, Naebe M, Song H. Phase transformation evolution in NiTi shape memory alloy under cyclic nanoindentation loadings at dissimilar rates. *Sci Rep*. 2013;3:1–7.
9. Chen X, Peng X, Chen B. Shape memory and transformation behavior of high strength 60NiTi in compression. *Smart Mater Struct*. 2016;25:1–8.
10. Mirzaeifar R, Gall K, Zhu T, Yavari A, Desroches R. Structural transformations in NiTi shape memory alloy nanowires. *J Appl Physics*. 2014;194307(May):1–8.

11. Gou L, Liu Y, Ng T. Effect of Cu Content on Atomic Positions of Ti50Ni50–xCux Shape Memory Alloys Based on Density Functional Theory Calculations. *Metals (Basel)* [Internet]. 2015;5(4):2222–35.
12. Otsuka K, Ren X. Physical metallurgy of Ti-Ni-based shape memory alloys. *Prog Mater Sci* [Internet]. 2005;50(5):511–678.
13. Tom.Duerig@Nitinol.com.
14. Wang XB, Verlinden B, Van Humbeeck J. R-phase transformation in NiTi alloys. *Mater Sci Technol* [Internet]. 2014;30(13):1517–29.
15. Metallurgica S, Vol M, Press P, September R, October R. (Received September 18, 1991) (Revised October 14, 1991). *Scr Metall Mater*. 1992;26(c):1149–51.
16. Bowles JS, Wayman CM. The bain strain, lattice correspondences, and deformations related to martensitic transformations. *Metall Trans*. 1972;3(5):1113–21.
17. Zhang X, Sehitoglu H. Crystallography of the $B2 \rightarrow R \rightarrow B19'$ phase transformations in NiTi. *Mater Sci Eng A*. 2004;374(1–2):292–302.
18. H.K.D.H. Bhadeshia, *Bainite in Steels*, 2nd Ed, The Institute of Materials, University of Cambridge, London, 2001, p. 378.
19. Jin YM, Weng GJ. A direct method for the crystallography of martensitic transformation and its application to TiNi and AuCd. *Acta Mater*. 2002;50(11):2967–87.
20. Peigney M, Peigney M. Energy minimizing strains in martensitic microstructures To cite this version : HAL Id : hal-00877461. 2013;6–8.
21. Waitz T, Spišák D, Hafner J, Karnthaler HP. Size-dependent martensitic transformation path causing atomic-scale twinning of nanocrystalline NiTi shape memory alloys. *Europhys Lett*. 2005;71(1):98–103.
22. Ojha A, Sehitoglu H. Critical Stresses for Twinning, Slip, and Transformation in Ti-Based Shape Memory Alloys. *Shape Mem Superelasticity* [Internet]. 2016;2(2):180–

- 95.
23. Karaman I, Kulkarni A V., Luo ZP. Transformation behaviour and unusual twinning in a NiTi shape memory alloy ausformed using equal channel angular extrusion. *Philos Mag.* 2005;85(16):1729–45.
24. Kashchenko MP, Chashchina VG. Orientations of type II twin boundaries in B2→B19' martensitic transformation in dynamic theory. *Phys Mesomech [Internet]*. 2016;19(1):107–14.
25. Zhang Y, Li Z, Esling C, Muller J, Zhao X, Zuo L. A general method to determine twinning elements. *J Appl Crystallogr.* 2010;43(6):1426–30.
26. Liu Y, Xie Z. Detwinning in shape memory alloy [Internet]. *Progress in Smart Materials and Structures, Nova* . 2007. 29-65 p.
27. Sanusi KO, Ayodele OL, Khan MTE. A concise review of the applications of NiTi shape-memory alloys in composite materials. *S Afr J Sci.* 2014;110(7–8):5–9.
28. Stoeckel D. The Shape Memory Effect - Phenomenon, Alloys, and Applications. *Shape Mem Alloy Power Syst EPRI.* 1995;1–13.
29. Aversa R, Tamburrino F, Petrescu RV V., Petrescu FIT, Artur M, Chen G, et al. Biomechanically inspired shape memory effect machines driven by muscle like acting NiTi alloys. *Am J Appl Sci.* 2016;13(11):1264–71.
30. Liu Y. The superelastic anisotropy in a NiTi shape memory alloy thin sheet. *Acta Mater [Internet]*. 2015;95:411–27.
31. Frenzel J, Wiecek A, Opahle I, Maaß B, Drautz R, Eggeler G. On the effect of alloy composition on martensite start temperatures and latent heats in Ni-Ti-based shape memory alloys. *Acta Mater [Internet]*. 2015;90:213–31.
32. Frenzel J, George EP, Dlouhy A, Somsen C, Wagner MFX, Eggeler G. Influence of Ni on martensitic phase transformations in NiTi shape memory alloys. *Acta Mater*

- [Internet]. 2010;58(9):3444–58.
33. Zhang YQ, Jiang SY, Zhao YN, Tang M. Influence of cooling rate on phase transformation and microstructure of Ti-50.9%Ni shape memory alloy. *Trans Nonferrous Met Soc China (English Ed.)* 2012;22(11):2685–90.
 34. Duerig TW, Pelton AR. Ti-Ni shape memory alloys. *Mater Prop Handb Titan Alloy*. 1994;683:1035–48.
 35. Wang L, Wang C, Zhang LC, Chen L, Lu W, Zhang D. Phase transformation and deformation behavior of NiTi-Nb eutectic joined NiTi wires. *Sci Rep [Internet]*. 2016;6(April):1–11.
 36. Chang PC, Ko ML, Ramachandran B, Kuo YK, Chien C, Wu SK. Comparative study of R-phase martensitic transformations in TiNi-based shape memory alloys induced by point defects and precipitates. *Intermetallics*. 2017;84:130–5.
 37. Khalil Allafi J, Ren X, Eggeler G. The mechanism of multistage martensitic transformations in aged Ni-rich NiTi shape memory alloys. *Acta Mater*. 2002;50(4):793–803.
 38. Frenzel J, Zhang Z, Somsen C, Neuking K, Eggeler G. Influence of carbon on martensitic phase transformations in NiTi shape memory alloys. *Acta Mater*. 2007;55(4):1331–41.
 39. Jiang SY, Zhao YN, Zhang YQ, Hu L, Liang YL. Effect of solution treatment and aging on microstructural evolution and mechanical behavior of NiTi shape memory alloy. *Trans Nonferrous Met Soc China (English Ed.)* 2013;23(12):3658–67.
 40. Haenschke T, Davis CL, Attallah MM. Influence of the microstructural inhomogeneities on the martensite-to-austenite phase transformation temperatures in TiNiCu-based shape-memory alloys. *Mater Chem Phys [Internet]*. 2013;141(1):272–7.

41. Schetky, L.M. and M. Wu. Issues in the further development of Nitinol properties and processing for medical device applications. in *Medical Device Materials: Proceedings from the Materials & Processes for Medical Devices Conference 2003*, 8-10 September 2003, Anaheim, California. 2004. ASM International.
42. Rahim M, Frenzel J, Frotscher M, Pfetzinger-Micklich J, Steegmüller R, Wohlschlägel M, et al. Impurity levels and fatigue lives of pseudoelastic NiTi shape memory alloys. *Acta Mater.* 2013;61(10):3667–86.
43. Zarinejad M, Liu Y. Dependence of transformation temperatures of NiTi-based shape-memory alloys on the number and concentration of valence electrons. *Adv Funct Mater.* 2008;18(18):2789–94.
44. Duerig T, Pelton A, Stöckel D. An overview of nitinol medical applications. *Mater Sci Eng A [Internet]*. 1999;273–275:149–60.
45. Stoeckel, Pelton, Duerig. Self Expanding Nitinol Stents - Material and Design Considerations. *Eur Radiol.* 2004;14(2):292–301.
46. Elahinia MH, Hashemi M, Tabesh M, Bhaduri SB. Manufacturing and processing of NiTi implants: A review. *Prog Mater Sci [Internet]*. 2012;57(5):911–46.
47. Prasad K, Bazaka O, Chua M, Rochford M, Fedrick L, Spoor J, et al. Metallic biomaterials: Current challenges and opportunities. *Materials (Basel)*. 2017;10:1-33.
48. Greiner C, Oppenheimer SM, Dunand DC. High strength, low stiffness, porous NiTi with superelastic properties. *Acta Biomater.* 2005;1(6):705–16.
49. Hussein MA, Mohammed AS, Al-Aqeeli N. Wear characteristics of metallic biomaterials: A review. *Materials (Basel)*. 2015;8(5):2749–68.
50. Tosun G, Ünsaldi E, Özler L, Orhan N, Durmuş AS, Eröksüz H. Biocompatibility of NiTi Alloy Implants in vivo. 2013;7(6):271–4.
51. Marattukalam JJ, Singh AK, Datta S, Das M, Balla VK, Bontha S, et al.

- Microstructure and corrosion behavior of laser processed NiTi alloy. *Mater Sci Eng C* [Internet]. 2015;57:309–13. Available from:
<http://dx.doi.org/10.1016/j.msec.2015.07.067>
52. Trepanier C, Venugopalan R, Pelton A. Corrosion Resistance and Biocompatibility of Passivated NiTi. *Shape Mem Implant SE - 3* [Internet]. 2000;35–45.
 53. Civile I. SMA Biomedical Applications. 2015. 307-341 p.
 54. Elahinia M.H., Hashemi M., Tabesh M., Bhaduri S.B. Manufacturing and processing of NiTi implants: A review. *Prog. Mater. Sci.* 2012;57:911–946. doi:
10.1016/j.pmatsci.2011.11.001.
 55. Hassan MR, Mehrpouya M, Dawood S. Review of the Machining Difficulties of Nickel-Titanium Based Shape Memory Alloys. *Appl Mech Mater* [Internet]. 2014;564(November):533–7.
 56. Tofail SAM, Butler J, Gandhi AA, Carlson JM, Lavelle S, Carr S, et al. X-ray visibility and metallurgical features of NiTi shape memory alloy with erbium. *Mater Lett.* 2014;137:450–4.
 57. Data PP. (12) United States Patent Boylan et a]. METHOD FOR PROVIDING RADIOPAQUE (10) Patent No .: (45) Date of Patent : i. 2011;2(12).
 58. Tuissi A, Carr S, Butler J, Gandhi AA, O'Donoghue L, McNamara K, et al. Radiopaque Shape Memory Alloys: NiTi–Er with Stable Superelasticity. *Shape Mem Superelasticity* [Internet]. 2016;2(2):196–203.
 59. Saedi, S.; Moghaddam, N.S.; Amerinatanzi, A.; Elahinia, M.; Karaca, H.E. On the effects of selective laser melting process parameters on microstructure and thermomechanical response of Ni-rich NiTi. *Acta Mater.* **2018**, *144*, 552–560.

60. Meier H, Haberland C. Experimental studies on selective laser melting of metallic parts. *Materwiss Werksttech* [Internet]. 2008;39(9):665–70.
61. Krishna BV, Bose S, Bandyopadhyay A. Laser Processing of Net-Shape NiTi Shape Memory Alloy. *Metall Mater Trans A* [Internet]. 2007;38(5):1096–103.
62. Dadbakhsh S, Speirs M, Kruth JP, Schrooten J, Luyten J, Van Humbeeck J. Effect of SLM parameters on transformation temperatures of shape memory nickel titanium parts. *Adv Eng Mater*. 2014;16(9):1140–6.
63. Walker JM, Haberland C, Taheri Andani M, Karaca HE, Dean D, Elahinia M. Process development and characterization of additively manufactured nickel–titanium shape memory parts. *J Intell Mater Syst Struct* [Internet]. 2016;27(19):2653–60.
64. Haberland C, Elahinia M, Walker JM, Meier H, Frenzel J. On the development of high quality NiTi shape memory and pseudoelastic parts by additive manufacturing. *Smart Mater Struct*. 2014;23(10).
65. Li S, Hassanin H, Attallah MM, Adkins NJE, Essa K. The development of TiNi-based negative Poisson's ratio structure using selective laser melting. *Acta Mater* [Internet]. 2016;105:75–83.
66. Bormann T, Müller B, Schinhammer M, Kessler A, Thalmann P, De Wild M. Microstructure of selective laser melted nickel-titanium. *Mater Charact*. 2014;94:189–202.
67. Haberland C, Elahinia M, Walker JM, Meier H, Frenzel J. On the development of high quality NiTi shape memory and pseudoelastic parts by additive manufacturing. *Smart Mater Struct* [Internet]. 2014;23(10):104002.
68. Bormann T, Schumacher R, Müller B, Mertmann M, de Wild M. Tailoring Selective Laser Melting Process Parameters for NiTi Implants. *J Mater Eng Perform* [Internet]. 2012;21(12):2519–24.

69. Hamilton RF, Palmer TA, Bimber BA. Spatial characterization of the thermal-induced phase transformation throughout as-deposited additive manufactured NiTi bulk builds. *Scr Mater* [Internet]. 2015;101:56–9.
70. Saedi S, Turabi AS, Andani MT, Haberland C, Karaca H, Elahinia M. The influence of heat treatment on the thermomechanical response of Ni-rich NiTi alloys manufactured by selective laser melting. *J Alloys Compd* [Internet]. 2016;677:204–10.
71. Bagheri A, Mahtabi MJ, Shamsaei N. Fatigue behavior and cyclic deformation of additive manufactured NiTi. *J Mater Process Technol* [Internet]. 2018;252(October 2017):440–53.
72. Meier H, Haberland C, Frenzel J. Structural and functional properties of NiTi shape memory alloys produced by selective laser melting. *Innov Dev Des Manuf Adv Res virtual rapid Prototyp* [Internet]. 2011;291–6.
73. Saedi S, Turabi AS, Andani MT, Moghaddam NS, Elahinia M, Karaca HE. Texture, aging, and superelasticity of selective laser melting fabricated Ni-rich NiTi alloys. *Mater Sci Eng A* [Internet]. 2017;686(January):1–10.
74. Halani PR, Kaya I, Shin YC, Karaca HE. Phase transformation characteristics and mechanical characterization of nitinol synthesized by laser direct deposition. *Mater Sci Eng A* [Internet]. 2013;559:836–43.
75. Shishkovsky I, Yadroitsev I, Smurov I. Direct Selective Laser Melting of Nitinol Powder. *Phys Procedia* [Internet]. 2012;39:447–54.
76. Shiva S, Palani IA, Mishra SK, Paul CP, Kukreja LM. Investigations on the influence of composition in the development of Ni-Ti shape memory alloy using laser based additive manufacturing. *Opt Laser Technol* [Internet]. 2015;69(1):44–51.
77. Mokgalaka MN, Popoola API, Pityana SL. In situ laser deposition of NiTi intermetallics for corrosion improvement of Ti-6Al-4V alloy. *Trans Nonferrous Met*

- Soc China (English Ed [Internet]. 2015;25(10):3315–22.
78. Zhang B, Chen J, Coddet C. Microstructure and transformation behavior of in-situ shape memory alloys by selective laser melting Ti-Ni mixed powder. *J Mater Sci Technol* [Internet]. 2013;29(9):863–7.
 79. Guo S, Lu Y, Wu S, Liu L, He M, Zhao C, et al. Preliminary study on the corrosion resistance, antibacterial activity and cytotoxicity of selective-laser-melted Ti6Al4V-xCu alloys. *Mater Sci Eng C* [Internet]. 2017;72:631–40.
 80. Qiu C, Fones A, Hamilton HGC, Adkins NJE, Attallah MM. A new approach to develop palladium-modified Ti-based alloys for biomedical applications. *Mater Des.* 2016;109.
 81. Habijan T, Haberland C, Meier H, Frenzel J, Wittsiepe J, Wuwer C, et al. The biocompatibility of dense and porous Nickel-Titanium produced by selective laser melting. *Mater Sci Eng C* [Internet]. 2013;33(1):419–26.
 82. Cox SC, Jamshidi P, Eisenstein NM, Webber MA, Burton H, Moakes RJA, et al. Surface Finish has a Critical Influence on Biofilm Formation and Mammalian Cell Attachment to Additively Manufactured Prosthetics. *ACS Biomater Sci Eng.* 2017;3(8):1616–26.

Chapter 3

Materials and Experimental Methods

3.1. Selective Laser Melting

SLM fabrication within this thesis was carried out using a Concept Laser M2 Cusing SLM system, shown in figure 3.1. Technical specifications of the machine can be found in table 3.1.



Figure 3.1: The Concept Laser M2 Cusing SLM System

Table 3.1: The technical specifications of the Concept Laser M2 machine

SLM System	Concept Laser M2
Laser Type	Yb-fibre Continuous Wave
Max. Laser Power	400 W
Max. Scan Speed	3500 mm/s
Spot Size	150 μm
Default Scan Strategy	Island Scan Strategy
Layer Thickness	20 – 50 μm
Max. Build Height	280 mm
Build Plate dimensions	250 mm x 250 mm
Reducer	90 mm x 90 mm
Operating Atmosphere	Ar (<0.1% O ₂)

Concept Laser created the island scan strategy (as reported in table 3.1) to reduce the residual stresses within SLM parts. Each layer of the build is divided into smaller squares ‘islands’, and these are then melted by the laser in a random order. Within each island, scanning vectors are alternated. Furthermore, the vectors in neighbouring islands are perpendicular to each other. A schematic diagram of the island scanning strategy can be seen in figure 3.2.

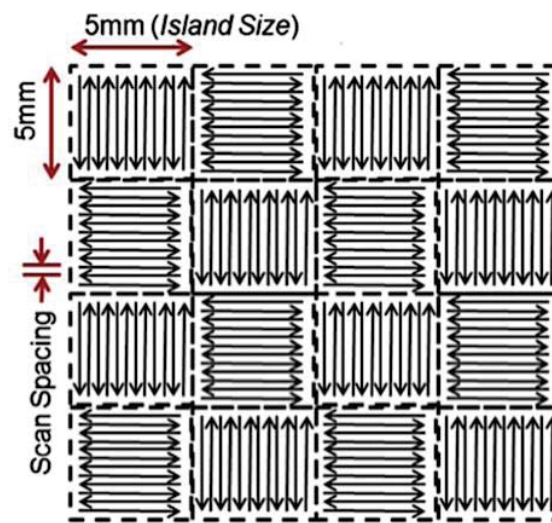


Figure 3.2: Schematic diagram of the island scanning strategy

SLM parts are fabricated using layer based technology. A 3D CAD model is virtually sliced into a series of layers using specialist ‘Magics’ (Materialise NV, Belgium) software. Once the sliced model file has been transferred to the Concept Laser M2 operating system, each slice is fabricated using the following procedure:

- 1). The powder platform is raised and the rubber re-coater blade moves across the powder bed to spread a thin layer of powder across the build platform (after this stage, powder will be spread on previously scanned layers).
- 2). The laser selectively scans the surface of the bed. The scanning area of each layer corresponds to its cross section as determined from the CAD model. The laser scanning re-melts the previously melted layer to ensure successful bonding and full build density.

3). The build platform is then lowered by the layer thickness of the slice. The re-coater returns to its original position and the process repeats. The deposition and scanning of subsequent powder layers continues until a 3D solid part is manufactured.

To achieve dense SLM parts, parametric studies were used to optimise processing parameters. The laser power, scanning speed, scan spacing and layer thickness were varied in the following ranges: 60-200 W, 115 – 2500 mm/s, 40 – 90 μm and 20 – 40 μm respectively. An island scanning strategy was employed for all builds.

3.1. Materials

Equiatomic, pre-alloyed NiTi powder was used within the investigations. The powder was produced by plasma atomisation technology and supplied by AP&C Advanced Powders and Coatings. The plasma atomisation process produces highly spherical and pure powders, which have exceptional flowability and packing properties. Hence, this powder production technology has proven popular within powder bed, additive manufacturing. As shown in the schematic diagram in figure 3.1, wire is used as the material feedstock. When the wire is introduced at the peak of three converging plasma torches, it melts and atomises. The atomisation occurs in an inert, argon atmosphere, to avoid contamination of the molten, metallic droplets. As the molten droplets are travelling down the extended hot zone, surface tension forces form spherical particles (1).

Following atomisation, AP&C used vibratory, ultrasonic assisted stainless steel sieves in accordance with the ASTM standard B214 – 16, to sieve the pre-alloyed NiTi powder into the following particle size ranges: < 15 μm , 15 - 63 μm , 64 - 180 μm , > 180 μm . During SLM, to achieve a good spreading and uniform powder layer, the advised powder particle size range is

between 15 to 63 μm . Thus, this size range was used throughout the investigations. Additionally, after each SLM run, the powder would be recycled and re-sieved using a 63 μm mesh. This was carried out to eliminate any splatter or irregular particles which may affect the next SLM run.

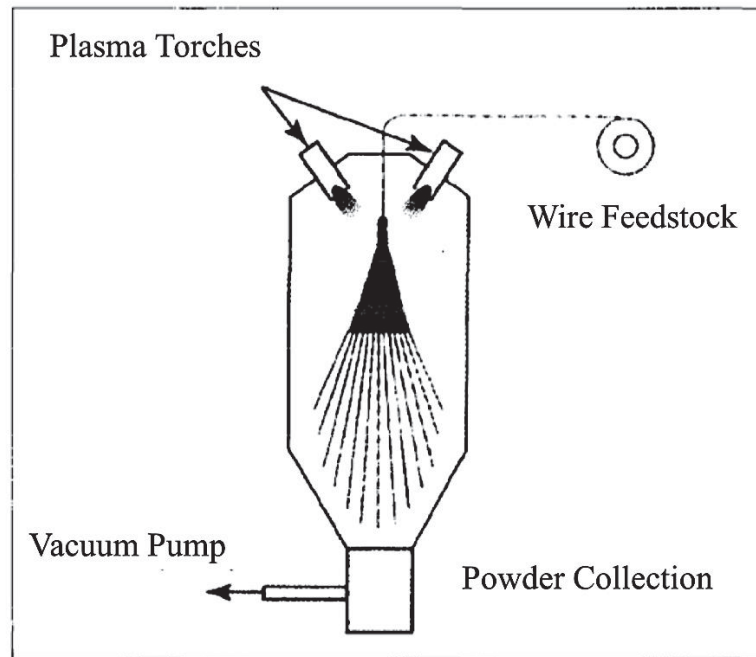


Figure 3.1: A schematic diagram of the plasma atomisation process (1)

3.1.1. Powder Blending

As the project involves the SLM of NiTi SMA containing precious metals, Johnson Matthey supplied gas atomised Pd powder, with a 20 – 40 μm particle size distribution range. Gas atomisation differs from plasma, as an ingot is used as the feedstock instead of wire. This powder manufacturing technique produces powders which are less pure and spherical in shape.

The NiTi and Pd powder blended mixture was created by mixing pre-alloyed NiTi powder and elemental Pd powder in the correct quantities to produce an overall target composition. This was achieved by calculating per weight percent, to give the amount of each element required in grams per 100 gram of powder mixture. The separate powders were weighed and added

together into a plastic container (the powder quantities can be seen in table 4.5). This is done in a glove box, where water and oxygen is removed from the atmosphere. Thus, ensuring the powders do not pick up oxygen or moisture. Following this, the plastic container which contains the powder mixture, is placed onto a roller ball mill for 24 hours to ensure homogeneous mixing, as schematically shown in figure 3.2.

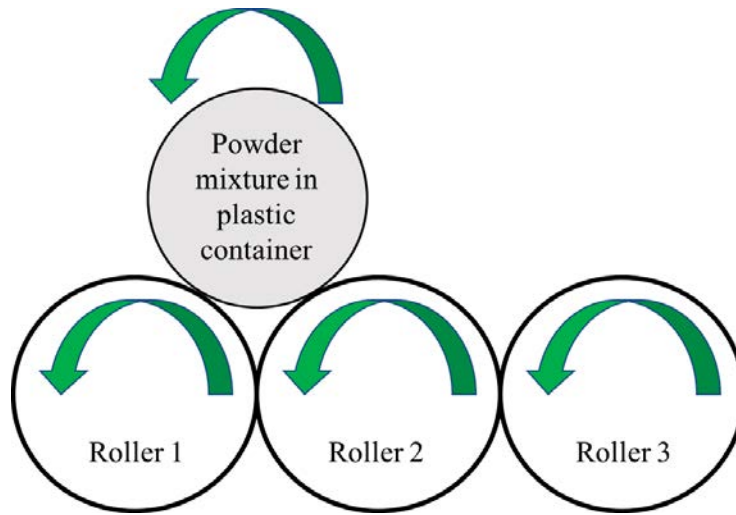


Figure 3.2: A schematic diagram of the roller ball mill set up

3.2. Powder Particle Size Distribution

The particle size distribution (PSD) analysis was carried out to verify the powder size ranges as supplied by AP&C. Furthermore, it was used to assess the PSD of the NiTi & Pd powder blended mixture. A Coulter LS230 laser diffraction particle size analyser was used. The process involves suspending a small sample of the powder mixture in distilled water. As the laser beam passes through the dispersed sample, the angle variation in the light scatter is measured. Large particles scatter light at small angles in respect to the laser beam, whereas, small particles scatter light at large angles. The angular scattering intensity data is then analysed to calculate the size of the particles responsible for creating the scattering pattern (2).

3.3. Hall Flowmeter

The bulk and tap densities of the powder was measured in accordance to the ASTM standard B855-17, using the hall flowmeter funnel. Subsequently, the Hausner ratio (2) was calculated to give an indication of the powder's flowability. A Hausner ratio greater than 1.25 indicates a powder with a poor flowability.

$$\text{Hausner ratio} = \frac{\text{Tap density}}{\text{Bulk density}}$$

3.4. Chemical Compositional Analysis

Inductively coupled plasma mass spectrometry (ICP-MS) was used to measure the concentration of Ni and Ti in the powder and SLM fabricated builds. It's a highly accurate analysis technique, which can trace elements in concentrations as low as one part in 10^{15} . The process uses the emission spectra of a sample to identify and quantify elements. A sample is heated up by a plasma which ionises and excites the atoms. This produces light energy emissions with differing wavelengths. The elements can then be identified by the emission lines and the quantity of the elements can be measured by the emission line's intensity.

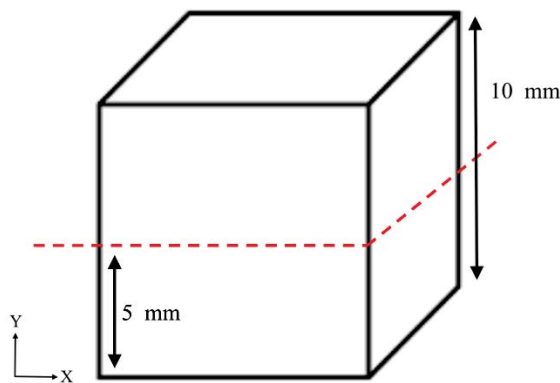
Even though SLM is carried out in an argon atmosphere, due to the high processing temperatures and the reactivity of Ti, oxygen pick up is unavoidable. Furthermore, as mentioned in the previous chapter, the initial oxygen content of the powder can have a detrimental effect on the final SLM build. Thus, the oxygen content of the powder and the SLM fabricated builds were measured using an inert gas fusion method, which is capable of measuring oxygen at 50 ppm. This involved heating a sample in an inert atmosphere, using a high purity graphite crucible. The oxygen within the sample will then react with the carbon in the crucible. Consequently, the CO or CO₂ formed, is measured by infrared detection.

3.5. Heat Treatment

A tube furnace, operating at temperatures up to 1200 °C, was used to perform heat treatments on the SLM fabricated parts. Samples were sealed into quartz capsules and filled with argon to prevent oxidation during the heat treatment. The solution heat treatment remained constant through-out all investigations. Samples were heated up to 950°C for 5.5 hours, followed by immediate water quenching. A thermocouple was positioned close to the sample to monitor the temperature and ensure the samples were being heated up to the correct temperature.

3.6. Metallurgical Sample Preparation

After SLM processing, the cubic samples were sectioned along the XY plane, transverse to the building direction. A precision cutter fitted with a silicon carbide cutting disc, sectioned the samples 5mm below the top surface of the build. Samples were hot mounted in conductive bakelite to reveal the XY plane. Following this, the XY plane was ground to a 1200 grit paper and polished with diamond suspensions of 3 and 1 μm . The final polished used a 0.04 μm colloidal silica OP-S suspension. Grain and precipitation size and structure required etching. Samples were submerged in Kroll's reagent (2 % HF, 10 % HNO_3 + 88% H_2O), then rinsed with water and ethanol.



3.7. Chemical Homogeneity Methodology

As the aim was to alloy in-situ the elemental Pd powder with the pre-alloyed NiTi using SLM, the chemical homogeneity of the fabricated part was investigated. To establish a relationship between the SLM processing parameters and the diffusion of Pd powder particles into the NiTi matrix, a parametric study was carried out to fabricate a large number of 10x10x10 mm, cubic samples. Each sample was processed using a different set of parameters. The sets of parameters differed by changes in either the laser power, scan speed or scan spacing.

After the samples had been hot mounted and polished, the XY plane was divided into a 5 x 4 grid, as shown in figure 3.3. Microstructural analysis was performed using scanning electron microscopy (SEM), this method will be discussed in more detail in following paragraphs. Using the SEM in backscattered electron (BSE) detector mode, 20 BSE SEM images were taken across the XY plane, centrally in each square of the grid. As BSE are more sensitive to the atomic mass of the nuclei from which they scatter, they produce a difference in contrast on the SEM image (3). Heavier elements appear brighter, whereas lighter elements appear darker. Thus, undissolved Pd will appear brighter in comparison to the NiTi matrix.

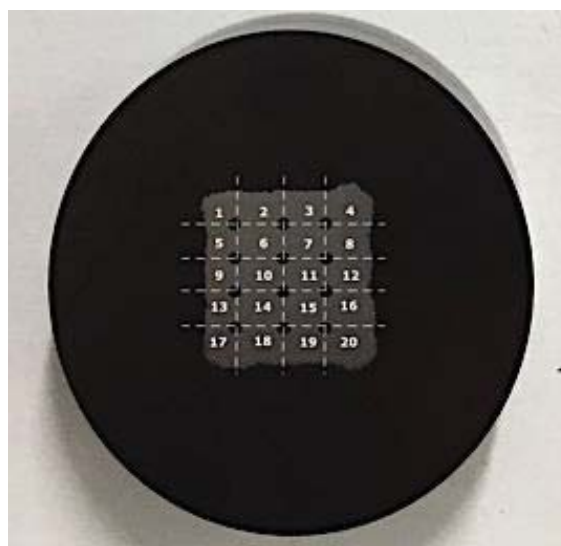


Figure 3.3: A diagram of the grid used to take 20 BSE SEM images across the XY plane

The 20 BSC SEM images were then analysed using ImageJ software. A colour threshold was applied to the images to obtain a percentage area fraction of undissolved Pd powder particles. To ensure that only undissolved palladium powder particles were being measured, the allowable circularity was set to 0.8 - 1. The circularity is a measure of how spherical a particle is. A circle has a circularity of 1, whilst a straight line has a circularity of 0.

To further investigations between the SLM processing parameters and chemical homogeneity, melt pool dimensions were measured. The SLM fabricated cubic samples were sectioned at a 45° angle to the XY plane to reveal the XZ plane, hot mounted in conductive bakelite, ground and polished (as described in section 3.6). Following this, the XZ plane was etched with Kroll's reagent, so that the melt pools would be visible under optical microscopy. The melt pool depth was measured, as shown in figure 3.4.

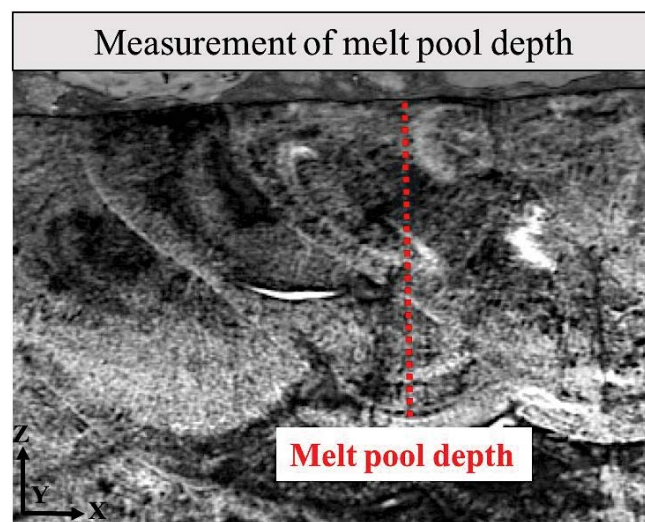


Figure 3.4: The melt pool depth measurement

3.8. Optical Microscopy

Optical microscopy was employed to characterise the porosity within the SLM build and measure the build's melt pool depth (as previously mentioned). A Zeiss Axioskop 2 optical microscope with a monochrome CCD camera was used. An image of the whole XY plane was achieved through the use of a motorised stage and Axiovision (Carl Zeiss) software stitching multiple images together and reconstructing the plane.

Furthermore, ImageJ software was then used to quantify the porosity and provide an area fraction of porosity on the XY plane. A global scale was set based on the scale bar of the stitched, reconstructed micrograph of the XY plane. Following this, a colour threshold was applied to isolate the porous features and particle measurement was used to obtain an area fraction percentage.

Additionally, the internal porosity of powder particles was measured in a similar way. A small sample of powder was hot mounted in bakelite, ground and polished (section 3.6), to reveal the powder's cross section. Optical images were analysed using ImageJ.

3.9. Scanning Electron Microscopy (SEM)

A JOEL 6060 Tungsten Filament Scanning Electron Microscope equipped with Oxford Inca Energy-Dispersive X-ray Spectroscopy (EDS) was applied for microstructural and chemical analysis. The morphology and composition of intermetallics within the fabricated build were investigated, using an accelerating voltage of 21 KeV. Additionally, EDS was used to measure the differences in composition before and after SLM processing. The measurements would later be confirmed using ICP-MS. Finally, the backscatter detector was used to observe the chemical homogeneity of SLM build and chemical segregation in the powder particles.

3.10. X-ray Diffraction (XRD)

XRD was used to confirm the crystallographic phases present in the SLM build at room temperature. XRD was performed on a Philips X'pert diffractometer, which used a Cu K α radiation source. The X-ray tube was operated at 40 kV. Scan angles ranged from 0 - 160°, with a minimum size step of 0.005°. As x-ray beams are shot through a crystal of an atom, the interaction of the incident rays with the sample produces a diffracted ray when the conditions satisfy Bragg's law ($n\lambda = 2d \sin \theta$). A detector processes this X-ray signal and converts the signal to a count rate. To identify the peaks corresponding to the different phases, XRD graphs were compared to published data in literature.

3.11. Differential Scanning Calorimetry (DSC)

Phase transformation temperatures of the powders and SLM builds were determined using the Mettler Toledo DSC1 DSC system. Testing temperatures ranged from -80°C to 140°C, with a heating cooling rate of 10°C per minute. For thermal analysis investigations, 5 x 5 x 5 mm cubes were fabricated. A small rectangular piece was cut from the cube for DSC analysis. The testing piece was cut from the centre of the SLM cube to ensure no oxidised surface layer remained. To keep testing conditions constant, the sample was no more than 1.5 mm thick and the length was kept between 3 to 4 mm. Samples are placed in an aluminium pan and DSC measures the amount of energy absorbed or released by the sample when it is heated and cooled. Thus, providing information on the endothermic and exothermic processes.

3.12. Mechanical Testing

3.12.1. Elevated Temperature Compression Testing

For superelastic experiments, samples were compressively loaded and unloaded using a Servo Hydraulic test machine, ranged to ± 100 kN. A 20 kN force was applied and loading occurred in stroke control at a constant actuator speed of 0.5 mm/min. Load and stroke data were recorded simultaneously at a frequency of 10 Hz.

Cylindrical testing specimens were fabricated with a 2.5 mm diameter and 7 mm length. The contact faces were polished to ensure uniform contact between the specimen and the compression plates. No modifications, such as grinding and polishing, were made to the sides of the SLM specimens prior to compression testing.

To guarantee the specimen was fully austenitic before testing, a furnace was used to heat the sample 10°C above its A_F temperature. A N-type thermocouple was placed between the compression platens to measure the specimen temperature. The machine was put into load control during heating. However, once the correct temperature had been reached, the experiment ran in stroke control.

An extensometer was not attached to the specimen's gauge length during testing. Thus, the calculated strain will include the strain of the whole test specimen and the machine fixturing's. Consequently, giving an approximation not a true strain value.

3.12.2. Hardness Testing

Vickers micro-hardness measurements were performed on polished, XY planes of SLM fabricated samples. An automated Struers tester was used, applying a 0.5 kg load for 8 s at 1 mm intervals across a 10 mm distance. The determination of the Vickers Hardness Number (VHN) allowed the microstructural evolution with heat treatment to be investigated. In order

the calculate the VHN, image analyser software incorporated within the testing machine, accurately measured the diagonal lengths of the indentation.

3.13. Micro Computed Tomography (Micro-CT)

Micro-CT was used to qualitatively observe the X-ray absorption of SLM fabricated samples. CT scanning was carried out on a Bruker SkyScan 1172 Micro-CT. The scan used an 80kV voltage, a tungsten filament and a current of 200 μ A. An aluminium copper filter was positioned between the source and the specimen. Each sample was scanned over 360°, with a rotation step of 0.40° and a four-frame averaging was applied.

The sample is placed on a rotating table and X-ray images are taken as the sample is rotated. Differences in X-ray absorption can be visually observed as the sample will produce a contrast against its background. The contrast can then be quantified using ImageJ software to measure the differences in greyscale between the background and sample.

3.14. Electrochemical Testing

The corrosion behaviour of SLM fabricated parts was tested using a series of electrochemical tests on the XY plane of solution heat treated sample. Samples were mounted in resin, ground to a 1200 grit paper and polished using colloidal silica OP-S suspension. Following this, samples were wiped with ethanol and placed in an ultrasonic cleaner for 15 minutes to ensure all polishing residue had been removed. Coverlac stopping lacquer was used to cover edges of the surface which touched the resin, leaving approximately a 0.7 cm² testing area. A saturated calomel reference electrode and platinum foil counter electrode was used. The testing solution was phosphate-buffered saline (PBS) solution, deaerated by argon bubbling for 1 hour before the samples were placed in the cell. The deaeration continued throughout the experiment. The

temperature of the water bath was kept at 37°C to body temperature. Measurements were taken using a GILL12 potentiostat. The potentiostat and experimental set up can be seen in figures 3.5 and 3.6.



Figure 3.5: The GILL12 potentiostat

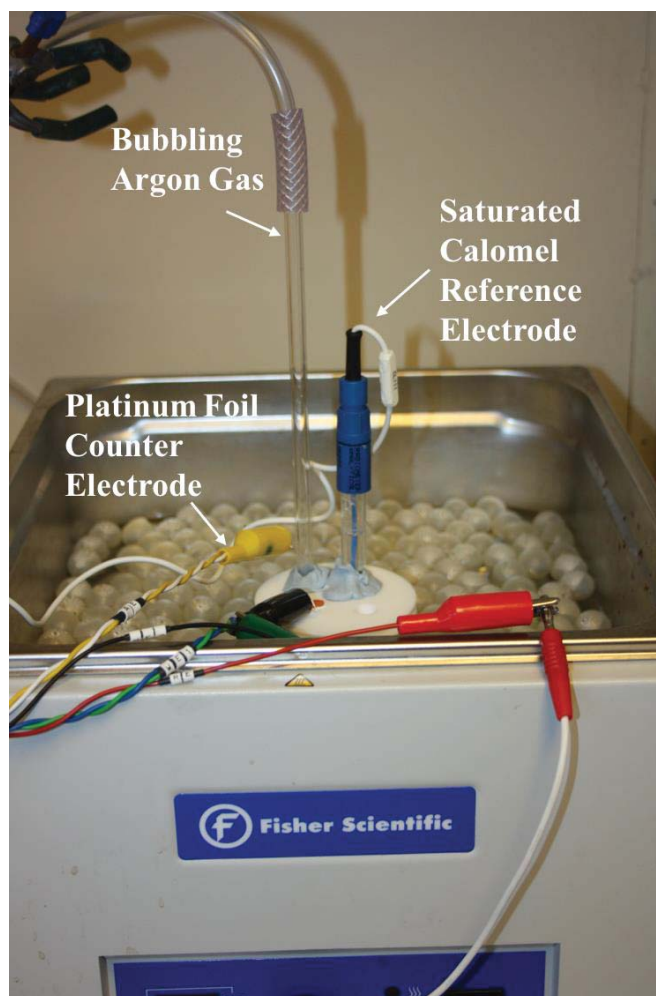


Figure 3.6: Experimental set up of electrochemical tests

3.15. Cell Viability Testing

Biocompatibility testing was performed on polished surfaces to eliminate factors such as surface roughness which could affect cell adhesion. Prior to in vitro experiments, samples were autoclaved, washed with ethanol and left overnight under ultraviolet light.

MC3T3-E1 preosteoblast cells were cultured in complete growth media. The complete growth media contained Alpha Minimum Essential Media (α -MEM) with 10% fetal bovine serum, 2.4% L-glutamine and 1% penicillin/streptomycin.

SLM, solution heat-treated, samples were individually placed into wells and MC3T3-E1 cells were seeded onto the XY plane of the samples. The seeding density was 1×10^4 cells/cm². Following this, samples were incubated in 5% CO₂ atmosphere, maintained at 37°C. Cells had 1 hour to adhere to the sample's surface for 2 hours, before complete growth media was added to the each well to slightly cover the surface. Samples were then incubated again until further testing.

The viability of cells after culturing was tested on day 1, 3 and 7. The sample surface was stained with calcein AM (live cells) and propidium iodide (dead cells). Calcein AM is a green fluorescent dye which converts into fluorescent calcein by the activity of a live enzyme found in cells called intracellular esterase. Whereas, propidium iodide is a red dye that is membrane impermeable and excluded from living cells. The stained cultures on the sample's surface were observed using the Olympus FV1000 mutiple Ar laser scanning confocal microscope.

3.16. References

1. Foil M. New technology for spherical powder. *Met Powder Rep.* 48(3):28–9.
2. Spierings AB, Voegtlin M, Bauer T, Wegener K. Powder flowability characterisation methodology for powder-bed-based metal additive manufacturing. *Prog Addit Manuf* [Internet]. 2016;1(1–2):9–20.
3. Lloyd GE. Atomic Number and Crystallographic Contrast Images with the SEM: A Review of Backscattered Electron Techniques. *Mineral Mag* [Internet]. 1987;51(359):3–19.

Chapter 4

The Influence of the SLM Processing Parameters on the Microstructure and Structural Integrity

4.1. Introduction

Chapter 4 focuses on the process optimisation for manufacturing NiTi and TiNiPd SMA using SLM. A fully dense part requires an energy input high enough for complete melting of the powder particles and successful fusion and solidification of the powder layers. However, from literature it is clear that operating at high laser energies brings disadvantages such as impurity pick up and microstructural defects. Thus, it is essential to find an energy input that is high enough to achieve a good melt but does not compromise on other important characteristics. A poor quality SLM fabricated part will have detrimental effects on the other alloy properties tested in this thesis. For example, oxygen pick up will result in the formation of $Ti_4Ni_2O_x$. This brittle intermetallic will have negative consequences during the superelasticity investigations. Furthermore, structural defects produced by inadequate process optimisation could act as pitting sites during the corrosion studies. Therefore, processing parameters must be identified that can repeatedly produce a highly dense build with no cracking.

When alloying an elemental Pd powder into a pre-alloyed NiTi powder using SLM an in-situ alloying methodology must be produced which can manufacture a chemically homogeneous build. Homogeneity is essential when investigating the influence of Pd on the properties of NiTi, especially when identifying the phase transformation temperatures.

The powder feedstock is the starting point for manufacturing a high quality SLM part. Thus, part one of this chapter discusses the powder characterisation for the powders used within this thesis. The second part of the chapter involves a discussion of the experimental research performed to optimise the SLM processing route for both binary and Pd modified NiTi.

Part 1: Powder Characterisation

4.2: Pre-alloyed NiTi Powder Characterisation

The SEM micrograph in fig 4.1 a). displays the overall NiTi pre-alloyed powder morphology as spherical particles with smooth surfaces. Evident from the histogram and pie chart in fig 4.2. and 4.3, nearly 80 percent of the 2000 particles analysed had a perfect circularity of 1. Circularity is a measure of how circular each particle is. A circularity of 0 is a straight line, whereas a circularity of 1 is a perfect sphere. An SEM micrograph taken at a higher magnification reveals (fig 4.1 b) a small percentage of irregular shaped particles. Fig 4.1 c). displays an irregular shaped particle. Small satellites are visible in fig 4.1 d). An acorn shaped coated powder particle can be seen in fig 1 e). Whereas, dented and connected particles are displayed in fig 4.1 f). and h). Finally, visible dendrites are present on the surface of powder particles in fig 4.1 g), reducing the smoothness of the surface.

Due to the reductions in flow-ability and pack density, the powder particles with poor morphological properties could hinder the deposition of uniform powder layers during SLM processing. Consequently, leading to microstructural defects within the final part. Spherical particles with smooth surfaces are the desired morphology as they reduce friction and the risk of particles interlocking (1).

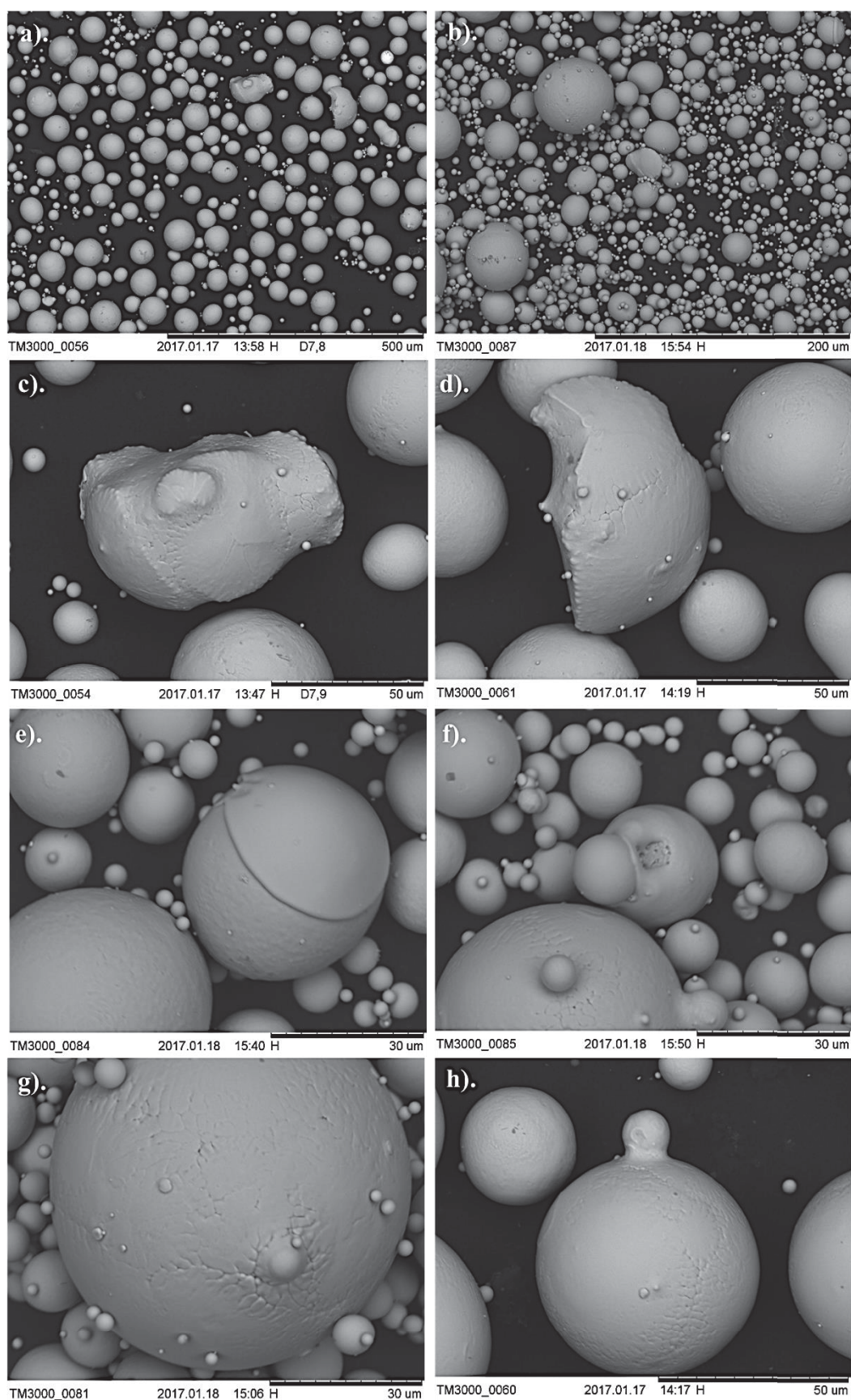


Figure 4.1: SEM micrographs a). the overall NiTi powder morphology b). the powder morphology at a higher magnification c). an irregular shaped particle d). small satellites e). a coated particle f). a dented particle g). visible dendrites on the surface of a powder particle h). connected powder particles

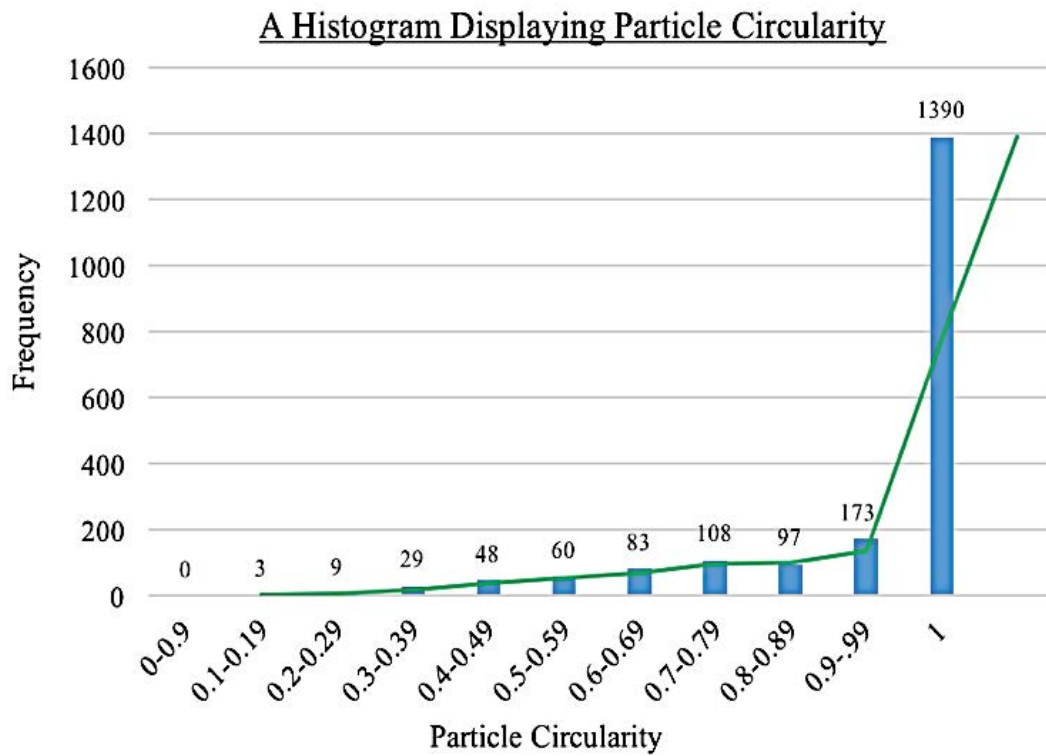


Figure 4.2: A histogram displaying the particle circularity of the 2000 powder particles tested

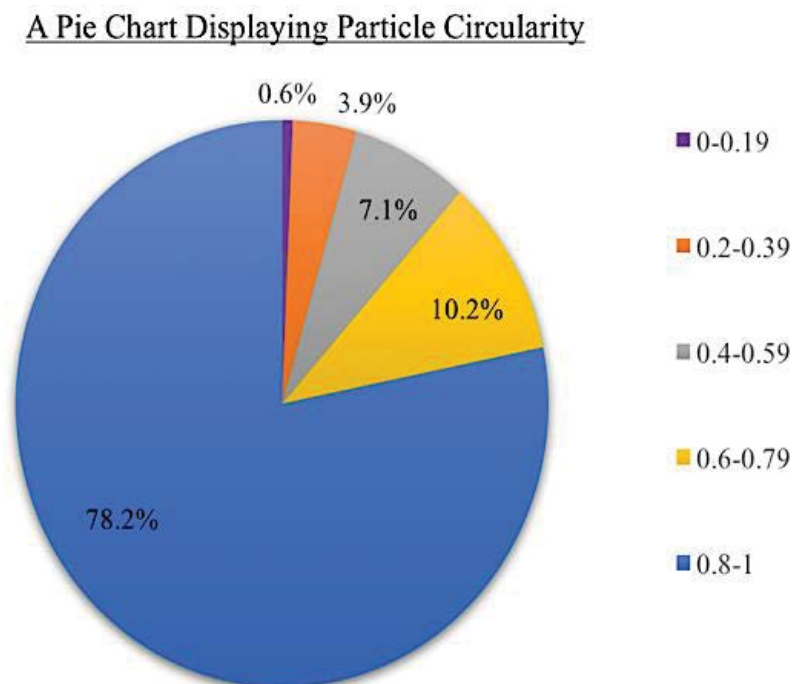


Figure 4.3: A pie chart displaying the particle circularity of the 2000 powder particles tested

A powder's particle size distribution (PSD) can be closely linked to the powder's flowability and packing density during SLM processing. Figure 4.4 (a) shows the particle size distribution curve for the pre-alloyed NiTi powder, the corresponding numerical values can be seen in table 4.1. The powder appears to show a normal distribution with a slight negative skew as shown by slightly larger mean than median value. The distribution lies slightly outside the ideal powder size range for SLM with 80% of the powder particles being between 10 μm and 50 μm , having a median value of 26 μm . Having a mixture of finer and coarser size particles is advantageous for the packing density as the fines can pack in between the small gaps of the larger particles. However, having too many fine particles will hinder the powder's flowability as fine sizes tend to form clusters which will prevent uniform spreading during processing.

Table 4.1: The PSD data for the NiTi pre-alloyed powder

NiTi pre-alloyed powder (15 -63 μm)	
Mean size (μm)	28.08
D ₁₀	9.90
D ₅₀	26.01
D ₉₀	49.53

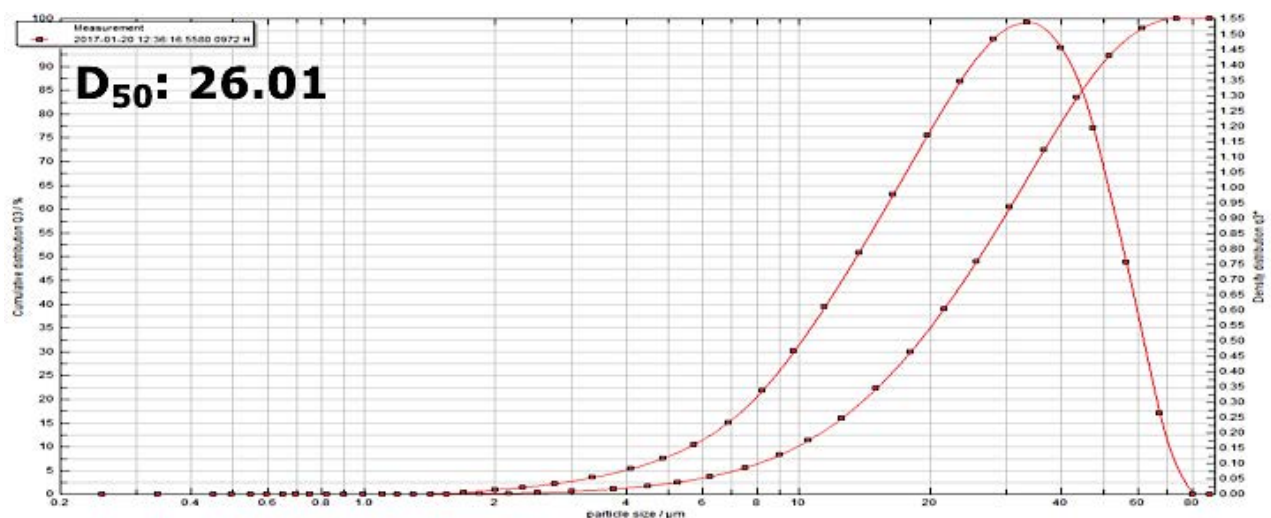


Figure 4.4 (a): The PSD curve for the NiTi pre-alloyed powder

Good powder flowability is required to achieve uniform powder layers which allows uniform laser absorption, thus improving the overall quality of the SLM fabricated part. ρ_T represents the tapped density of the powder and ρ_A is apparent density of the powder. Apparent and tapped densities were measured to calculate the Hausner ratio (H), shown in equation 4.1.

$$H = \frac{\rho_T}{\rho_A}$$

A Hausner ratio greater than 1.25 is an indication of poor flowability with high powder cohesion. The NiTi powder has a Hausner ratio of 1.14, thus, proving to be a free-flowing powder. This high flowability can be related to the morphology of the powder. The spherical particles will reduce particle interlocking. Furthermore, the small percentage of fine sized particles will improve flowability as finer particles possess higher Van der Waals forces because of the higher surface area-to-volume ratio. The densities and the flowability of the powder are displayed in table 4.2.

Table 4.2: A table showing the densities and flow-ability of the pre-alloyed NiTi powder

Apparent density (g/cm ³)	3.91
Tapped density (g/cm ³)	4.46
Hausner ratio	1.14
Flow-ability (sec)	24.15

Fine powder particles not only affect the flowability of the powder during SLM but they also have a great influence on the oxygen content of the final SLM part. The oxygen content of four pre-alloyed NiTi powder batches were tested using the inert gas fusion method. The powder batches were separated according to their size. From figure 4.4 (b), it is clear that due to their increased surface to volume ratio, finer sized particles contain the highest percentage of oxygen.

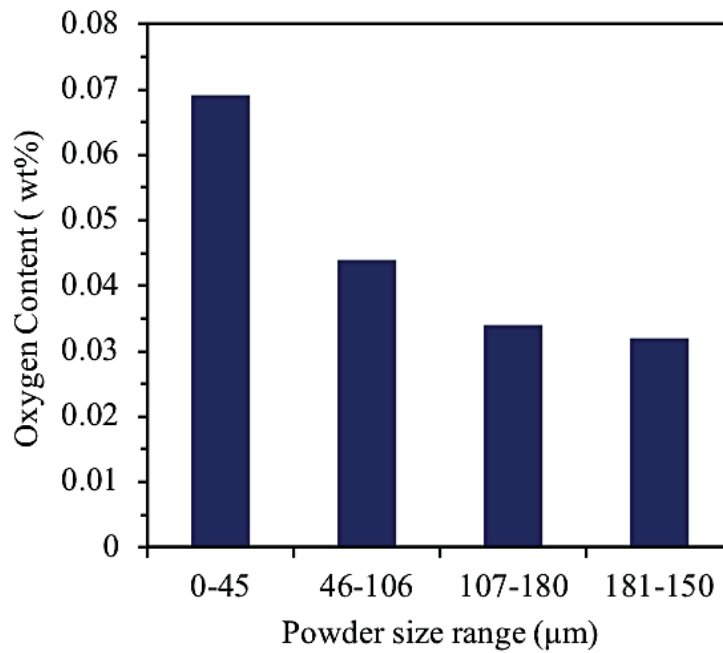


Figure 4.4 (b): The relationship between the powder particle size and oxygen content

Due to the use of inert gases during powder atomisation, it is expected that the powder particles will contain some degree of porosity. However, because of the rapid solidification associated with SLM processing, this entrapped gas can be transferred to the final part. Table 4.3. display the results of the 667 pre-alloyed NiTi powder particles tested for internal porosity. 74% of particles contained internal porosity, with the most common type of porosity being gas entrapment instead of porosity being formed as two particles collide and join. Out of the 667 particles analysed, the mean pore diameter was very small at a size of 1.56 µm. This very small diameter is to be expected when using wire fed plasma atomisation. Fig 4.5 a). displays the cross section of a powder particle revealing a large pore. The white arrow in fig 4.5 b). highlights porosity formed due to molten collision and fig 4.5 c). shows porosity due to gas entrapment.

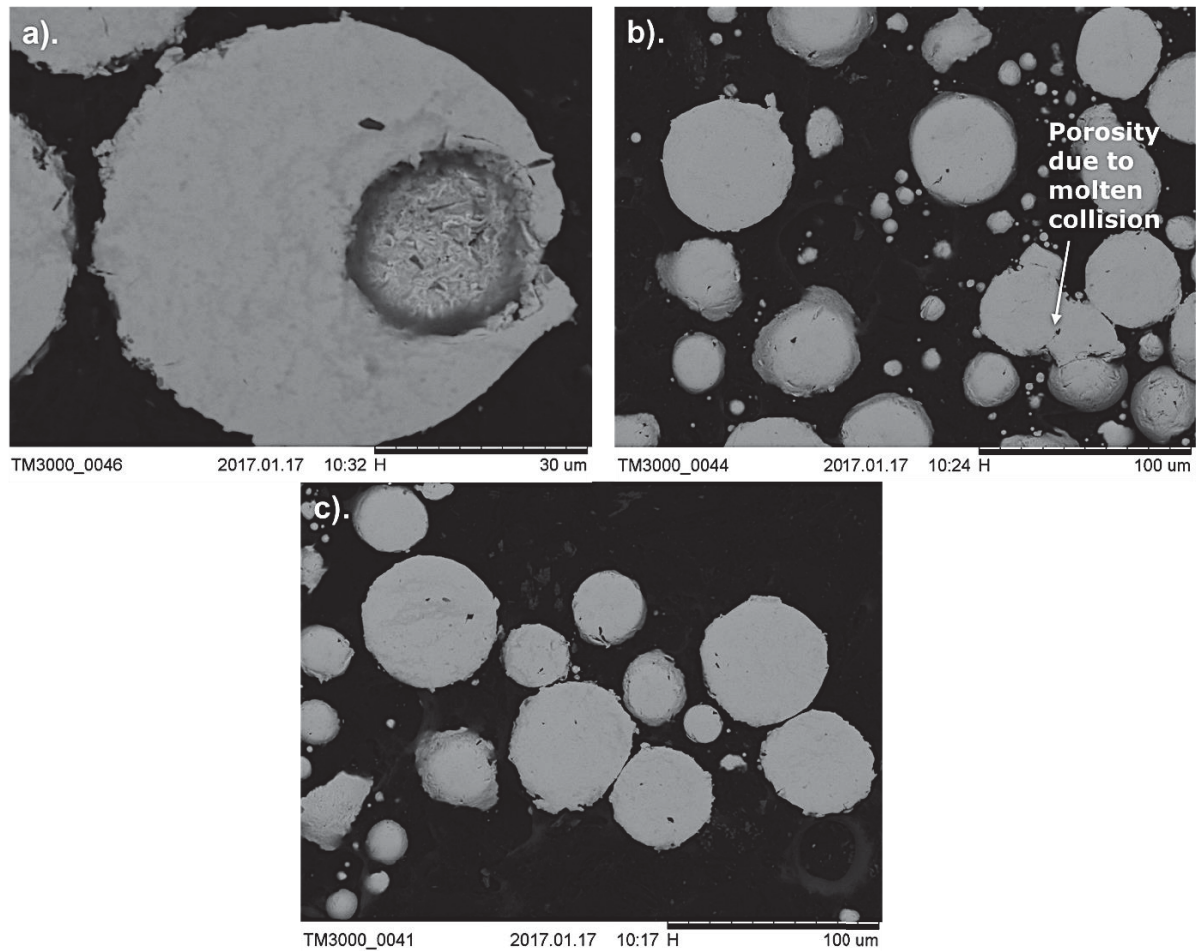


Figure 4.5: a). The internal cross section of a NiTi pre-alloyed powder particle revealing internal porosity b). porosity due to molten collision c). porosity due to gas entrapment

Table 4.3: A table showing the internal porosity within a sample of the NiTi pre-alloyed powder

Number of particles analysed	667
Percentage containing internal porosity	74 %
Mean pore diameter	1.56 μm

During atomisation of the pre-alloyed wire, the metal is in a liquid and homogeneous state as the composition is equal everywhere. During solidification, the liquid melt is cooled too quickly to allow the equilibrium NiTi phase to form. Consequently, as the diffusion rate was too slow to reach equilibrium, Ti_2Ni deposited at the surface of the powder as the particle solidified. The BSE image in fig 4.6 a). displays the internal cross section of a powder particle. The particle is chemically inhomogeneous microstructure with Ti-rich areas. Furthermore, fig

4.6 b). displays the segregated Ti_2Ni phase on the powder's surface. EDX mapping shown in fig 4.7. confirms the presence of Ti-rich phases.

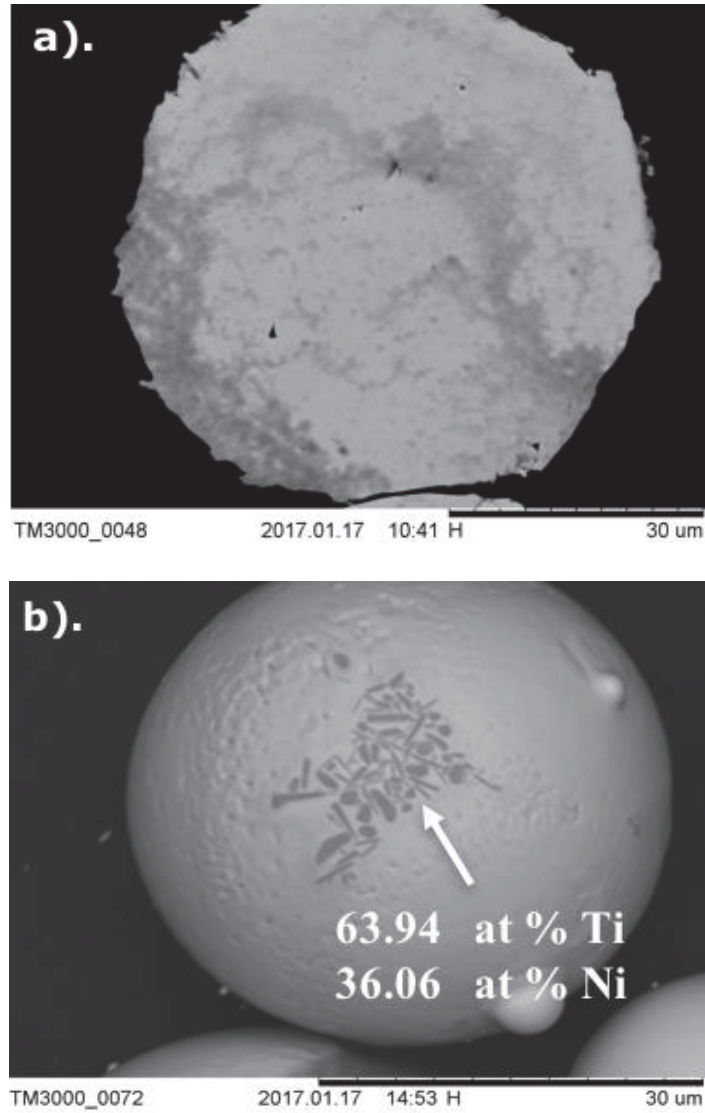


Figure 4.6: a). A BSE image of the internal cross section of a NiTi pre-alloyed powder particle b). a SEM image of Ti_2Ni phase on the powder surface

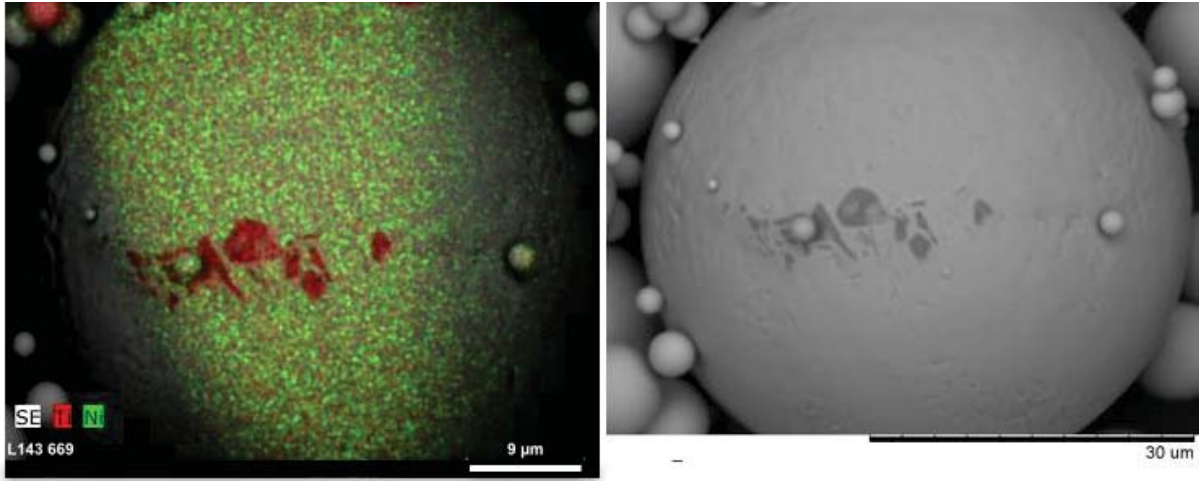


Figure 4.7: EDX mapping on the surface of a pre-alloyed NiTi powder particle

The EDX maps, shown in fig 4.8, indicate that during atomisation the pre-alloyed powder must have been contaminated with elemental Ni and Ti powder particles. As the plasma atomisation process was undertaken with pre-alloyed wire feedstock it is likely contamination would have occurred during the sieving process, as the same sieves would have been used during Ti and Ni atomisation. The work throughout the thesis involves alloying with elemental powders and thus the elemental Ni and Ti contamination will not have a significant impact. However, if this off-specification powder were to be used directly in SLM, the contamination would be extremely disadvantageous as small shifts in the Ni:Ti ratio can lead to drastic changes in the phase transformation temperature.

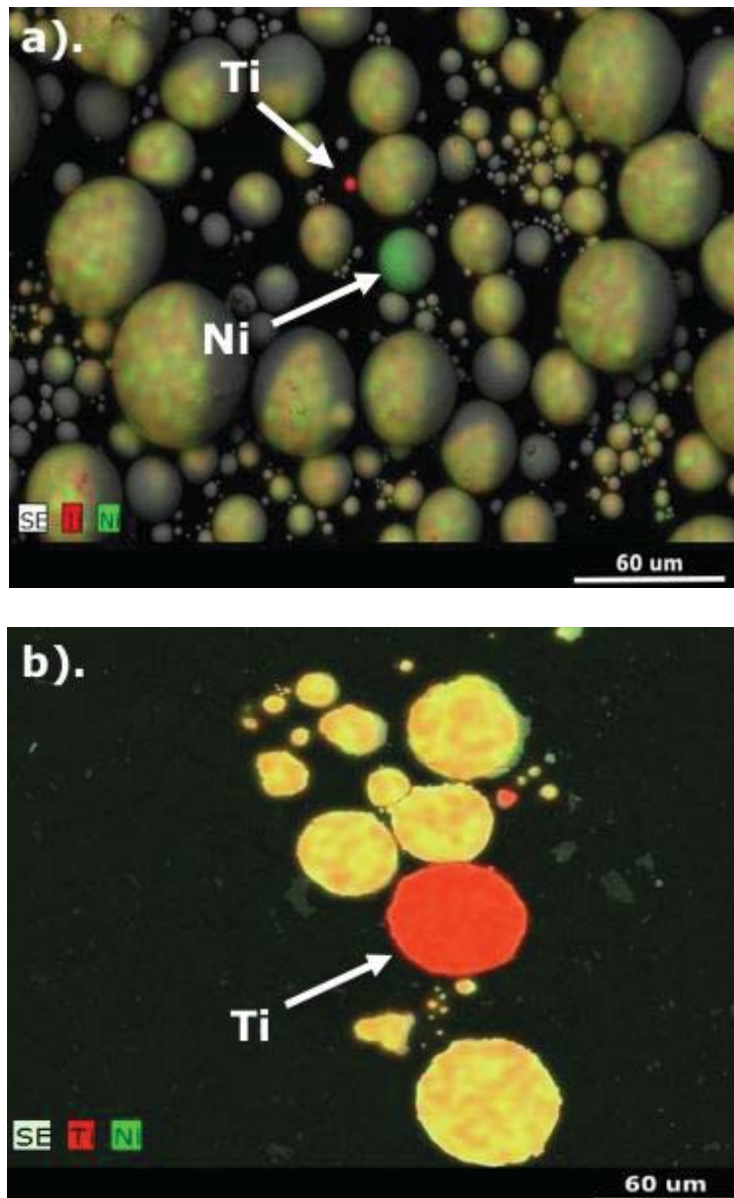


Figure 4.8: EDX mapping of the NiTi pre-alloyed powder

The chemical composition and A_F temperature of the powder can be seen in table 4.4. This Ni-rich composition is also reflected the powder's low transformation temperatures. The A_F temperature is 9°C below body temperature. Thus, the alloy is ideal for self-expanding vascular stent applications.

Table 4.4: The chemical composition and A_F temperature of the NiTi pre-alloyed powder

	Ni content (at %)	Ti content (at %)	A_F temperature (°C)
NiTi pre-alloyed powder	51.09	48.91	28

4.2.1. Pd Powder Blended Mixture Characterisation

Due to the high cost of the elemental Pd powder, only the powder morphology was observed. Fig 4.9 displays a SEM image of the Pd powder. In comparison to the pre-alloyed NiTi powder, the morphology is much more irregular. This can be attributed to the differences in atomisation processes used to produce the powders. The NiTi pre-alloyed powder was plasma atomised whereas, the Pd powder was gas atomised. The plasma atomisation process is renowned for producing highly spherical powder particles. However, gas atomisation produces spherical particles along with some blocky, irregular and asymmetrical particles (2).

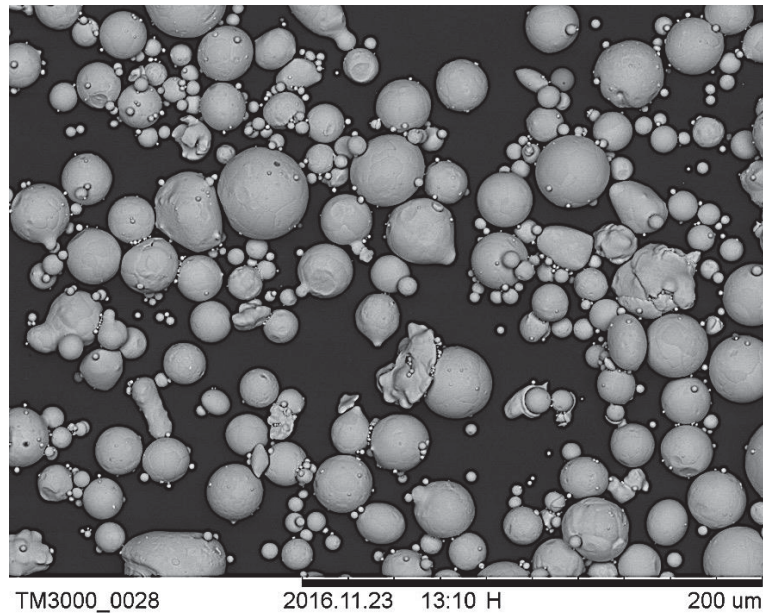


Figure 4.8: A SEM image showing the Pd powder morphology

Two ternary TiNiPd compositions were chosen when creating a powder mixture to be used in SLM. These compositions were chosen based on the work reported by *Boylan et al.* which said that to improve the radiopacity of binary NiTi whilst maintaining superelasticity, palladium must be alloyed in quantities equal or above 2.5 at % to less than or equal to 20 at % (3). Furthermore, the palladium must substitute only the Ni and the Ti content must remain at 50 at %.

The first powder mixture was created to a target composition where 2 at % of Ni was substituted with Pd. This composition was used in the initial parametric studies to gain an understanding into the SLM of TiNiPd. The second powder mixture was created where 7 at % Ni was substituted with Pd. Due to the larger Pd content, this composition would most likely be used in biomedical applications because of its improved radiopacity. Thus, this composition was used to investigate the radiopacity, corrosion resistance and biocompatibility of SLM fabricated TiNiPd.

Elemental Ni and Ti powder were added to the elemental Pd and pre-alloyed NiTi powders to achieve two powder batches with a composition of $\text{Ti}_{50}\text{Ni}_{48}\text{Pd}_2$ (at %) and $\text{Ti}_{50}\text{Ni}_{43}\text{Pd}_7$ (at %). After the powders were weighed and added together, the bottles were placed on a powder roller mill for 24 hours to ensure sufficient mixing. Figure 4.9. shows elemental EDX mapping performed on the $\text{Ti}_{50}\text{Ni}_{43}\text{Pd}_7$ (at %) powder batch after mixing for 24 hours. Table 4.5. displays the quantity of elements added per 100 grams of powder mixture. The powder particles still appear spherical and round, indicating the powder mixing did not damage the powder particles. Additionally, the pre-alloyed and elemental powders appear to have successfully mixed.

Table 4.5: A table showing the quantities within 100g of the $\text{Ti}_{50}\text{Ni}_{43}\text{Pd}_7$ (at %) powder mixture

Powder	Element per 100 g of powder mixture (g)
Pre-alloyed NiTi powder	81.72
Ti powder	5.49
Ni powder	0.57
Pd powder	12.22
	Total weight percent (%): 100

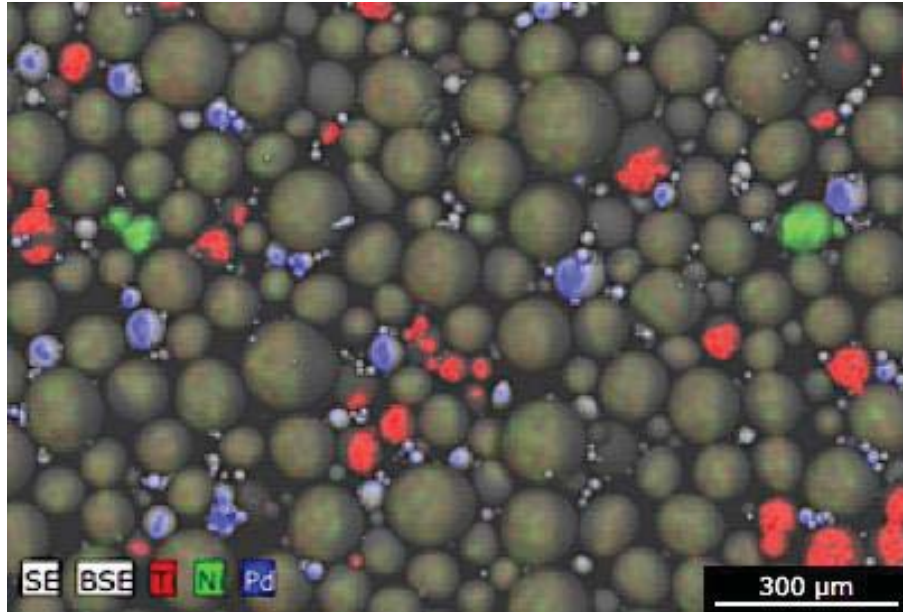


Figure 4.9: An elemental EDX map of the $Ti_{50}Ni_{43}Pd_7$ (at %) powder mixture

Part 2: SLM Parametric Studies

4.3. The influence of SLM Processing Parameters on the Microstructure and Structural Integrity of Binary NiTi

The parametric study investigated the influence of the three main SLM processing parameters on the structural defects (cracking and porosity) in additively manufactured NiTi. The processing parameters included the laser power, the laser scan speed and the scan spacing. Table 4.6 displays the list of parameters used to produce samples. The parameters were chosen based upon findings in previous literature. As mentioned in chapter 3, the SLM fabricated samples were sectioned along the XY plane, 5 mm below the top surface. The samples were then hot mounted, ground and polished. The porosity percentage of the XY plane was then quantified using ImageJ software.

Table 4.6: The list of parameters used during the parametric study

Laser Power (W)	Laser Scan Speed (mm/s)	Scan Spacing (μm)			Layer Thickness (μm)	
100	125	75			20	
100	250	75			20	
100	500	75			20	
150	125	75			20	
150	250	75			20	
150	500	75			20	
150	1000	75			20	
200	125	75			20	
200	250	75			20	
200	500	75			20	
200	1000	75			20	
100	1000	45	60	75	20	40
100	1100	45	60	75	20	40
100	1300	45	60	75	20	40
100	1400	45	60	75	20	40
100	1500	45	60	75	20	40

The volumetric energy density equation (VED) takes into consideration the amount of power from the laser and the geometric volume into which it is directed. The VED is calculated using the following equation (laser power, P ; scan speed, V ; hatch spacing, H ; layer thickness, T :

$$\text{VED} = \frac{P}{V * H * T}$$

Figure 4.10 (a), shows porosity in relation to the VED. The overall porosity increased with VED. There is a noticeable increase in part porosity at energy densities greater than approximately 600 J/mm^3 . High powers with a slower scan speed correspond to high VEDs. The increased energy input during processing leads to a wavy, unstable surface. This can prevent the spreading of a uniform powder layer during re-layering, consequently resulting in higher porosity. Similar behaviour was published by *Walker et al.* (8). Additionally, all porosity was spherical in shape. Higher VEDs increase the energy input from the laser and causes porosity due to vaporisation of the melt. High energy inputs and vaporisation are directly linked as overheating causes greater gas evolution which can become entrapped during the solidification of the melt.

In contrast to the work published by *Li et al.* (5) cracking was not evident during this parametric study. This is due to the equiatomic composition of the build and the absence of the brittle Ti_2Ni phase.

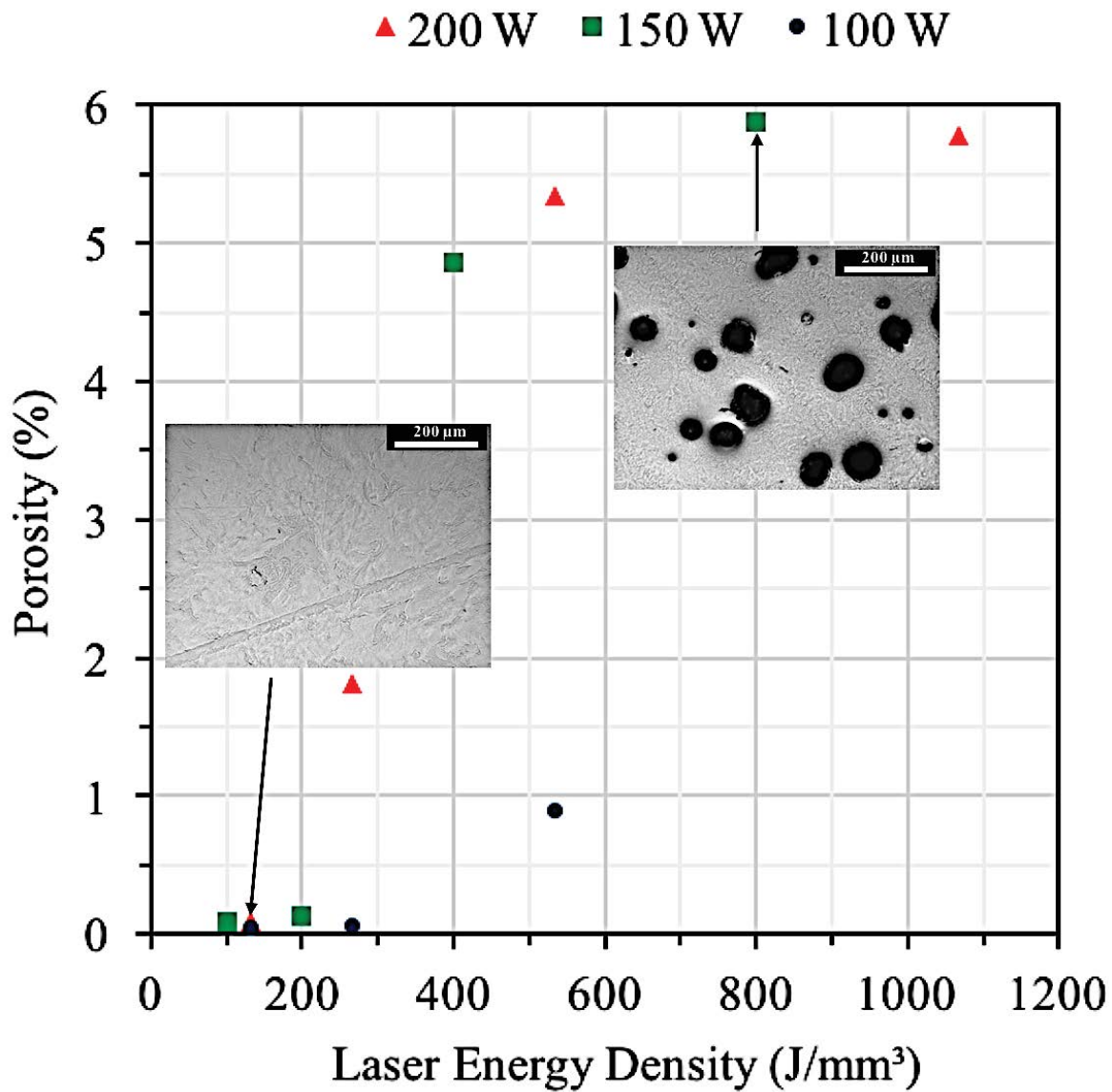


Figure 4.10 (a): Porosity plotted against the laser VED. Porosity measurement error: ± 0.001 %

A comparison of micrographs can be seen in figure 4.10 for parts with the lowest (0.035 %) and highest (6.362 %) porosity. The part with the lowest porosity was manufactured using a VED of 133 J/mm³. On the other hand, the part with the highest porosity was manufactured using a VED of 1067 J/mm³. In agreeance with *Walker et al.* (8), a general trend can be concluded that processing at lower VEDs (133 to 444 J/mm³) results in lower part porosity. When determining the optimal processing parameters for manufacturing dense parts, this trend is very desirable as the VED is directly related to impurity pick up during the SLM process.

These samples have been manufactured with a scan spacing of 75 μm . A second parametric study was carried out to study the influence of scan spacing on the structural integrity of SLM NiTi. The laser power and scan speed which produced the lowest porosity during the first parametric study was kept constant whilst the scan spacing was altered. Thus, samples were produced using a laser power of 100 W, a scan speed of 500 mm/s and the scan spacing varied from 15 – 90 μm .

Although changes in the scan spacing can alter the laser VED, from figure 4.10 (b) it is evident that the scan spacing had negligible effect on the build porosity. All samples were processed with a porosity below 0.2 %. Indicating that the laser power and scan speed have the most significant influence in manufacturing high density NiTi. If these SLM parameters are optimised then pore and crack free NiTi can be processed over a range of different scan spacing.

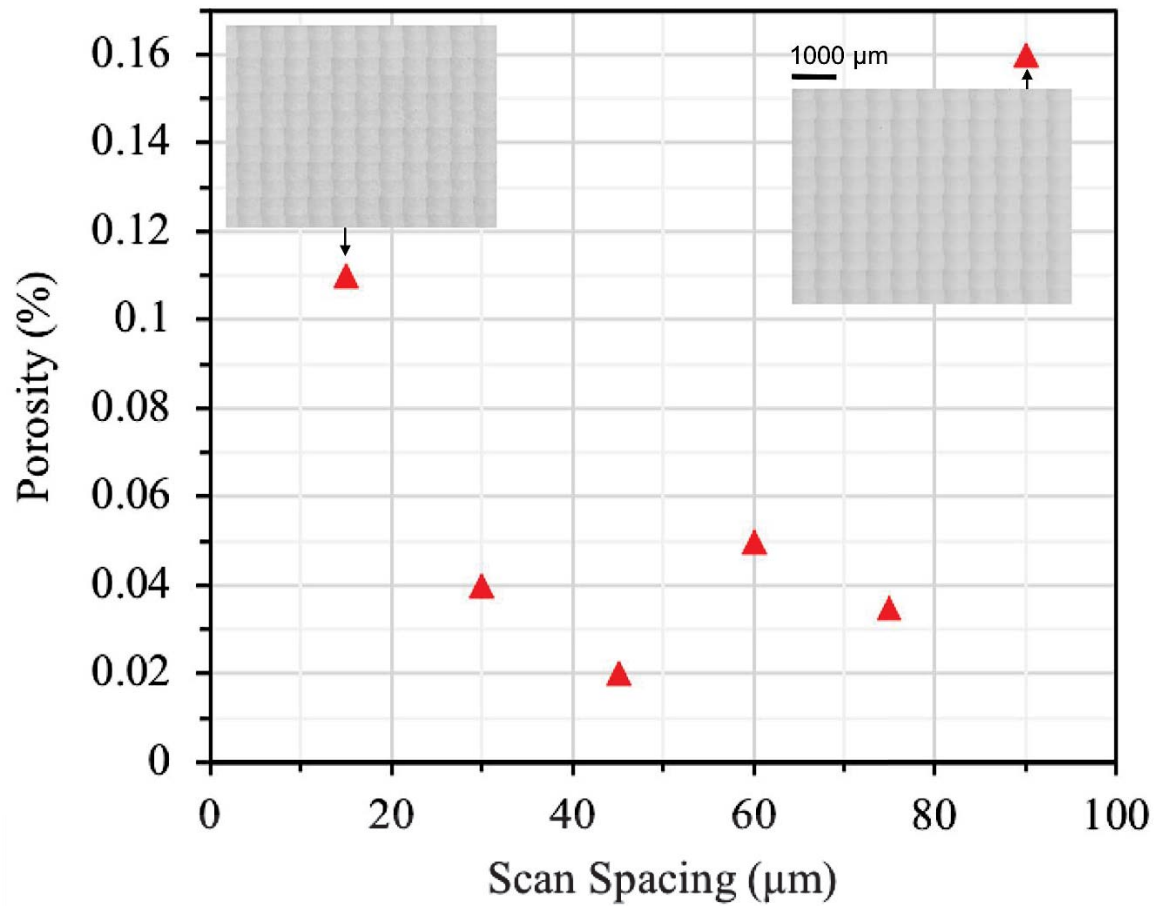


Figure 4.10 (b): Porosity plotted against scan spacing. Porosity measurement error: $\pm 0.001\%$

Oxygen analysis (via the inert gas fusion method) was performed on samples manufactured using differing VEDs. From figure 4.11, it is clear the oxygen content of the part increases with VED. This can be attributed to the high reactivity of Ti and the increased temperatures of the melt. Similar findings were published by *Haberland et al.*(15).

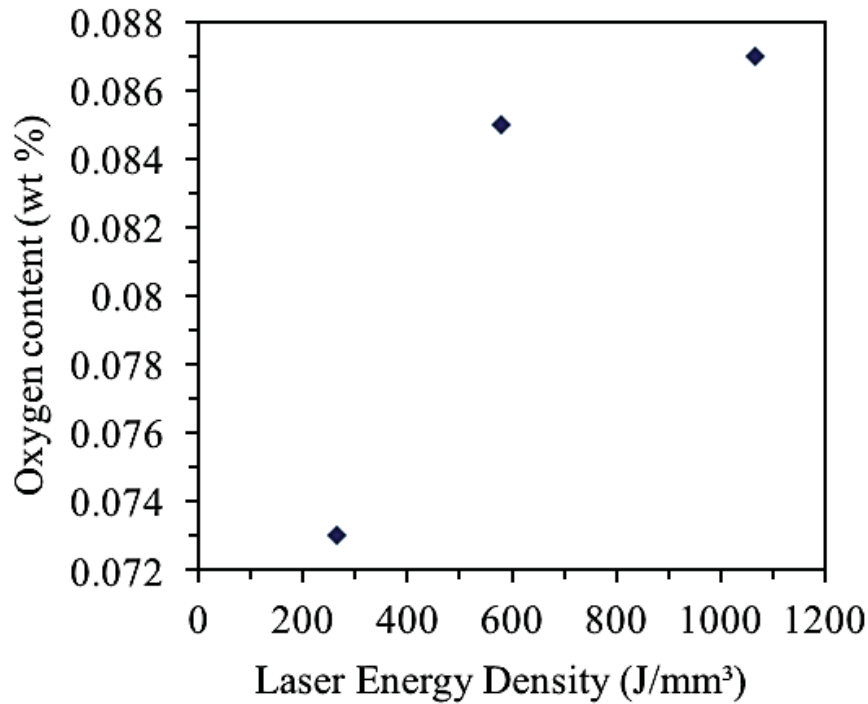


Figure 4.11: The oxygen content of the as-fabricated SLM parts manufactured using differing VEDs

Table 4.7. shows the oxygen content of the pre-alloyed NiTi powder in comparison to the oxygen content of the SLM part with the lowest porosity (manufactured using a VED of 133 J/mm³). The powder had an oxygen content of 0.033 wt %. However, after SLM processing this increased by 45 %.

Table 4.7: The oxygen content of the pre-alloyed powder and SLM fabricated part

	O ₂ content (wt %)
NiTi pre-alloyed powder	0.033
NiTi SLM manufactured part	0.073

While VED is a useful calculation in generalising the trends, it must be highlighted that it is a very simplistic equation. Many different processing parameters can be combined to give the same VED. Processing with a laser power of 100 W, a scan speed of 250 mm/s, 75 µm scan spacing and a 20 µm layer thickness produces a VED of 267 J/mm³. Processing at these conditions produces a part with a 0.077% porosity. On the other hand, processing using a laser power of

200 W, a scan speed of 500 mm/s, 75 μm scan spacing and a 20 μm layer thickness produces the same VED of 267 J/mm^3 . However, processing at these conditions produces a part with a 1.812 % porosity. The relationship between processing parameters, VED and porosity was first identified by *Dadbakhsh et al.*(14). Figure 4.12. displays two micrographs of the parts with differing porosity, however, manufactured using the same 267 J/mm^3 VED.

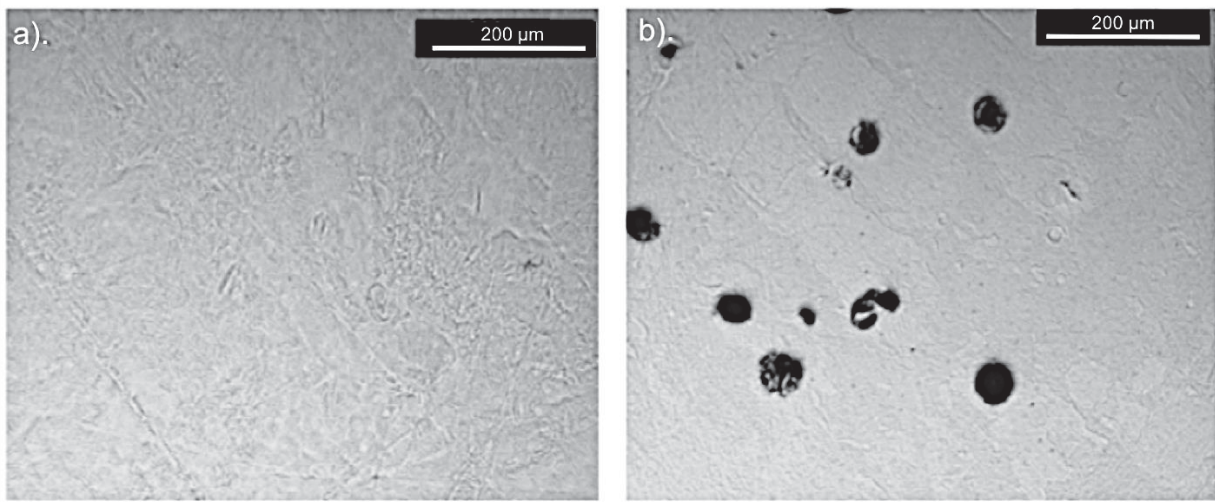


Figure 4.12: A micrograph display the porosity in SLM parts for samples manufactured using a). 100 W and 250 mm/s b). 200 W and 500 mm/s

Visible in figure 4.13. the porosity decreases as scan speed increases for a given laser power. From an economical point of view, reducing manufacturing time by increasing the scanning speed is extremely beneficial in reducing overall production costs. Thus, further investigations were performed considering the effects of increasing scan speed on part porosity.

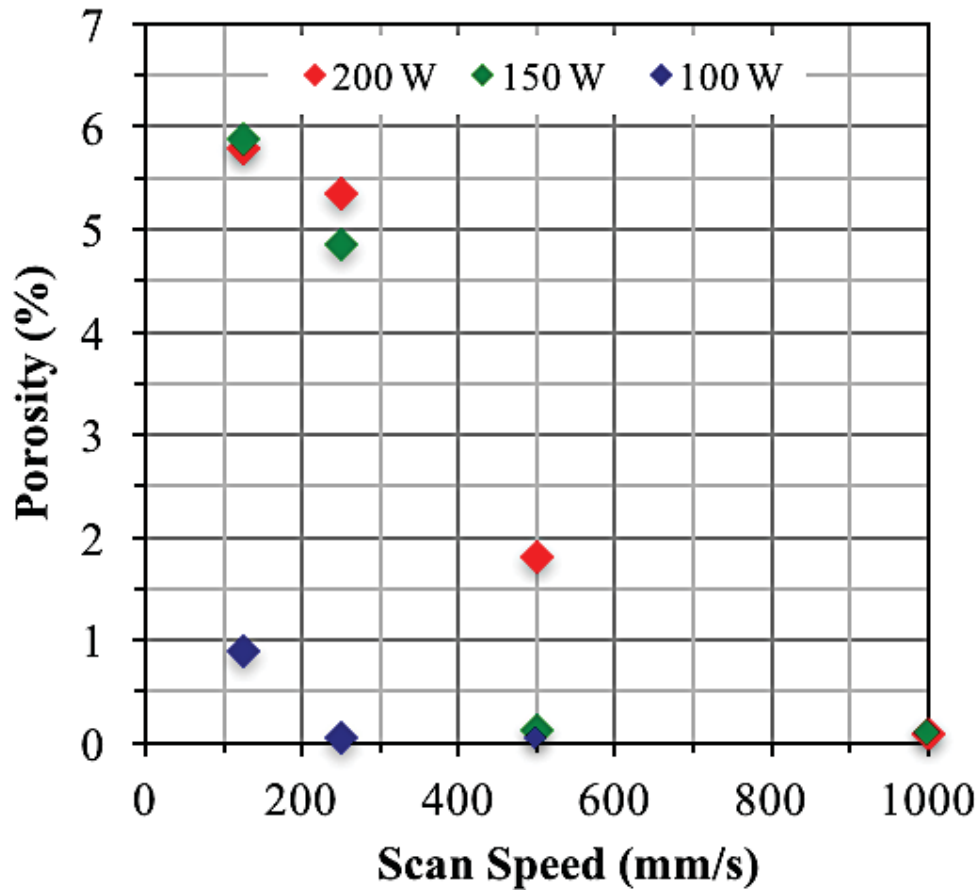


Figure 4.13: The influence of scan speed on the porosity of SLM manufactured NiTi. Porosity measurement error: ± 0.001 %

In figure 4.14, the laser power stayed constant at 100 W, and parts were manufactured using increasing scan speeds, with either a scan spacing of 45 μm or 60 μm . For a given scan speed, processing at a larger scan spacing consistently fabricated parts with a higher porosity. Additionally, porosity increased at scan speeds higher than 1000 mm/s. As shown in figure 4.15, the morphology of the porosity changed from spherical to irregular. Indicating that increases in porosity was no longer due to over-heating. As the scan speed increases, the laser VED and the energy absorbed by the powder decreases. Consequently, porosity is formed in the part as there is not enough energy to enable full consolidation and melting of the powder particles. Spherical powder particles, approximately 45 μm in size are visible in figure 4.15. As the particles are still perfectly spherical, it indicates that the powder remained solid during laser scanning.

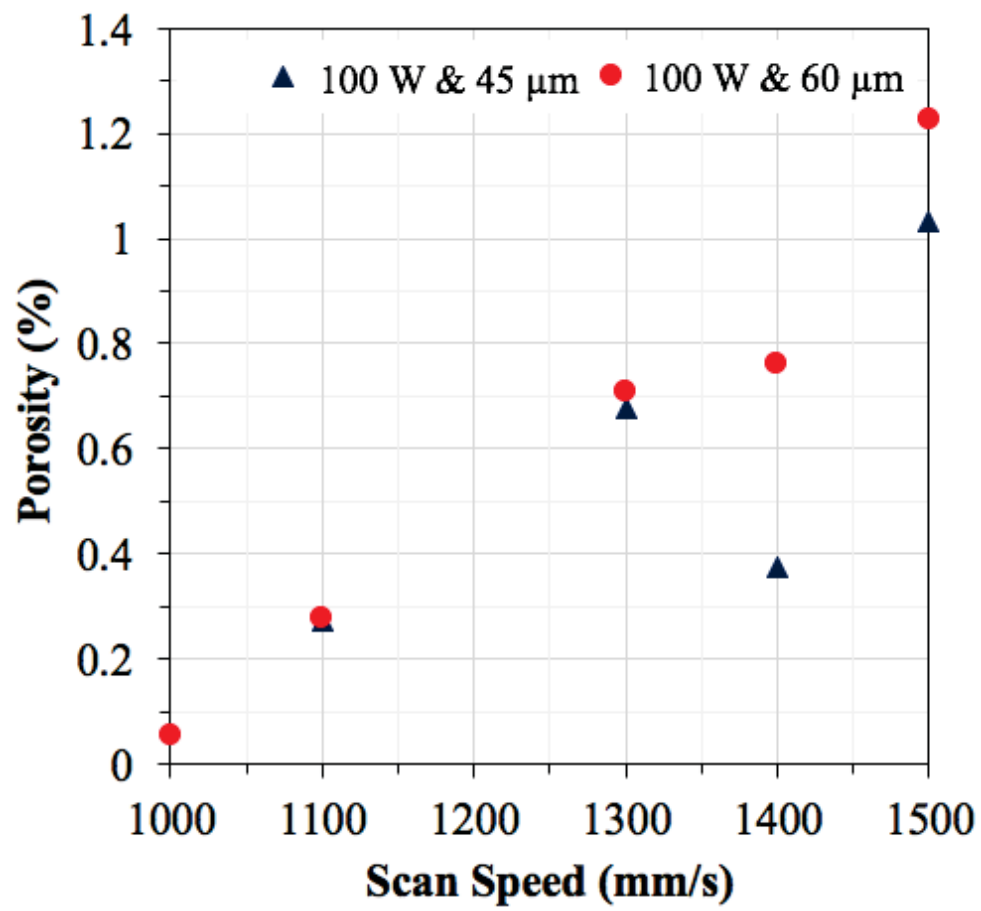


Figure 4.14: The influence of high scan speeds on the porosity of SLM NiTi manufactured using a laser power of 100 W.
Porosity measurement error: $\pm 0.001\%$

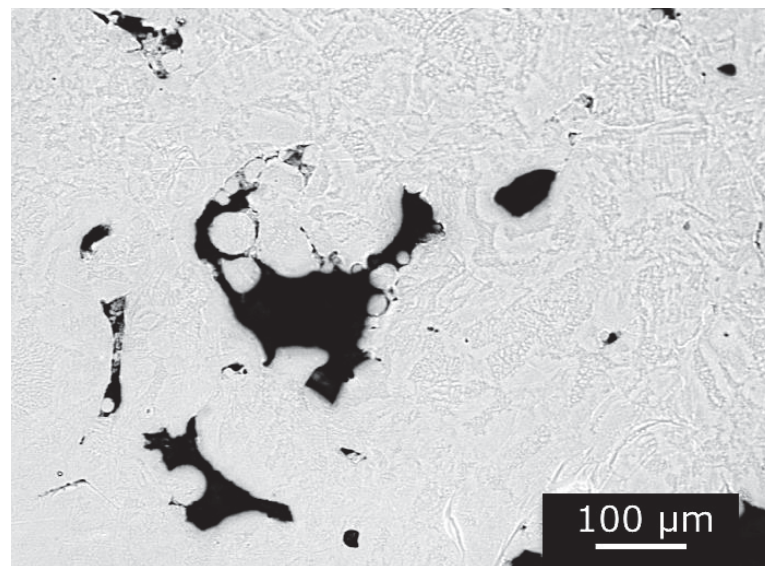


Figure 4.15: A micrograph of the irregular porosity formed when processing at high scan speeds

Although, processing at high speeds can produce parts with low porosity it was found that processing at speeds above 1000 mm/s resulted in inter-layer cracking, as shown in figure 4.16. This cracking is believed to be caused by differences in the cooling rate and residual thermal stresses. Faster scan speeds are associated with higher cooling rates and the precipitation of the brittle Ti_2Ni intermetallic. As the laser scans the surface of the powder bed, the interface between the powder and the previously solidified layer will experience re-melting to ensure good bonding. Whereas, the previously solidified layers will experience re-heating from the laser. The cooling rate of the solidified layers will be much higher than that of the molten material, producing brittle Ti_2Ni within the layer. Thermal stresses arise within the material as the lower cooler layers restrict the expansion of the hotter upper layers. As the brittle Ti_2Ni phase is subjected to the same thermal stresses as the NiTi phase, is it more likely to crack.

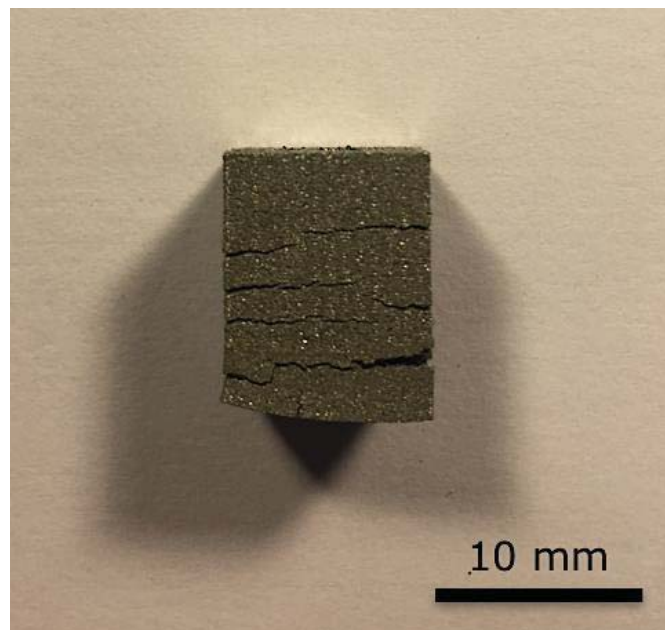


Figure 4.16: Inter-layer cracking produced when manufacturing at scan speeds above 1000 mm/s

Following this study, the layer thickness of the parts was increased. This was done to reduce the re-heating of the previously solidified layers, thus, eliminate the cracking. Figure 4.17. displays the surface contour plot for samples manufactured using a 20 μm layer thickness.

Whereas, figure 4.18. displays the surface contour plot for samples manufactured using a 40 μm layer thickness.

After SLM processing, increasing the layer thickness did not eliminate the cracking. The surface contour plots show similar trends for both layer thicknesses: as the scan spacing and scan speed decrease, so does the porosity. However, samples processed using a 40 μm layer thickness displayed higher porosity percentages. Thus, it can be concluded that although manufacturing at faster scan speeds is more economically advantageous these fast speeds are not viable for processing NiTi as they have a detrimental effect on the structural integrity of SLM component.

From the parametric studies, an optimised set of SLM processing parameters can be identified which can produce defect free NiTi parts. The parameters shown in table 4.8. manufacture NiTi parts with no cracking, extremely low porosity and an oxygen content of 0.077 wt %.

Table 4.8: The optimised SLM processing parameters for NiTi

Material	Laser Power (W)	Laser Scan Speed (mm/s)	Scan Spacing (μm)	Layer Thickness (μm)	VED (J/mm^3)
NiTi	100	500	75	20	133

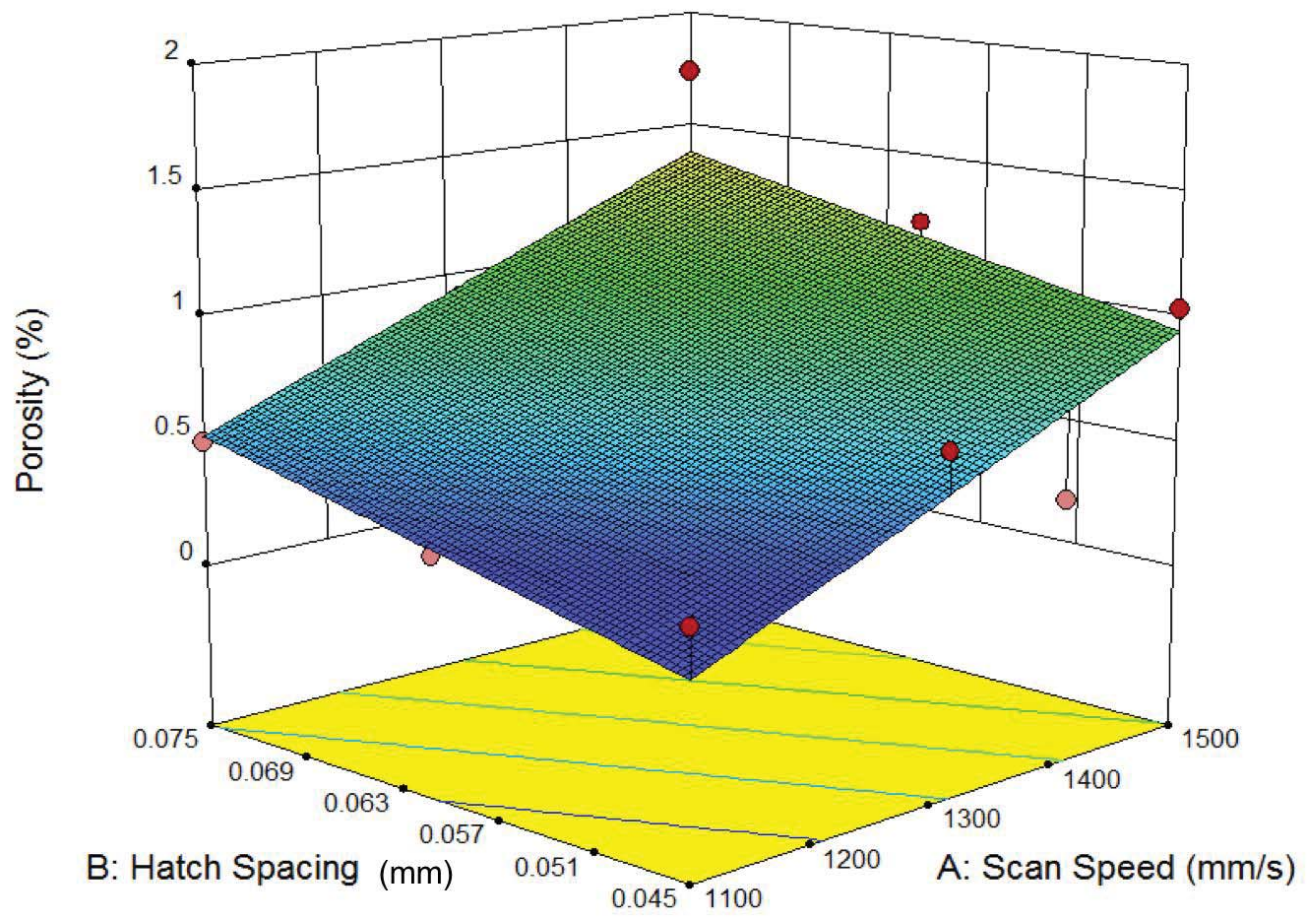


Figure 4.17: A surface contour plot for samples manufactured using a layer thickness of $20\ \mu\text{m}$ and laser power of $100\ \text{W}$.
Porosity measurement error: $\pm 0.001\ \%$

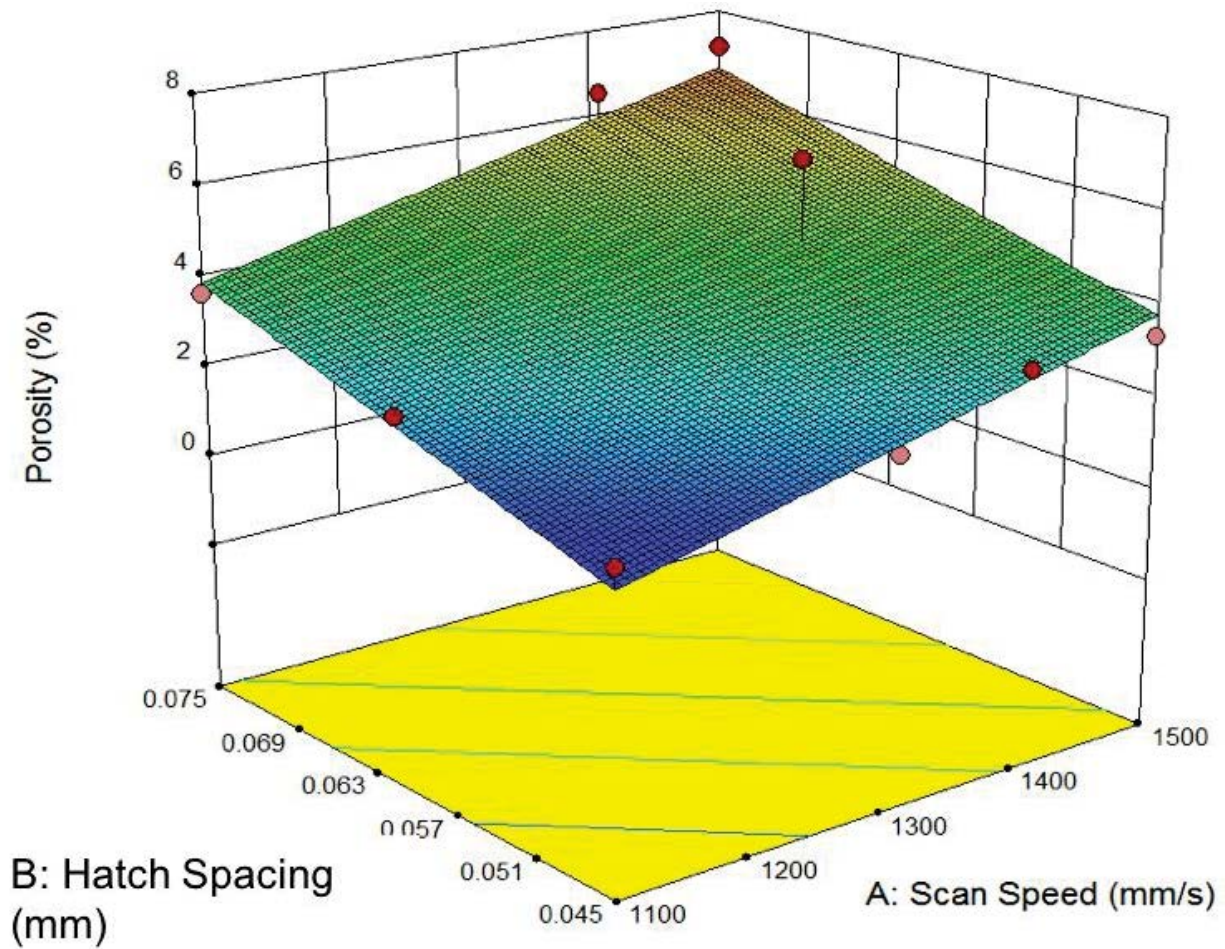


Figure 4.18: Surface contour plot for samples manufactured using a layer thickness of 40 μm and laser power of 100 W. Porosity measurement error: $\pm 0.001\%$

4.3.1. The Influence of SLM Processing Parameters on the Microstructure and Structural Integrity of Ternary TiNiPd

Pd has a melting temperature of 1555°C, 113°C below Ti (1668°C) but 245°C above Ni₅₀Ti₅₀ (1310°C). Therefore a ternary TiNiPd parametric study was performed, which contained the same parameter combinations used for the binary NiTi parametric tests. It was assumed that if the energy input from the laser could melt the Ti during the previous NiTi parametric studies, it should be high enough to successfully melt the Pd powder particles.

Figure 4.19 displays the results from the Ti₅₀Ni₄₈Pd₂ (at %) parametric study. The ternary alloy behaves similarly to the binary NiTi: The porosity decreases for each laser power as the scan

speed increases. Furthermore, the optimised processing parameters shown in table 4.8, also produced the as-fabricated part with the lowest porosity at 0.204 %. The overall porosity percentages are lower in comparison to the binary NiTi alloy, indicating less keyhole porosity occurred as vaporisation of the melt decreased. This behaviour indicates that the presence of Pd powder particles prevented over heating of the melt as they absorbed a portion of the laser energy density.

Following the porosity investigations, the sample fabricated using the optimised processing parameters from the parametric study (same as shown in table 4.8) was analysed using the backscatter detector on the SEM. Due to differences in elemental atomic numbers, imaging in the backscatter mode produces contrasts between different phases. The image obtained in figure 4.20 suggests that the elemental Pd and Ti powder particles, which were added to the powder mixture did not successfully alloy into the NiTi matrix.

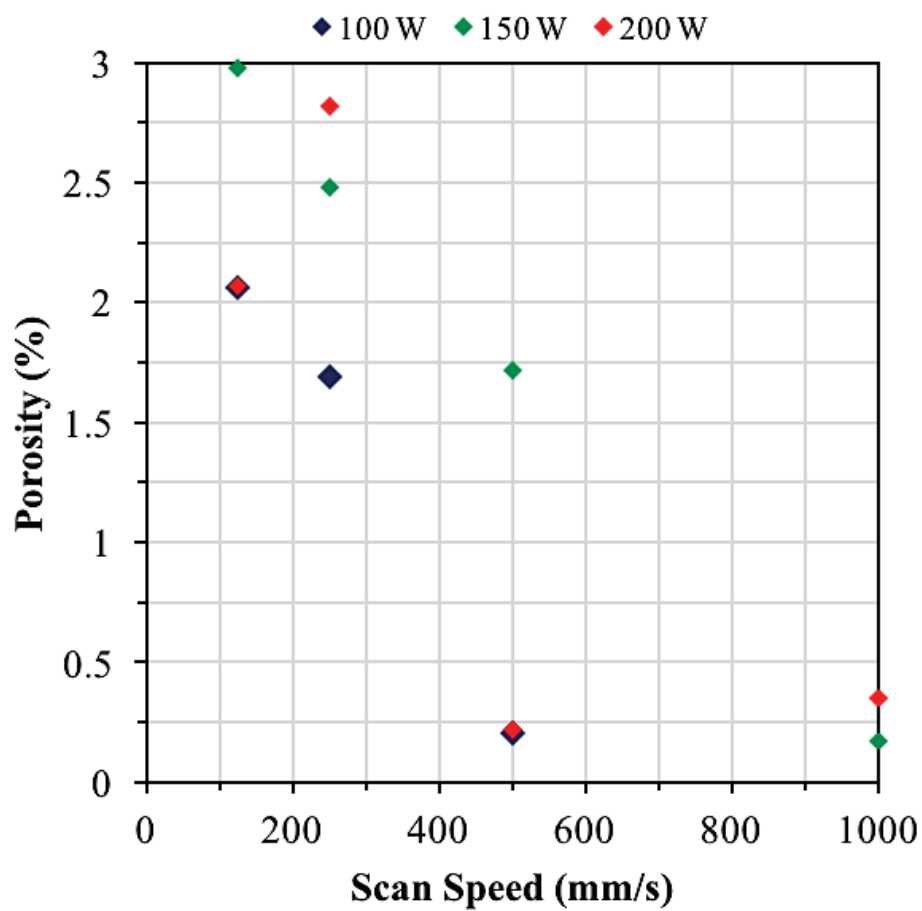


Figure 4.19: The influence of scan speed on the porosity of ternary $Ti_{50}Ni_{48}Pd_2$ (at %). Porosity measurement error: ± 0.001 %

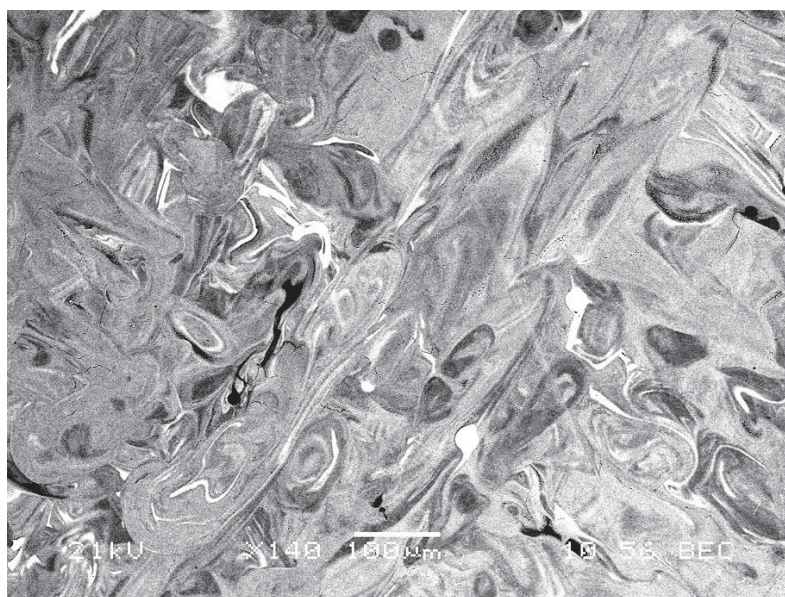


Figure 4.20: A BSE image of the $Ti_{50}Ni_{48}Pd_2$ (at %) sample processed using the optimised processing parameters for high density and no cracking

Figures 4.21 a) and b) show an image of a backscattered Pd powder particle with its corresponding EDX analysis. The white spherical particle, approximately 38 μm in diameter, is deposited within the NiTi matrix. The EDX results reveal the white phase to be nearly pure Pd.

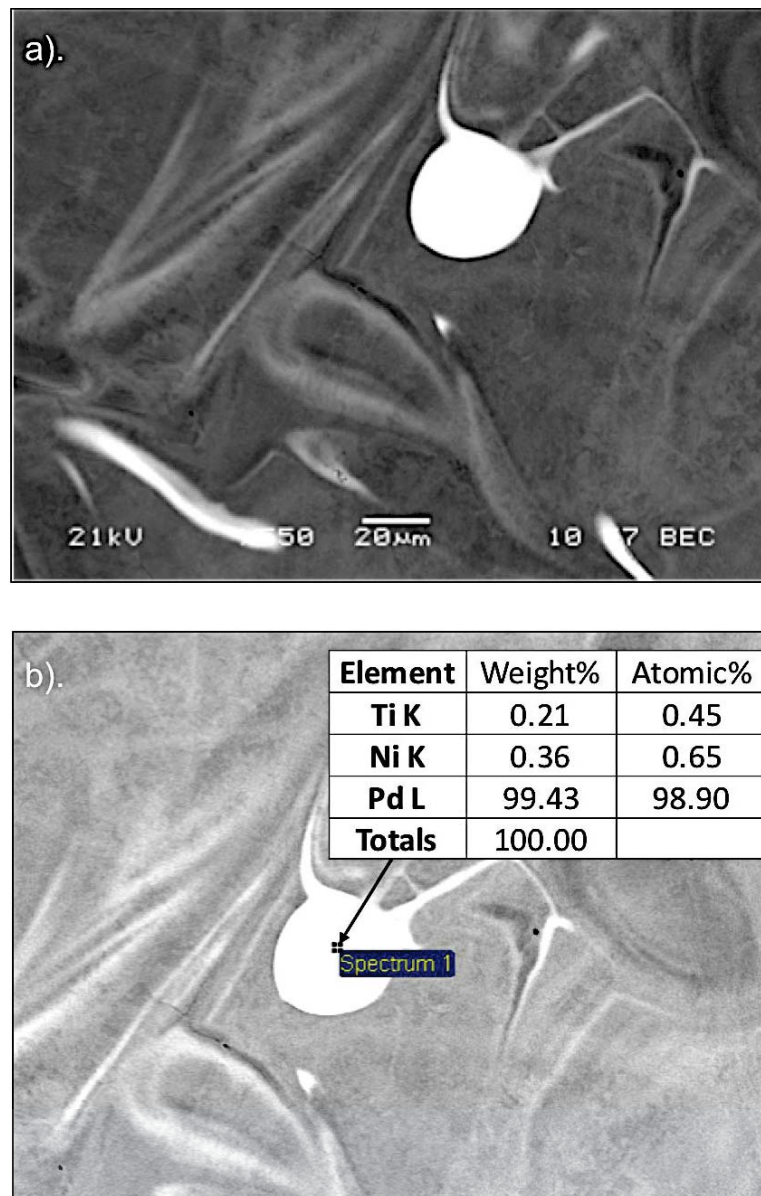


Figure 4.21: a). BSE image of a Pd particle within the NiTi matrix b). EDX analysis of the Pd particle

Three different phases are visible in figure 4.22. The phases are indicated by numbers and their corresponding compositions can be seen in table 4.9. As shown in table 4.9 and the EDX line

scan in figure 4.23, phase 1 is pure Ti. Phase two appears dark grey in the BSE image, indicating a reduction in the Ti content. The EDX results prove this to be correct as although Ti is still the dominant element, the phase now contains both Ni and Pd. By phase three, the composition is approximately equal to the target $\text{Ti}_{50}\text{Ni}_{48}\text{Pd}_2$ (at %) composition, indicating a homogeneous matrix.

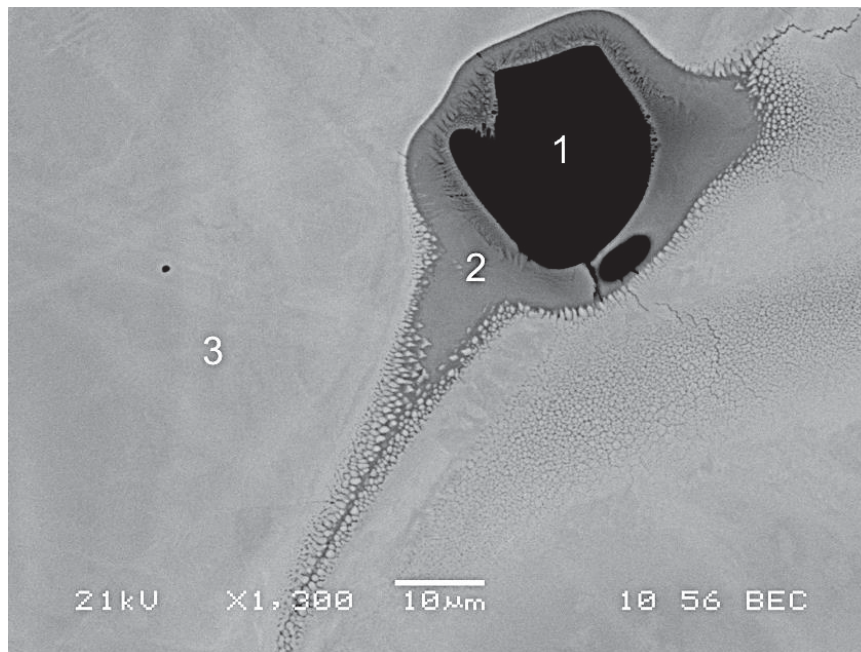


Figure 4.22: A BSE image of a Ti powder particle within the NiTi matrix

Table 4.9: The EDX compositional analysis results for the three phases shown in figure 4.22

Phase	Element composition (at %)		
	Ti	Ni	Pd
1	99.61	0.39	-
2	63.81	34.12	2.07
3	50.17	46.96	2.87

EPMA mapping of Pd particles within the NiTi matrix can be seen in figures 4.24 and 4.25. Due to the change in concentration and the colour variation of the powder particle in the map from white at the centre, to red through to green and finally blue at the Pd - NiTi interface, it

is evident Pd atoms had started to diffuse during SLM processing. However, it is probable that the Pd particle has not fully molten and was dissolving slowly in the molten NiTi.

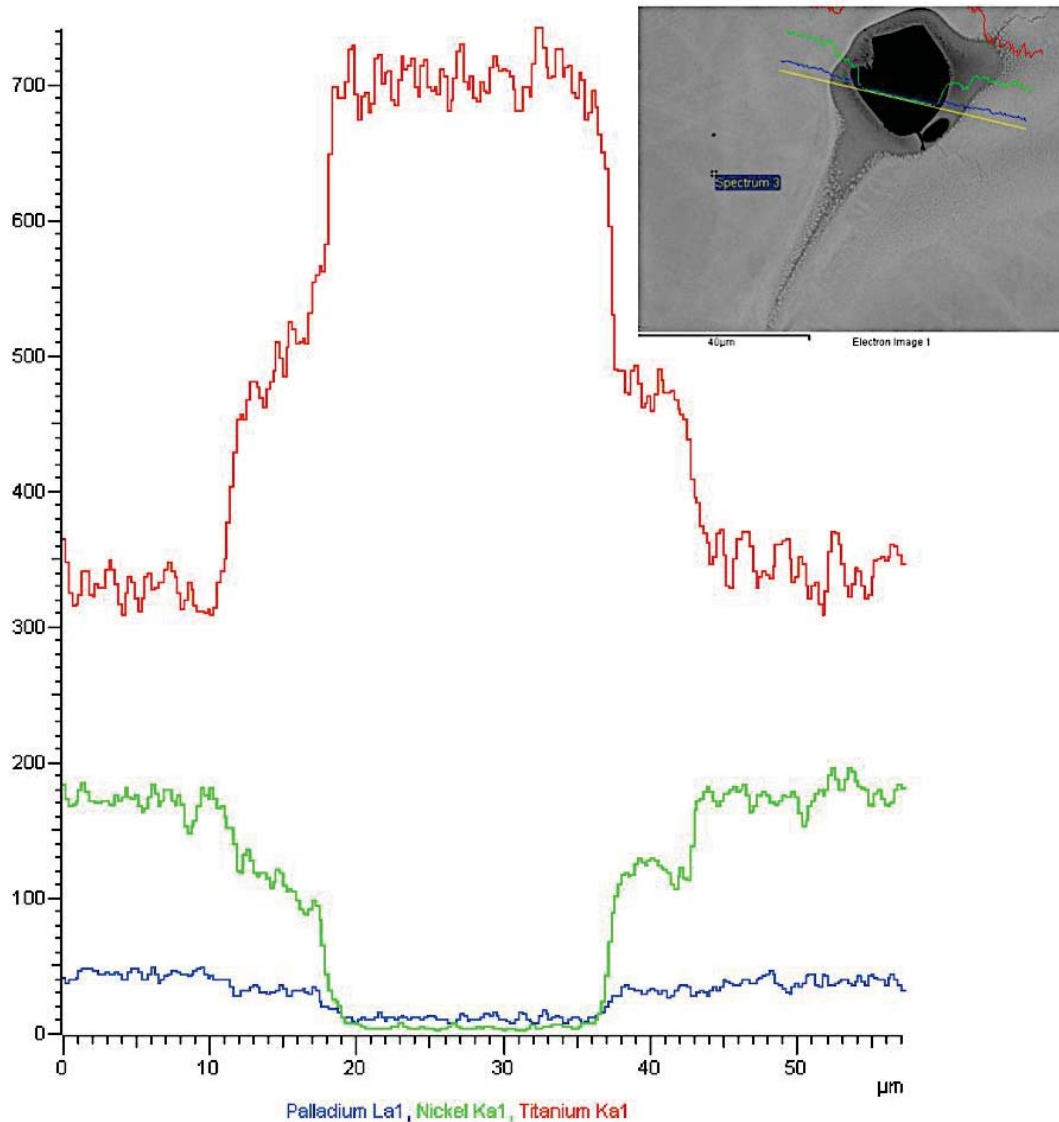


Figure 4.23: The EDX line scan over the Ti powder particle within the NiTi matrix

Phase transition during SLM is governed by energy absorption and heat transfer within the powder bed. As energy from the laser is absorbed into the powder bed, thermal energy spreads by diffusion and the temperature of the powder particles in the immediate area increases until the liquidus temperature of the powder particles is reached. Firstly, the solid-liquid phase consumes increasing heat energy until the solid powder particles are completely liquid, forming

a molten melt pool. The melt pool moves with the laser beam, meaning the powder experiences very fast melting and solidification. This rapid solidification and cooling rate of the melt pool directly affect the build microstructure. From figures 4.20-4.25, it is clear the Pd and Ti powder particles were not fully molten within the liquid NiTi matrix. Meaning, the liquid life span of the melt pool was too short to allow the Pd and Ti powder particles to fully diffuse into the NiTi matrix. Whilst the Pd and Ti powder particles are still partially solid, their diffusion rate is much slower into the liquid NiTi matrix. Consequently, due to the slower diffusion rate, the solid spherical Pd and Ti particles remain in the microstructure as the molten NiTi matrix re-solidifies. In order to improve the chemical homogeneity of the final build, an energy input must be achieved which can fully melt the Pd and Ti powder particles. Thus, enabling faster diffusion and mixing of the elements.

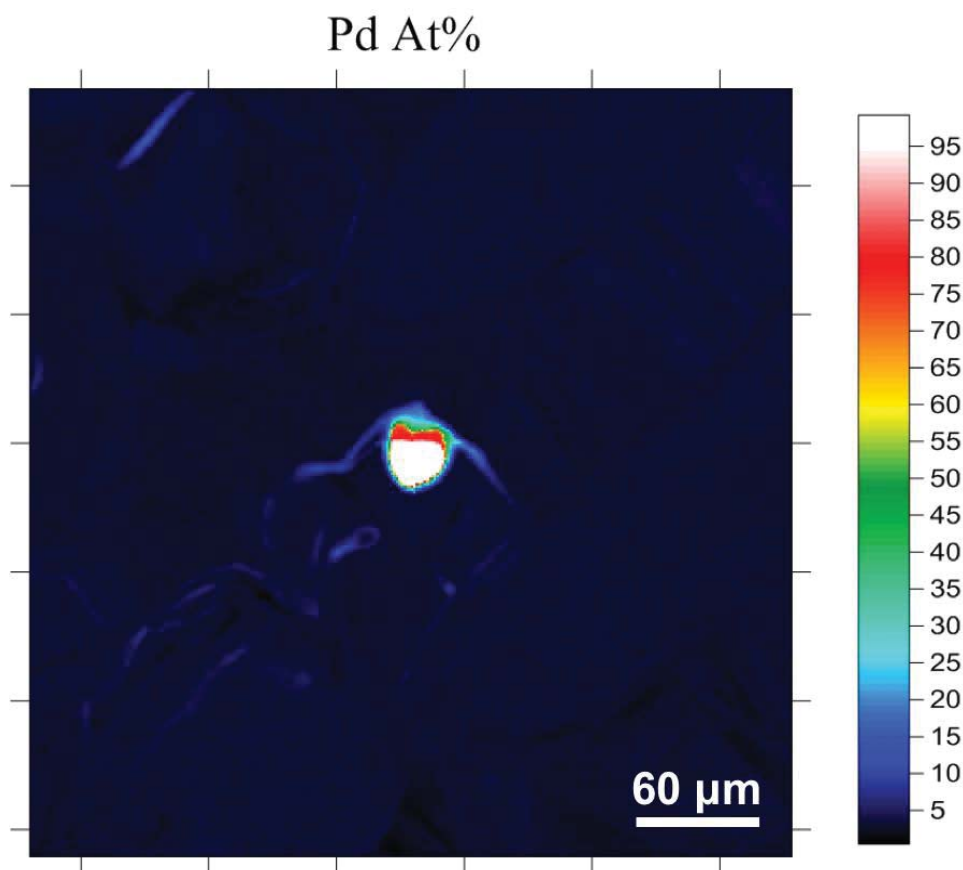


Figure 4.24: EPMA mapping of Pd within the NiTi matrix

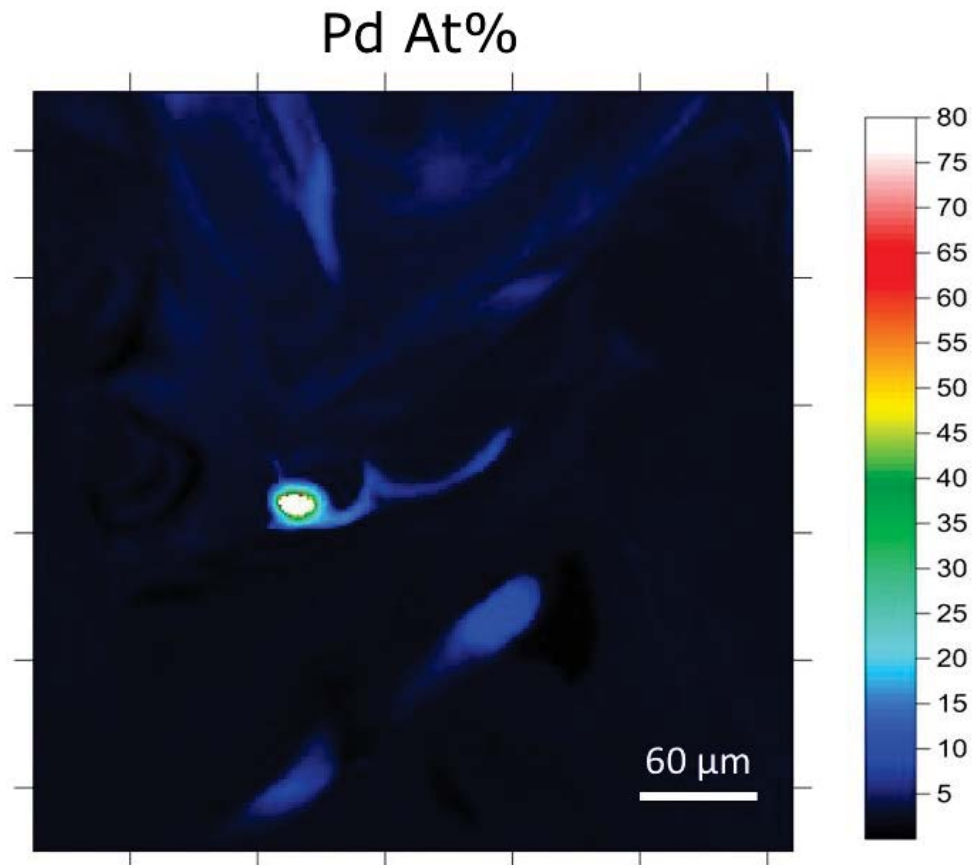


Figure 4.25: EPMA mapping of Pd within the NiTi matrix

The evolution of the melt pool is dominated by the interaction between the laser radiation and the powder bed. Thus, it would be correct to assume melt pool geometry can be altered by changes in the processing parameters (scan speed, laser power and scan spacing) that work to modify the energy from the laser being absorbed into the powder bed. Previous studies, show that NiTi requires processing at lower laser powers to achieve high build density and low elemental evaporation. Consequently, an in-situ alloying methodology must be identified that accounts for build density, chemical homogeneity and elemental vaporisation.

It is important to mention that chemical homogeneity in these as-fabricated builds could not be achieved through the use of solution heat treatments. The homogenising heat treatments rely on solid state diffusion, where the sample is held at high temperatures long enough for a solid

solution to form and afterwards it is rapidly cooled. The solid solution forms due to a driving force produced from a concentration gradient. As diffusion is much slower in solids in comparison to liquids or gases, it would be unrealistic to use this as a method to diffuse nearly whole Pd and Ti powder particles (up to 63 μm in size) into the NiTi matrix.

4.3.1 a. The In-Situ Alloying Methodology

As Pd is the alloying element, the in-situ alloying methodology primarily focuses on the dissolution of the Pd powder particles into the NiTi matrix. However, the same in-situ alloying methodology can be applied to the elemental Ti powder particles also observed in the microstructure. Hence, the resulting as-fabricated microstructure is a homogeneous TiNiPd matrix with no re-solidified elemental powders.

Figure 4.26. shows that reducing the laser scan speed will significantly improve the build's chemical homogeneity. For samples processed at 80 W, decreasing the scan speed from 500 mm/s to 120 mm/s, increased the melt pool depth by 34 μm and reduced the area fraction of undissolved Pd powder particles to 0%. No spherical particles remained and the Pd had been successfully alloyed into NiTi, producing a homogeneous TiNiPd matrix.

When the scan speed decreases, the VED from the laser increases. This leads to a rise in the melt pool depth as more energy is absorbed into the powder bed. An increase in the melt pool depth is accompanied by a longer melt pool liquid life span and slower variations in the temperature field of the powder bed. Consequently, the solid-liquid-solid transformation occurs over a longer period and the Pd atoms have more time to fully diffuse into the NiTi matrix before the melt pool re-solidifies. As all the Pd atoms in the powder particle are able to disperse and diffuse, a homogeneous TiNiPd microstructure is formed.

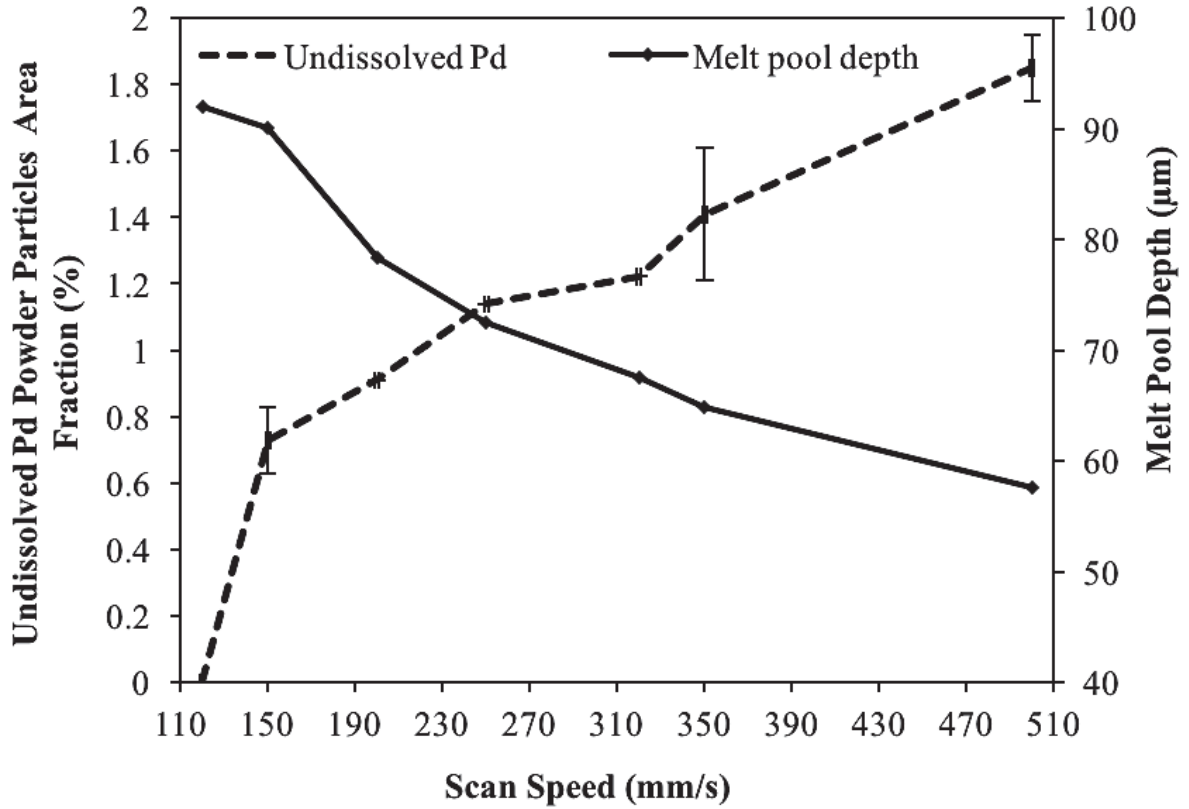


Figure 4.26: The relationship between scan speed, melt pool depth and undissolved Pd powder particles

ImageJ was used to quantify the area of half the melt pool for a number of samples processed using a range of SLM parameters. Half the cross sectional area of the melt pool was measured as this area was visible on the optical images taken across the XZ plane. Theoretically, the entire melt pool cross sectional area could be estimated by multiplying the half area by two. However, work within this thesis reports the half cross sectional area values. As shown in figure 4.27, the melt pool cross sectional area increased with laser VED. This behaviour is expected as the enhanced thermal energy absorbed into the powder bed will melt more powder particles.

Figure 4.28. shows that the observed area fraction of undissolved Pd particles decreases with increasing laser VED and melt pool area. As the scan speed is reduced, the laser VED increases causing an increase in the cross sectional area of the melt pool. As the increase in laser VED produces a larger liquid formation from the metallic powders, the melt pool liquid life span is

also increased as larger liquid formation will take longer to re-solidify. Consequently, the Pd atoms have greater time to successfully diffuse. Optical images of the melt pools along the XZ plane can be seen in figure 4.29 (a) and (b). The samples in the image were processed using a laser power of 80 W and a scan spacing of 56 μm . However (b) was processed using a laser scan speed that was 380 mm/s slower than (a), resulting in an increase in the laser VED of 452 J/mm^3 . From both images it is visible that as the laser VED increased, so did the melt pool depth and cross sectional area.

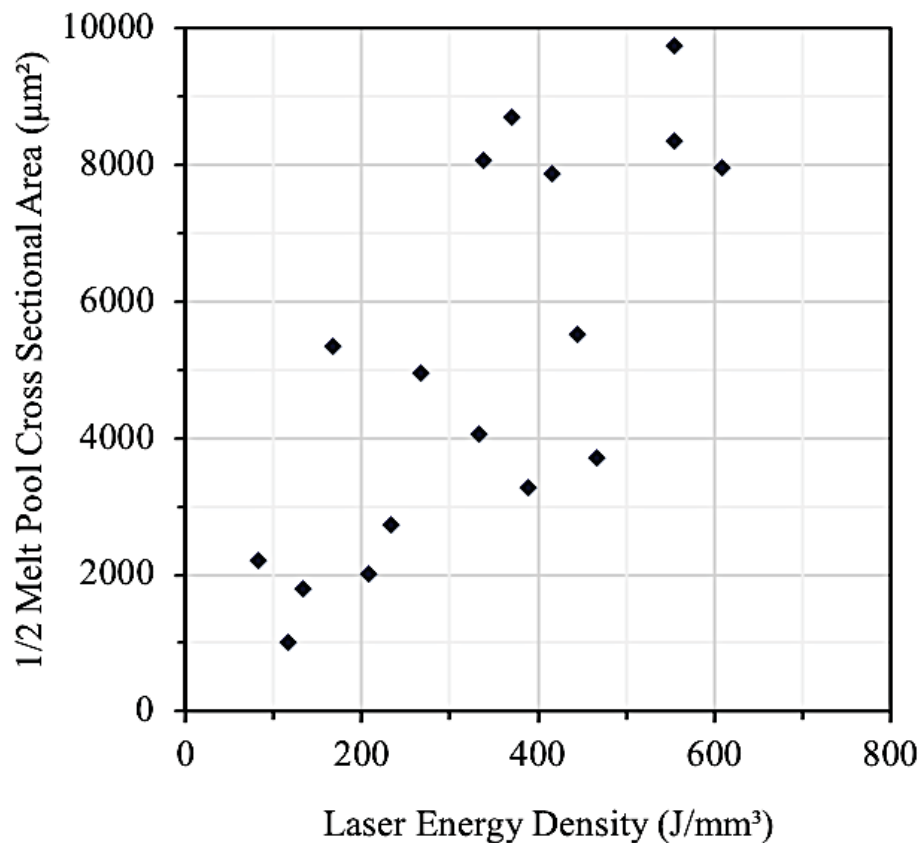


Figure 4.27: The relationship between $\frac{1}{2}$ melt pool cross sectional area and the laser VED.

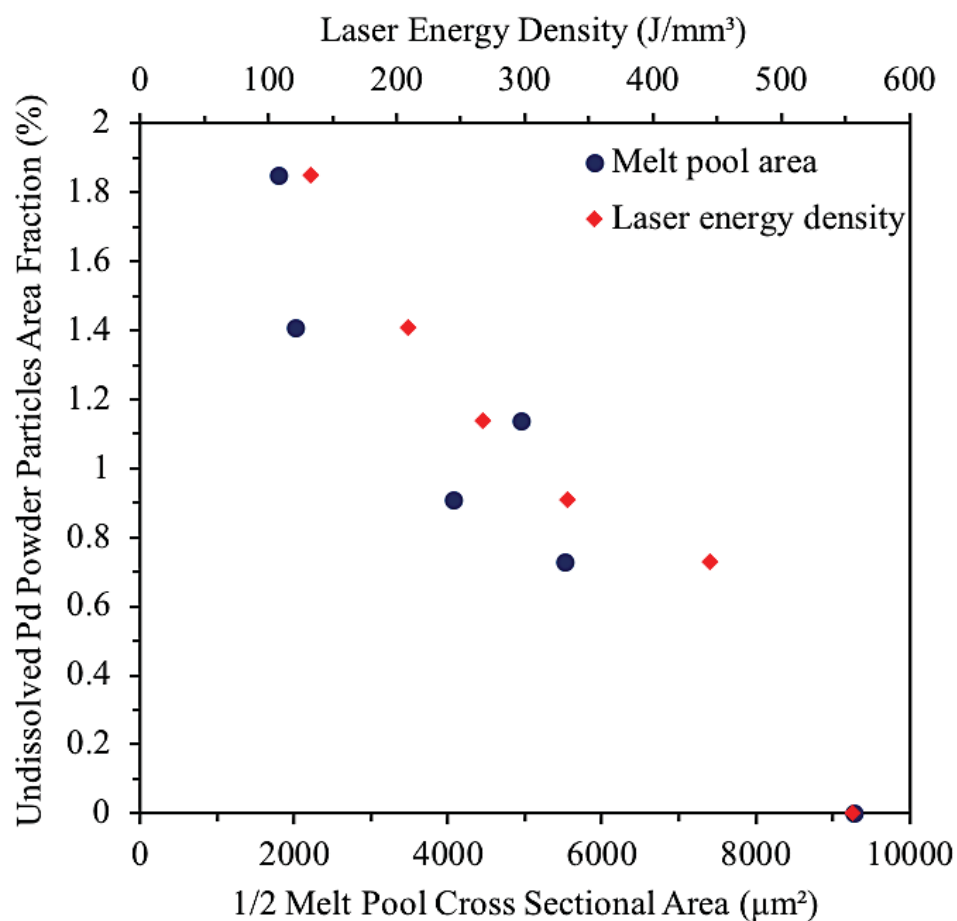


Figure 4.28: The relationship between the melt pool area, laser VED and undissolved Pd powder particles for samples processed at 80 W

Thus, it can be concluded that reducing the scan speed from 500 mm/s to 120 mm/s, increased the melt pool depth to 96 μm and produced a melt pool with a half cross sectional area of 9726 μm². These modified melt pool dimensions proved to have a melt pool liquid life span that was long enough to allow melting and full diffusion of the Pd elemental powders as the area fraction of undissolved Pd reduced to 0%.

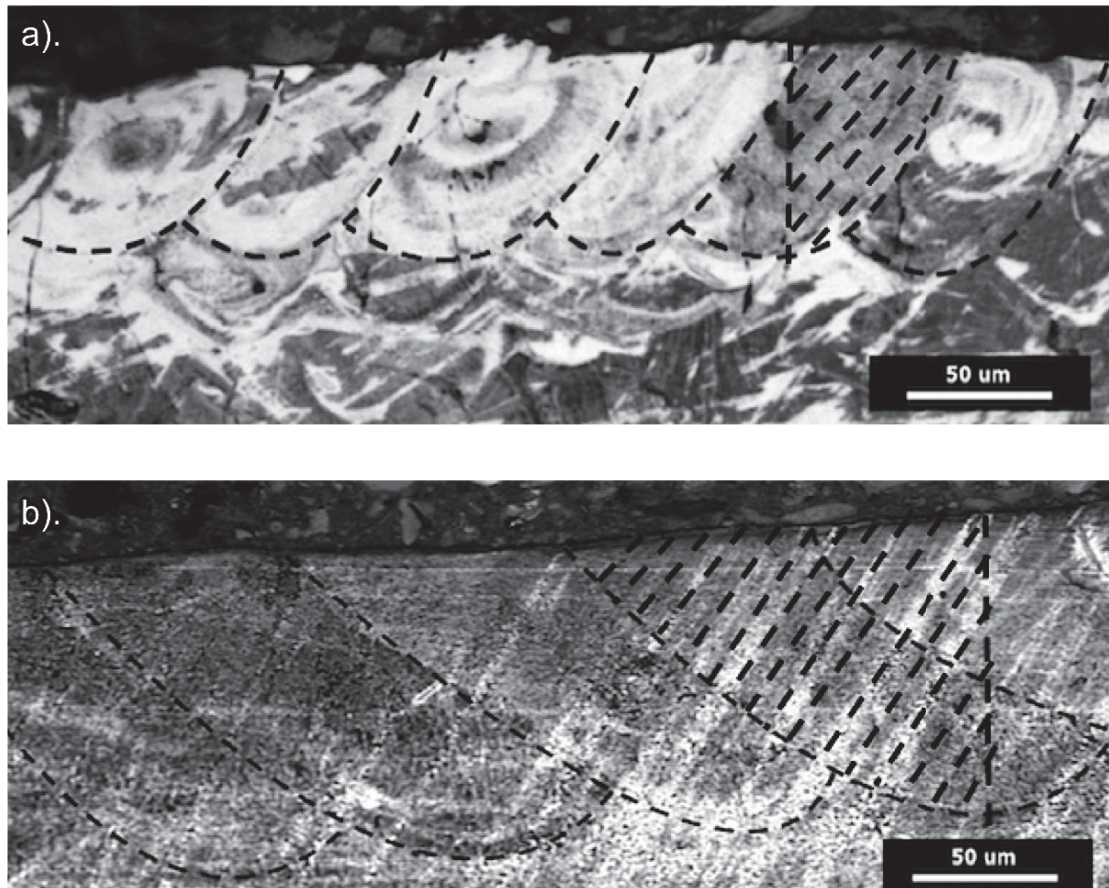


Figure 4.29: Optical images of the melt pools processed at (a). 80 W, 500 mm/s, 56 μm (b). 80 W, 120 mm/s, 56 μm

The morphology of the Pd-rich streaks in the microstructure of the samples processed at faster scan speeds (figure 4.30), shows interesting melt pool behaviour. As highlighted in the figure, the streaks have a lower Pd concentration compared to the white spherical particles, indicating that these streaks have partially diffused into the matrix before re-solidification. The swirling morphology of the streaks indicates a turbulent stirring in the melt pool called the Marangoni effect. As the scan speed is decreased, the energy density from the laser increases, leading to a higher temperature gradient at the solid-liquid interfaces of the melt pool. This temperature gradient generates greater surface tension gradients and a resultant greater Marangoni flow. This enhanced stirring can additionally contribute towards the improved chemical homogeneity when processing at slower scan speeds, as the Pd atoms are better distributed and can dissolve faster.

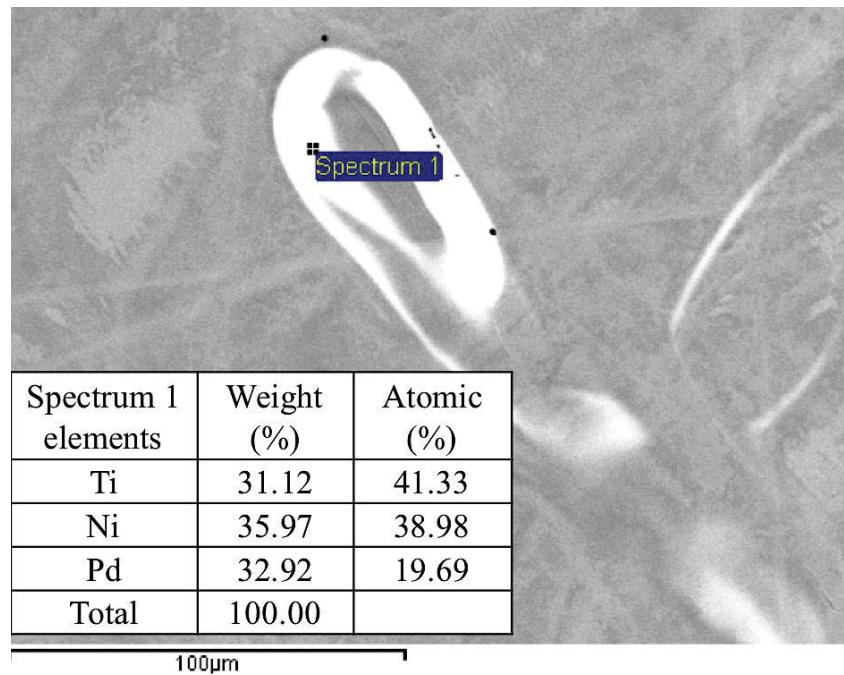


Figure 4.30: EDX quantification of the white swirling phase visible under backscatter imaging

From the previous parametric study of SLM TiNiPd, like binary NiTi, the alloy requires processing at lower energy densities to produce defect (porosity & cracking) free builds. However, decreases in the scan speed from 500 mm/s to 120 mm/s, increase the energy input from the laser. By reducing the laser power by 20 W, the laser energy density can be reduced by 149 J/mm^3 , producing a good compromise between the lower energy inputs required for defect free builds and the higher energy required for chemical homogeneity.

The energy density of the laser is increased by 78 J/mm^3 , when reducing the scan spacing from $90 \text{ }\mu\text{m}$ to $45 \text{ }\mu\text{m}$ for samples processed using a laser power of 80 W and 500 mm/s scan speed. Figure 4.31. shows that decreases in scan spacing did not improve the chemical homogeneity of the build. The increase in the energy absorbed into the powder bed due to reductions in scan spacing was insufficient at increasing the melt pool depth. Thus, the melt liquid life span remained similar for all builds. This was evidently too short to allow full diffusion of the Pd atoms into the NiTi matrix. Additionally, the optical images (shown in figure 4.32) of the melt

pools in samples processed using a scan spacing of (a). 90 μm (b). 45 μm , indicate no significant difference in the melt pool cross sectional area. The cross sectional area of half the melt pool shown in figure 4.32 (a) was 2467 μm^2 . Whereas the melt pool shown in image (b) has a half melt pool cross sectional area of 2155 μm^2 .

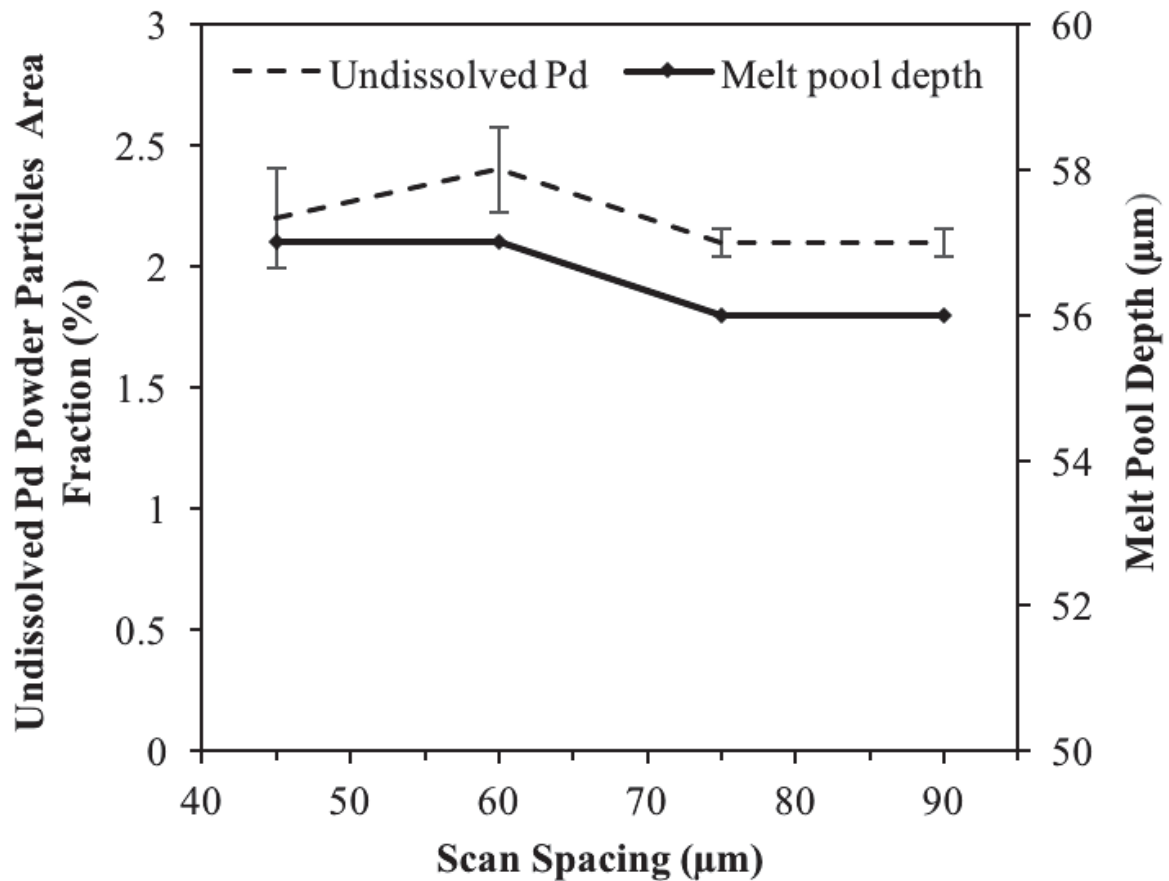


Figure 4.31: The relationship between scan spacing, melt pool depth and undissolved Pd powder particles

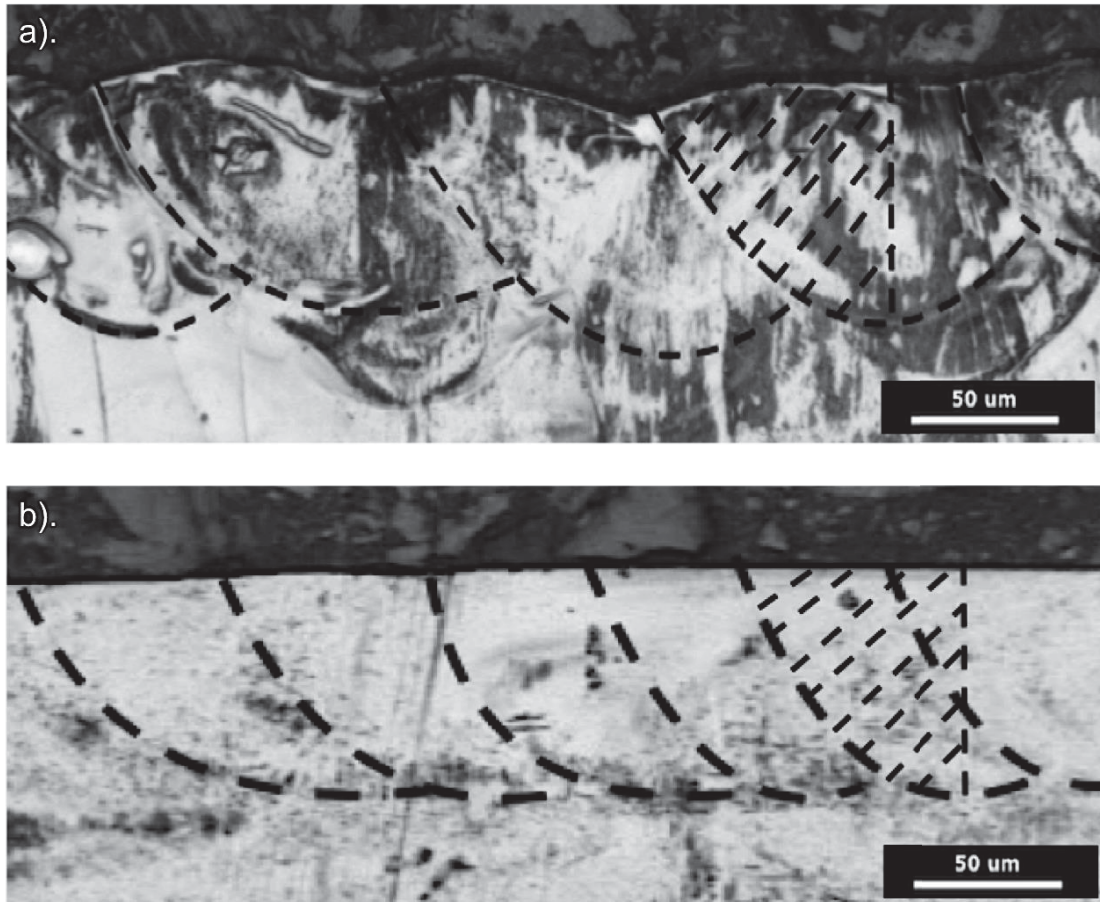


Figure 4.32: Optical images of the melt pools processed at (a). 80 W, 500 mm/s, 90 μm (b). 80 W, 500 mm/s, 45 μm

As expected increasing the laser power for a given scan speed and scan spacing increased the melt pool dimensions. Processing at a laser power of 70 W and a scan speed of 500 mm/s produced a melt pool with a cross sectional area of 865 μm^2 . When increasing the laser power to 100 W, the melt pool cross sectional area increased to 5374 μm^2 . However, processing with these parameters still did not achieve a chemically homogeneous microstructure by successfully alloying the Pd into the NiTi matrix. Increasing the laser power further would not be an option, as from the parametric study it is evident that processing at higher laser powers induces keyhole porosity due to over-heating of the melt pool.

4.1.3 b. The In- Situ Alloying Optimised Processing Parameters

To successfully alloy Pd into the NiTi matrix using SLM, it was found that decreasing the scan speed had the most significant effect on the chemical homogeneity, whilst maintaining high build density and elemental evaporation. Using the optimised processing parameters as stated in table 4.10, SLM can be used to in-situ alloy NiTi with Pd, whilst simultaneously building a near net-shape component with a homogeneous microstructure, as shown in figure. 4.33. The SLM as-fabricated part can now be effectively solution heat treated to complete the homogenisation process, as discussed in the next chapter.

Table 4.10: The optimised SLM processing parameters to in-situ alloy elemental Pd powder into pre-alloyed NiTi powder

Laser Power (W)	Scan Speed (mm/s)	Scan Spacing (μm)	Layer thickness (μm)
80	120	56	20

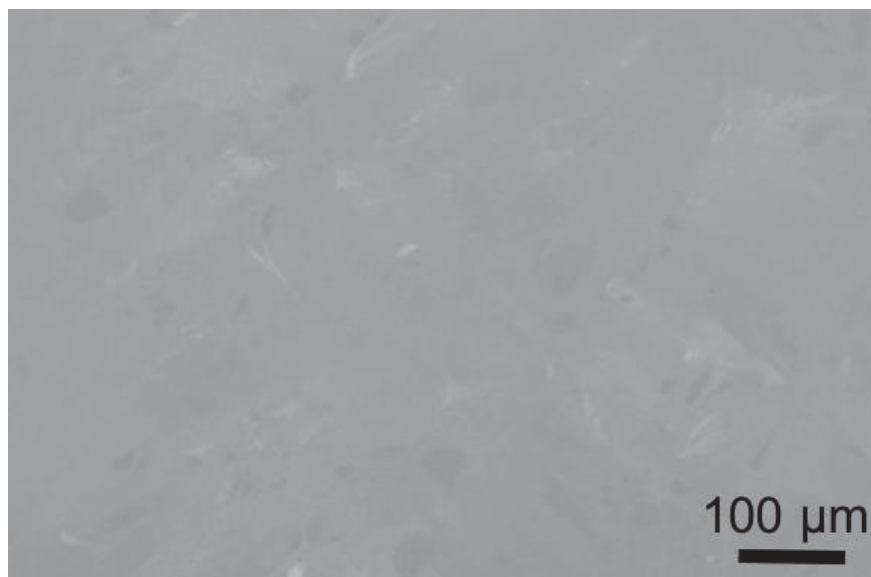


Figure 4.33: The microstructure of the $\text{Ti}_{50}\text{Ni}_{48}\text{Pd}_2$ alloy, SLM fabricated using the optimised processing parameters

4.4. Conclusion

The aim of the experimental work within this chapter was to identify a set of SLM processing parameters that could manufacture highly dense binary and Pd modified NiTi SMA. Furthermore, the processing parameters were individually investigated to see which one had

the greatest effect at achieving a homogeneous microstructure when alloying elemental Pd powder into pre-alloyed NiTi powder.

Initial powder characterisation revealed the pre-alloyed NiTi powder to have a much more spherical morphology in comparison to the elemental Pd powder. This is believed to be due to the fact that the pre-alloyed NiTi powder was plasma atomised, whereas the Pd powder was gas atomised. Powder mixtures can be made up to the target compositions of $\text{Ti}_{50}\text{Ni}_{48}\text{Pd}_2$ and $\text{Ti}_{50}\text{Ni}_{43}\text{Pd}_7$ (at %) by adding elemental Ti, Ni and Pd to the pre-alloyed NiTi powder batch. It was found that placing the powder mixture on a roller mill for 24 hours prior to use, ensured sufficient and homogeneous mixing of the powder particles.

SLM parametric studies were firstly performed using only the pre-alloyed NiTi powder. It was found to produce highly dense NiTi parts using SLM, a low laser VED must be used. The optimum laser VED for high density was found to be 133 J/mm^3 . Above 444 J/mm^3 , the melt would overheat causing the formation of keyhole porosity. High scan speeds (above 1000 mm/s) were investigated as if the process were to become industrialised, manufacturing at high speeds would reduce production time, thus costs. However, it was found manufacturing NiTi at such fast speeds induced severe cracking due to the formation of the brittle Ti_2Ni intermetallic between the layers.

Manufacturing at lower laser VED translated to the least oxygen contamination. Processing at higher VED increased the impurity content of the SLM parts due to the increased temperature of the melt pool and Ti's strong affinity for oxygen. The optimum laser VED for manufacturing highly dense NiTi parts resulted in a 0.04 wt % increase in oxygen. Since the maximum allowable oxygen content for NiTi devices to be used medical devices is 0.05 wt %, to industrialise the SLM of NiTi for biomedical applications, the oxygen content of the as-

fabricated parts must be decreased. A possible option could be to use a powder batch with fewer fine particles, as it was found during powder characterisation that due to the increase in surface to volume ratio, finer particles have the highest oxygen content.

The optimised processing parameters for manufacturing highly dense NiTi could be directly translated to TiNiPd alloys. The ternary alloy behaved similarly to the binary and the porosity decreased with the laser VED. However, although the build density was high, the microstructure was chemically inhomogeneous and undissolved elemental powder particles were present. Further investigations were carried out to study the effects of each processing parameter on the dissolution of Pd into the NiTi matrix, hence the chemical homogeneity of the SLM part. It was found that decreasing the scan speed from 500 mm/s to 120 mm/s had the most significant effect at improving the chemical homogeneity of the as-fabricated parts. This is believed to be due to the increase in melt pool depth and area, hence the increase in the melt pool liquid life span. Additionally, decreasing the scan speed enhances the Marangoni effect and this stirring motion helps to promote the dissolution of the powder particles into the NiTi matrix.

4.5. References

1. Spierings AB, Voegtlin M, Bauer T, Wegener K. Powder flowability characterisation methodology for powder-bed-based metal additive manufacturing. *Prog Addit Manuf* [Internet]. 2016;1(1–2):9–20.
2. Polizzi MA, Franchville J, Hilden JL. Assessment and predictive modeling of pharmaceutical powder flow behavior in small-scale hoppers. *Powder Technol* [Internet]. 2016;294:30–42.
3. Lumay G, Boschini F, Traina K, Bontempi S, Remy JC, Cloots R, et al. Measuring the flowing properties of powders and grains. *Powder Technol* [Internet]. 2012;224:19–27.
4. Tomas J, Kleinschmidt S. Improvement of flowability of fine cohesive powders by flow additives. *Chem Eng Technol*. 2009;32(10):1470–83.
5. Li S, Hassanin H, Attallah MM, Adkins NJE, Essa K. The development of TiNi-based negative Poisson's ratio structure using selective laser melting. *Acta Mater* [Internet]. 2016;105:75–83.
6. Foil M. New technology for spherical powder. *Met Powder Rep*. 48(3):28–9.
7. United States Patent Boylan et al. METHOD FOR PROVIDING RADIOPAQUE (10) Patent No .: (45) Date of Patent : i. 2011;2(12).
8. Walker JM, Haberland C, Taheri Andani M, Karaca HE, Dean D, Elahinia M. Process

- development and characterization of additively manufactured nickel–titanium shape memory parts. *J Intell Mater Syst Struct* [Internet]. 2016;27(19):2653–60.
9. Gokuldoss PK, Kolla S, Eckert J. Additive manufacturing processes: Selective laser melting, electron beam melting and binder jetting-selection guidelines. *Materials* (Basel). 2017;10(6).
 10. Prior DJ, Boyle a P, Brenker F, Cheadle MC, Day a, Lopez G, et al. The application of electron backscatter diffraction and orientation constrast imaging in th SEM to textural problems in rocks. *Am Mineral*. 1999;84:1741–59.
 11. Körner C, Bauereiß A, Attar E. Fundamental consolidation mechanisms during selective beam melting of powders. *Model Simul Mater Sci Eng* [Internet]. 2013;21(8):85011.
 12. Li Y, Zhou K, Tor SB, Chua CK, Leong KF. Heat transfer and phase transition in the selective laser melting process. *Int J Heat Mass Transf*. 2017;108(April):2408–16.
 13. Antony K, Arivazhagan N. Studies on Energy Penetration and Marangoni Effect During Laser Melting Process E P. 2015;10(4):509–25.
 14. Dadbakhsh S, Speirs M, Kruth JP, Schrooten J, Luyten J, Van Humbeeck J. Effect of SLM parameters on transformation temperatures of shape memory nickel titanium parts. *Adv Eng Mater*. 2014;16(9):1140–6.
 15. Haberland C, Elahinia M, Walker JM, Meier H, Frenzel J. On the development of high quality NiTi shape memory and pseudoelastic parts by additive manufacturing. *Smart Mater Struct*. 2014;23(10).

Chapter 5

The Thermal Behaviour of NiTi SMA

5.1. Introduction

DSC was used to investigate the transformation temperatures of SLM manufactured NiTi and TiNiPd SMA. Additionally, the influence of heat treatment on the transformation temperatures was studied using DSC. Finally, the microstructural evolution and precipitate formation following heat treatment was studied using a range of microscopy techniques.

During laser processing, the powder feedstock will experience two phase changes: The laser selectively scans the powder surface, particles will melt to form a liquid, before fusing and re-solidifying as the laser moves away. Vascular implants, such as self-expanding stents, require an A_F temperature below body temperature. Thus, during SLM, if the powder feedstock is austenitic at body temperature, the manufactured part must have the same thermal properties. To ensure this, it is imperative to gain an understanding into how SLM processing parameters and the consequent powder phase change effect the transformation temperatures of the final fabricated part.

5.2. Evaporation of Elements in SLM

5.2.1. The Vapour Pressure of Ni and Ti

Four processes govern the evaporation procedure from a metallic melt. Firstly, there is a mass transport of atoms from the bulk of the melt to its surface. A phase change occurs to a gaseous state at the melt's surface, and next the gas phase is transported above the melt. Finally, as a continuous supply of argon is required during SLM, it is assumed the gaseous phase is sucked into the filter where it then condensates. Furthermore, condensation can occur on the chamber interior surfaces. Due to the extremely high temperatures that occur during laser processing, it is possible the melt surface will experience superheating and exceed the boiling temperature for Ni or Ti. Hence, elemental evaporation will be unavoidable.

Vapour pressure is the pressure exerted by a gas in equilibrium with its solid. Thus, it can be used as a measure of the material's tendency to turn into the gaseous state. The boiling point of a liquid is the temperature at which the vapour pressure is equal to the atmospheric pressure. At temperatures above the boiling point, the vapour pressure overcomes the atmospheric pressure and atoms can escape from the liquid's surface. Materials with a higher vapour pressure require less energy to reach an equilibrium between the vapour and atmospheric pressure. Thus, it can be said that as vapour pressure increases, the boiling point decreases.

Vapour pressure (P), enthalpy of vaporisation (DH_{vap}) and temperature (T) are related using equation 5.1. Where R is the gas constant ($8.3145 \text{ J mol}^{-1}$) and A is a constant unique to every element.

$$P = A \exp \left(-\frac{DH_{vap}}{RT} \right)$$

The Clausius-Clapeyron equation (5.2) advances the association between vapour pressure and temperature to create a linear relationship. If the vapour pressure and enthalpy of vaporisation are known at some temperature, this mathematical expression can plot vaporisation curves.

Hence, the vapour pressure at alternative temperatures can be estimated. P1 and P2 are the pressures at two temperatures T1 and T2.

$$\ln \left(\frac{P1}{P2} \right) = \frac{DH_{vap}}{R} \left(\frac{1}{T2} - \frac{1}{T1} \right)$$

To estimate the vapour pressure of Ni and Ti during SLM processing, the Clausius-Clapeyron equation was applied. P1, DH_{vap} and T1 were known constants. These values were taken from published data recorded at Ni and Ti's melting temperature. The vapour pressure of Ni at 1726 K (melting temperature) is 237 Pa (1). The vapour pressure of Ti at 1933 K is 0.49 Pa (1). As it is not possible to accurately measure the exact temperature of the melt pool, T2 was an estimated value. The vaporisation curves can be seen in figure 5.1. Ni has a lower boiling temperature (3003 K) in comparison to Ti (3560 K). This is evident in the figure as the vapour pressure for Ti remains at 0 atmospheric pressure for higher temperatures. The vaporisation curve for Ni rises much more rapidly with temperature in comparison to Ti. Highlighting the weaker intermolecular bonding in Ni and its greater tendency to evaporate in comparison to Ti, as less heat energy is required to free the atoms from the melt's surface.

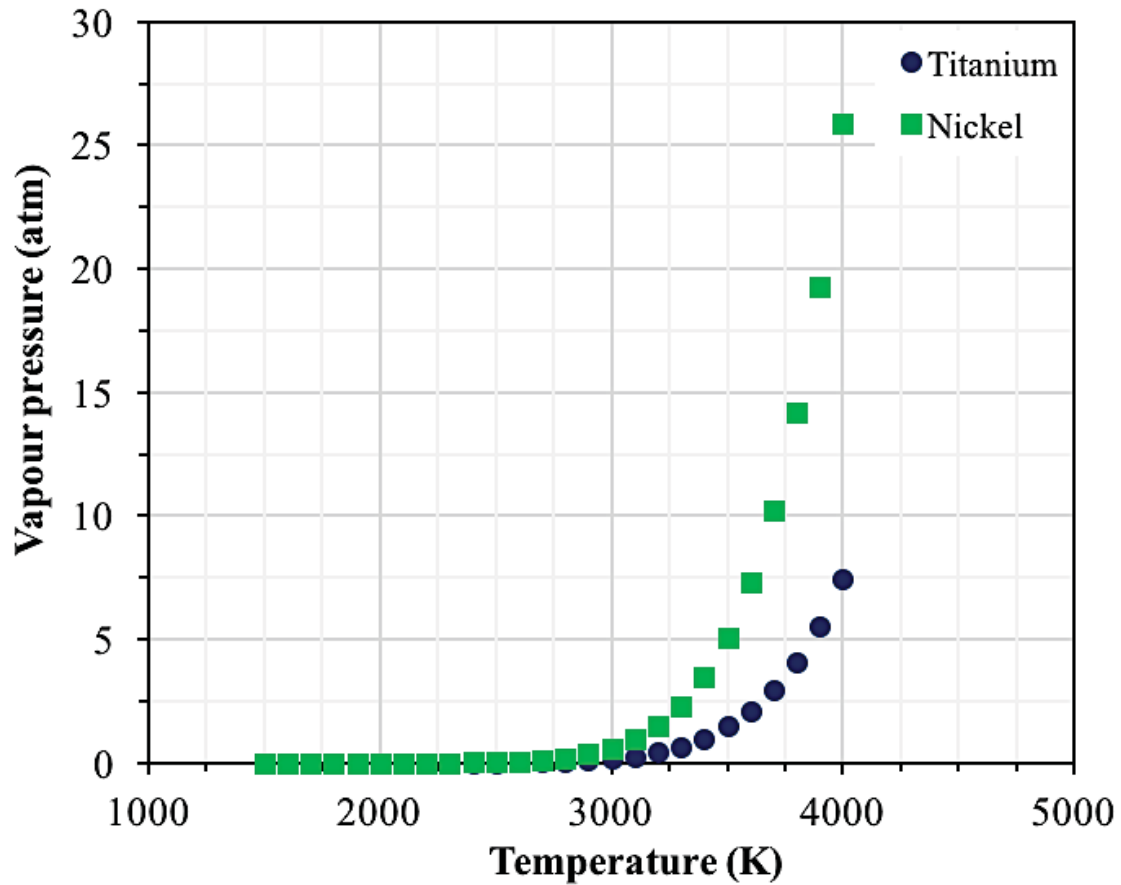


Figure 5.1: Vaporisation curves for Ni and Ti

5.2.2. The Influence of SLM Processing Parameters on Ni Evaporation

During SLM as the laser selectively scans the surface of the powder bed, the powder particles are heated as they absorb energy from the laser. Once temperatures reach the powder's solidus temperature and the latent heat is sufficient, a solid-liquid phase transformation will occur forming a melt pool (2). As the heat energy will transfer to surrounding solid powder particles, the dimensions of this melt pool are controlled by thermal diffusion (3).

The laser energy density is a measurement of the average applied energy per volume of the material. The linear energy density (LED) equation (5.3) assesses the combined effects of laser power and scan speed on energy input and estimates the laser energy input to the powder surface layer being melted. The laser power (W) is represented by P in the LED equation and the scan speed (mm/s) by V .

$$LED = \frac{P}{V} \text{ J/mm}$$

Overall, increasing the laser power means melting will occur at faster speeds. Additionally, this increase in energy input will penetrate deeper into the powder bed via thermal conduction. For a given laser power, reductions in the scan speed cause the laser power to be applied for longer. Consequently, there is more time for heating to occur and heat energy to diffuse to surrounding powder particles.

When manufacturing NiTi SMA using the SLM processing route, a relationship can be observed between the processing parameters (laser power and scan speed) and the amount of Ni lost through evaporation. Figure 5.2. displays the Ni loss (at %) plotted against scan speed for a given laser power. The extent of Ni loss increases as the scan speed is decreased for each laser power. The sample fabricated using the highest LED experienced the greatest Ni lost. In contrast, the least Ni evaporation was evident in samples processed at the lowest LED. A 1.6 LED, experienced the greatest Ni loss, rounded to 6 at %. Alternatively, a 0.2 LED lost approximately 0.4 at % Ni.

The relationship between Ni loss and SLM processing parameters can be explained using the dimensions of the melt pool. The temperature of the melt pool significantly increases with LED as greater energy is absorbed at the surface of the powder bed. This increased heat energy conducts through to a larger volume of solid powder particles, creating an increase in molten metal formation. Consequently, the melt pool provides a larger surface area for Ni to evaporate from whilst in its molten state. Additionally, the poor thermal conductivity of NiTi means the melt pool is kept at elevated temperatures for longer. Thus, more time is available for Ni to evaporate from the melt pool before it re-solidifies. As mentioned in chapter 2, changes in the

Ni composition can have a dramatic effect on the alloy's transformation temperature (4). If manufacturing NiTi using SLM is to become an industrialised, the effects of processing parameters on the transformation temperature must be investigated.

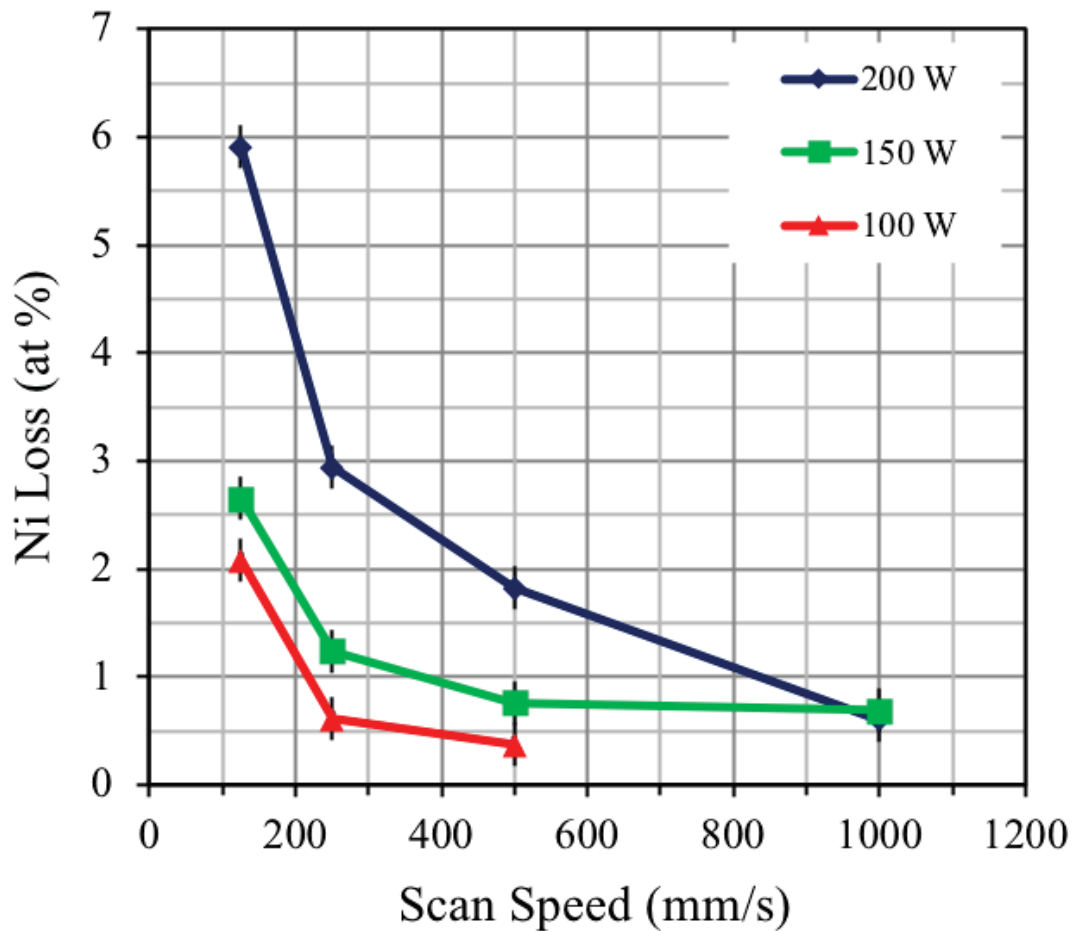


Figure 5.2: The Ni loss after SLM processing as a function of laser power and scan speed. Ni loss was measured using EDX

To study the combined effects of all SLM processing parameters on the alloy's Ni loss and hence its transformation temperature, Ni loss was plotted against the VED of the laser, as shown in figure 5.3 (a) and (b). As expected, in figure 5.3 (a) the Ni evaporation increased with laser VED, due to the greater surface area of the melt pool. The A_F temperature was plotted as some biomedical applications require a fully austenitic structure at body temperature. DSC measurements confirm that the transformation temperature increases with laser energy density and Ni evaporation. This phenomenon was studied and published by *Haberland et al.* (18). To

confirm the increase in transformation temperature was due to the Ni loss, ICP compositional analysis was used. Table 5.1 highlights how Ni loss increases by 2.8 at % when the VED increases by 967 J/mm³.

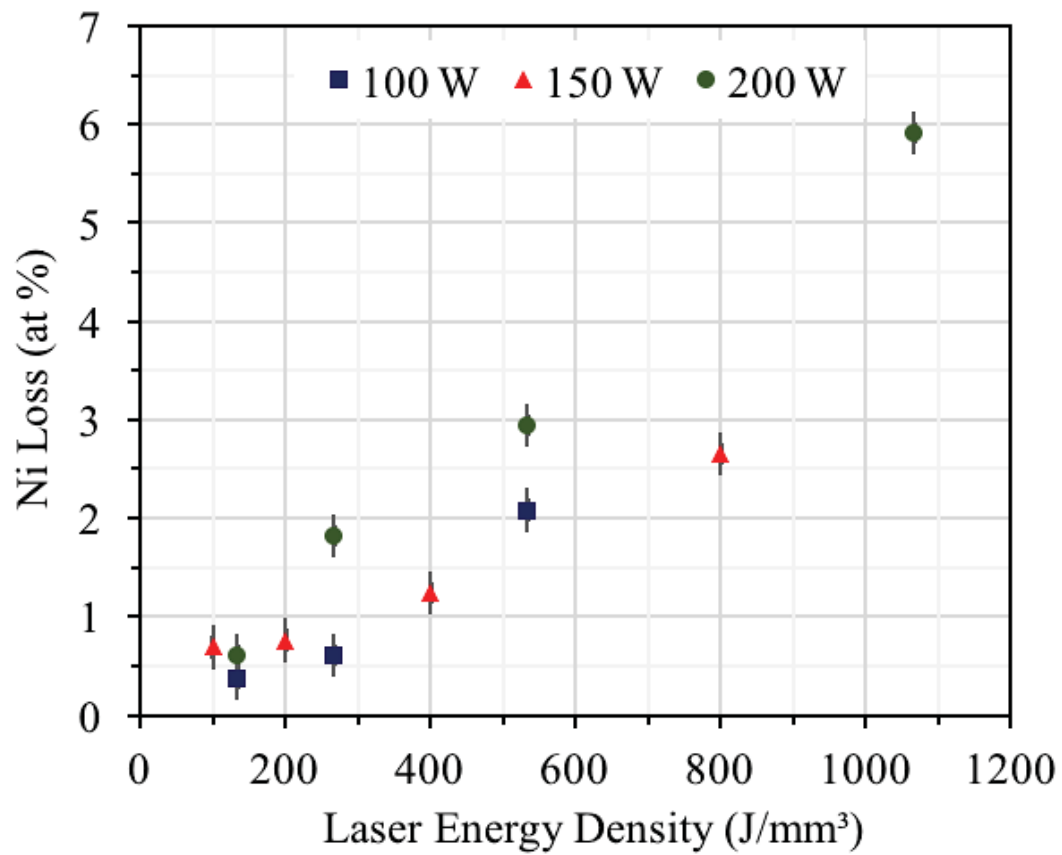


Figure 5.3 (a): The influence of laser VED on Ni evaporation

Table 5.1: ICP results of Ni loss with VED

VED (J/mm ³)	Ni Loss (at %)
100	2.1
1067	4.9

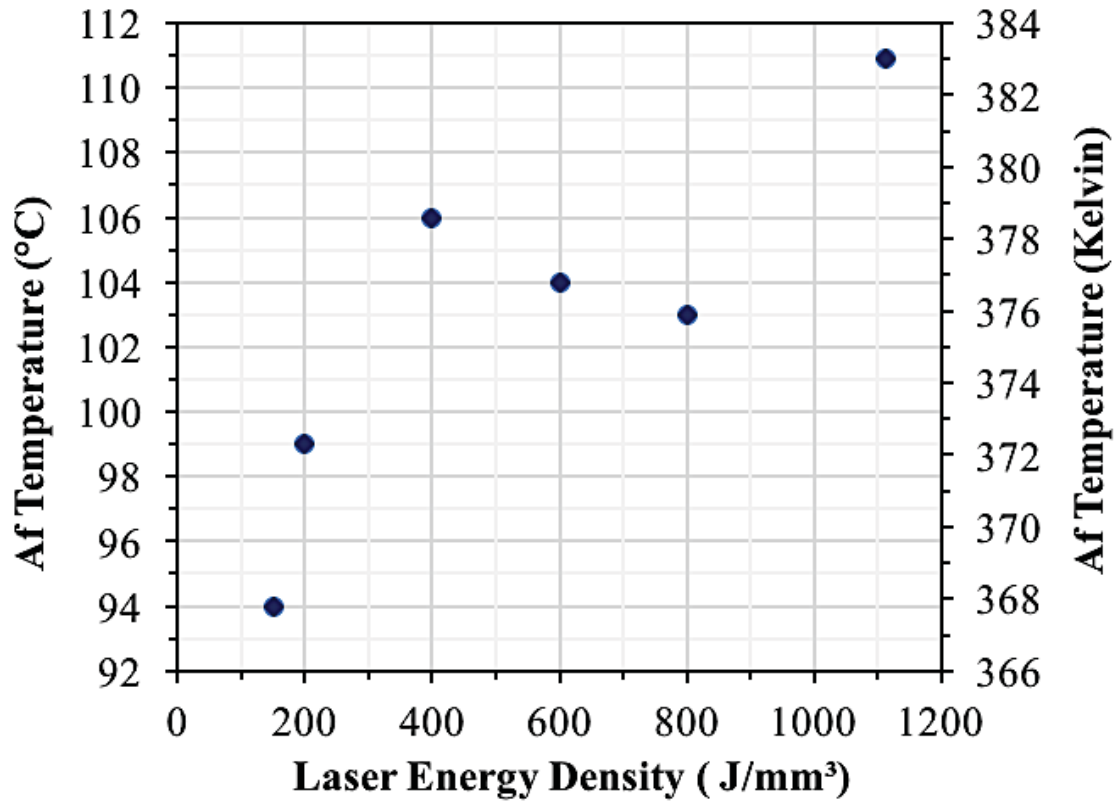


Figure 5.3 (b): The influence of VED on the A_f transformation temperature

During SLM, Ni evaporation can also effect the structural integrity of the alloy. When the heat energy input from the laser is high enough to cause evaporation, the recoil pressure from the vapour drills a depression in the melt pool. As the recoil pressure exceeds the surface tension, molten metal is forced to the sides of the melt pool and upwards out of the melt pool. In turn, forming a long and narrow vapour cavity, also known as a 'keyhole' in the melt pool (5). This cavity is filled with metal vapours and enhances the penetration from the laser making it deeper. As the temperature of the laser is much higher than the temperature at the bottom of the cavity, the pressures from the molten metal flow is much greater in the downwards direction. The flowing molten metal towards the bottom of the melt pool causes the cavity to collapse, resulting in 'keyhole porosity' as the metallic evaporation vapours cannot escape (6).

Figure 5.4. displays the melt pools of an NiTi alloy processed using an VED of 1066.6 J/mm^3 . Compositional analysis has confirmed that Ni evaporation occurs when manufacturing at this

VED. However, the optical image also indicates the presence of elemental evaporation as there is keyhole porosity at the bottom of the melt pool. Furthermore, the shape of the melt pool displays distinct characteristics of 'keyholing', as the depth is much greater than its width (7).

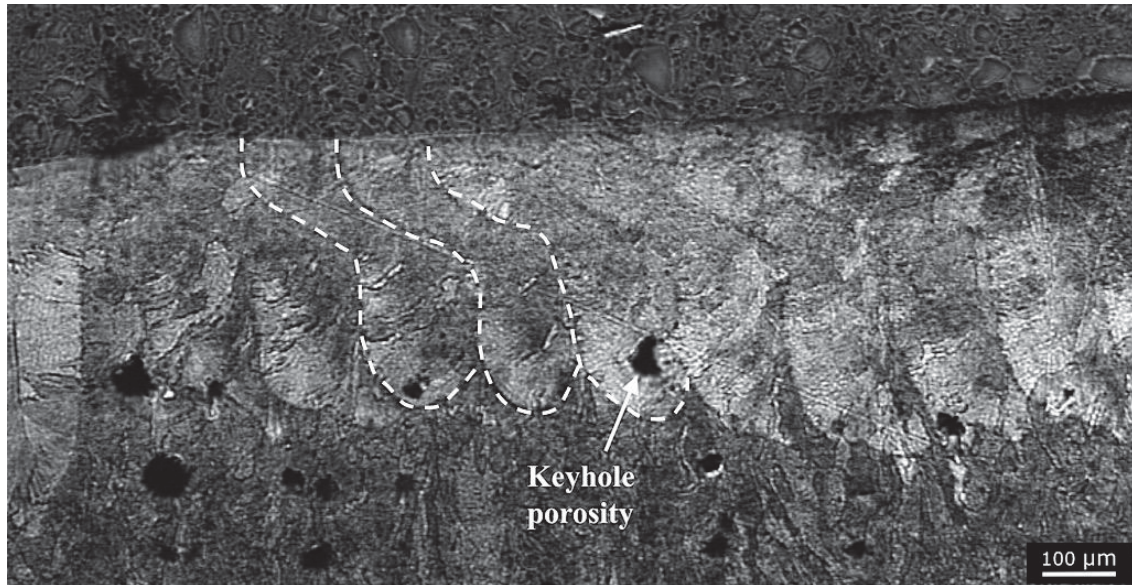


Figure 5.4: A NiTi alloy displaying keyhole porosity (processed at 1066.6 J/mm^3)

Processing NiTi using the optimised processing parameters for high build density, there is an unavoidable increase in transformation temperature due to Ni evaporation. Table 5.2. compares the transformation temperature and Ni content for both the pre-alloyed NiTi powder and the as-fabricated SLM build. The increased transformation temperature after SLM also causes a phase change from the austenitic structure of the powder feed stock. It is clear from the XRD pattern, shown in figure 5.5, that the as-fabricated SLM part is now fully martensitic. Due to the rapid heating and slower cooling rates associated with SLM processing, the secondary phase Ti_2Ni is present in the as-fabricated microstructure.

Table 5.2: A comparison of the Ni content and A_F temperature for the pre-alloyed powder and SLM part fabricated using the optimised processing parameters

Material	A_F temperature ($^{\circ}\text{C}$)	Ni content (at %)
NiTi pre-alloyed powder	28	51.1
SLM fabricated part	86	49.2

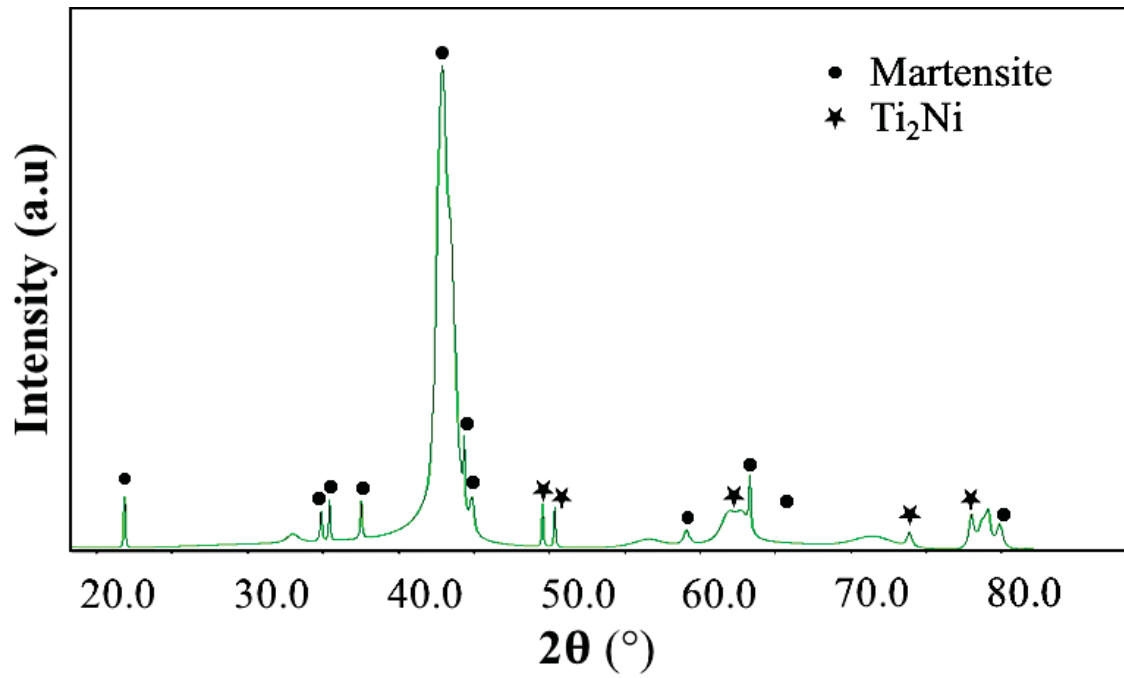


Figure 5.5: The XRD pattern for the as-fabricated NiTi manufactured using the optimised processing parameters

5.2.3. Overcoming Ni Evaporation During SLM

As the pre-alloyed NiTi powder was Ni-rich (51.1 at %), the Ni evaporation that occurred during SLM was advantageous when fabricating a near equiatomic alloy. However, when manufacturing the target composition $\text{Ti}_{50}\text{Ni}_{48}\text{Pd}_2$ (at %), the Ni loss was problematic. This was because using a powder mixture with the desired composition could not ensure a SLM fabricated part with the same composition.

As optimised SLM processing parameters had been established for manufacturing TiNiPd ternary SMAs, it was possible to account for the Ni loss. Firstly, a part was fabricated using the powder mixture with the target composition. The Ni content of the SLM part could then be measured. Thus, by subtracting from the Ni content of the powder mixture, the Ni loss which occurs during SLM could be quantified. Consequently, this amount of elemental Ni powder could be re-added to the initial powder mixture to compensate for the evaporation. From figure 5.6, it is evident that the extra Ni successfully alloyed into the matrix to produce a homogenous

microstructure. Additionally, table 5.3. shows the SLM builds compositions before and after adding the Ni powder to compensate.

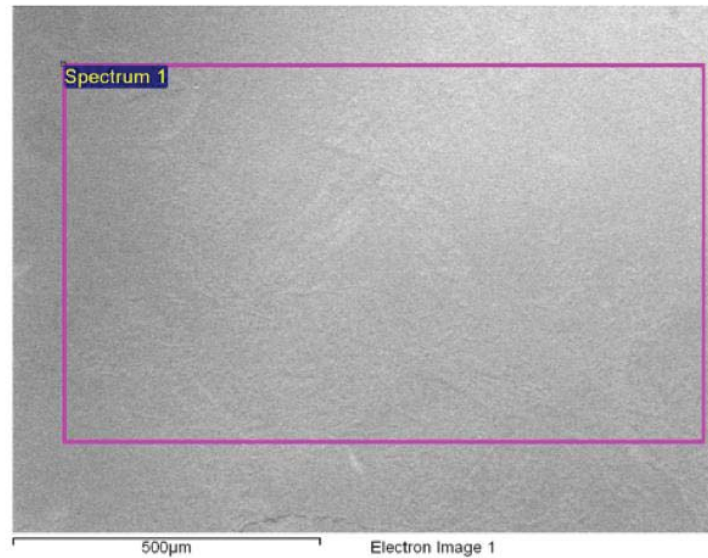


Figure 5.6: Bse image of the $Ti_{50}Ni_{48}Pd_2$ (at %) SLM alloy containing extra Ni to account for the Ni evaporation and achieve the target composition

Table 5.3: A table comparing the composition before and after adding extra Ni into the powder mixture used during SLM. $Ti_{50}Ni_{48}Pd_2$ (at %) being the target composition

Element	Composition before addressing Ni evaporation (at %)	Composition after addressing Ni evaporation (at %)
Ti	52.39	50.33
Ni	44.06	47.92
Pd	3.55	1.75

5.3. The Influence of Post Processing Heat Treatment

5.3.1. The Effects of Homogenising Solution Heat Treatment

It is accepted that SLM fabricated parts will require a form of solution heat treatment to homogenise the microstructure. Not only will chemical inhomogeneities alter the transformation temperature, they will extend the temperature range over which the transformations occur.

Figure 5.6. (a), (b) and (c), display the transformation curves for the three alloys: $\text{Ni}_{49.2}\text{Ti}_{50.8}$, $\text{Ti}_{50}\text{Ni}_{48}\text{Pd}_2$ and $\text{Ti}_{50}\text{Ni}_{43}\text{Pd}_7$ (at %). Unlike in Ni-rich alloys reported by *Saedi et al.* (10), the figures suggest that solution heat treatment causes an increase in transformation temperature for Ti-rich alloys. Due to the extremely high temperatures associated with laser processing, Ti-rich phases will form in the microstructure. The formation of these precipitates cause a change in the matrix composition, a shift to Ni-richer compositions and consequently a decrease in the transformation temperature (8). Thus, when solution heat treating at 950°C for 5.5 hours, the Ti-rich inhomogeneities dissolve back into the matrix. As the solution heat treatment is followed by water quenching, a supersaturated solid solution is formed due to the rapid cooling (9). This increase in Ti content, increases the transformation temperature. The dissolution of Ti-rich secondary phases increased the transformation temperature by 17 °C for the binary NiTi alloy. Additionally, 7°C and 1°C for the $\text{Ti}_{50}\text{Ni}_{48}\text{Pd}_2$ and $\text{Ti}_{50}\text{Ni}_{43}\text{Pd}_7$ (at %) alloys, respectively.

Not only does solution heat treatment cause a change in the phase temperature, it also modifies the shape of the transformation peak curves. The transformation peaks appear broader for all three alloys whilst in the as-fabricated state. Additionally, shoulders appear on all the martensitic transformation curves. After solutionising the peaks sharpen, indicating the solution heat treatment has been successful at dissolving the microstructural inhomogeneities and homogenising the microstructure (10).

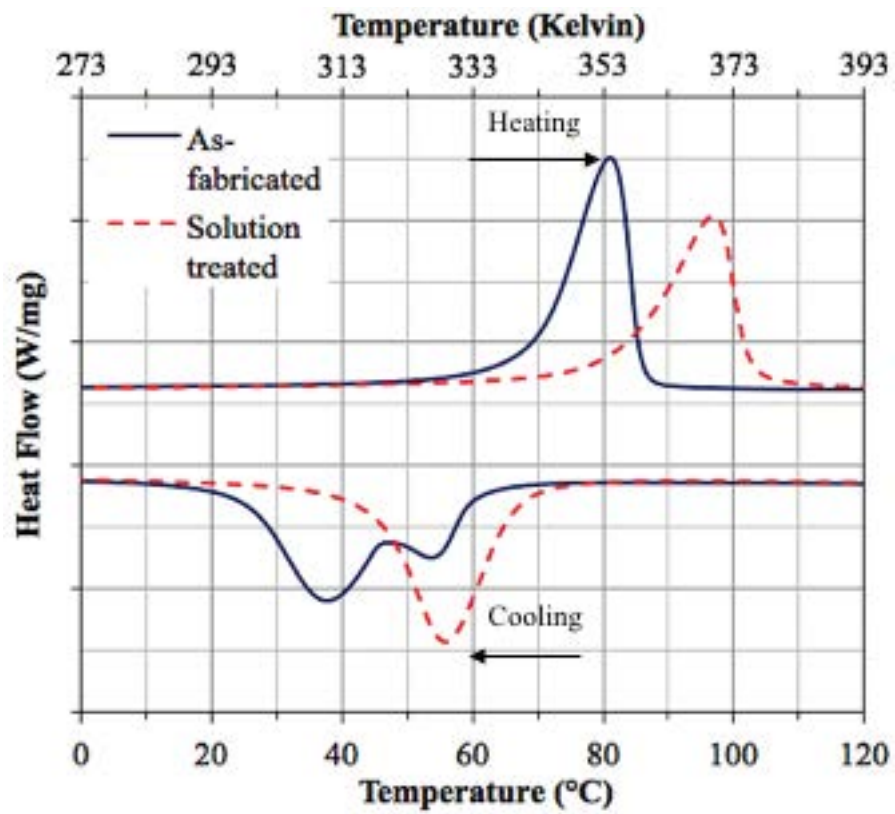


Figure 5.6 (a): The DSC curves for SLM as-fabricated and solution heat treated NiTi

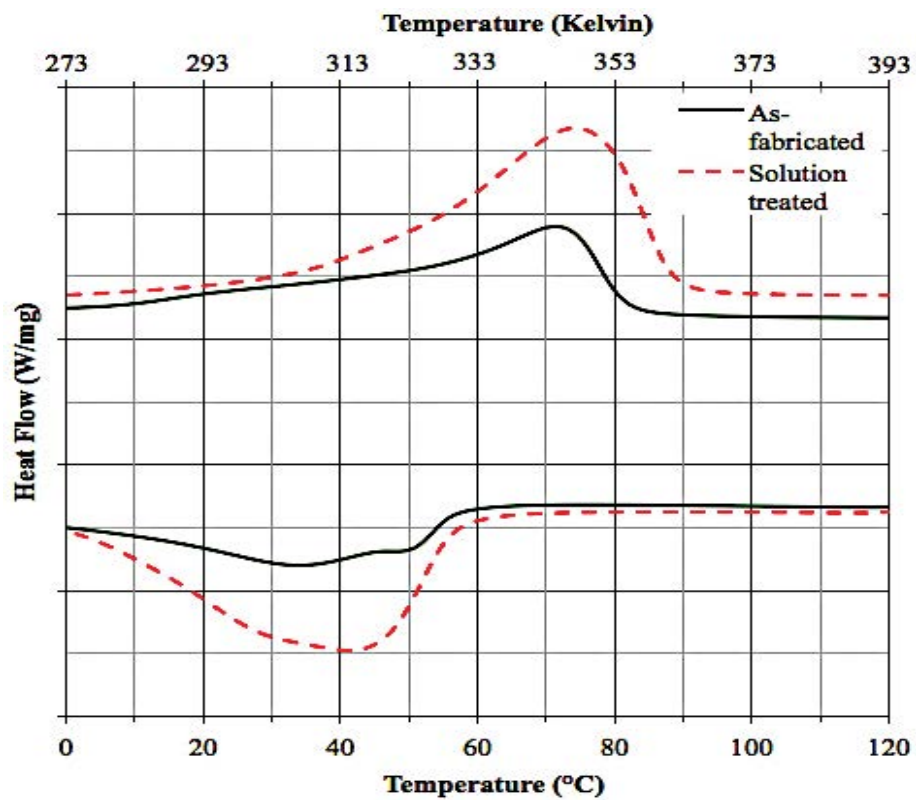


Figure 5.6 (b): The DSC curves for SLM as-fabricated and solution heat treated Ti₅₀Ni₄₈Pd₂

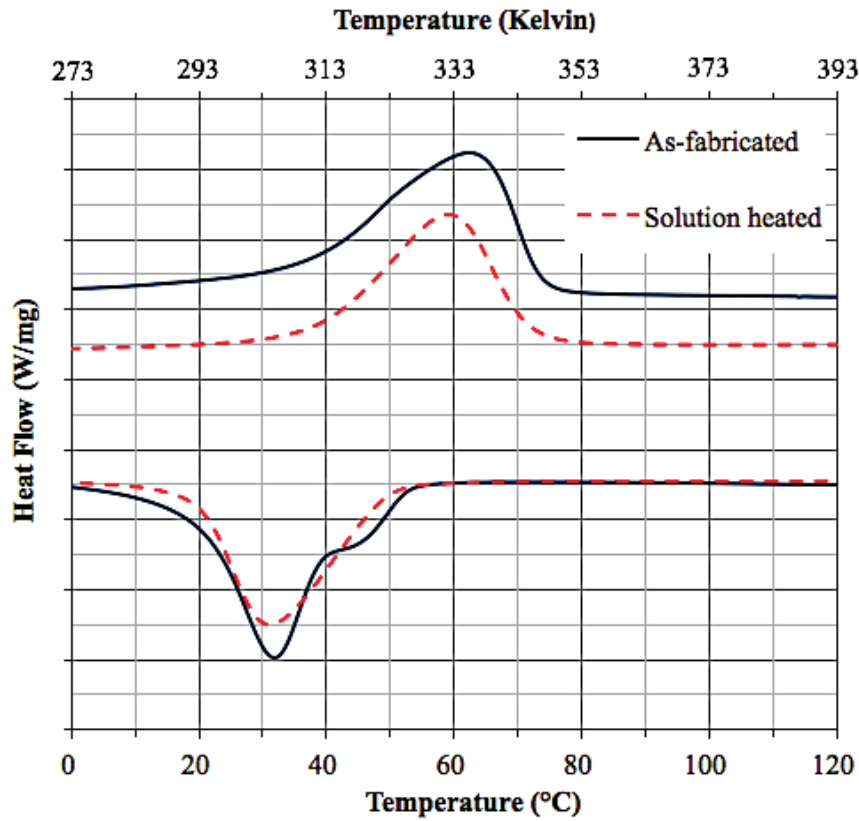


Figure 5.6 (c): The DSC curves for SLM as-fabricated and solution heat treated $Ti_{50}Ni_{43}Pd_7$

5.3.2. Compositional and Microstructural Analysis of Ti-rich Secondary Phases present in SLM Binary NiTi and Ternary TiNiPd

As mentioned by *Meier et al.* (19), NiTi has a narrow processing window. Thus, due to the extremely high temperatures associated with SLM, the as-fabricated part will inevitably contain secondary phases. Ti_2Ni is a secondary phase intermetallic present in both equiatomic and Ti-rich NiTi alloys. These coarse and globular intermetallics form during a peritectic reaction at $948^{\circ}C$ and precipitate along inter-dendritic boundaries. Figure 5.7 (a) displays the microstructure of an as-fabricated SLM NiTi alloy, processed using a laser volumetric energy density (VED) of $1067 J/mm^3$. White arrows on the SEM image mark the Ti_2Ni secondary phase and the NiTi matrix.

The composition of the Ti_2Ni intermetallic phase can be seen in table 5.4. As this phase is Ti-rich, its precipitation will decrease the alloy's transformation temperature as a greater amount

of Ti is being depleted from the NiTi matrix. Ti_2Ni can further decrease the transformation temperature of the alloy as it is stabilised by the pick-up of oxygen. Above 900°C , the NiTi matrix has no solubility for oxygen. However, Ti_2Ni has a high solubility for oxygen and the Ti ties up the oxygen disproportionately to form the stable $\text{Ti}_4\text{Ni}_2\text{O}$ intermetallic. However, since the SLM process is performed in argon atmosphere, $\text{Ti}_4\text{Ni}_2\text{O}$ intermetallic phases were not observed in any of the builds.

Table 5.4: The chemical composition of the secondary phase Ti_2Ni

Secondary Phase	Ti content (at %)	Ni content (at %)
Ti_2Ni	67.52	32.48

During SLM, the cooling rate of solidification strongly influences the volume fraction of Ti_2Ni present within the part. Faster cooling rates favour larger volumes of the Ti_2Ni phase. Whereas, less Ti_2Ni precipitates when the cooling rates are slower. This is because slower cooling rates promote the formation of a homogeneous NiTi single phase. Twenty SEM micrographs were taken across the XZ plane of an as-fabricated NiTi part, processed using a laser VED of 1067 J/mm^3 . ImageJ software was used to quantify the amount of Ti_2Ni within each micrograph by giving an overall area fraction percentage. From figure 5.8. it is clear the area fraction percentage of Ti_2Ni does not stay consistent through-out the build. During SLM, as a thin NiTi build plate was glued onto a substrate, the glue reduced the conduction of heat away from the build plate into the substrate. As a consequence, the NiTi build plate experienced greater heating during laser processing and the bottom layers are associated with reduced thermal conduction. Thus, the base layers of the build are exposed to higher temperatures for longer with slower cooling rates. Unlike the bottom layers of the build, the top surfaces can transfer excess heat energy through radiation. As the heat energy transfers to the atmosphere during

SLM, the cooling rate increases and as expected a larger area fraction percentage of Ti_2Ni precipitates at the top layers of the build.

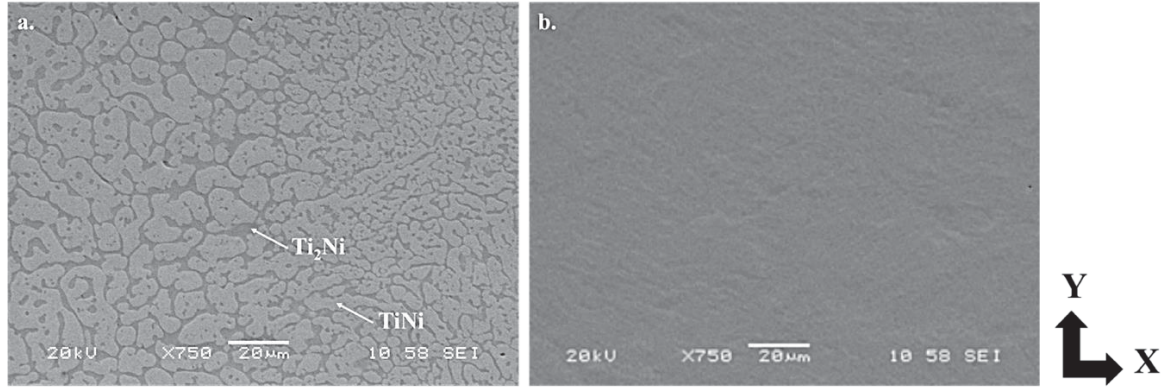


Figure 5.7 (a): The microstructure of an as-fabricated NiTi build processed at 1067 J/mm^3 (b): The microstructure of an as-fabricated NiTi build processed at 100 J/mm^3

In addition to the cooling rate, the laser VED (J/mm^3) can also influence the formation of Ti_2Ni . Larger volume fractions of Ti_2Ni were evident in samples processed at higher VED. However, the secondary phase was not present in samples processed using low VED. This behaviour can be ascribed to the differences in thermal gradients. A low VED reduces the energy input from the laser. Thus, correlating to a smaller thermal gradient and a slower cooling rate which encourages the single NiTi phase. The differences in the as-fabricated microstructures can be seen in figure 5.7 (a) and (b). Figure 5.7 (a) displays an as-fabricated alloy processed at 1067 J/mm^3 . The as-fabricated alloy in figure 5.7 (b) was processed using a laser VED of 100 J/mm^3 .

Ti-rich secondary phases can also form in ternary TiNiPd alloys during SLM processing. When processed at higher laser VEDs, the intermetallic $\text{Ti}_2\text{Ni(Pd)}$ phase was present in both the $\text{Ti}_{50}\text{Ni}_{48}\text{Pd}_2$ and $\text{Ti}_{50}\text{Ni}_{43}\text{Pd}_7$ (at %) SLM alloys. The elemental EDX map (figure 5.10) and table 5.5 show that the composition of $\text{Ti}_2\text{Ni(Pd)}$ shares similarities with the Ti_2Ni phase. They are both Ti-rich with a Ti:Ni ratio of 2:1. According to literature the phase is isostructural to Ti_2Ni and it also stabilised by oxygen.

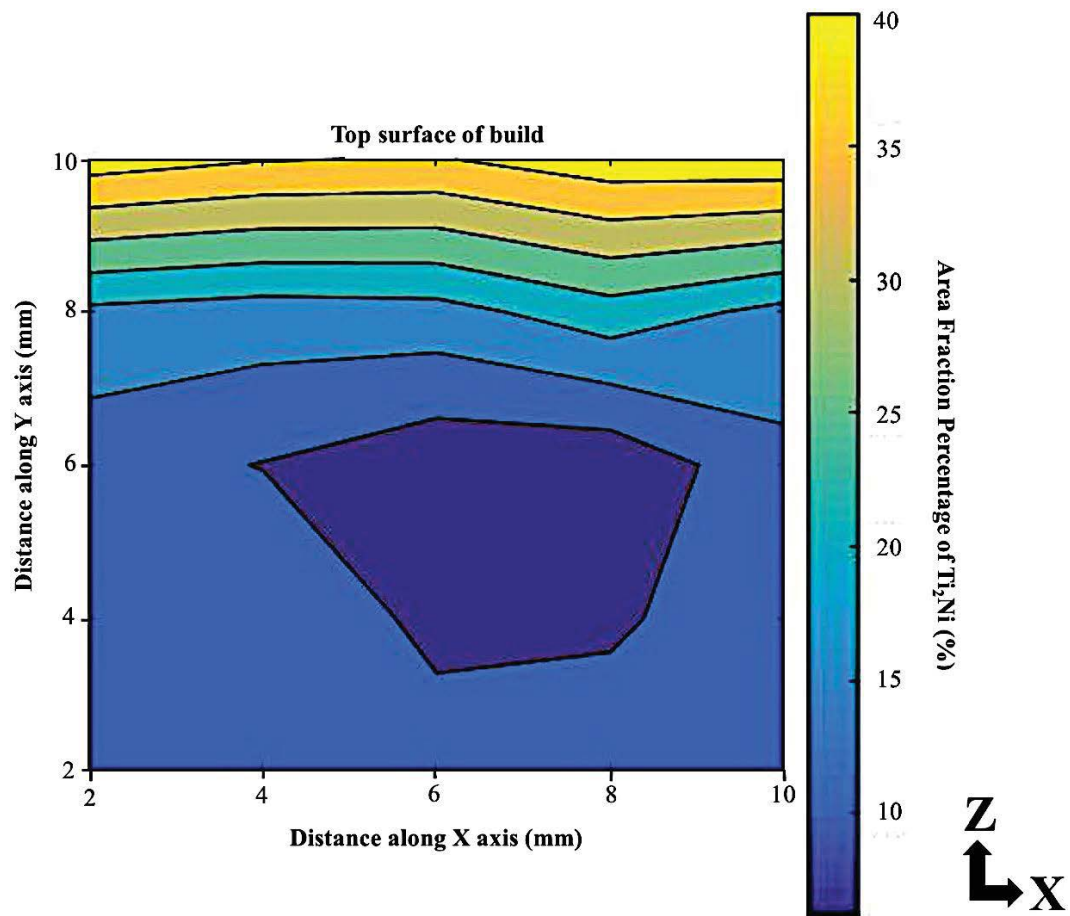


Figure 5.8: A phase contour plot showing the area fraction percentage of Ti_2Ni precipitation along the XZ plane of an as-fabricated NiTi cubic SLM part

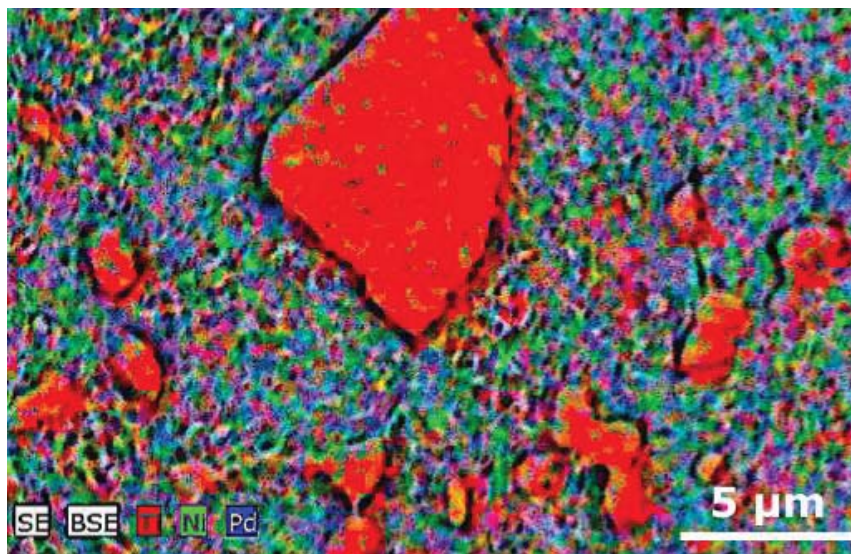
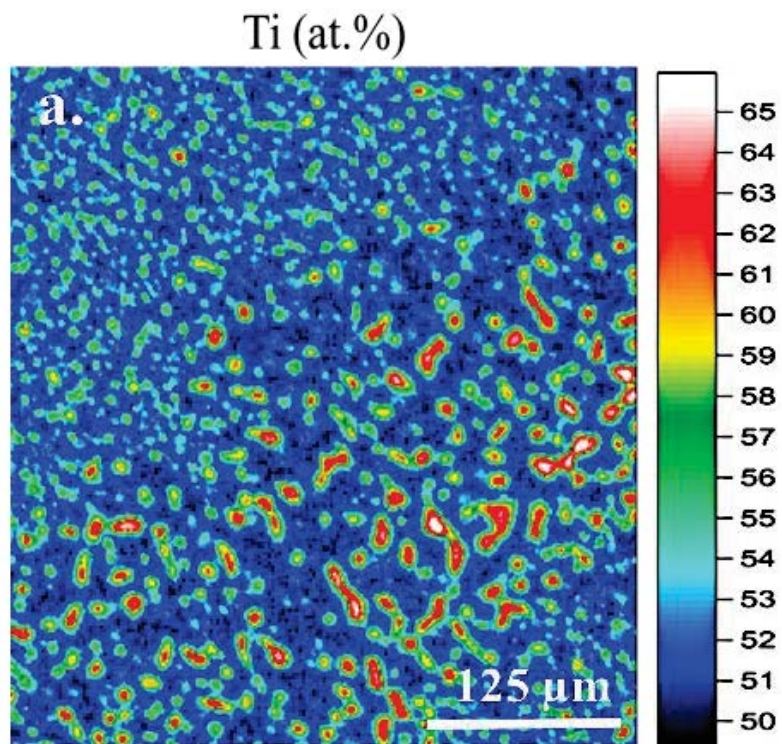


Figure 5.10: EDX mapping of the $Ti_2Ni(Pd)$ precipitation within a TiNiPd matrix taken along the XY plane

EPMA analysis was used to investigate the morphology and elemental composition of the $\text{Ti}_2\text{Ni(Pd)}$ phase. The elemental distribution map (figure 5.11) matches well to the EDX results shown in table 5.5. The intermetallic is Ti-rich, with a Ti:Ni:Pd ratio of 2:1:1. Furthermore, the intermetallic shares the same coarse and globular morphology as the Ti_2Ni secondary phase.

Table 5.5: The chemical composition of the secondary phase $\text{Ti}_2\text{Ni(Pd)}$

Secondary Phase	Ti content (at %)	Ni content (at %)	Pd content (at %)
$\text{Ti}_2\text{Ni(Pd)}$	70	27	3



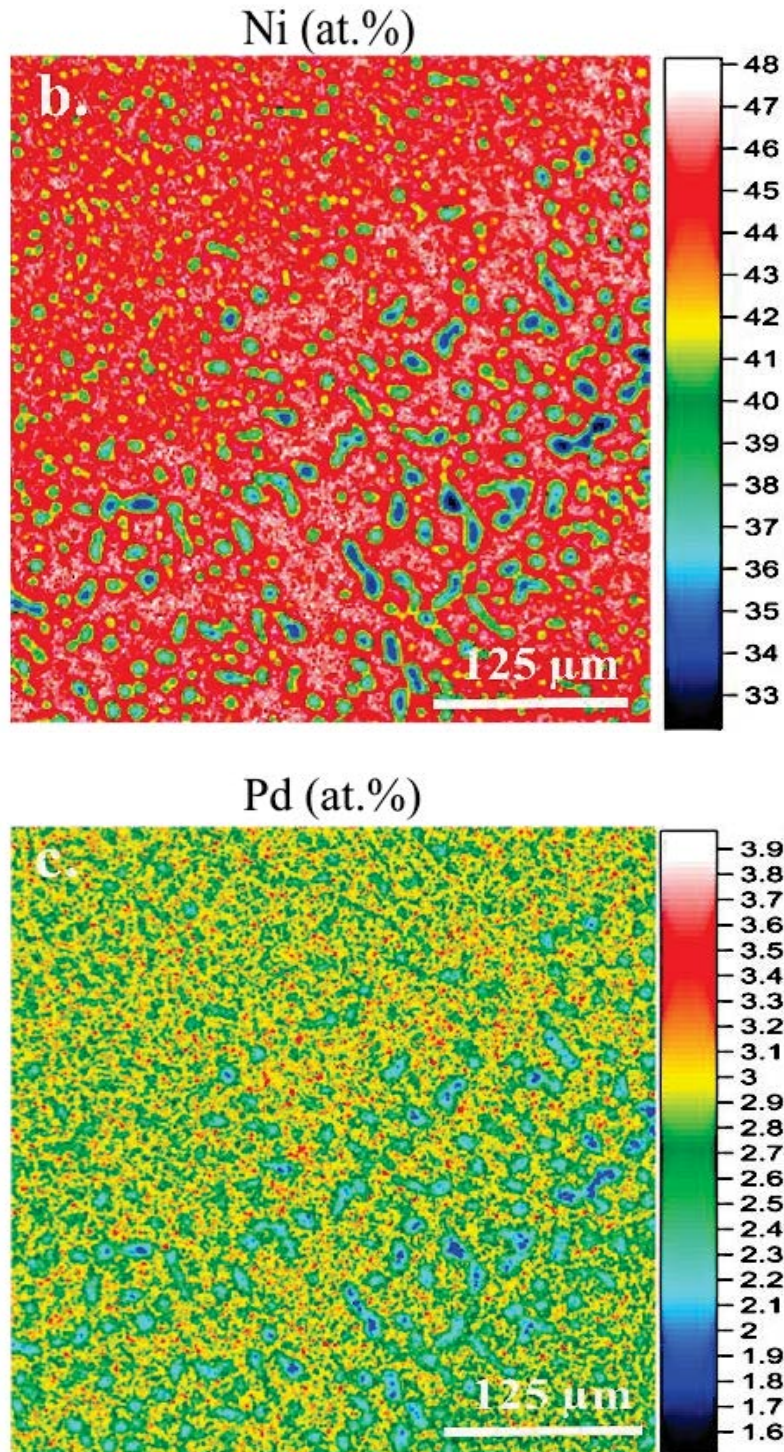


Figure 5.11: EPMA elemental distribution maps for the $\text{Ti}_2\text{Ni(Pd)}$ intermetallic taken along the XY plane

Figure 5.12. displays a phase distribution map for a $\text{Ti}_{50}\text{Ni}_{43}\text{Pd}_7$ (at %) SLM alloy. As predicted from the alloy's DSC curves shown in figure 5.6 (c), the grains within the alloy are multi-phase

and contain both martensite and austenite at room temperature. Furthermore, the $\text{Ti}_2\text{Ni}(\text{Pd})$ phase appears to precipitate at the grain boundaries along the build direction.

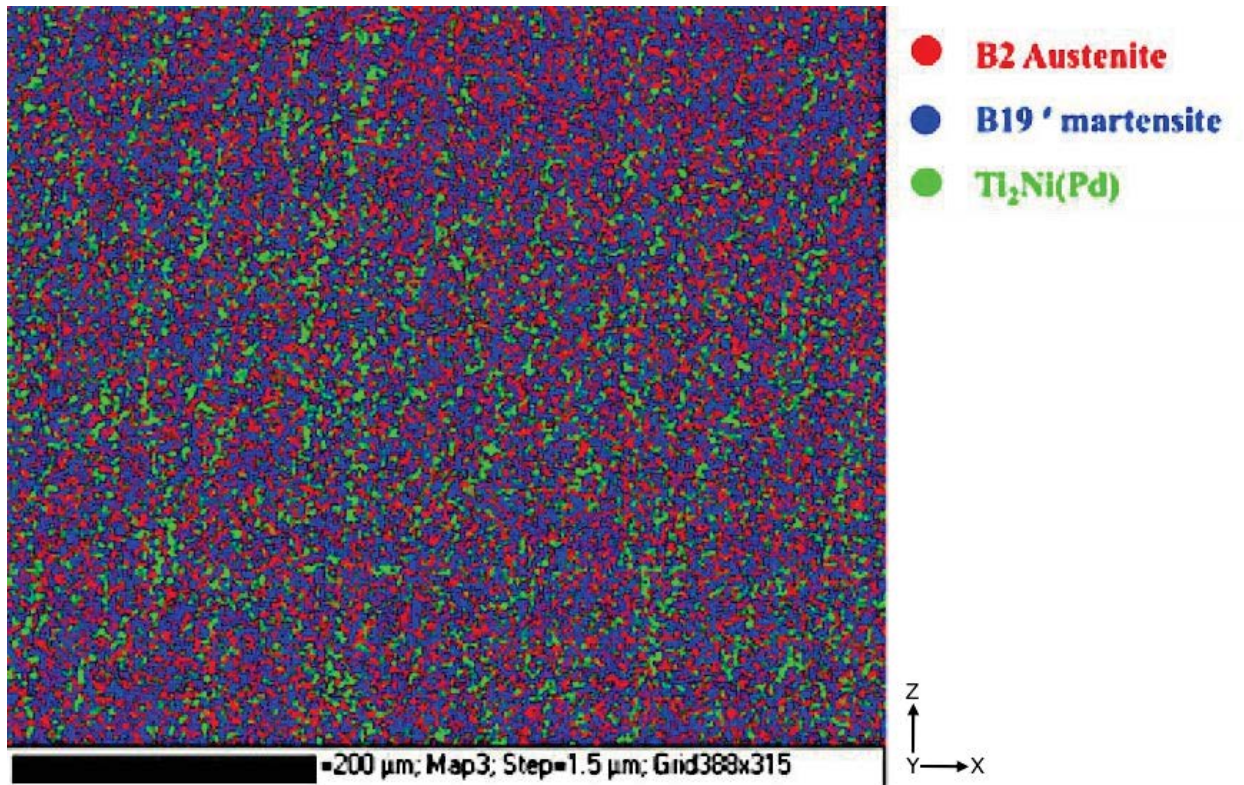


Figure 5.12: A phase distribution map for solution heat treated $\text{Ti}_{50}\text{Ni}_{43}\text{Pd}_7$ (at %)

5.3.3. The Influence of Post Processing Heat Treatment on the Transformation Temperature of Ternary TiNiPd (at %):

The precipitation of the $\text{Ti}_2\text{Ni}(\text{Pd})$ phase will cause a shift in chemical composition and decrease the alloy's transformation temperature. As some biomedical applications require a fully austenitic SMA at body temperature, the growth of the $\text{Ti}_2\text{Ni}(\text{Pd})$ phase could be beneficial for TiNiPd SMAs. Heat treatment is one of the most effective ways to modify precipitate characteristics. Thus, it could potentially be used to tailor the alloy's transformation temperature.

To investigate the effects of heat treatment on the transformation temperature of Pd modified NiTi alloys, samples were solution heat-treated and subsequently aged at 350 or 450 °C for various periods of time. Studies were carried out using the ternary $\text{Ti}_{50}\text{Ni}_{43}\text{Pd}_7$ (at %) alloy, as this composition is most likely to be used in the biomedical industry due to its improved radiopacity

Figure 5.13. depicts the DSC responses for the SLM $\text{Ti}_{50}\text{Ni}_{43}\text{Pd}_7$ (at %) alloy. Apart from the as-fabricated, all samples were solution heat treated at 950°C for 5.5 hours with instant water quenching. Following this, samples were aged at 350°C for time scales varying from 1.5 to 18 hours. The immediate water quenching that followed the solution heat treatment resulted in a single phase, supersaturated TiNiPd solid solution microstructure (9). Due to the dissolution of chemical inhomogeneities throughout the microstructure, there is a 1°C increase in transformation temperature as the matrix becomes Ti-richer.

Visible in figure 5.13. the transformation temperature decreases with aging time. When aging at 350°C for 1.5 hours, $\text{Ti}_2\text{Ni(Pd)}$ finely disperses within the matrix. As the Ti-rich solid solution formed during the solution heat treatment is not stable, the atoms will diffuse short distances to nucleation sites and precipitate as $\text{Ti}_2\text{Ni(Pd)}$ intermetallics. As shown in figure 5.14 (a, b & c), the size of these precipitates grow with aging time as more atoms diffuse.

The A_F temperature for the as-fabricated alloy was 74 °C. However, this temperature can be reduced by 10 °C when aging at 350 °C for 3 hours. As expected, the transformation temperature of the alloy alters as the $\text{Ti}_2\text{Ni(Pd)}$ intermetallics grow. Larger $\text{Ti}_2\text{Ni(Pd)}$ precipitates, deplete more Ti from the matrix and as a result the transformation temperature decreases. Table 5.6. displays the relationship between the aging time, precipitate size and

transformation temperature. From the table, it is evident that a 3.8 μm difference in the average precipitate size can alter the transformation temperature by as much as 5 $^{\circ}\text{C}$.

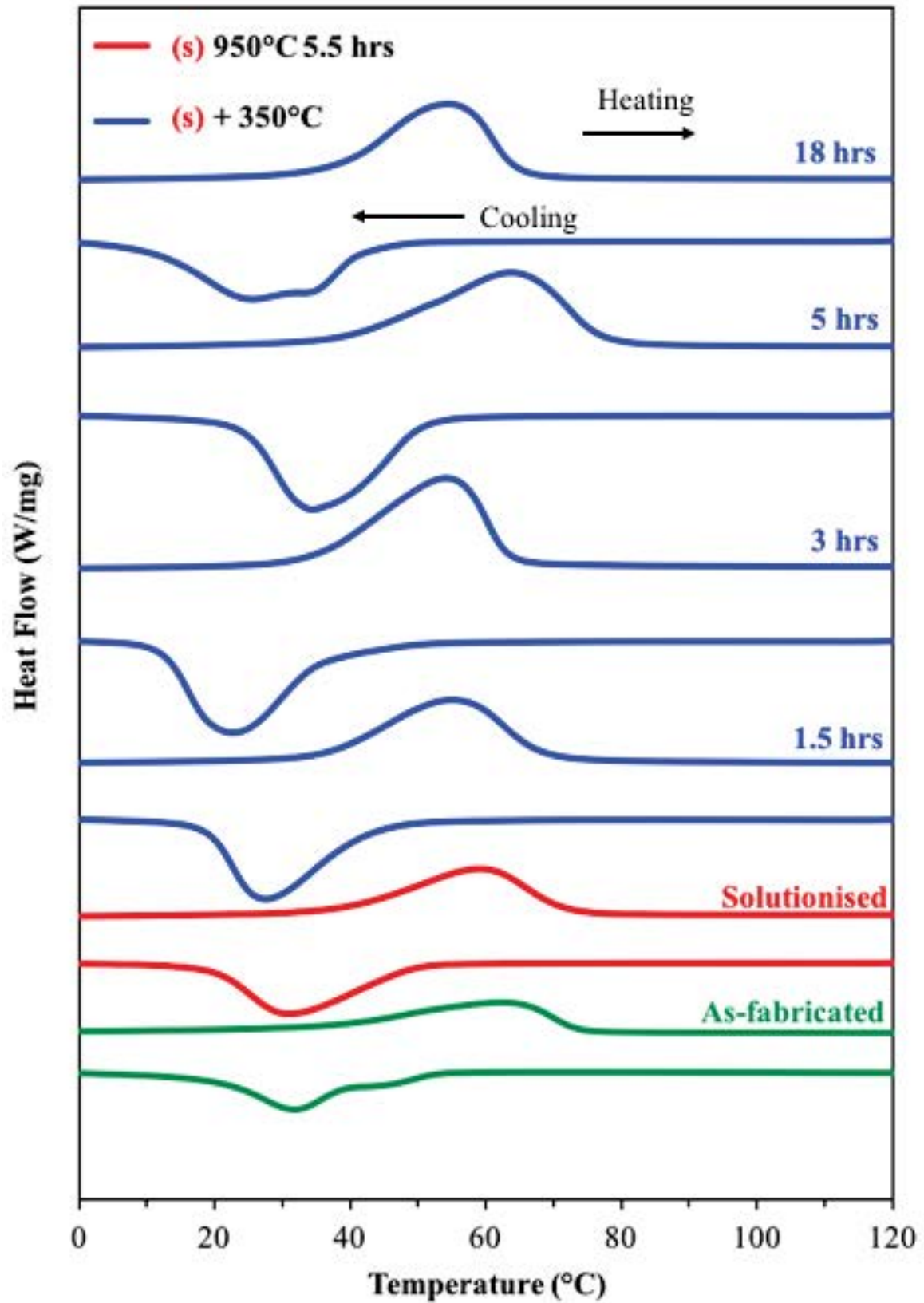
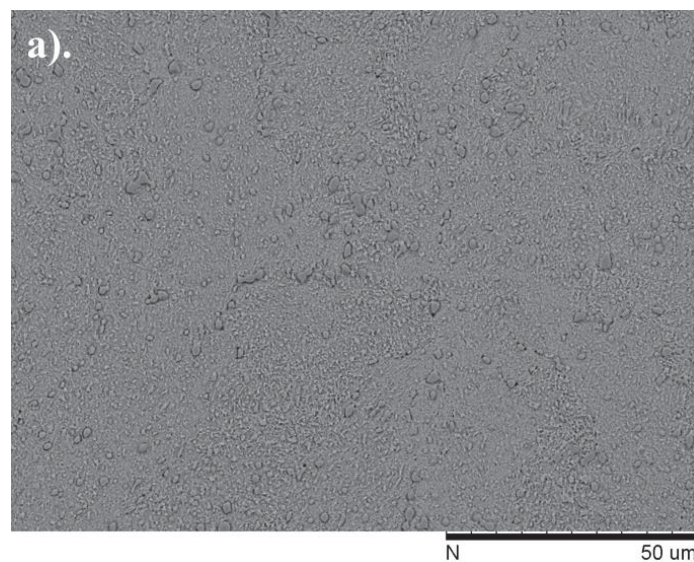


Figure 5.13: The DSC responses of the heat treated $\text{Ti}_{50}\text{Ni}_{43}\text{Pd}_7$ (at %)

A shoulder appears on the martensitic transformation peak for the sample aged at 350°C for 18 hours. As the $\text{Ti}_2\text{Ni(Pd)}$ intermetallic phase grows within the matrix, their corresponding stress fields increase due to the elastic moduli mismatches between the $\text{Ti}_2\text{Ni(Pd)}/\text{TiNiPd}$ matrix interface (11). Stress fields surrounding the intermetallic can cause local transformations which appear as a shoulder on the martensitic transformation peak (12). As the peak shoulder is only visible for the sample aged for 18 hours, it is possible that the stress fields are related to the size of the intermetallic. As the intermetallic increases in size, the elastic moduli mismatch for the $\text{Ti}_2\text{Ni(Pd)}/\text{TiNiPd}$ matrix interface reaches a critical limit and produces stress fields strong enough to assist local transformations.



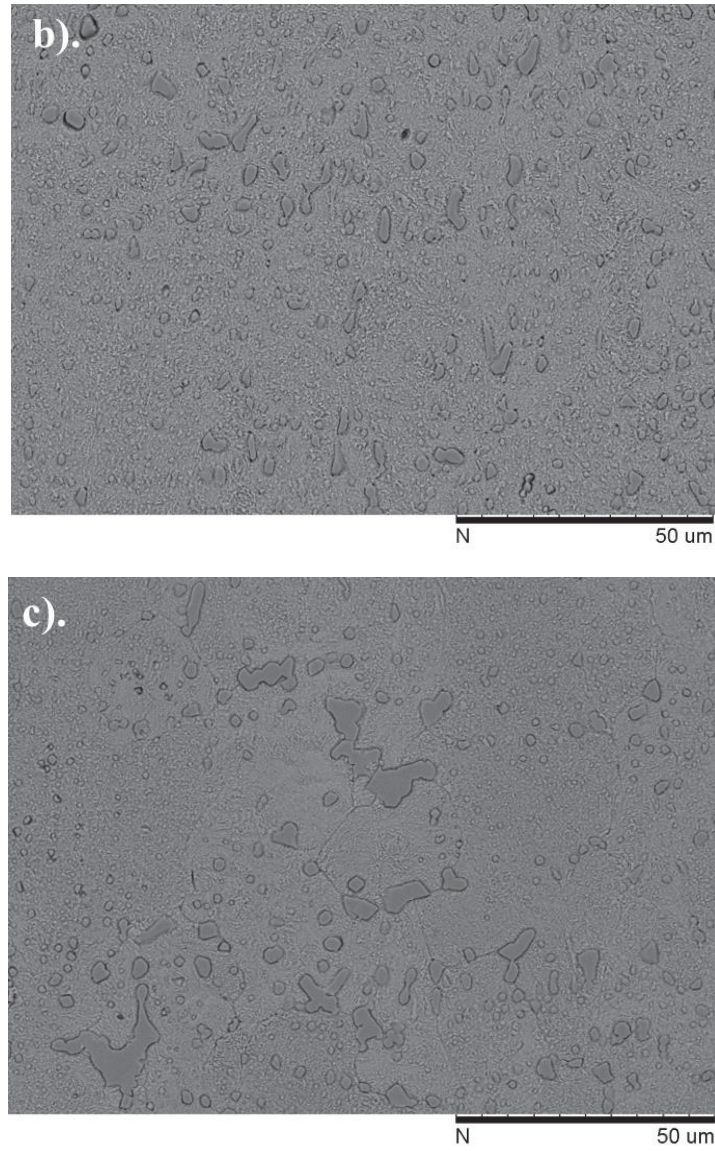


Figure 5.16: $\text{Ti}_2\text{Ni(Pd)}$ precipitation in an alloy aged at (a) 350 °C for 1.5 hours (b) 350 °C for 3 hours (c) 350 °C for 18 hours

Table 5.6: A table showing the effects of aging time on the A_F temperature and the average precipitate size

Aging Time (hrs)	A_F Transformation Temperature (°C)	Average Precipitate Size (μm)
1.5	69	2.82
3	64	6.80
18	64	22.32

Figure 5.15. compares the transformation temperature of samples aged at 350 °C and 450 °C. The DSC curves clearly show the transformation temperature increases with aging temperature.

Visible in figure 5.16, the volume fraction of $\text{Ti}_2\text{Ni(Pd)}$ precipitation decreases as the aging temperature increases from 350°C to 450°C for an aging time of 1.5 hours. Consequently, less Ti is depleted from the matrix and the transformation temperature increases. The average micro-hardness of the XY plane for both aging temperatures were measured. The alloy aged at 350°C for 1.5 hours had an average Vickers hardness number of $303 \pm 9\text{HV}$. The alloy aged for 1.5 hours at 450°C had a lower Vickers hardness number of $260 \pm 9\text{HV}$. This reduction in hardness relates to the reduction in the volume fraction of the brittle $\text{Ti}_2\text{Ni(Pd)}$ phase.

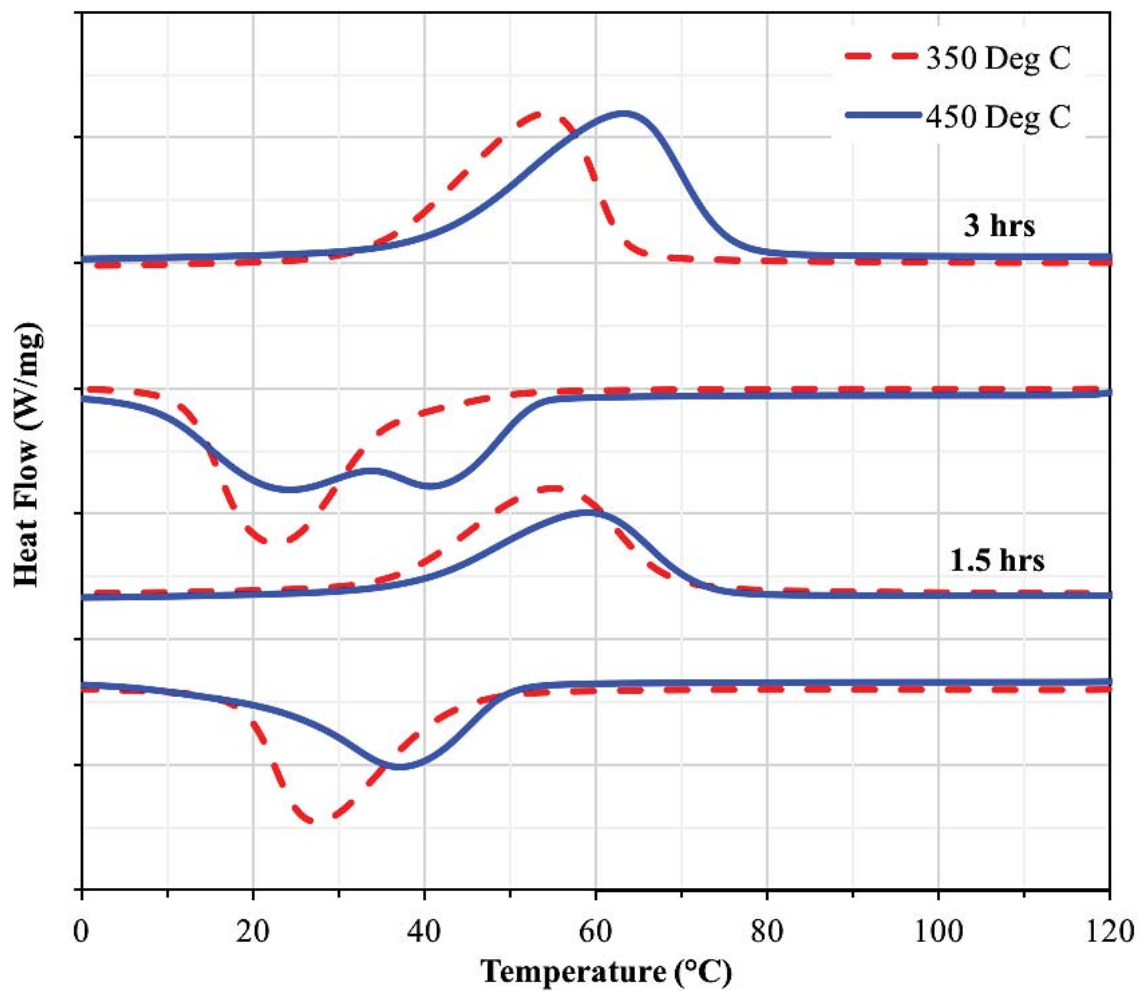


Figure 5.15: The DSC curves for samples aged at 350°C and 450°C

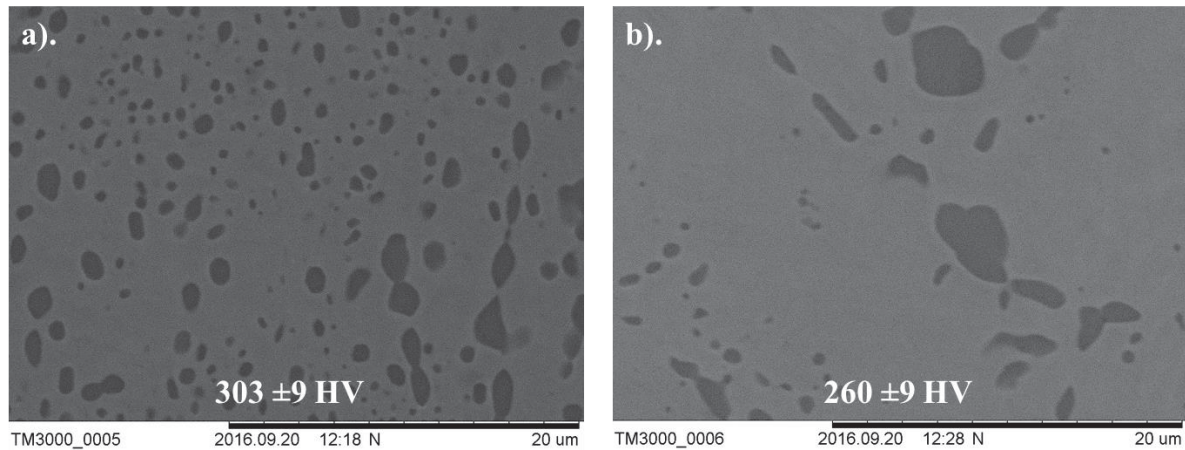


Figure 5.16: The microstructure and corresponding hardness for samples (a) aged at 350 °C for 1.5 hours (b) aged at 450 °C for 1.5 hours

5.4.1. The Influence of Pd on the Transformation Temperature of Binary SLM NiTi

Figure 5.17 displays the A_F temperature of all three alloys after receiving the homogenising solution heat treatment. Alloying binary NiTi with 2 and 7 at % Pd decreases the transformation temperature of the SMA. When alloying with up to 7 at % Pd, the concentration of valence electrons increases, as does the valence electron density (13). This increase in electrons strengthens the bonds within the alloy and hardens the elastic constants of the B2 phase (14)(15). Consequently, the transformation temperatures drop because an increase in cooling is required to initiate the martensitic transformation.

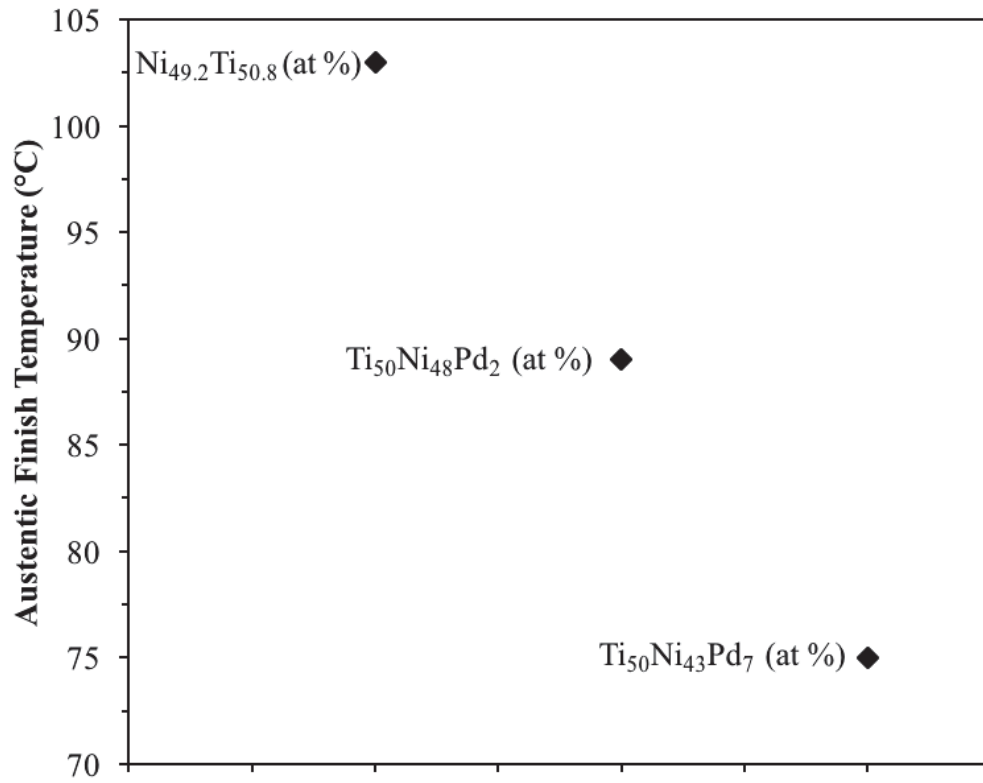


Figure 5.17: The A_F temperatures for binary and Pd modified NiTi

Comparing the temperatures of the SLM fabricated alloys to conventionally produced TiNiPd alloys (figure 5.18) implies that SLM can manufacture alloys with comparable phase transformation behaviours. A conventionally produced TiNiPd alloy with 10 at % Pd has a M_s temperature of approximately 37 °C . Whereas, the SLM alloy with 7 at % Pd has a M_s temperature of 50 °C. The M_s temperatures for the three alloys after solution heat treating can be seen in table 5.8.

Table 5.8: The M_s temperature of solution heat treated binary NiTi and ternary TiNiPd alloys

Alloy Composition (at %)	M _s Temperature	
	M _s (°C)	M _s (K)
NiTi	68	341
Ti ₅₀ Ni ₄₈ Pd ₂	57	330
Ti ₅₀ Ni ₄₃ Pd ₇	50	323

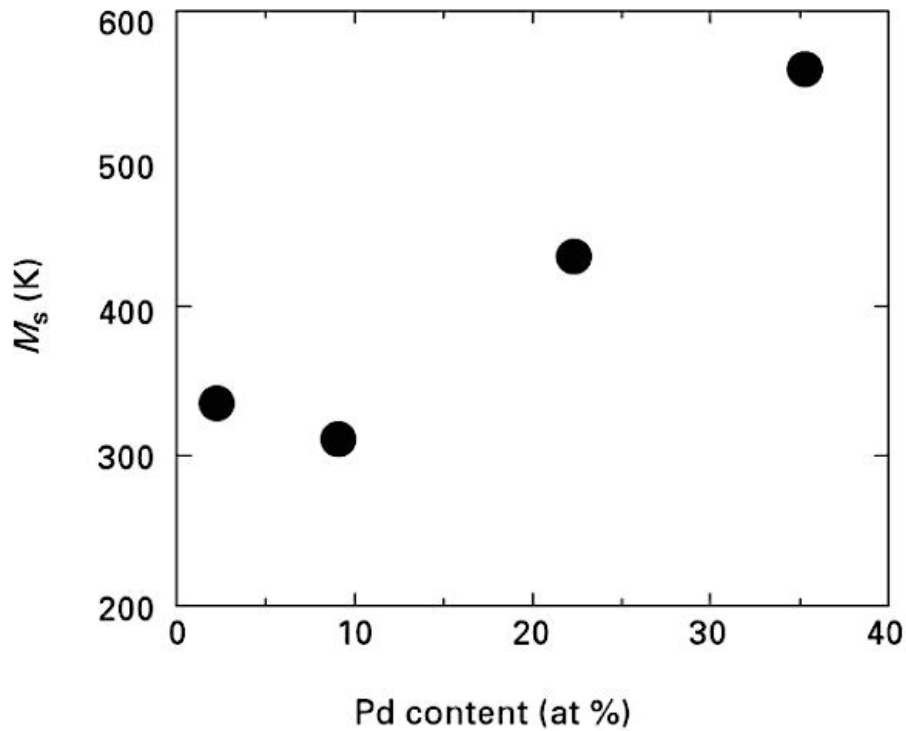


Figure 5.18: Literature data published on the M_s temperatures of TiNiPd alloys (16)

Although the Pd has been shown to reduce the transformation temperature of binary NiTi. As the alloys do not have an A_F temperature below body temperature, they would not be suitable for some biomedical applications. *Ren et al.* showed that many elements could substitute Ni and reduce the transformation temperature of binary NiTi (15). Therefore, to further reduce the transformation temperature of ternary TiNiPd, a fourth element was added.

1 at % Ni in the ternary $Ti_{50}Ni_{43}Pd_7$ (at %) alloy was substituted with chromium (Cr). During SLM processing, as Cr had the highest melting point of $1907^{\circ}C$, the optimised processing parameters for the TiNiPd alloy had to be modified to ensure the laser energy input was enough to melt the Cr powder particles. Therefore, to successfully diffuse the Cr into the TiNiPd matrix, the scan speed was retained at 120 mm/s but the laser power increased by 20 W. The new processing parameters to SLM quaternary TiNiPdCr can be seen in table 5.9.

Table 5.9: The SLM processing parameters for manufacturing TiNiPdCr

Laser Power (W)	Scan Speed (mm/s)	Layer Thickness (μm)	Scan Spacing (μm)	Laser VED (J/mm^3)
80	120	20	56	595

Figure 5.19 (a) shows the A_F temperatures of the solution heat treated alloys. The addition of Cr reduced the A_F temperature of the ternary alloy to approximately 34 °C. As Cr is an element used in many materials for medical devices such as cobalt-chrome (CoCr), it is proven to be biologically compatible (17). Therefore, not only does the 7 at % palladium improve the radiopacity of the alloy, substituting extra Ni with Cr could potentially improve the alloys biocompatibility.

Although the microstructure appears homogeneous under backscattered SEM observation (figure 5.18 (b)). The austenite DSC transformation curve displayed in figure 5.18 (c) has a relatively broad transformation peak. This indicates that further research must be completed to identify a heat treatment that can fully homogenise the microstructure after SLM processing.

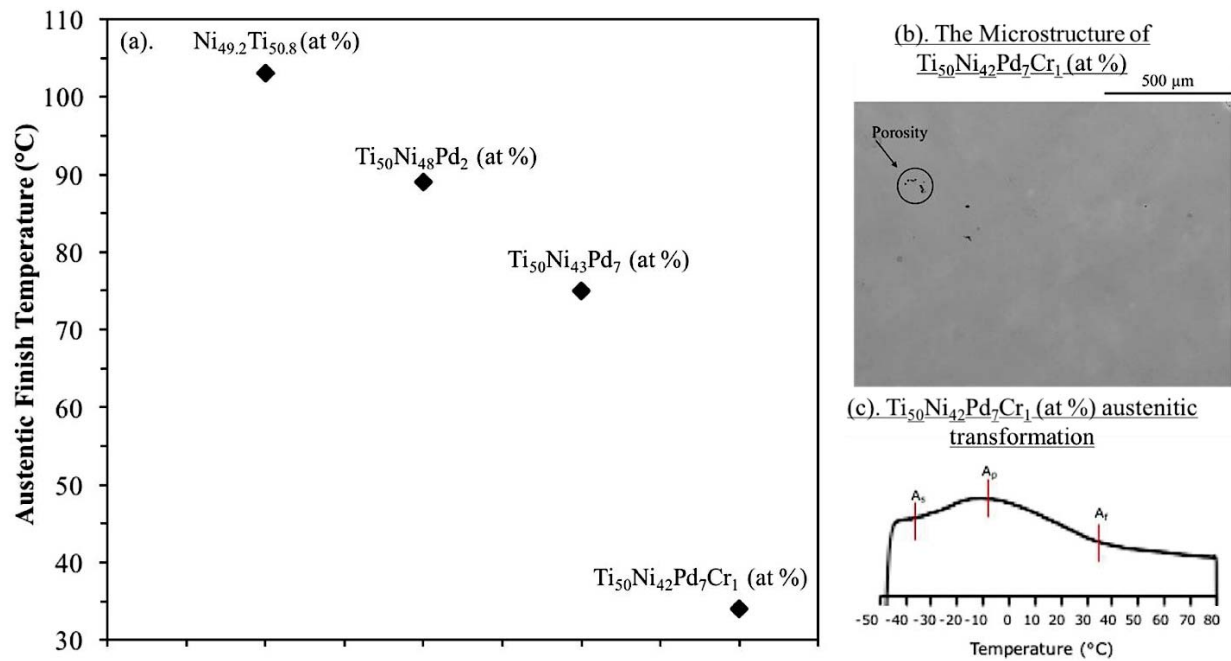


Figure 5.18 (a): The A_f temperatures of the solution heat treated binary, ternary and quaternary alloy compositions (b): The microstructure of solution heat treated $\text{Ti}_{50}\text{Ni}_{42}\text{Pd}_7\text{Cr}_1$ at % alloy (c): The DSC austenitic transformation curve for the treated $\text{Ti}_{50}\text{Ni}_{42}\text{Pd}_7\text{Cr}_1$ at % alloy

5.5. Conclusion

Within this chapter, the thermal behaviour of SLM NiTi and TiNiPd SMAs has been investigated through experimental research and discussion. The in-situ alloying methodology (chapter 4) has been used to SLM ternary TiNiPd alloy compositions. Thus, the influence of the Pd on the transformation temperature of the binary NiTi has been identified. Additionally, the in-situ alloying technique was further applied to investigate the transformation temperatures of quaternary alloys NiTi alloys.

The biggest problem faced when manufacturing NiTi SMA using SLM is the Ni evaporation that occurs when laser processing. It was found that using an austenitic NiTi powder does not ensure an austenitic manufactured part. To reduce the extent of Ni evaporation during processing, it is important to process at the lowest laser energy densities possible. Thus, creating a melt pool with a smaller surface area from which the Ni can evaporate. The optimised SLM processing parameters for manufacturing NiTi had an LED of 0.2 J/mm and VED of 133

J/mm³. This resulted in a 1.9 at % Ni loss and increased the transformation temperature by 58 °C.

A solution heat treatment is vital in fully homogenising the final SLM fabricated part. Dissolving the chemical inhomogeneities within the microstructure for both the binary NiTi and ternary TiNiPd resulted in an increase in the transformation temperature as the matrix composition shifted towards a Ti-rich ratio. Immediate water quenching after the solution heat treatment suppressed the precipitation of any secondary phases and produced a homogeneous supersaturated solid solution.

Subsequent aging heat treatments can decrease the transformation temperature of the ternary TiNiPd alloy through the precipitation of the Ti-rich Ti₂Ni(Pd) intermetallic. Aging at 350 °C for 3 hours reduced the transformation temperature by 10 °C.

It was found that alloying with a Pd content up to 7 at % decreased the transformation temperatures of the binary NiTi alloy. The transformation temperatures of the SLM fabricated alloys appear to be within a comparable range to conventionally produced alloys. However, the A_F temperature is still above body temperature, making the alloy unsuitable for some vascular implant applications. A promising quaternary Ti₅₀Ni₄₂Pd₇Cr₁ composition has been identified which can lower the transformation temperature to 34 °C. However, further work must be carried out to optimise the solution heat treatment and sharpen the transformation peaks on the DSC curves.

Although the ternary TiNiPd alloy is not suitable for some vascular implant applications. Orthopaedic applications can still take advantage of its martensitic structure at body temperature. Most metallic implants are made from 316 stainless steel, Ti or Co-Cr. Each of

these materials can be up to 15 times stiffer than the surrounding bone tissue. During long time fixation, this can result in a redistribution of loads from the surrounding tissue to the implant itself, eventually leading to degradation of surrounding bone tissue. This stress shielding can lead to implant loosening and potential implant failure. However, martensitic NiTi has mechanical properties which match much closer to bone tissue. Thus, these similarities in their elastic behaviour will reduce the risk of stress shielding and ultimately implant failure. Furthermore, the ternary TiNiPd alloy can be used for martensitic bone staples, where the alloyed Pd will improve the X-ray visibility of these small devices.

5.6. References

1. C. B. Alcock VPI& MKH. Vapour Pressure Equations for the Metallic Elements: 298–2500K. Can Metall Q. 1984;23(3):309–13.
2. Li Y, Zhou K, Tor SB, Chua CK, Leong KF. Heat transfer and phase transition in the selective laser melting process. Int J Heat Mass Transf. 2017;108(April):2408–16.
3. Antony K, Arivazhagan N. Studies on Energy Penetration and Marangoni Effect During Laser Melting Process E P. 2015;10(4):509–25.
4. Frenzel J, George EP, Dlouhy A, Somsen C, Wagner MFX, Eggeler G. Influence of Ni on martensitic phase transformations in NiTi shape memory alloys. Acta Mater [Internet]. 2010;58(9):3444–58.
5. King WE, Barth HD, Castillo VM, Gallegos GF, Gibbs JW, Hahn DE, et al. Observation of keyhole-mode laser melting in laser powder-bed fusion additive manufacturing. J Mater Process Technol [Internet]. 2014;214(12):2915–25.
6. Khan MI. Pulsed Nd:YAG Laser Processing of Nitinol. 2011;

7. Verhaeghe F, Craeghs T, Heulens J, Pandelaers L. A pragmatic model for selective laser melting with evaporation. *Acta Mater* [Internet]. 2009;57(20):6006–12.
8. López HF, Salinas-Rodríguez A, Rodríguez-Galicia JL. Microstructural aspects of precipitation and martensitic transformation in a Ti-rich Ni-Ti alloy. *Scr Mater*. 1996;34(4):659–64.
9. Jiang SY, Zhao YN, Zhang YQ, Hu L, Liang YL. Effect of solution treatment and aging on microstructural evolution and mechanical behavior of NiTi shape memory alloy. *Trans Nonferrous Met Soc China (English Ed)*. 2013;23(12):3658–67.
10. Saedi S, Turabi AS, Andani MT, Haberland C, Karaca H, Elahinia M. The influence of heat treatment on the thermomechanical response of Ni-rich NiTi alloys manufactured by selective laser melting. *J Alloys Compd* [Internet]. 2016;677:204–10.
11. Tadayyon G, Mazinani M, Guo Y, Zebarjad SM, Tofail SAM, Biggs MJ. The effect of annealing on the mechanical properties and microstructural evolution of Ti-rich NiTi shape memory alloy. *Mater Sci Eng A* [Internet]. 2016;662:564–77.
12. Acton QA. *Issues in Structural and Materials Engineering: 2013 Edition* [Internet]. 2013th ed. ScholarlyEditions, 2013; 1190 pages.
13. Zarinejad M, Liu Y. Dependence of transformation temperatures of NiTi-based shape-memory alloys on the number and concentration of valence electrons. *Adv Funct Mater*. 2008;18(18):2789–94.
14. Singh N, Talapatra A, Junkaew A, Duong T, Gibbons S, Li S, et al. Effect of ternary additions to structural properties of NiTi alloys. *Comput Mater Sci* [Internet].

- 2016;112:347–55.
15. Otsuka K, Ren X. Physical metallurgy of Ti-Ni-based shape memory alloys. *Prog Mater Sci* [Internet]. 2005;50(5):511–678.
 16. Shuichi Miyazaki, Yong Qing Fu WMH. *Thin Film Shape Memory Alloys: Fundamentals and Device Applications* Title [Internet]. illustrate. Cambridge University Press, 2009; 2009. 459 p.
 17. Ivanova EP, Bazaka K, Crawford RJ. Metallic biomaterials: types and advanced applications. *New Funct Biomater Med Healthc* [Internet]. 2014;121–47.
 18. Haberland C, Elahinia M, Walker JM, Meier H, Frenzel J. On the development of high quality NiTi shape memory and pseudoelastic parts by additive manufacturing. *Smart Mater Struct*. 2014;23(10).
 19. Meier H, Haberland C. Experimental studies on selective laser melting of metallic parts. *Materwiss Werksttech* [Internet]. 2008;39(9):665–70.

Chapter 6

An Investigation into the Suitability of SLM Pd Modified NiTi for use in Biomedical Applications

6.1. Introduction

The first part of this thesis focused on understanding the SLM processing parameters for manufacturing dense and chemically homogeneous TiNi and TiNiPd. Following this, the processing parameters were studied to gain an insight into their influence on the phase transformation temperature of the as-fabricated SLM alloys. Now the structural integrity of these SLM processed alloys have been optimised, it is vital to assess their performance as a biomedical material. Thus, not only assessing the influence of the alloying Pd element on the behaviour of binary NiTi, but also gaining an insight into the behaviour of SLM manufactured NiTi compared to the conventionally produced alloy.

As covered in the literature review, NiTi is a desirable material for minimally invasive implants due to its superelastic behaviour whilst in the austenitic phase. Additionally, its similarity to the behaviour of bone during mechanical loading makes it an excellent choice of material for larger, orthopaedic implants (1). Although conventionally produced NiTi can reach up to 8 % recoverable strains during loading (2), this chapter studies the superelastic ability of SLM fabricated NiTi and TiNiPd alloys.

It is essential that any implantable material has excellent corrosion resistance whilst in the human body. Although it is accepted that NiTi has a good resistance to corrosion due to its

passive TiO_2 layer (2), the same cannot be said for SLM fabricated NiTi, where interlayer microstructural defects due to the additive layer manufacturing process may accelerate corrosion (3). This chapter studies the corrosion resistance of binary NiTi and ternary TiNiPd. Thus, investigating the impact of the Pd alloying element and SLM manufacturing on the corrosion resistance of NiTi. Furthermore, changes in the corrosion resistance of the alloy due to either SLM processing or Pd will have an impact on its biocompatibility. Hence, initial biocompatibility trials of the alloys are conducted during this chapter.

Finally, one of NiTi's greatest limitations for use in biomedical applications is its lack of radiopacity. This chapter will compare the X-ray visibility of SLM fabricated NiTi and TiNiPd, to assess the impact of alloying the binary alloy with 7 at % Pd.

During the SLM parametric studies in chapter 4, the ternary composition $\text{Ti}_{50}\text{Ni}_{48}\text{Pd}_2$ at % was used to gain an understanding into how the alloy behaved during processing. However, the ternary composition used in this chapter is $\text{Ti}_{50}\text{Ni}_{43}\text{Pd}_7$ (at %), as this composition will most likely be used in biomedical applications due to its enhanced radiopacity (4) .

6.2. The Superelastic Response of SLM Fabricated NiTi and TiNiPd

As the superelastic response requires a fully austenitic crystal structure, all samples were heated 10°C above their A_F temperature prior to and during the loading-unloading testing. Figure 6.1. displays the initial stress strain curve for the $\text{Ti}_{50}\text{Ni}_{43}\text{Pd}_7$ (at %) alloy under compression. An SLM as-fabricated compressive sample was loaded past its yield point to identify the stress that corresponded to the onset of plastic deformation. Three different regions can be observed and are highlighted on the curve. Before region I, the austenite structure elastically deforms. At region I, there is a stress-induced martensitic transformation and this continues until the structure is fully martensitic at region II. Past region II, the martensite elastically deforms

before reaching region III, where permanent deformation starts to occur. Deformation accumulated past region III cannot be recovered. As displayed in figure 6.2, the same regions are exhibited in the stress-strain curve for the binary NiTi.

The binary NiTi alloy elastically deforms in the austenitic state to much greater loads than the ternary TiNiPd alloy. The stress induced martensitic transformation occurs at approximately 800 MPa for binary NiTi whilst martensitic transformation initiates at approximately 400 MPa for the Pd modified alloy. Furthermore, the TiNiPd alloy appears to complete martensitic detwinning earlier than the binary NiTi alloy. Finally, it appears that the onset of plastic deformation occurs at approximately the same stress for both the binary and Pd modified NiTi. Irreversible strain would accumulate in both the binary and ternary NiTi alloys if loaded past 1600 MPa. Thus, during the superelastic loading-unloading investigations the alloys will be loaded to 1000 MPa before unloading.

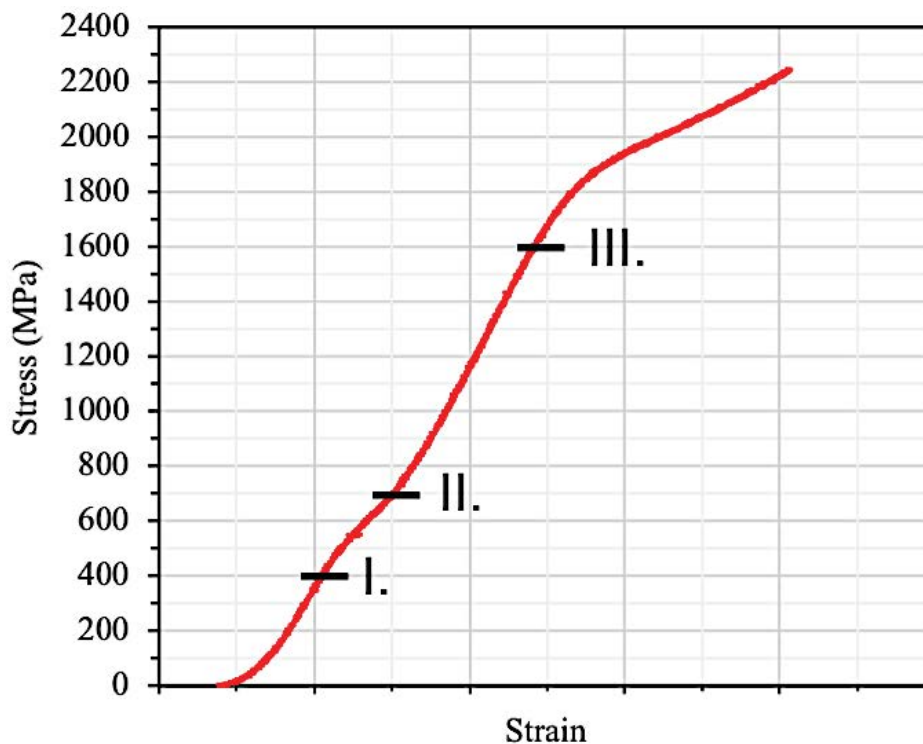


Figure 6.1: A stress-strain curve for the $Ti_{50}Ni_{43}Pd_7$ (at %) alloy under compression

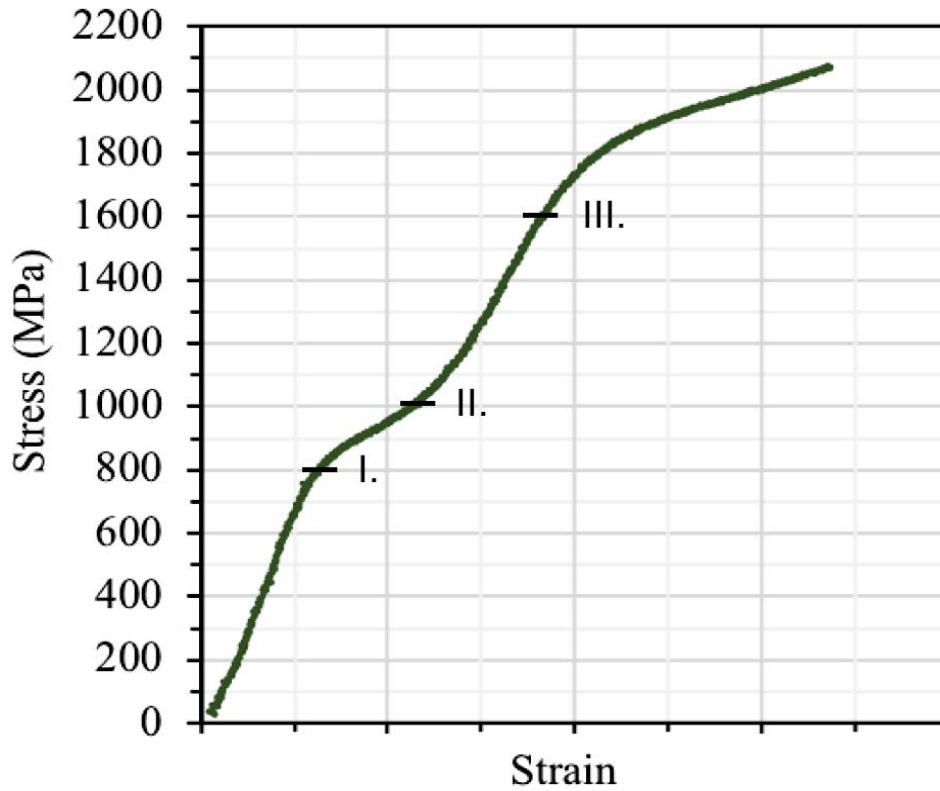


Figure 6.2: A stress-strain curve for the binary NiTi under compression

As stated in the literature review, as- fabricated SLM alloys do not show superelastic recovery as a solution heat treatment is required to relax the internal stresses that build up during manufacturing (5). Thus, the solution heat treatment used in chapter 5 was applied and samples were heated to 950°C for 5.5 hours followed by immediate water quenching.

Figure 6.3 (a) shows the superelastic response of the solution heat treated binary NiTi and ternary TiNiPd SLM manufactured alloys when loaded to 1100 MPa and unloaded. The NiTi solution heat treated alloy experienced a recoverable strain of 3.75% and an irrecoverable strain of 4%. Loading up to 1100MPa, caused the ternary solution heat treated TiNiPd alloy to experience plastic deformation at approximately 1000 MPa. Thus, in order to assess the alloy's superelastic potential, it was loaded to 900 MPa (shown in figure 6.3. (b)). The alloy experienced a 4 % recoverable strain. However, the irrecoverable strain was much higher for

the Pd modified alloy in comparison to the binary NiTi, accumulating an 8 % irrecoverable strain.

Heat treatment is one of the most effective methods of increasing the strength of Ni-rich NiTi alloys through the use of precipitation hardening (6). Thus, the ternary TiNiPd solution heat treated alloy could have experienced plastic deformation due to the lack of $\text{Ti}_2\text{Ni}(\text{Pd})$ precipitates in the TiNiPd matrix's homogeneous microstructure. In an attempt to improve and tailor the superelastic response of the TiNiPd alloy, samples were solution heat treated and aged at 350 °C or 450 °C for varying time periods.

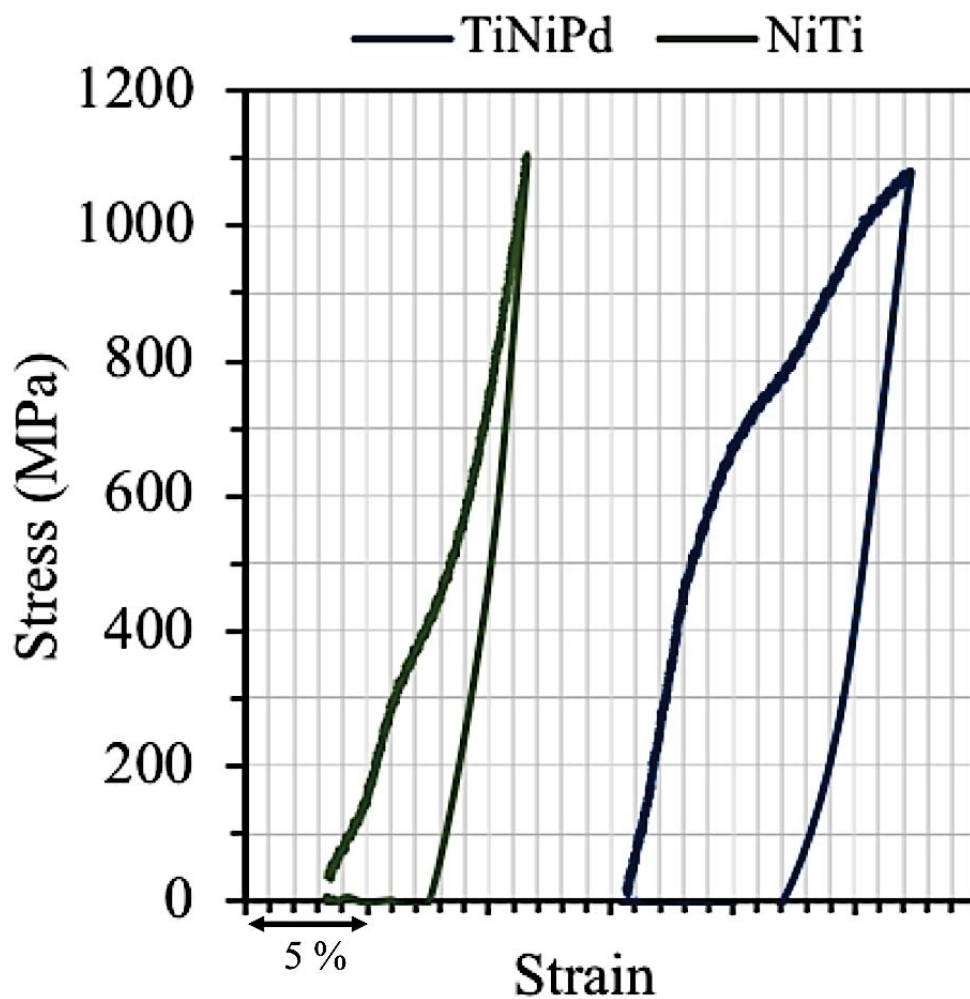


Figure 6.3 (a): The superelastic response for the binary NiTi and ternary TiNiPd alloys when loaded to 1100 MPa and unloaded

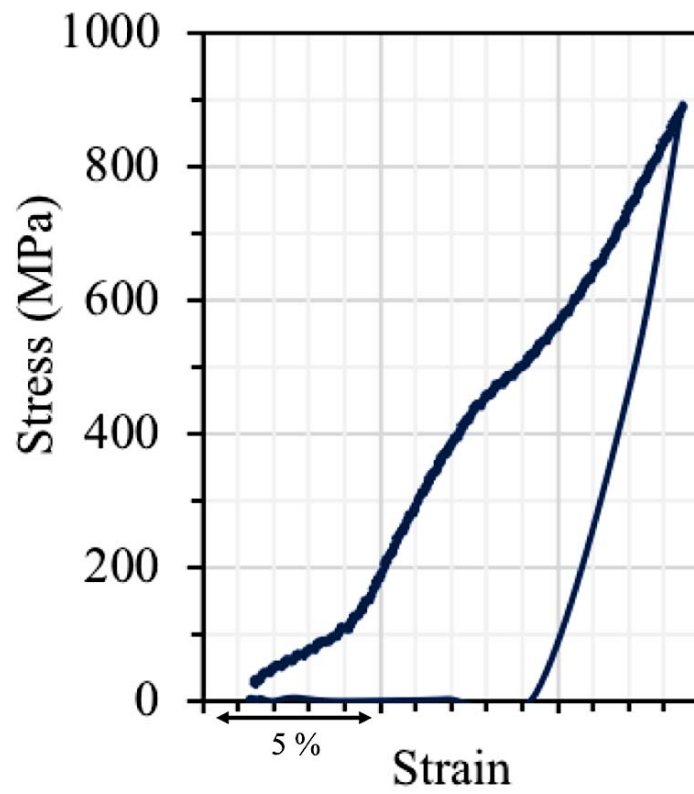


Figure 6.3 (b): The superelastic response of the ternary TiNiPd alloy when loaded to 900 MPa and unloaded

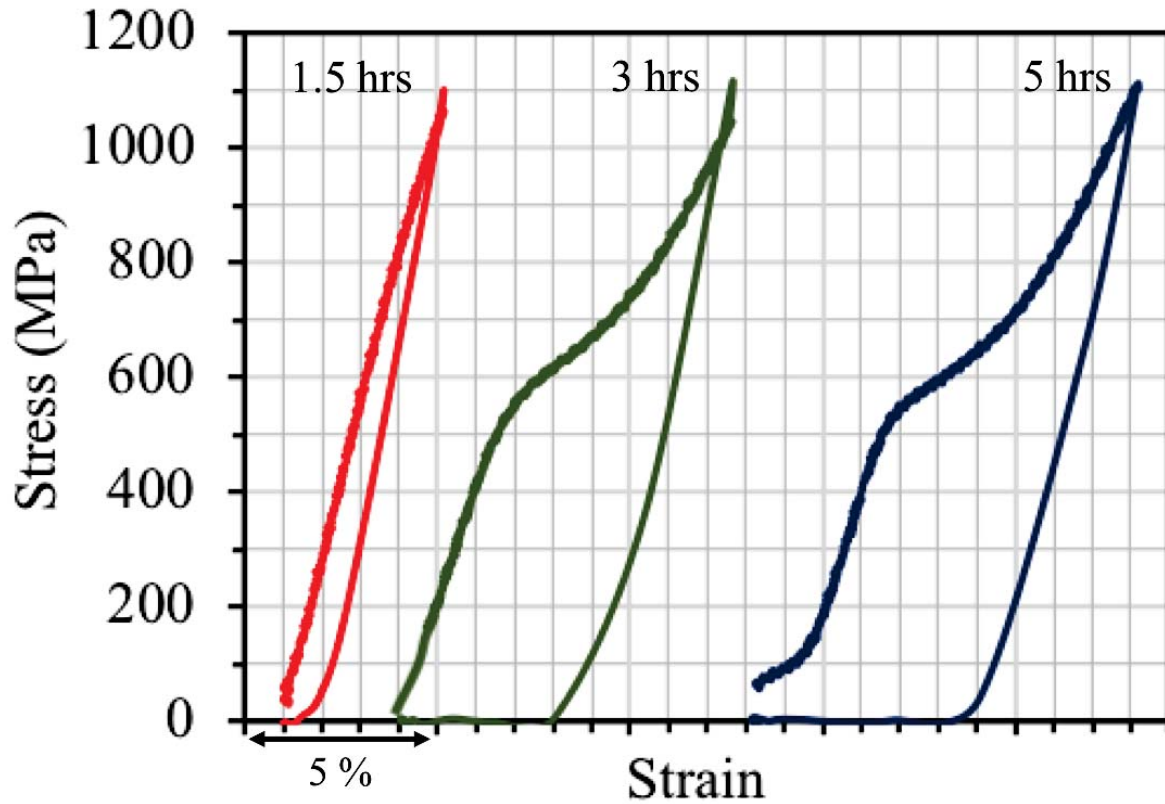


Figure 6.4: The superelastic response for samples solution heat treated and aged for 350 °C for 1.5hrs, 3hrs and 5 hrs

Figure 6.4. displays the superelastic response for the samples solution heat treated followed by aging at 350 °C for 1.5 hours, 3 hours and 5 hours. Figure 6.5. displays the superelastic response for the samples solution heat treated followed by aging at 450 °C for 1.5 hours, 3 hour and 5 hours. Finally, table 6.1. lists the recoverable and irrecoverable strains for all the heat treated samples.

When observing the loading-unloading curves, the samples aged at 350°C for 1.5 hours and 450°C for 5 hours noticeably lacked the stress-induced martensitic plateau. This is believed to be due to the sample's inhomogeneous microstructure and the $\text{Ti}_2\text{Ni(Pd)}$ precipitates interacting with the martensitic variants. A local stress field builds up around the precipitates due to a mismatch between elastic strain energy of the Ti-rich precipitates and the NiTi matrix (7). As the martensitic transformation requires a lattice structural change, the presence of this stress field will influence the transformation (8). Thus, the presence of this intermetallic precipitation can prevent the transformation of small localised areas of the specimen. These areas will gradually transform with increasing strain. However, this causes a delay in the stress-induced martensitic transformation.

From the figures and the table, it is clear that for both aging temperatures the irrecoverable strain is lowest in the samples aged for 1.5 hours. The specimen aged at 350°C had a irrecoverable stain of 0.7 %. Whilst, the specimen aged at 450°C had an irrecoverable strain of 3.7 %. This observable trend can be related to the increase in the alloy's strength due to the precipitation hardening effect after aging. When the $\text{Ti}_2\text{Ni(Pd)}$ precipitates are small and coherent within the NiTi matrix, they work to increase the strength of the ternary alloy by impeding the movement of dislocations or defects. The precipitation characteristics can be controlled by aging temperature and time. Aging for longer periods of time results in the

formation of coarser precipitation which has a lower hardening effect. Additionally, aging at high temperatures reduces the volume fraction of precipitates within the NiTi matrix (6). Consequently reducing the hardening effect as the movement of dislocations and defects is less successfully hindered. This explains why the samples aged at 450°C for 1.5 hours had a higher irrecoverable strain of 3.7%, in comparison to the samples aged at 350°C for 1.5 hours, that had an irrecoverable strain of 0.70 %.

When relating the superelastic response to the change in strength produced through aging heat treatments. As expected the samples aged for 5 hours accumulated the largest irrecoverable strain. Due to the decrease in the volume fraction of precipitation with increasing aging temperature, the sample aged at 450°C should have had a larger irrecoverable strain in comparison to the sample aged for the same time period at 350°C. However, the sample aged at 350°C had an 0.8 % higher irrecoverable strain of 5.8%.

Although the recoverable and irrecoverable strains did vary with the different aging heat treatments used. For each aging time period, no clear trend can be defined between the samples aged at 350°C and 450°C. However, it can be concluded that for a selected aging temperature, the irrecoverable strain appears to increase with aging time.

A comparison between the precipitation for the heat treated samples can be seen in the micrographs in figure 6.6, 6.7 and 6.8. Figure 6.6 displays the fine and relatively consistent $\text{Ti}_2\text{Ni(Pd)}$ precipitation in the sample aged at 350°C for 1.5 hours. An increase in the precipitate size and decrease in the volume fraction occurs in figure 6.7, where the aging time period remained at 1.5 hours, however the temperature increased to 450°C. Finally, an overall

increase in precipitation size and a decreased interparticle distance can be observed in figure 6.8. where the sample was aged at 450°C for an aging time period of 5 hours.

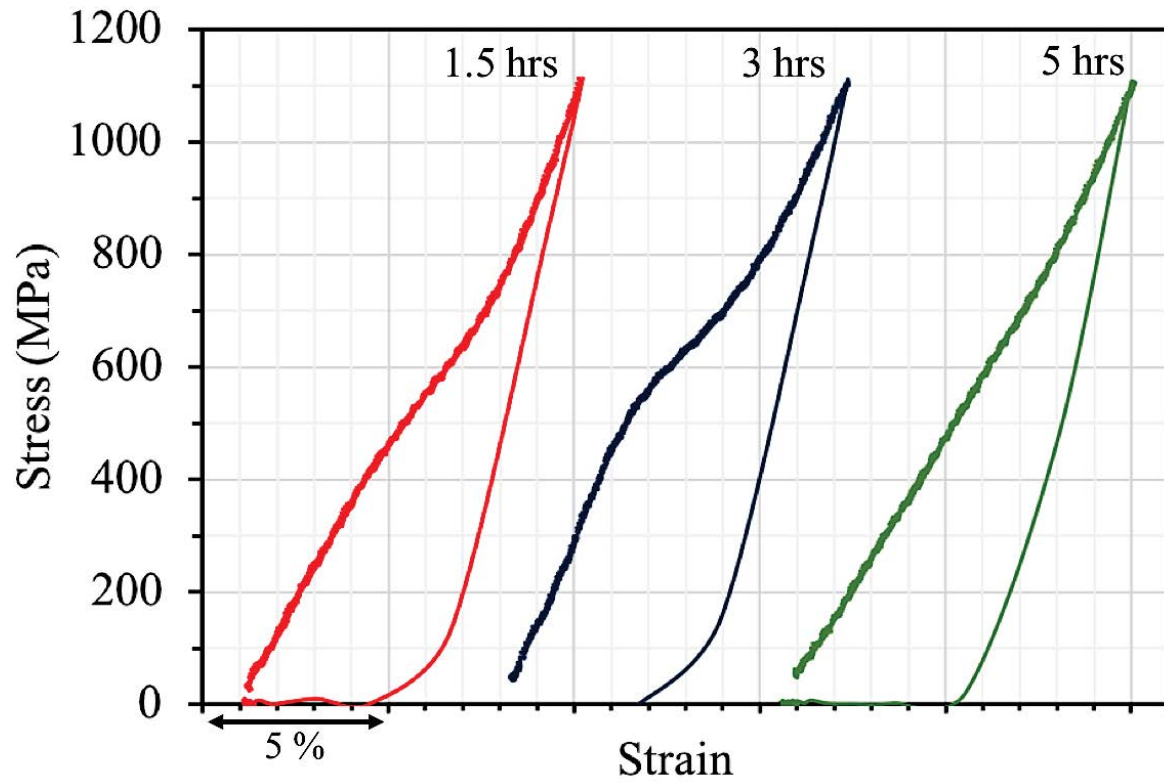


Figure 6.5: The superelastic response for samples solution heat treated and aged for 450 °C for 1.5 hrs, 3hrs and 5 hrs

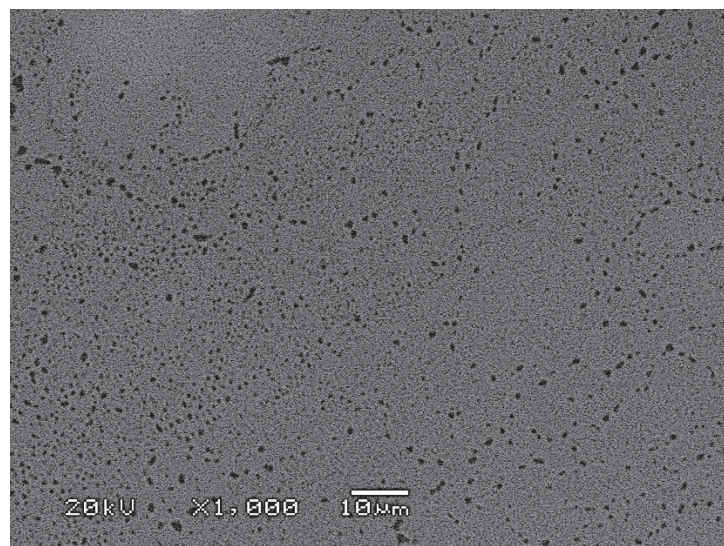


Figure 6.6: A micrograph showing the $Ti_2Ni(Pd)$ precipitation in a sample solution heat treated and aged at 350 °C for 1.5 hrs

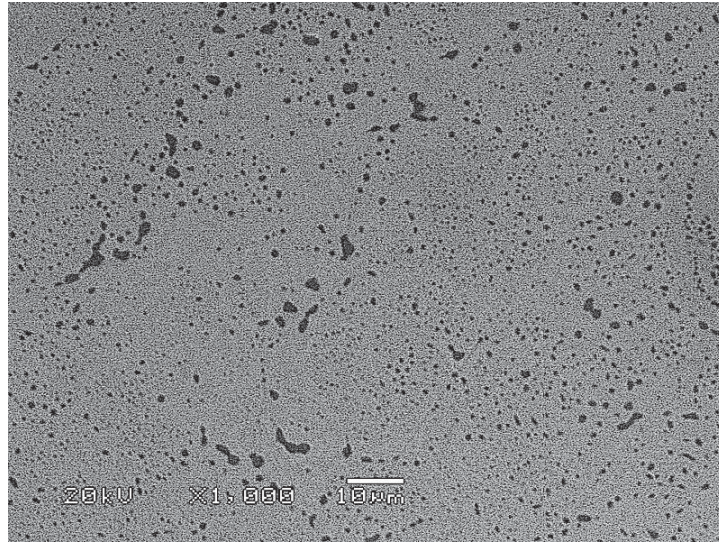


Figure 6.7: A micrograph showing the $Ti_2Ni(Pd)$ precipitation in a sample solution heat treated and aged at 450 °C for 1.5 hrs

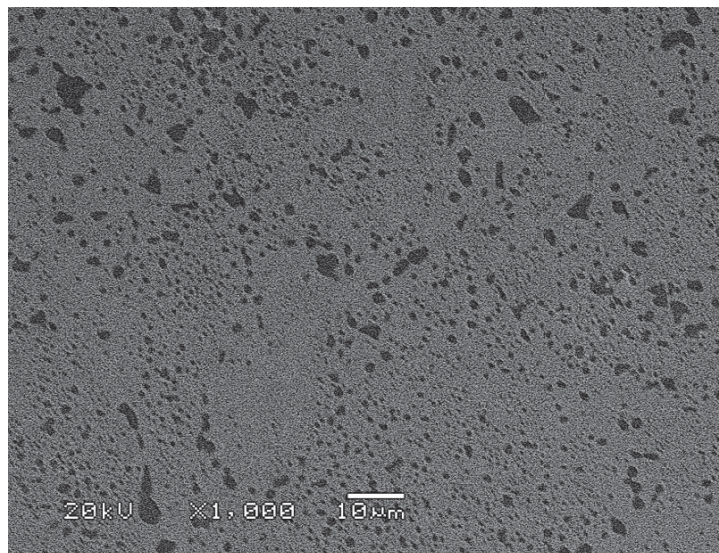


Figure 6.8: A micrograph showing the $Ti_2Ni(Pd)$ precipitation in a sample solution heat treated and aged at 350 °C for 5 hrs

Table 6.1: A table showing the recoverable and irrecoverable strains of the heat treated samples

Aging Temperature (°C)	Aging Time (hrs)	Recoverable Strain (%)	Irrecoverable Strain (%)
350	1.5	4.0	0.7
350	3	4.8	4.0
350	5	4.7	5.8
450	1.5	5.3	3.7
450	3	5.1	3.9
450	5	4.8	5.0

6.3. The Radiopacity of SLM Pd modified NiTi SMAs

The main disadvantage for using NiTi in small biomedical devices is its lack of radiopacity i.e. its visibility in the human body via x-ray. X-ray visibility is vital to allow the surgeon to accurately place the device whilst keeping the x-ray exposure of the patient to a minimum (9). To investigate the influence of Pd addition on the radiopacity of binary NiTi when processed using SLM, micro CT was used to qualitatively compare the difference in contrast, thus the difference in X-ray absorption. The chosen ternary composition was $\text{Ti}_{50}\text{Ni}_{43}\text{Pd}_7$ (at %), as alloying with 7 at % Pd would work to enhance the radiopacity of binary NiTi whilst preserving its superelastic characteristics.

Binary NiTi and ternary TiNiPd stent shaped components were manufactured using SLM. The stent shape can be seen in figures 6.9 and 6.10. The possibility of fabricating a stent using SLM, that can be inserted straight into the human body is a long way off. However, the SEM images display the capability of SLM to manufacture complex, micron scale structures directly from metallic powders. The stents spanned a total width of 2000 μm with a strut size of 300 μm .

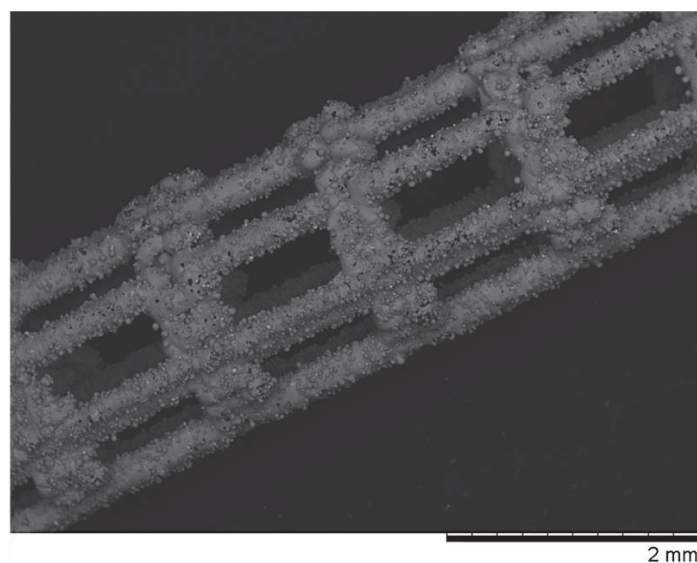


Figure 6.9: SEM image of the SLM fabricated stent

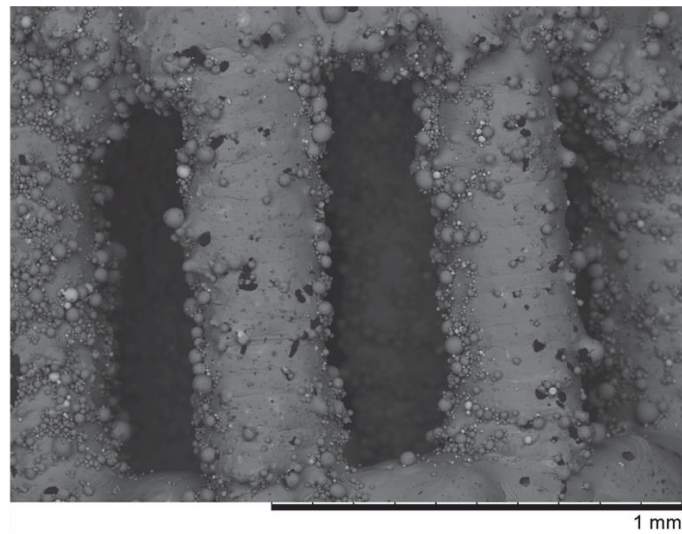


Figure 6.10: SEM image of the SLM fabricated stent's struts

Elemental Pd has a higher atomic number and density in comparison to elemental Ni and Ti (10). Table 6.2. compares the differences in general properties for the three elements. A denser element with a higher atomic number will increase the X-ray attenuation, hence it will be more radiopaque (10). When alloying Pd into the NiTi matrix, the material acts as an absorber during X-raying. The radiation has a lower probability of passing through the ternary alloy and due to this the attenuation increases. The enhanced interaction between the X-ray beam and ternary TiNiPd is responsible for its darker contrast in comparison to binary NiTi during fluoroscopic imaging.

As attenuation increases with thickness, the thickness can affect its contrast during X-ray imaging. A stent thickness of 40 μm for both alloys was used to obtain accurate qualitative representations between the differences in contrast.

Table 6.2: The general properties for elements Pd, Ni and Ti

Element	Atomic number	Density (g.cm^3)
Pd	46	11.9
Ni	28	8.9

Ti	22	4.5
----	----	-----

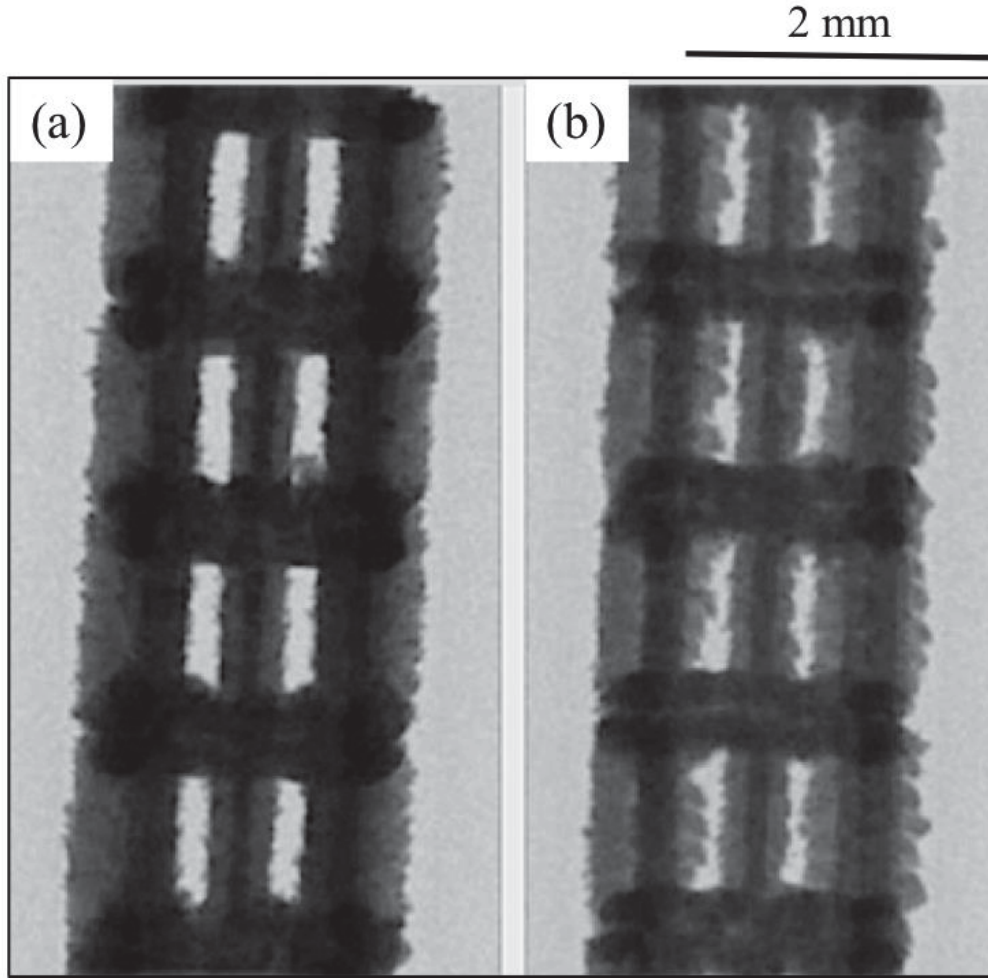


Figure 6.11: X-ray images comparing the x-ray absorptivity between (a) ternary TiNiPd (b) binary NiTi

Due to the high radiation absorption coefficient of Pd, the X-ray visibility of binary NiTi is noticeably improved when alloying with 7 at%. Pd. The higher density of Pd, means more energy from the photons of the X-ray beam are absorbed by the atoms in the alloy, resulting in increased attenuation and producing a higher contrast in comparison to the background. As shown in figure 6.11 the ternary TiNiPd alloy has a darker contrast in the X-ray fluoroscopy image. Figure 6.12 displays the differences in contrast along the width of the stent for each alloy. The ternary TiNiPd stent consistently has a greyscale value closer to zero, explaining its darker contrast in comparison to binary NiTi. ImageJ software was used to quantify the greyscale across the X-ray images for both the binary NiTi and ternary TiNiPd stents in

comparison to the X-ray background. Figure 6.13 shows that the contrast of NiTi against the X-ray background can be improved by 25 % when alloying with 7 at % Pd.

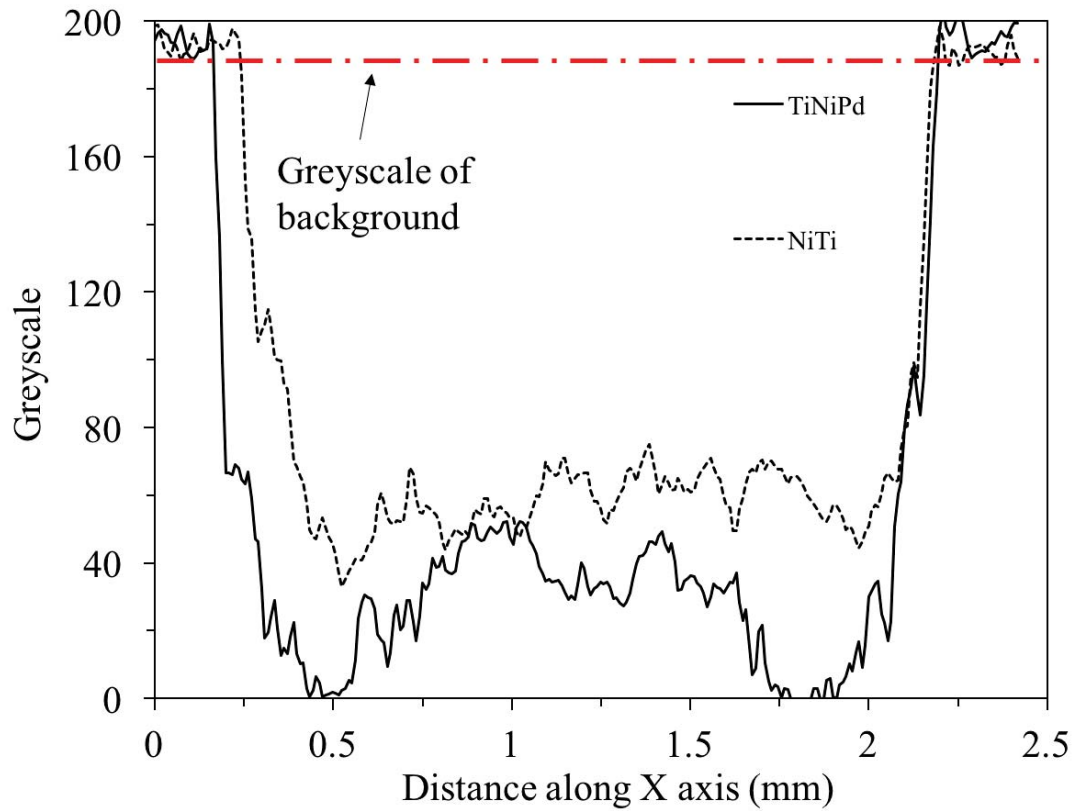


Figure 6.12: The greyscale of the X-ray image across the width of the binary and ternary stents

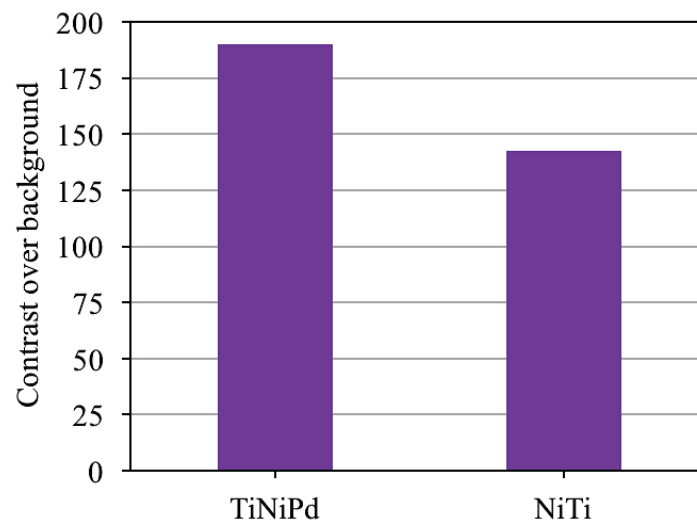


Figure 6.13: A histogram showing quantitative values of the contrast of samples against the X-ray background

6.4. The Biocompatibility of SLM binary NiTi and ternary TiNiPd

The biocompatibility testing was carried out on SLM fabricated 10x10x10 mm cubic samples. The cell viability was qualitatively compared between the SLM fabricated binary NiTi alloys and the ternary TiNiPd. Furthermore, cubic samples were cut from a pure Ti ingot to be used as the experimental control. Ti was chosen as the control due to its excellent biocompatibility and corrosion resistant properties (11). Furthermore, the control sample was conventionally manufactured to eliminate microstructural defects associated with SLM that may affect the results.

The SLM fabricated cubic samples were solution heat treated and immediately water quenched to fully homogenise the microstructure. However, after heat treating, the testing surface was ground using Silicon Carbide paper and polished up to a 0.04 μm colloidal silica OP-S solution. This was carried out because heat treatment would result in a Ti enriched surface. Thus, an accurate representation between the biocompatibility of each alloy would not be produced. Additionally, previous literature has stated that surfaces with a higher roughness favour cell adhesion (12). A polished surface eliminates the experimental factor of surface roughness and ensures the effect of chemical composition is the primarily focus of the study.

The viability of cells after culturing for 1, 3 and 7 days were tested by staining with calcein-AM and propidium iodine. Thus, stained cultures could be visualised using a scanning confocal microscope where live cells appear florescent green and dead cells red. The results of the live/dead imaging for alloys can be viewed in figure 6.14.

As evident in figure 6.14 during culture cells were able to adhere to all three surfaces by day one of testing. The fluorescent green indicates the good viability of the cells, suggesting a good cell compatibility of the surfaces. Successful cell adhesion was expected during day one testing because all three alloys are accepted as biocompatible materials.

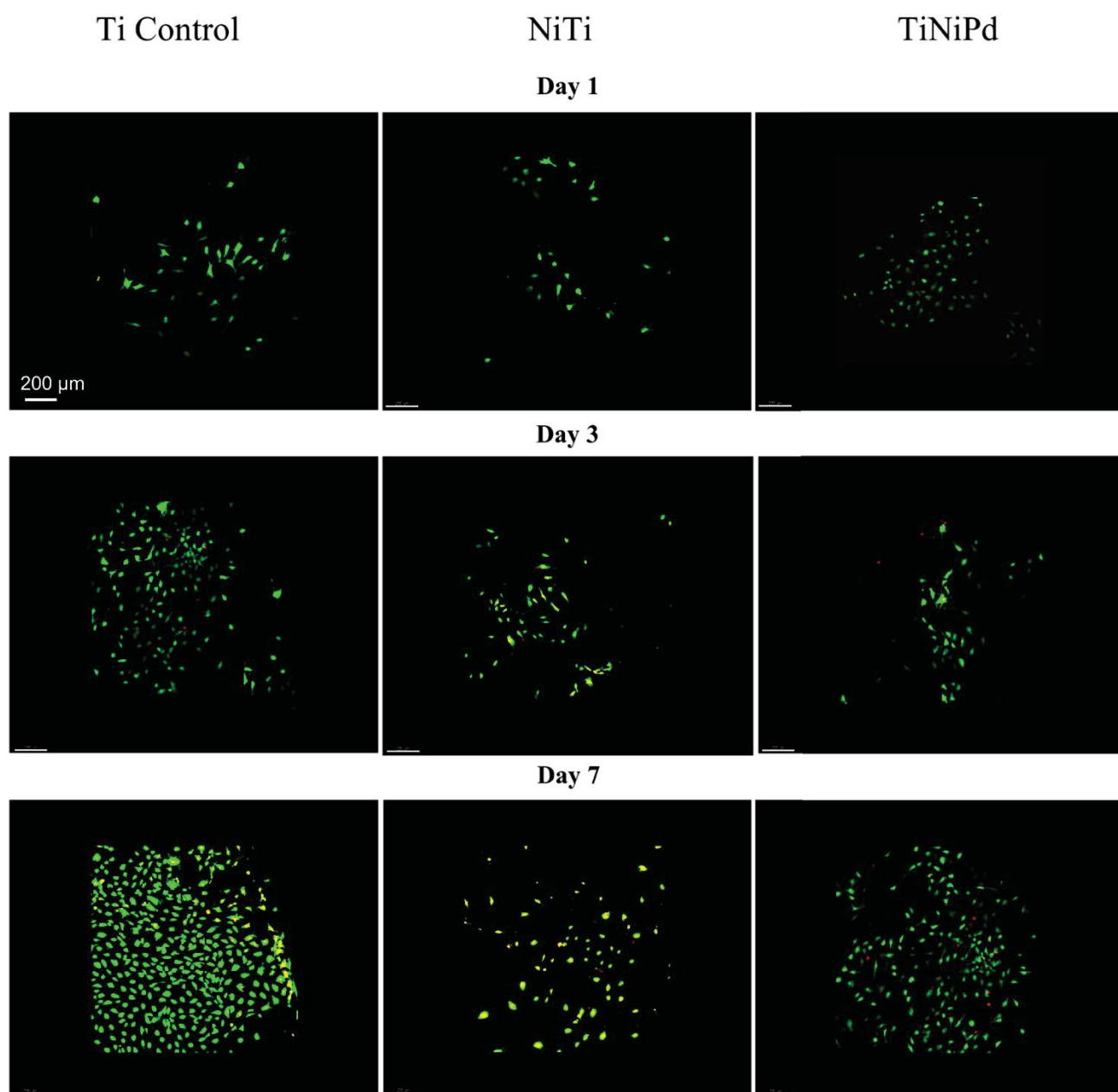


Figure 6.14: Live/dead imaging for cells seeded onto the polished surface of Ti, NiTi and TiNiPd after 1, 3 and 7 days

By day three, cells have proliferated on all of the alloy's surfaces. For each alloy the majority of cells are live and healthy. However, dead cells are now visible. It appears that cell spreading and growth is enhanced on the Ti surface compared to the binary NiTi and ternary TiNiPd. Indicating, the presence of elemental Ni in both alloys could have a potential cytotoxic effect.

On the seventh testing day, cells have continued to proliferate and spread. For all alloys there appears to be a large number of live cells and a few dead cells, thus cells are mostly in the viable state. The Ti control sample was found to have the fewest dead cells and had a homogeneous covering of predominately healthy cells. The addition of Pd in the ternary TiNiPd appeared to have no negative effect on the adhered cells, as by day seven a large number of live cells were present.

The cells grown on the ternary TiNiPd alloy appear much more healthy in comparison to the cells seeded on the binary NiTi alloy surface. A large number of cultivated cells on the surface of NiTi appear red in the centre, whilst their outer areas are green. An example of this cell can be seen in figure 6.15. Cells in this state indicate bad health where the cell is stressed and dying. This behaviour can be explained by the Ni content in each alloy. In the ternary alloy, 7 at % Ni was substituted with Pd. Thus, the lower Ni content reduces the cytotoxicity of the alloy.

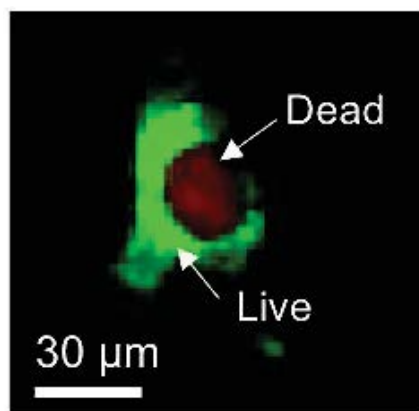


Figure 6.15: A live/dead cell

As mentioned previously, both the binary and ternary samples were ground and polished after the solution heat treatment. During heat treatment, the highly reactive Ti atoms react with oxygen to form a stable TiO₂ layer. It is believed this protective TiO₂ oxide layer promotes biocompatibility (13). The Ti-rich oxide layer will protect the alloy's bulk material from

corrosion whilst removing Ni atoms from the surface of the material. Furthermore, the TiO_2 layer acts as a physical barrier against Ni oxidation. Thus, preventing the release of toxic Ni into the human body and reducing the risk of allergic responses (14).

6.5. The Corrosion Resistance of SLM binary NiTi and Ternary TiNiPd

To study the influence of Pd on the corrosion resistance of binary NiTi, electrochemical tests were performed in phosphate-buffered saline (PBS) solution at 37°C . The solution and temperature were chosen in order to simulate the body fluid environment. Tests were carried out on the surface of solution heat treated and water quenched SLM samples. As for the biocompatibility tests, after heat treatment the samples were ground and polished to remove the TiO_2 layer and surface defects that may affect the corrosive behaviour. Furthermore, to investigate the effect of SLM manufacturing, the corrosive properties of SLM fabricated samples were compared to that of a conventionally produced NiTi ingot.

Prior to running the potentiodynamic polarisation tests, it is vital to maintain stability of the open circuit potential (OCP). The OCP is the potential at which the sample is in equilibrium with the standard calomel electrode when no current is being applied to the corrosion system (15). At potentials below the OCP, the alloys are more thermodynamically stable and are less susceptible to corrosion. As shown in figure 6.16. the OCP of the samples is measured as a function of time. This test continues to run until the OCP curve stabilises and the corrosion reactions have assumed a constant rate.

A steady state condition is reached for all samples (SLM and conventionally produced) after being immersed in the PBS solution for approximately 1800 seconds. This is because the variation of potential with time is negligible and the curve shows linear behaviour, verifying the steady state condition dominates.

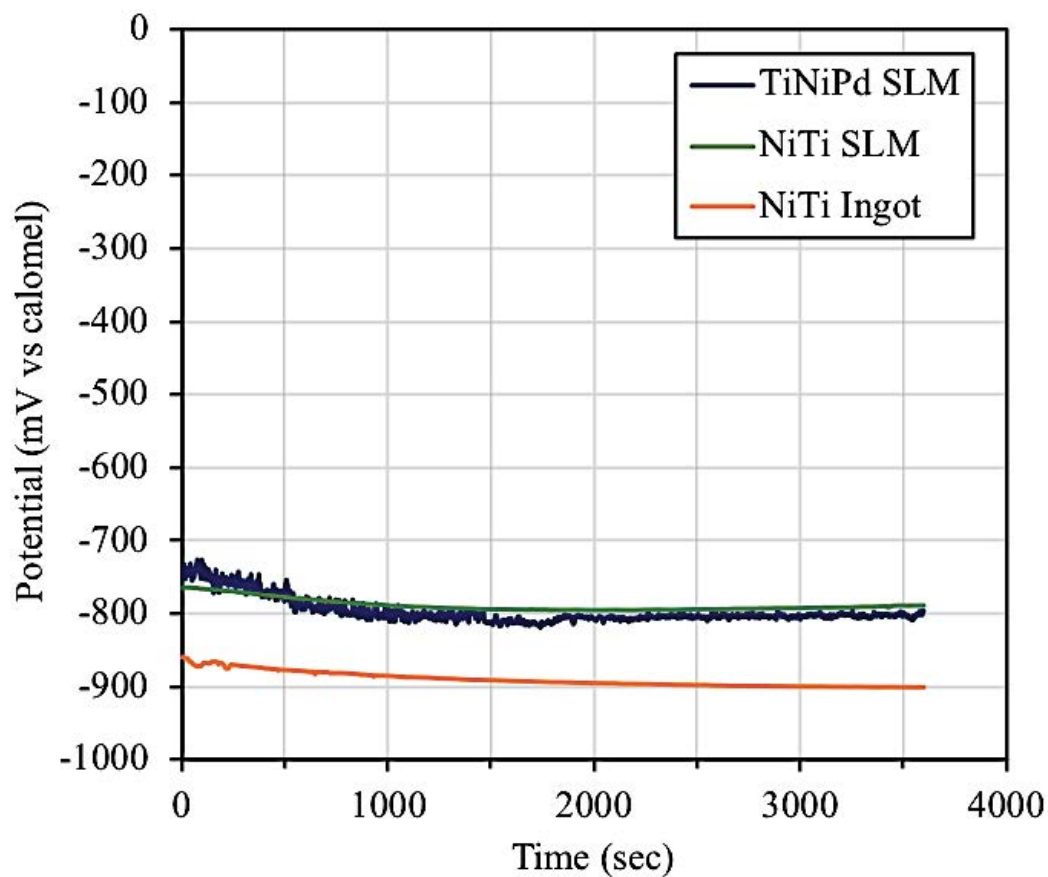


Figure 6.16: The open circuit potential of NiTi, TiNiPd (SLM fabricated) and conventionally produced NiTi ingot in PBS solution

Until approximately 400 seconds, the Pd modified NiTi SLM fabricated sample has the most positive OCP. Indicating the presence of Pd can initially improve the alloy's corrosion resistance. All of the OCP curves show a similar trend of initially decreasing the OCP towards more negative values before stabilising after 1800 seconds. This indicates the initial dissolution of the air formed oxide film on the sample's surface. There appears to be no significant difference between the OCP for the binary and ternary SLM fabricated alloys. Binary SLM NiTi had a slightly higher OCP of -795 mV, whilst ternary SLM TiNiPd had a OCP of -802 mV. However, the NiTi ingot has a more negative OCP of -896 mV, signifying it is less resistant to corrosion in comparison to the SLM fabricated samples in PBS solution. After 1800

seconds, the potential did not drop for all three alloys, suggesting the surface oxide layer had developed a stable resistance to chemical dissolution in the PBS solution.

The cyclic potentiodynamic polarisation curves for all three samples can be seen in figures 6.17-6.19. Both the forward and backwards scans are shown, highlighted by their different shade in colour. The forward scan curve has the darkest shade, during this scan the voltage is increased in the anodic (noble) direction. The backward scan is represented by the lightest shade, during this scan the voltage scan direction is reversed towards the cathodic (active) direction.

For the forward scanning direction, the values of current density and corrosion potential are 8.5×10^{-6} mA/cm² and -812.5 mV for the binary SLM fabricated NiTi alloy. The ternary SLM fabricated Ti₅₀Ni₄₃Pd₇ (at %) alloy had a current density of 3.9×10^{-6} mA/cm² and corrosion potential of 858.77 mV. Finally, the conventionally manufactured NiTi ingot had a 2.4×10^{-6} mA/cm² current density and a corrosion potential of 935.8 mV.

The conventionally manufactured NiTi ingot was the most resistant to corrosion during the forward scan, as the curve shifts towards the region of lower current density and higher potential. The NiTi ingot and SLM fabricated binary alloy do not show comparable corrosion characteristics. This indicates that common defects associated with SLM manufacturing could have deteriorated the corrosion properties. The potential presence of submicron porosity in the SLM fabricated NiTi alloy could have resulted in a passive oxide layer with an inhomogeneous thickness. The aggressive chloride in the PBS solution would attack and damage weak regions of the boundary layer. Thus, initiating pitting as the oxide layer breaks.

The presence of Pd appears to improve the corrosion resistance of the SLM fabricated NiTi. It is believed that as Ti dissolves, the oxide layer becomes enriched with the passivating Pd atoms and this acts to provide anodic passivation of the NiTi matrix. In addition to reacting with the oxygen to form TiO₂, the Ti will react with the Pd at the surface to form Ti₂Pd. The Ti₂Pd acts as cathodic depolarisation sites on the metal's surface (16). The cathodic sites shift the corrosion potential in the more noble direction. Consequently, reducing the driving force of the corrosion reactions.

During the backwards scanning direction, the Pd modified SLM NiTi alloy appeared to be the most corrosion resistant. The ternary SLM Ti₅₀Ni₄₃Pd₇ (at %) had a corrosion potential of -451.02 mV and a current density of 2.5×10^{-8} mA/cm². Whereas, the conventionally manufactured NiTi ingot had a corrosion potential of 2.1×10^{-7} mA/cm² and a current density of 564.92 mV. A potential reason for the enhanced corrosion resistance of the ternary TiNiPd alloy could be due to the surface layer becoming increasingly enriched with the passivating Pd atoms during the backwards scan. Finally, the binary SLM fabricated NiTi alloy was the least corrosion resistance with a 2.9×10^{-5} mA/cm² current density and a corrosion potential of -738.73 mV.

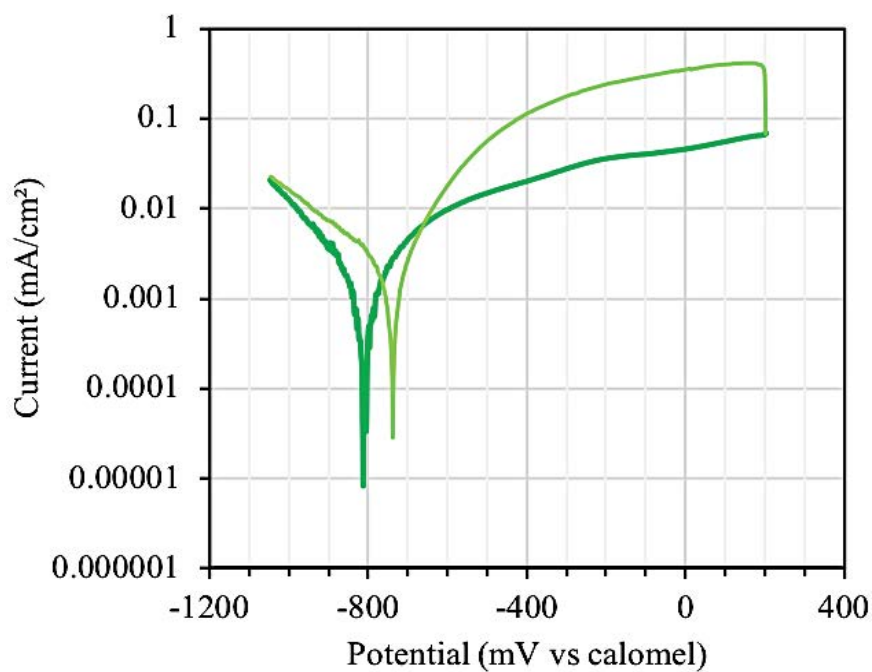


Figure 6.17: The potentiodynamic polarisation curve for SLM binary NiTi in PBS solution

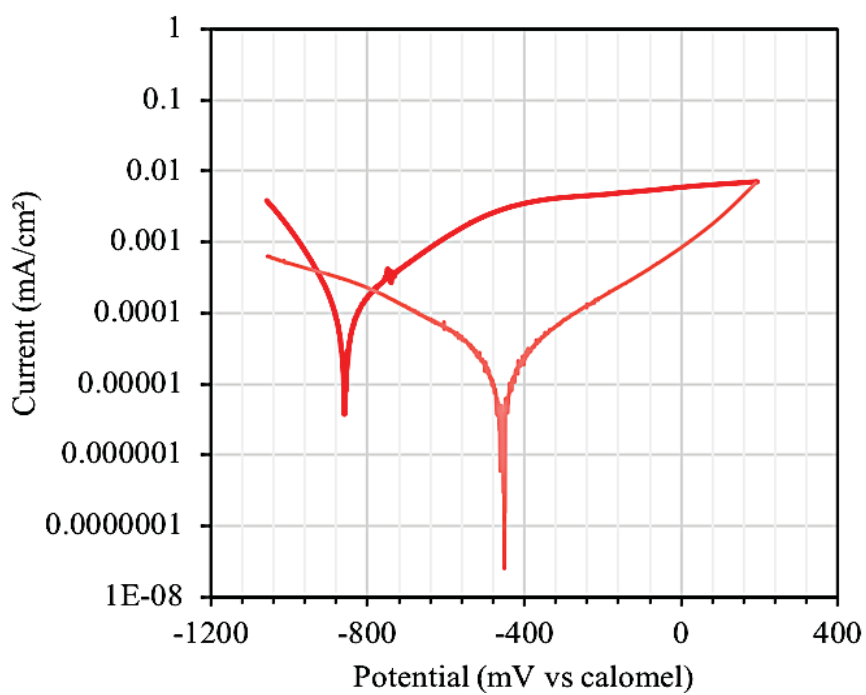


Figure 6.18: The potentiodynamic polarisation curve for SLM ternary Ti₅₀Ni₄₃Pd₇ (at%)

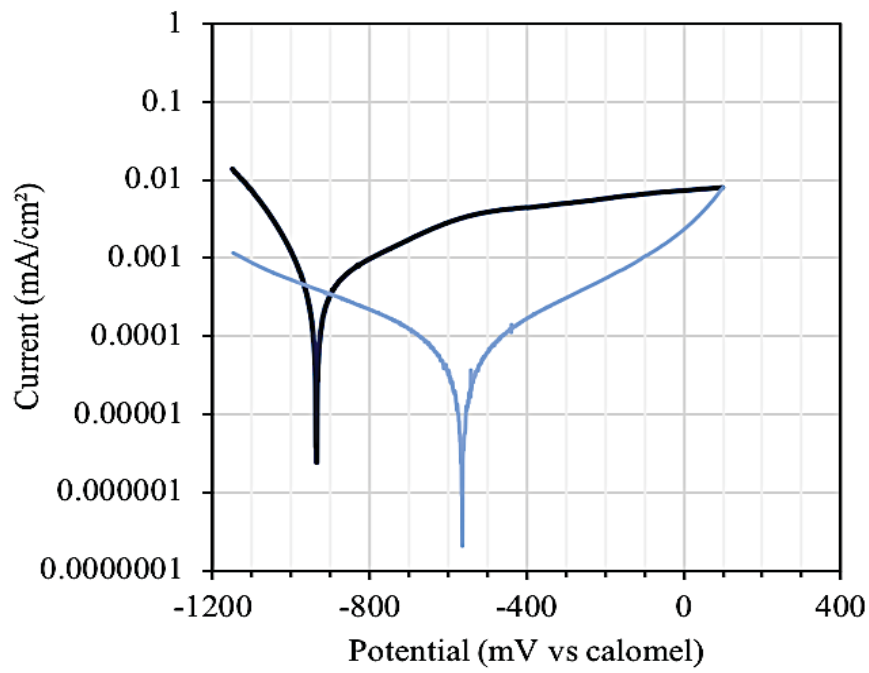


Figure 6.19: The potentiodynamic polarisation curve for conventionally produced NiTi ingot

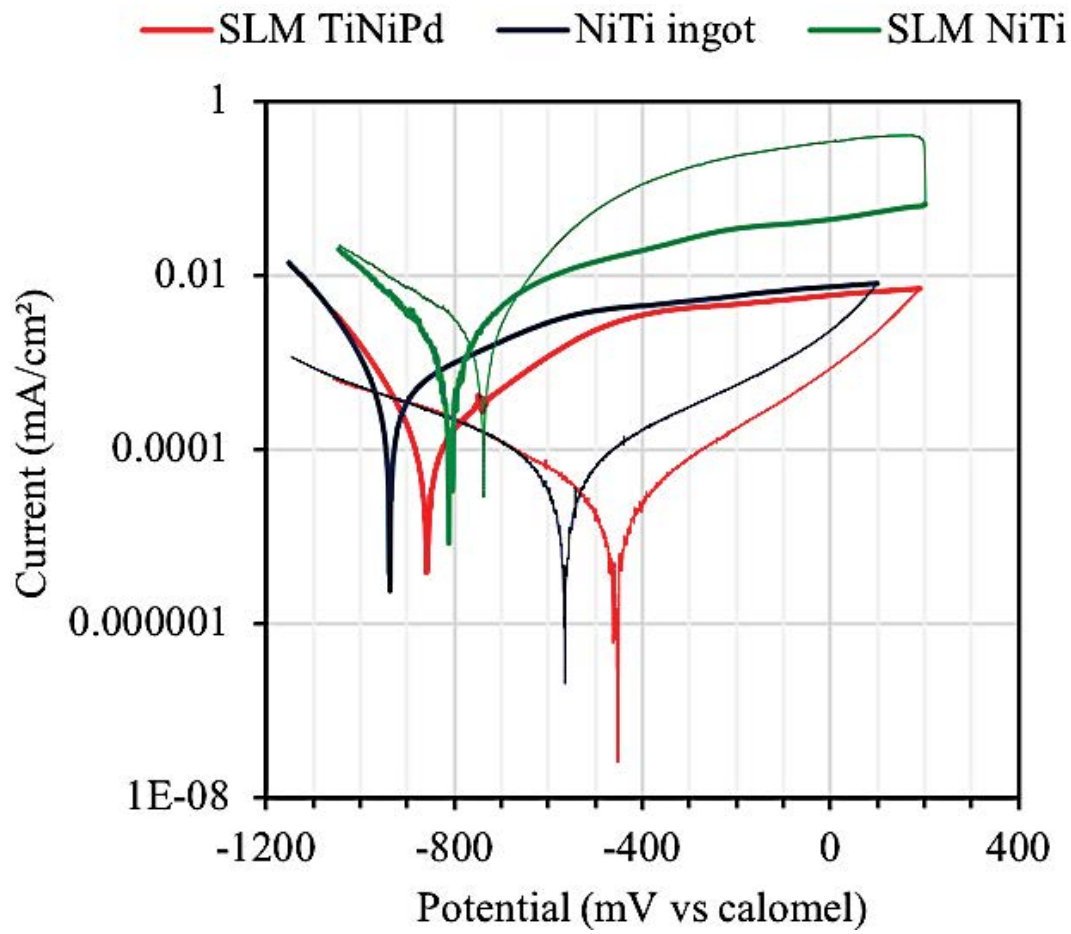


Figure 6.20: A comparison of the potentiodynamic polarisation curves for all three samples

Figure 6.20. displays the potentiodynamic polarisation curves for all three alloys plotted in the same graph. It is visible from the curves that only the binary NiTi SLM fabricated sample experienced a localised breakdown of passivity. Upon removal of the sample from the corrosion cell set up, a small pit was visible on its surface. Figure 6.21 and 6.22 display optical images of different regions on the SLM fabricated NiTi alloy's surface. The surface shown in figure 6.22. remains uniform and consistent across the whole area. Thus, indicating no breakdown of the passive layer. However, corrosion products are visible on the surface in figure 6.21. The corrosion products appear to surround a centralised cavity. This suggests the oxide layer experienced damage during the corrosion testing. However, it was not able to successfully re-passivate before a pit formed.

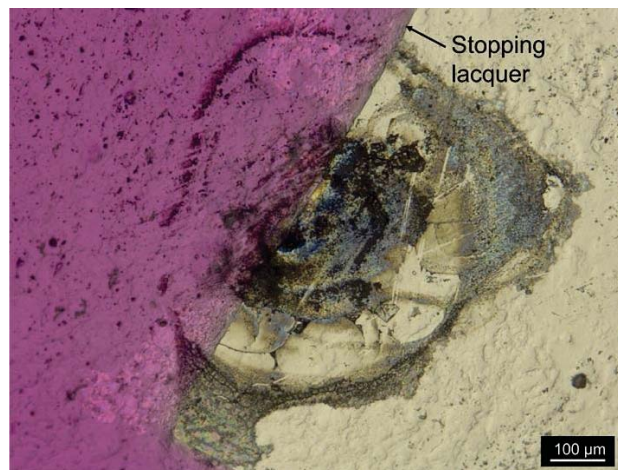


Figure 6.21: An optical image showing the occurrence of pitting on the surface of the SLM fabricated NiTi alloy



Figure 6.22: An optical image showing a non-corroded region on the surface of the SLM fabricated NiTi alloy

Higher magnification SEM images of the pit on the surface of the SLM fabricated NiTi alloy can be seen in figures 6.23 – 6.25. The centre of the pit has a diameter of approximately 5 μm . Cracks appear to propagate from the pit. Residual stresses that had formed in the material during SLM manufacturing (17) could be the cause of the stress corrosion cracking.

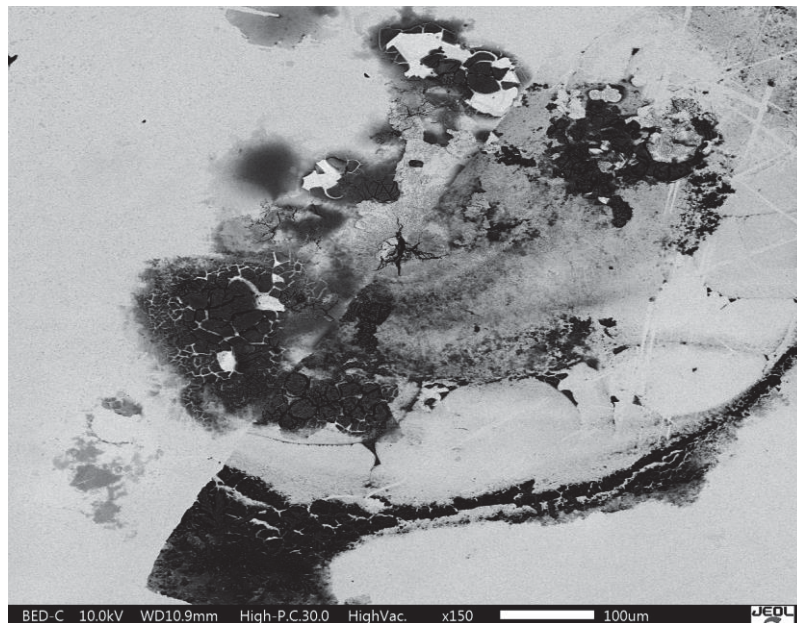


Figure 6.23: A SEM image of the pitting corrosion on the surface of the SLM fabricated NiTi alloy (x150 magnification)

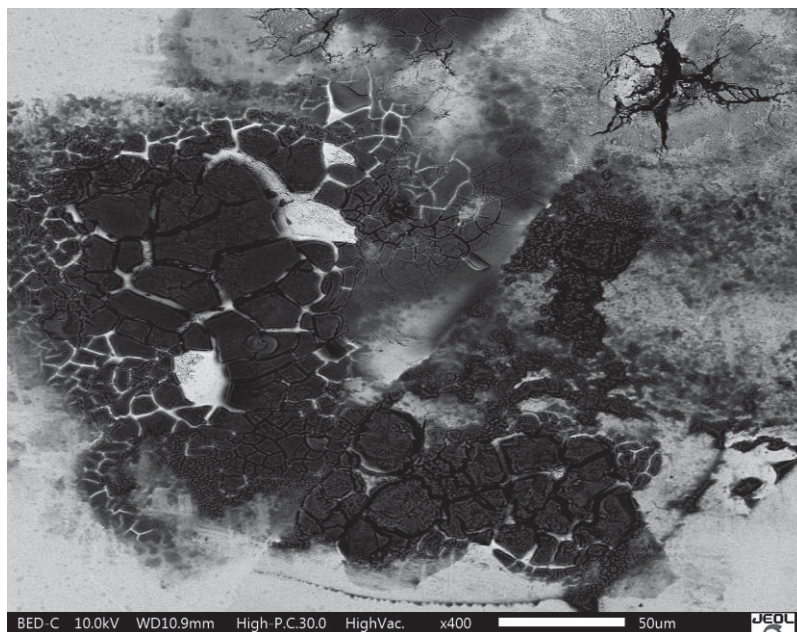


Figure 6.24: A SEM image of the pitting corrosion and resultant corrosion products on the surface of the SLM fabricated NiTi alloy (x400 magnification)

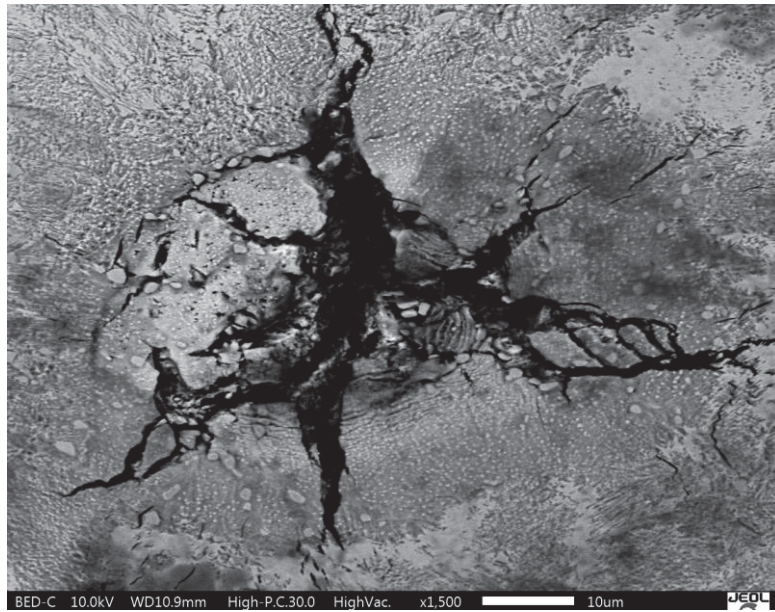


Figure 2.25: A SEM image of the pitting corrosion on the surface of the SLM fabricated NiTi alloy (x 1500 magnification)

Figures 2.26 and 2.27 display the SEM images taken of the surface of the SLM fabricated ternary $\text{Ti}_{50}\text{Ni}_{43}\text{Pd}_7$ (at %) alloy and the conventionally produced NiTi ingot. As the alloys did not experience a breakdown of passivity during the electrochemical testing, as expected no pitting corrosion was visible.

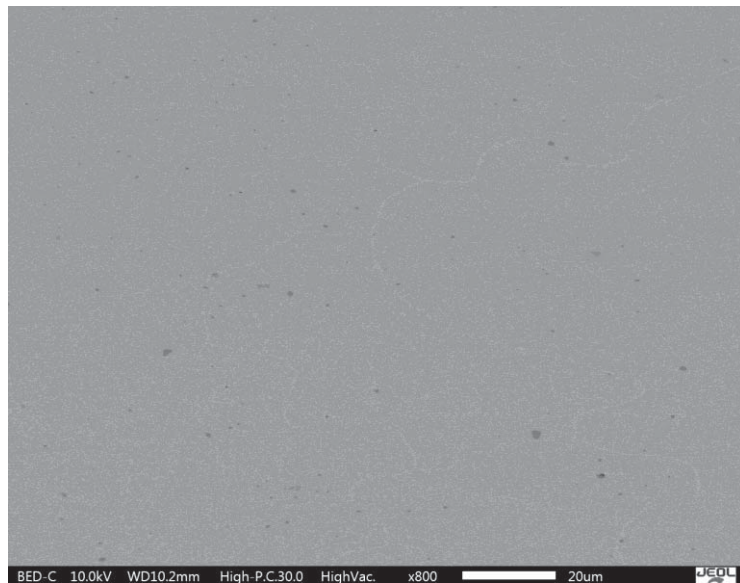


Figure 6.26: A SEM image of the surface of the SLM fabricated ternary $\text{Ti}_{50}\text{Ni}_{48}\text{Pd}_7$ (at %) alloy (x 800 magnification)

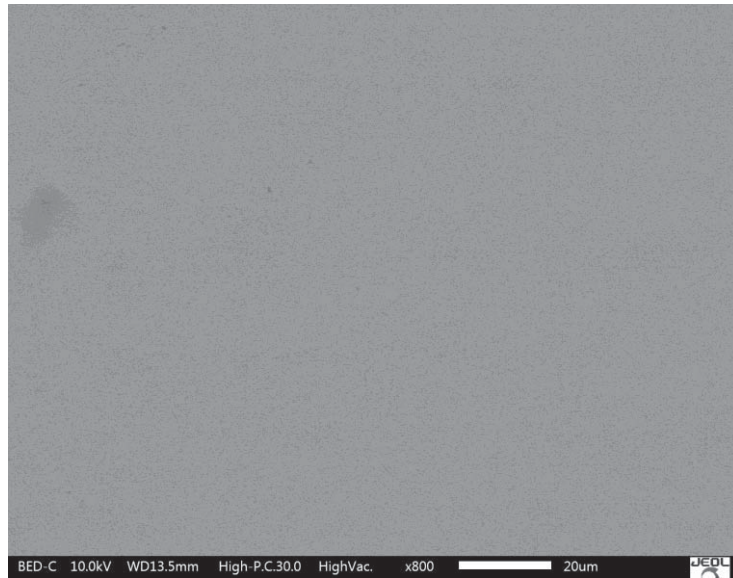


Figure 6.27: A SEM image of the surface of the conventionally produced NiTi alloy (x 800 magnification)

6.6. Conclusion

The aim of this chapter was to be able to draw a comparison between SLM manufactured NiTi and $\text{Ti}_{50}\text{Ni}_{43}\text{Pd}_7$ (at %), whilst investigating its practicality for use in biomedical applications. Overall, the addition of 7 at % Pd to NiTi SMA appeared to have a positive impact on the properties of binary NiTi. All samples were successfully manufactured, showing exciting prospects for the future of SLMing binary and ternary NiTi SMAs. However, this manufacturing process did not achieve the same results as conventionally produced NiTi.

It was found that heat treatment is an essential step towards improving the superelastic response of SLM fabricated alloys. The lowest irrecoverable strain of 0.7 % was found in samples that had been solution heat treated (950°C for 5.5 hours, followed by water quenching) and aged at 350°C for 1.5 hours. From the SEM micrographs it is evident that this heat treatment resulted in the precipitation of the small and coherent $\text{Ti}_2\text{Ni}(\text{Pd})$ intermetallic within the NiTi matrix. This secondary phase appeared to improve the strength of the alloy through the precipitation hardening effect. However, as the precipitation grew in size with increased aging time, its

strengthening effect decreased as the precipitates became less effective at hindering dislocation motion.

As expected, when 7 at % Ni was substituted by Pd, the X-ray visibility of the binary NiTi alloy improved by 25 % against the X-ray background. The higher atomic number and density of the Pd atoms, increases the X-ray attenuation. Thus, enhancing the contrast during X-ray for the Ti₅₀Ni₄₃Pd₇ at % alloy. The increased radiopacity of the alloy will be extremely beneficial during minimally invasive surgeries where keyhole surgeries will help to decrease patient trauma and recovery time.

Both the binary and Pd modified NiTi alloy proved to be biocompatible, where successful cell culture occurred on both of the SLM manufactured alloy's polished surfaces. By the seventh day of testing, cells appeared more healthy on the Ti₅₀Ni₄₃Pd₇ (at %) alloy. A possible reason for this could be due to the replacement of toxic Ni atoms with inert Pd atoms. Although live cells were evident on both of the SLM fabricated alloys by the seventh day of testing. The conventionally produced Ti64 alloy appeared to have the highest biocompatibility. The alloy experienced the greatest cell proliferation, with the fewest dead cells by day seven testing.

For the SLM manufactured alloys, the addition of Pd appeared to improve the corrosion resistance of the NiTi alloy and strengthen the protective oxide layer. The SLM binary NiTi alloy experienced a localised breakdown of passivity. SEM micrographs revealed a pit had formed on the surface of the NiTi alloy. During the forward scan, the conventionally produced NiTi ingot had the highest corrosion resistance with a 2.4×10^{-6} mA/cm² current density and a corrosion potential of 935.8 mV. However, the ternary TiNiPd alloy was the most corrosion resistant during the backwards scan with a corrosion potential of -451.02 mV and a current

density of $2.5 \times 10^{-8} \text{ mA/cm}^2$. The improved corrosion protection is believed to be due to the surface layer becoming more enriched with Pd.

6.7. References

1. Greiner C, Oppenheimer SM, Dunand DC. High strength, low stiffness, porous NiTi with superelastic properties. *Acta Biomater.* 2005;1(6):705–16.
2. Civile I. SMA Biomedical Applications. 2015. 307-341 p.
3. Leon A, Aghion E. Effect of surface roughness on corrosion fatigue performance of AlSi10Mg alloy produced by Selective Laser Melting (SLM). *Mater Charact.* 2017;131(December):188–94.
4. United States Patent Boylan et al. METHOD FOR PROVIDING RADIOPAQUE (10) Patent No .: (45) Date of Patent : i. 2011;2(12).
5. Haberland C, Elahinia M, Walker JM, Meier H, Frenzel J. On the development of high quality NiTi shape memory and pseudoelastic parts by additive manufacturing. *Smart Mater Struct* [Internet]. 2014;23(10):104002.
6. Saedi S, Turabi AS, Andani MT, Haberland C, Karaca H, Elahinia M. The influence of heat treatment on the thermomechanical response of Ni-rich NiTi alloys manufactured by selective laser melting. *J Alloys Compd* [Internet]. 2016;677:204–10.
7. Chluba C, Ge W, Dankwort T, Bechtold C, de Miranda RL, Kienle L, et al. Effect of crystallographic compatibility and grain size on the functional fatigue of sputtered TiNiCuCo thin films. *Philos Trans R Soc A Math Phys Eng Sci* [Internet]. 2016;374(2074):20150311.

8. Efstathiou C, Sehitoglu H. Local transformation strain measurements in precipitated NiTi single crystals. *Scr Mater* [Internet]. 2008;59(12):1263–6.
9. Tofail SAM, Butler J, Gandhi AA, Carlson JM, Lavelle S, Carr S, et al. X-ray visibility and metallurgical features of NiTi shape memory alloy with erbium. *Mater Lett*. 2014;137:450–4.
10. Limkitjaroenporn P, Kaewkhao J, Chewpraditkul W, Limsuwan P. Mass attenuation coefficient and effective atomic number of Ag/Cu/Zn alloy at different photon energy by compton scattering technique. *Procedia Eng* [Internet]. 2012;32:847–54.
11. Nava-Dino CG, Lopez-Melendez C, Bautista-Margulis RG, Neri-Flores MA, Chacon-Nava JG, de la Torre SD, et al. Corrosion Behavior of Ti-6Al-4V alloys. *Int J Electrochem Sci*. 2012;7(3):2389–402.
12. Cox SC, Jamshidi P, Eisenstein NM, Webber MA, Burton H, Moakes RJA, et al. Surface Finish has a Critical Influence on Biofilm Formation and Mammalian Cell Attachment to Additively Manufactured Prosthetics. *ACS Biomater Sci Eng*. 2017;3(8):1616–26.
13. Liu JX, Yang DZ, Shi F, Cai YJ. Sol-gel deposited TiO₂ film on NiTi surgical alloy for biocompatibility improvement. *Thin Solid Films*. 2003;429(1–2):225–30.
14. Michiardi A, Aparicio C, Planell JA, Gil FJ. New oxidation treatment of NiTi shape memory alloys to obtain Ni-free surfaces and to improve biocompatibility. *J Biomed Mater Res - Part B Appl Biomater*. 2006;77(2):249–56.
15. Fern CD, Vimalanandan A, Altin A, Mondrag JS, Kreth K, Keil P, et al. *Soft Matter at Aqueous Interfaces* [Internet]. Vol. 917. 2016.

16. Cotton JB. The Role of Palladium In Enhancing Corrosion Resistance of Titanium. 1967;(2):50–2.
17. Liu Y, Yang Y, Wang D. A study on the residual stress during selective laser melting (SLM) of metallic powder. Int J Adv Manuf Technol [Internet]. 2016;1–10.

Chapter 7

Conclusion, Evaluation and Future Work

7.1. Overall Conclusions

From the work presented in this thesis, it can be said that alloying NiTi with 7 at % Pd improved the binary alloy for application in biomedical applications although with an increased cost as Pd is a precious metal. The enhanced corrosion resistance, radiopacity and biocompatibility would improve the quality and longevity of the implantable device, reducing the risk of implant failure and need for replacement. Furthermore, the addition of Pd improved the alloy's X-ray visibility by 24 %. Thus, the Pd modified alloy would be able to aid the use of minimally invasive surgeries. Not only decreasing patient recovery time but also patient trauma.

Although the ternary alloy remained martensitic at body temperature, the addition of up to 7 at % Pd appeared to decrease the transformation temperature of the binary NiTi alloy. The ternary TiNiPd alloy would be a good choice for orthopaedic implants such as hip implants where the material's martensitic structure has a Young's modulus similar to that of human bone. Thus, this material selection would reduce the risk of bone degradation that ultimately leads to aseptic loosening and implant failure. However, for angioplasty and vascular implants, such as self-expanding stents, a promising composition has been identified, where the A_F transformation temperature of the ternary alloy decreased to 35 °C after the addition of 1 at % Cr. Consequently the quaternary $Ti_{50}Ni_{42}Pd_7Cr_1$ (at %) alloy would be fully austenitic at body temperature and show superelastic behaviour once inserted inside the human body.

It was found that the transformation temperature of ternary $Ti_{50}Ni_{43}Pd_7$ (at %) could be tailored through the use of heat treatments. To achieve a homogeneous microstructure, a solution heat

treatment was identified where the alloy was heated up to 950 °C for 5.5 hours, followed by immediate water quenching. However, additional aging after the solution heat treatment resulted in the precipitation of a Ti-rich, $\text{Ti}_2\text{Ni(Pd)}$ intermetallic. The presence of this secondary phase depleted Ti from the matrix and the Ni:Ti ratio of the matrix shifted towards Ni-richer values. Aging up to 3 hours at 350 °C decreased the transformation temperature of the alloy by 10 °C.

The $\text{Ti}_2\text{Ni(Pd)}$ intermetallic phase was also found to have an effect on the superelastic response of the alloy. A fine and uniform dispersion of these precipitates improved the strength of the alloy through the precipitation hardening effect and thus enhanced the superelastic response of the alloy. However, it was found that aging for prolonged periods had a negative effect on the superelastic response of the ternary alloy. As with aging time, the size of the $\text{Ti}_2\text{Ni(Pd)}$ precipitates increased, resulting in a lower hardening effect.

It was found that the addition of 7 at % Pd improved the corrosion resistance of the SLM fabricated binary NiTi alloy. Unlike the binary alloy, the ternary $\text{Ti}_{50}\text{Ni}_{43}\text{Pd}_7$ (at %) did not experience a breakdown of its passive layer through the occurrence of pitting corrosion, indicating that the presence of the passivating Pd element offered anodic protection. The enhanced corrosion resistance of the ternary alloy was reflected during the biocompatibility testing. After day seven of testing, the cultured MC3T3-E1 cells appeared to have proliferated and spread better on the surface of the ternary alloy. Additionally, the substitution of 7 at % Ni for Pd appeared to improve the health and viability of the cells after the seventh day of testing, suggesting a potential improvement in biocompatibility, due to the reduction of Ni and its cytotoxic effects.

7.2. An Evaluation of the SLM Process for Manufacturing Ternary TiNiPd Alloys for Biomedical Applications

Manufacturing NiTi using SLM overcomes the current manufacturing issues as the alloy is extremely difficult to machine. Furthermore, it opens up the possibility of creating more complex geometries that would not be possible using conventional techniques. Parametric studies have proven the ability of SLM to produce highly dense (> 99%) NiTi and TiNiPd parts with no cracking. Furthermore, a methodology has been identified that can alloy elemental powders (Pd and Cr) homogeneously into the NiTi matrix, whilst simultaneously manufacturing a high quality, near net-shape component. Thus, highlighting the capabilities of SLM to be a more cost and time efficient manufacturing process in comparison to traditional methods.

The binary SLM NiTi had a lower corrosion resistance during testing in comparison to the conventionally produced NiTi ingot. This indicates more attention is required to investigate the influence of SLM microstructural defects. The presence of these defects could accelerate the alloy's corrosive behaviour.

If SLM is to become an industrialised process, that can manufacture NiTi and TiNiPd parts which can be placed directly inside the human body, then the surface quality and geometrical precision of the as-fabricated parts must be improved. The option of the as-fabricated parts receiving surface modification or final laser cutting, opens up exciting possibilities for the additive manufacturing of biomedical components. Chemical treatments such as acid etching or anodization can be used to improve the surface quality and the alloy's mechanical behaviour.

7.3 Future Work

In this research, the in-situ alloying of TiNiPd SMAs using the Concept Laser M2 SLM machine was performed for the first time. The effects of SLM processing parameters have been studied to obtain a greater understanding of the behaviour of this alloy during and after manufacturing. The recommendations for future work within the scope of this research thesis include further investigations into the elemental Ni evaporation and the quaternary TiNiPdCr alloy composition.

Ni evaporation during the laser processing of NiTi SMAs is one of the most problematic consequences of manufacturing using SLM. Due to the increase in the transformation temperature of the SLM fabricated part, in comparison to the metallic powder used, the material's intended application can be affected. Future work could look into providing a model that could predict the Ni loss during processing based on the processing parameters used and the consequence they have on the melt pool dimension. Thus, giving a better indication into the feedstock powder's Ni:Ti ratio, as this will be different to the composition of the final SLM NiTi part.

A quaternary alloy composition was identified in chapter 5, which could reduce the A_F transformation temperature of ternary $Ti_{50}Ni_{43}Pd_7$ (at %) to below body temperature. By alloying with 1 at % Cr in substitution for Ni, the transformation temperature dropped to approximately 35 °C. Future work could involve optimising a solution heat treatment, in order to create a sharper transformation peak. Additionally, although Cr is already used in metallic implants, it is critical to assess the effect this doping element has on the corrosion resistance and biocompatibility of the SLM fabricated ternary TiNiPd alloy. Finally, angioplasty and vascular implants, such as self- expanding stents require superelasticity below body temperature. As the $Ti_{50}Ni_{42}Pd_7Cr_1$ (at %) has an A_F below 37°C, it is suitable for this application. Thus, further work could look into optimising an aging treatment temperature and

time scale. By doing this a perfect strain recovery could be achieved through the alloy's enhanced intrinsic strength. Once this has been achieved, it is important to test the alloy's fatigue resistance. As traditionally, stents are subjected to approximately 400 million cycles under severe physiological pressures (equivalent to approximately ten years in the body) prior to being placed inside the human body (1).

7.4. References

1. Gong X-Y, Chwirut DJ, Mitchell MR, Choules BD. Fatigue to Fracture : An Informative , Fast , and Reliable. ASTM Int. 2009;6(7):1–10.